Using Non-Lubricated Squeeze Flow to Obtain Empirical Parameters for Modeling the Injection Molding of Long-Fiber Composites

Gregory Lambert

Dissertation submitted to the faculty of Virginia Polytechnic Institute and State University in partial fulfillment of the requirements for the degree of

Doctor of Philosophy
in
Chemical Engineering

Donald G. Baird, Chair
Richey M. Davis
Stephen M. Martin
Peter Wapperom

September 14th, 2018
Blacksburg, VA

Keywords: Shear Flow, Extensional Flow, Squeeze Flow, Fiber Composites, Fiber Orientation

Using Non-Lubricated Squeeze Flow to Obtain Empirical Parameters for Modeling the Injection Molding of Long-Fiber Composites

Gregory Lambert

Abstract

The design of fiber-reinforced thermoplastic (FRT) parts is hindered by the determination of the various empirical parameters associated with the fiber orientation models. A method for obtaining these parameters independent of processing doesn't exist. The work presented here continues efforts to develop a rheological test that can obtain robust orientation model parameters, either by fitting directly to orientation data or by fitting to stress-growth data.

First, orientation evolution in a 10 wt% long-glass-fiber-reinforced polypropylene during two homogeneous flows (startup of shear and planar extension) was compared. This comparison had not been performed in the literature previously, and revealed that fiber orientation is significantly faster during planar extension. This contradicts a long-held assumption in the field that orientation dynamics were independent of the type of flow. In other words, shear and extension were assumed to have equal influence on the orientation dynamics.

A non-lubricated squeeze flow test was subsequently implemented on 30 wt% short-glass-fiber-reinforced polypropylene. An analytical solution was developed for the Newtonian case along the lateral centerline of the sample to demonstrate that the flow is indeed a superposition of shear and extension. Furthermore, an existing fiber orientation model was fit to the gap-wise orientation profile, demonstrating that NLSF can, in principle, be used to obtain fiber orientation model parameters. Finally, model parameters obtained for the same FRT by fitting to orientation data from startup of steady shear are shown to be inadequate in predicting the gap-wise orientation profile from NLSF.

This work is rounded out with a comparison of the fiber orientation dynamics during startup of shear and non-lubricated squeeze flow using a long-fiber-reinforced polypropylene. Three fiber concentrations (30, 40, and 50 wt%) were used to gauge the influence of fiber concentration on the orientation dynamics. The results suggest that the initial fiber orientation state (initially perpendicular to the flow direction and in the plane parallel to the sample thickness) and the fiber concentration interact to slow down the fiber orientation dynamics during startup of shear when compared to the dynamics starting from a planar random initial state, particularly for the 40 and 50 wt% samples.

However, the orientation dynamics during non-lubricated squeeze flow for the same material and initial orientation state were not influenced by fiber concentration. Existing orientation models do not account for the initial-state-dependence and concentration-dependence in a rigorous way. Instead, different fitting parameters must be used for different initial states and concentrations, which suggests that the orientation models do not accurately capture the underlying physics of fiber orientation in FRTs.

Using Non-Lubricated Squeeze Flow to Obtain Empirical Parameters for Modeling the Injection Molding of Long-Fiber Composites

Gregory Lambert

General Audience Abstract

In order to keep pace with government fuel economy legislation, the automotive and aerospace industries have adopted a strategy they call "lightweighting". This refers to decreasing the overall weight of a car, truck, or plane by replacing dense materials with less-dense substitutes. For example, a steel engine bracket in a car could be replaced with a high-temperature plastic reinforced with carbon fiber. This composite material will be lighter in weight than the comparable steel component, but maintains its structural integrity.

Thermoplastics reinforced with some kind of fiber, typically carbon or glass, have proven to be extremely useful in meeting the demands of lightweighting. Thermoplastics are materials that can be melted from a feedstock (typically pellets), reshaped in the melted state through use of a mold, and then cooled to a solid state, and some common commodity-grade thermoplastics include polypropylene (used for Ziploc bags) and polyamides (commonly called Nylon and used in clothing). Although these commodity applications are not known for their strength, the fiber reinforcement in the automotive applications significantly improves the structural integrity of the thermoplastics.

The ability to melt and reshape thermoplastics make them incredibly useful for high-throughput processes such as injection molding. Injection molding takes the pellets and conveys them through a heated barrel using a rotating screw. The melted thermoplastic gathers at the tip of the barrel, and when a set volume is gathered, the screw is rammed forward to inject the thermoplastic into a closed mold of the desired shape. This process typically takes between 30-60 seconds per injection. This rate of production is crucial for the automotive industry, as manufacturers need to put out thousands of parts in a short period of time.

The improvement to mechanical properties of the thermoplastics is strongly influenced by the orientation of the reinforcing fibers. Although design equations connecting the part's mechanical properties to the orientation of the fibers do exist, they require knowledge of the orientation of the fibers throughout the part. Fibers in injection-molded parts have an extremely complicated orientation

state. Measuring the orientation state at each point would be too laborious, so empirical models tying the flow of the thermoplastic through the mold to the evolving orientation state of the fibers have been developed to predict the orientation state in the final part. These predictions can be used in lieu of direct measurements in the part design equations. However, the orientation models rely on empirical fitting parameters which must be obtained before injection molding simulations are performed. There is currently no standard test for obtaining these parameters, nor is there a standardized look-up table.

The work presented in this dissertation continues efforts to establish such a test using simple flows in a laboratory setting, independent of injection molding. Previous work focused exclusively on using shearing flow (e.g. pressure-driven flow found in injection molding) to obtain these parameters. However, when these parameters were used in simulations of injection molding, the agreement between measured and predicted fiber orientation was mediocre. The work here demonstrates that another type of flow, namely extensional flow, must also be considered, as it has a non-negligible influence on fiber orientation. this is crucial to injection molding, as injection molding flows have elements of both shearing and extensional flow.

The first major contribution from this dissertation demonstrates that extensional flow (e.g. stretching a film) has a much stronger influence than shearing flow, even at the same overall rate of deformation. The second major contribution used a combination shear/extensional flow to demonstrate that the empirical model parameters, thought to be characteristic of the composite, are actually strongly influenced by the type of flow experienced by the sample, and that no single set of model parameters can fit the full orientation state. The final major contribution extends the previous case to long-fiber reinforcement at multiple fiber concentrations which are of industrial interest. This finds the same results, that the model parameters are dependent on the type of flow experienced by the sample. The flow-dependence of the parameters is a crucial point to address in future work, as the flows found in injection molding contain both shearing and extensional flow. By further developing this flow-type dependence, future injection molding simulations should become more accurate, and this will make computer-aided injection-molded part design much more efficient.

Acknowledgements

Of all the sections of this dissertation, this has been both the easiest and hardest to write. Easy in that I have no shortage of thanks to give, yet hard because I don't think I can fully convey my thanks with my meager abilities.

First, I want to thank my advisor, Dr. Donald Baird. Without your support, both financial and professional, I would not be the researcher I am today. I would also be remiss if I didn't thank my advisory committee, Drs. Peter Wapperom, Stephen Martin, and Richey Davis. Your insights have been invaluable in helping me understand my project and how to conduct solid research. I also have to thank Dr. Michael Bortner for his help as well. You graciously let me access the equipment that has made my work possible and have been an excellent source of insight and a sounding board for ideas.

Next, I'd like to thank current and past members of the Baird lab (in no particular order): Mark Cieslinski, Kevin Herrington, Chen Qian, Hongyu Chen, Craig Mansfield, Rebecca Minnick, Jianger Yu, Mubashir Ansari, Juan Pretelt, Vikas Parakh, Kennedy Boyce, Jier Yang, and Tianran Chen. All of you have helped me in some way, whether with insightful comments, forcing me to think on my feet with questions, or just commiserating.

A big "Thank You" to the Chemical Engineering Department's staff: Diane Cannaday, Tina Russell, Stacey Ratcliffe, Jane Price, Mike Vaught, Kevin Holshouser, and Riley Chan. Sorry for forcing you to suffer through my boundless clerical and mechanical incompetence. Without your help, much of this work would not have been possible.

The grind of grad school would be insufferable if not for friends. I thank all of the friends I've made here for making my time richer than I could have hoped. In particular, and in no order: Yan Zhu, Ami Jo, Prudvi Gaddam, Jimmy Dickmann, Han Chen, Ethan Smith, Wenhui Li, Ayaan Kazerouni, Sai Mukherjee, Travis Murphy, Kathleen Chan, Jake Fallon, Mick Williams, Yow-Ren Chang, Andrew and Hillary Ford, and Sophie Orbach.

Last and most important, I thank my parents, Michael and Susan Lambert, and my brothers, Kevin and Dana Lambert. Without your unflagging support, grad school would have been much harder. I am incredibly fortunate to have you all in my corner.

Original Contributions

The following are considered original contributions to the larger body of work on fiber-reinforced thermoplastics:

1. This work shows conclusively that the rate of fiber reorientation during flow is influenced by the type of flow field experienced by the fibers. Work in the past has focused on fiber reorientation during startup of simple shear only. Comparisons between shear and extension only consider the steady state viscosity curves, which do not provide insight on the transient fiber orientation dynamics. This knowledge gap has led to the mistaken assumption throughout the literature that the rate of fiber reorientation does not change with the flow field.

2. This works demonstrates that non-lubricated squeeze flow can be a useful test for evaluating fiber orientation models. Both shear and extensional flow are present in the flow field, which allows researchers to investigate how the interaction between the two flows influences fiber orientation dynamics. This interaction is important because both shear and extensional flow are present in injection-molding flows.

3. This work suggests that the current theoretical treatment of the strain reduction phenomenon is lacking and provides a solid experimental justification for making the implementation of strain reduction in an orientation model dependent on the flow type. Currently, orientation models account for apparent strain reduction by using a single, constant scalar value.

Format of Dissertation

Chapter one consists of a brief overview of the general concepts behind this work. The rheological study of fiber-reinforced polymer suspensions is placed in the context of obtaining fiber orientation model parameters to assist in computer-aided design work for fiber-reinforced thermoplastic parts used in the automotive industry.

Chapter two provides a review of the existing literature, exploring in more detail the rheological behavior of fiber suspensions, the mathematical development of fiber orientation models and the assumptions that come with them, the justification for the squeeze flow technique proposed in this dissertation, and the use of rheological tests to obtain fiber orientation model parameters and their success in injection molding simulations.

Chapters three and four are two papers published before this dissertation. The manuscript for Chapter three was published as the article "Evaluating rigid and semiflexible fiber orientation evolution models in simple flows" by myself and Dr. Donald Baird in volume 139 of *the Journal of Manufacturing Science and Engineering* in March, 2017. Chapter four was published as the article "Obtaining short-fiber orientation model parameters using non-lubricated squeeze flow" by myself, Dr. Peter Wapperom, and Dr. Donald Baird in the 12th issue of volume 29 of *Physics of Fluids* in November, 2017. Minor edits have been made to keep the style of the papers consistent with this dissertation as a whole. Chapter five is in the form of a manuscript to be submitted for publication at a later date.

Chapter six proposes the direction future work should take and is followed by appendices containing the hard data used in the work presented in this dissertation. In line with standard manuscript submission guidelines, the figures and tables in chapters 3-5 are listed after the references in each chapter.

Table of Contents

Table of Figures

List of Tables

Chapter 1: Introduction

1.1 Fiber-Reinforced Thermoplastics

Government fuel economy targets and vehicle emissions regulations present the two most important long-term considerations for the automotive industry. Manufacturers have employed multiple strategies to meet these goals, but "lightweighting" has been a major focus in recent years.[1] The concept is simple: replace traditional, dense materials like steel with less dense materials like aluminum and, more pertinent to this work, fiber-reinforced polymers. The choice of polymer-fiber system is determined by cost, required part performance, and ease of processing.

Parts with very simple geometries or high performance requirements can be made using a thermosetting resin reinforced with continuous strands of fibers all oriented in the same direction. Sheets of this material can be laid onto a frame and cured. The theoretical treatment of these continuous-fiber-reinforced parts has reached a point at which the mechanical properties of the part can be accurately predicted before the part is made, so parts can be designed *a priori*. Complicated geometries, such as an engine bracket (Fig. 1.1), cannot be made this way. Instead, these parts must be injection molded with a fiber-reinforced thermoplastic (FRT).

Fig 1.1 Bracket used to secure an engine in a car. Note that the part is not a solid block of material and has narrow supporting beams. The beams and gross shape of the part make using thermosetting materials impossible. FRTs must be used to make this part. [Source: Amanda Jacob, "Daimler replaces aluminium engine support with composite in Mercedes GL class." 6 Mar 2013. http://www.materialstoday.com/composite-applications/news/daimler-replaces-aluminium-engine-support-with/]

Injection molding results in a broad fiber length distribution and a non-uniform fiber orientation state, both of which change throughout the part.[2] The mechanical properties of these parts can still be predicted, but *a priori* design work requires knowledge of the fiber length and orientation distribution throughout the part. Models that can predict fiber attrition and orientation during

injection molding are a boon to the engineer designing the injection-molded FRT part. Herein lies the problem facing engineers: existing models of fiber attrition and orientation dynamics are empirical and must be fit to experimental data, yet this data cannot be obtained without first making the part. Parts must be made using an iterative design methodology illustrated in Fig. 1.2. Without a reliable method for obtaining the fitting parameters independent of processing, the FRT part design process ends when the manufacturer runs out of time, money, material, or some combination of the three. This can result in parts with suboptimal, but still acceptable, mechanical performance. More importantly, the iterative nature of the design work severely hinders the speed at which FRT parts can be brought to market. The ultimate goal of this work is to identify a reliable test for obtaining fiber orientation model parameters that is independent of processing, allowing for *a priori* design of injection-molded FRT parts.

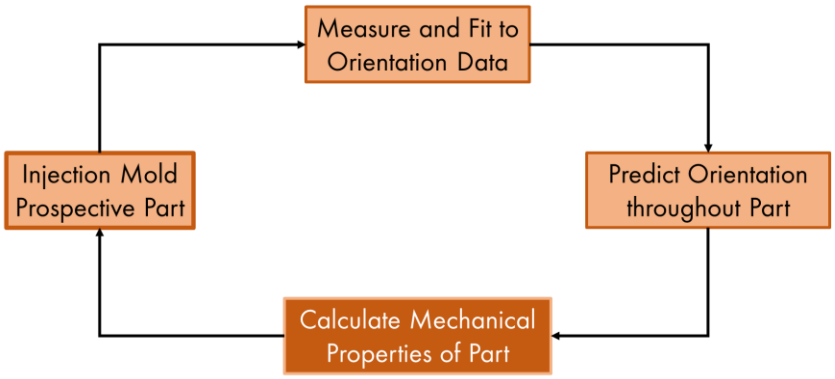

Fig. 1.2: Graphical representation of the design methodology for FRT parts. Bear in mind that the fiber orientation is only of interest in that it allows designers to predict the mechanical properties of the part. If the mechanical property predictions are not up to the manufacturer's standards then a new part is made and the cycle continues. A first principles design methodology would start by obtaining model parameters, then use processing simulation software to screen various mold designs and sets of processing conditions (barrel zone temperatures, screw speed, mold temperatures, &c.). A physical part would only be needed to verify the most promising designs.

Section 1.2 briefly covers the fiber orientation models, and section 1.3 provides a quick look at previous work on the fiber orientation dynamics in startup of simple shear and extension. These concepts are combined in section 1.4 for a brief discussion covering how various suspension stress models (which correlate the suspension stress and fiber orientation state) have been used to obtain fiber orientation model parameters. Section 1.5 then sketches out the successes and failures of injection molding simulations using fiber orientation model parameters obtained from rheological tests. This chapter closes with a statement of the ultimate objectives of this work.

1.2 Fiber Orientation Models

By all accounts, Jeffery[3] seems to have pioneered the investigation of fiber orientation dynamics with his treatment of a single fiber suspended in a Newtonian fluid. The primary result from this work was that fibers continuously rotate through a set orbit during homogeneous shear flow and align in the principal straining direction during uniaxial extension. Later, Folgar and Tucker[4] developed a model extending Jeffery's work to semi-concentrated suspensions, in which fibers can interact through the perturbations in the velocity field they induce. These hydrodynamic interactions randomize the fiber orientation, akin to Brownian motion, resulting in a lower degree of orientation relative to Jeffery's model. The interactions also stop fibers from continuously rotating during homogeneous shear flow, instead settling at a steady orientation state at large shear strains.

This modification did not adequately predict fiber orientation in injection-molded FRT parts with short-fiber reinforcement (i.e. average length less than 1 mm). Wang et al.[5] later rectified this by introducing a mechanism in the Folgar-Tucker model through which the total strain experienced by the suspension could be reduced using an empiricism in the hydrodynamic terms. Phelps et al.[6] introduced anisotropy to the rotary diffusion term introduced by Folgar and Tucker to obtain a better fit to the orientation profiles observed in FRT parts with long-fiber reinforcement (i.e. average length longer than 1 mm). Models from Tucker's research have been implemented in commercial injection molding simulation software and have been the basis of comparison for other orientation models. Tseng and coworkers[7, 8, 9, 10] have been the primary drivers of continued development of these models in recent years.

Long-fiber reinforcement results in significant improvements to important properties such as strength and fracture resistance over short-fiber reinforcement, so manufacturers are interested in making parts with long-fiber reinforcement. However, long fibers have been shown to flex during processing.[11] The Tucker family of models is fundamentally incapable of capturing this behavior, as they assume the fibers are rigid enough not to flex. Strautins and Latz[12] proposed an orientation model for dilute suspensions of semi-flexible fibers, and Ortman et al.[13] extended the analysis to concentrated suspensions. Although more recent than the Tucker models, the "Bead-Rod" model proposed by Ortman et al.[14] has shown promise in predicting orientation in injection molded parts.

All of these fiber orientation models feature empirical parameters. Recall from Section 1.1 that the fiber orientation state is only interesting inasmuch as it allows an engineer to predict the mechanical properties of a prospective injection-molded FRT part. The fiber orientation model of choice is fit to the orientation state at some point in a part, and the model is used to predict the orientation state

throughout the rest of the part. This circumvents the need to measure the fiber orientation state at several locations. It also ties the parameters to the processing conditions. Under this design methodology, the empirical parameters are not treated as material properties of the suspension, even though this interpretation of the parameters is implied. Unfortunately, a test which obtains a definitive set of empirical parameters independent of processing does not exist. A key objective of the work presented in this dissertation is to evaluate how well parameters obtained from two different flows, startup of simple shear and non-lubricated squeeze flow, perform in the simulation of an injection molded part.

1.3 Rheological Experiments for Obtaining Orientation Model Parameters

Traditionally, fiber orientation model parameters are obtained by fitting to fiber orientation measurements at some point in an injection-molded part.[6, 15] This takes considerable time and effort. Moreover, this strategy does not lend itself to *a priori* part design, requiring instead an iterative design methodology. An independent test for obtaining the orientation model parameters would remedy this. Rheological tests have been proposed as a solution.[13, 16] Orientation model parameters could be obtained by running startup of shear or extension to a specific strain unit and measuring the orientation at that strain. This can be done for increasingly larger strains, resulting in a profile of fiber orientation with strain. The orientation model of choice could then be fit to the measured orientation evolution data.

Standard rheological tests (e.g. startup of simple shear/uniaxial extension) are useful because they subject a sample to a well-defined and easily-controlled deformation history which can be expressed analytically, simplifying model validation and simulations. From the theoretical perspective, the transient nature of startup flow allows for the observation of the fiber reorientation dynamics. This is crucial for understanding the fiber orientation dynamics during injection molding, which is also a transient process. Fiber suspensions can be sheared using common test fixtures (e.g. parallel plates, cone and plate) with very little modification, so much work on the rheology of fiber suspensions has elected to use startup of shear.[13, 17, 18, 19, 20]

Very little work has investigated the orientation dynamics of fibers during extensional flows, mostly because pure extensional flows (i.e. shear-free flows) are difficult to obtain. Wagner et al.[21] considered sheet-stretching, but the fibers were limited to 2D motion. Mobuchon and coworkers[22] considered flow through a hyperbolic die, but this limited them to steady extensional flow. Dumont

et al.[23] reported perhaps the most promising work on extensional flow. In their work, they used lubricated squeeze flow through a rectangular channel to approximate planar extension and presented both orientation and stress growth data. Unfortunately, work by Venerus and coworkers[24, 25] suggests that adequate lubrication was not maintained during the entire squeeze flow. Proper lubrication hypothetically induces a perfect-slip boundary condition, resulting in shear-free (i.e. extensional) deformation. The breakdown of the lubricating layer introduces shearing. A proper description of the deformation history would require modeling the transition from a shear-free to a mixed shearing and extensional flow field.

The central assumption behind using rheological tests to obtain orientation model parameters is that, so long as the mathematical description of the kinematics is correct, it does not matter if a simple or complex flow field is used. This is the only way to justify extrapolating the orientation dynamics observed during very simple, homogeneous deformations in rheological tests to the orientation dynamics observed in the complex, inhomogeneous flow fields found in injection molding. This ultimately means that the orientation model parameters should not change depending on the type of flow used to obtain them. Even though this is a crucial assumption, no work has been done comparing the orientation dynamics from different flow fields, particularly shear and some extensional flow.

1.4 Suspension Stress Models

Direct measurements of the fiber orientation state require a great deal of time and effort. However, rheological studies have established that the orientation state of the fibers is correlated to the suspension stress, which is typically recorded during the test. An accurate suspension stress model could be used to obtain orientation model parameters by fitting to the stress data.

Lipscomb and Denn[26]derived a model based on Ericksen's Transversely Isotropic Fluid[27] and were able to use it to predict streamlines for a dilute fiber suspension in a Newtonian matrix flowing through a contraction. Their model provided the basis for many more models for semi-concentrated[28, 29] and concentrated[13, 16, 19] suspension stress models, and the models are capable of fitting to stress growth data during startup of simple shear. However, closer analysis by Cieslinski et al.[30] suggests startup of simple shear might not be the ideal case for obtaining orientation model parameters through fitting to stress data. This is because shear stress is dependent on the degree of fiber orientation skewness in the gap-wise direction. Skewness in this direction is small for compression- and injection-molded samples and is also very inconsistent between samples. The resulting signal-to-noise ratio makes experimentally validating the suspension stress models very difficult.

None of the suspension stress models have been used for pure extensional flows, but Cieslinski[11] suggested that these might be a better choice for evaluating the stress models. The extensional stresses are dependent on the flow- and gap-wise-direction orientation, not the skewness of the orientation in these directions. Unlike the skewness in orientation, the orientation itself should be very pronounced and consistent between samples from extensional flows, giving a better signal-to-noise ratio that makes validating the stress model much easier. Of course, this remains to be verified experimentally.

1.5 Injection Molding Simulations

The ultimate expectation is that orientation model parameters obtained from rheological tests accurately predict fiber orientation in an injection molded part. Eberle et al.[16] obtained orientation model parameters for a short-glass-fiber-reinforced poly(butylene terephthalate) by fitting to the stress growth data from startup of simple shear, and Mazahir and coworkers[31, 32] used the parameters to predict orientation in a center-gated disk (CGD; see Fig 1.3a). They found reasonable agreement with experimental data in this case. Ortman and coworkers[13, 14] continued this work, obtaining orientation model parameters for a long-glass-fiber-reinforced polypropylene by fitting to orientation evolution data and using the parameters to predict orientation in a CGD as well. Again, the predictions from the models were reasonable. However, when the short-fiber parameters were used to predict orientation in an end-gated plaque (EGP), they did not even qualitatively predict the fiber orientation (EGP; Fig. 1.3b).[33]

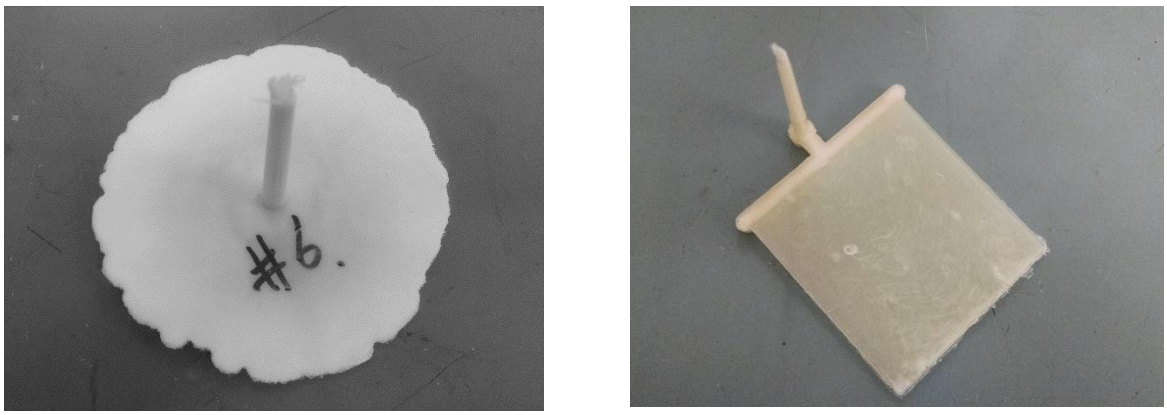

(a) (b)

Fig. 1.3: Photos of two model injection molding geometries: a center-gated disk (a) and an end-gated plaque (b).

Extensional flow might play a stronger role in the EGP than in the CGD. The thinness of the CGD suggests that the flow field is dominated by shearing, except at the center of the sample thickness and the advancing front. Therefore, the success of parameters obtained from startup of simple shear

seems reasonable. As the composite fills the EGP mold, however, it flows through contractions and expansions. These are dominated by extensional flow, yet, as mentioned in section 1.3, very little work has been done to investigate the fiber orientation dynamics in extensional flow. Molds for parts used in industry are even more complicated in shape and fill pattern and could feature extensional flow even more prominently. The assumption that the orientation model parameters are independent of flow type needs to be tested explicitly.

1.6 Research Objectives

The work presented in this dissertation seeks to develop a new rheological test for obtaining fiber orientation model parameters used to simulate the processing of FRTs. A successful test would allow manufacturers to design parts from first principles rather than using an iterative design methodology. In light of this goal, this work is guided by the following objectives:

1. Examine the assumption that the fiber orientation model parameters are independent of the flow field used to obtain them. Do this by fitting orientation models to orientation evolution data from startup of shear and planar extension and comparing the values of the orientation model parameters.

2. Develop a rheological test that incorporates both shear and extensional flow (non-lubricated squeeze flow), and verify that it can be used to obtain orientation model parameters through fitting to the measured fiber orientation.

3. Measure and compare the orientation dynamics between non-lubricated squeeze flow and startup of shear. Fit the orientation models to the orientation data and compare the values of the fitting parameters from non-lubricated squeeze flow with the values of the parameters from the startup of shear. Use this data to suggest which test should be used to obtain orientation model parameters for future injection molding simulation work.

References

1. N. Muller and T. Ellringmann *It's time to reassess materials for automotive lightweighting*; Automotive World: Penarth, UK, 2016; pp 4.
2. S. G. Advani and E. M. Sozer, *Process modeling in composites manufacturing*. Marcel-Dekker, Inc.: New York, NY, 2003; Vol. 59.
3. G. B. Jeffery, "The motion of ellipsoidal particles in a viscous fluid," *Proc. R. Soc. London, Ser. A* **102** (715), 161 (1922).

4. F. Folgar and C. L. Tucker III, "Orientation behavior of fibers in concentrated suspensions," *J. Reinf. Plast. Compos.* **3** (2), 98 (1984).
5. J. Wang, J. F. O'Gara and C. L. Tucker III, "An objective model for slow orientation kinetics in concentrated fiber suspensions: Theory and rheological evidence," *J. Rheol.* **52** (5), 1179 (2008).
6. J. H. Phelps and C. L. Tucker III, "An anisotropic rotary diffusion model for fiber orientation in short- and long-fiber thermoplastics," *J. Non-Newton. Fluid Mech.* **156** (3), 165 (2009).
7. H.-C. Tseng, R.-Y. Chang and C.-H. Hsu, "Phenomenological improvements to predictive models of fiber orientation in concentrated suspensions," *J. Rheol.* **57** (6), 1597 (2013).
8. P. H. Foss, H.-C. Tseng, J. Snawerdt, Y.-J. Chang, W.-H. Yang and C.-H. Hsu, "Prediction of fiber orientation distribution in injection molded parts using moldex3d simulation," *Polym. Compos.* **35** (4), 671 (2014).
9. H.-C. Tseng, R.-Y. Chang and C.-H. Hsu, "An objective tensor to predict anisotropic fiber orientation in concentrated suspensions," *J. Rheol.* **60** (2), 215 (2016).
10. H.-C. Tseng, R.-Y. Chang and C.-H. Hsu, "The use of principal spatial tensor to predict the anisotropic fiber orientatino in concentrated fiber suspensions," *J. Rheol.* **62** (1), 313 (2018).
11. M. J. Cieslinski. *Using a sliding plate rheometer to obtain material parameters for simulating long fiber orientation in injection molded composites*, PhD Thesis. Virginia Tech, 2015.
12. U. Strautins and A. Latz, "Flow-driven orientation dynamics of semiflexible fiber systems," *Rheol. Acta* **46** (8), 1057 (2007).
13. K. Ortman, D. Baird, P. Wapperom and A. Whittington, "Using startup of steady shear flow in a sliding plate rheometer to determine material parameters for the purpose of predicting long fiber orientation," *J. Rheol.* **56** (4), 955 (2012).
14. K. Ortman, D. Baird, P. Wapperom and A. Aning, "Prediction of fiber orientation in the injection molding of long fiber suspensions," *Polym. Compos.* **33** (8), 1360 (2012).
15. B. N. Nguyen, L. Fifield, G. Lambert, D. Baird, J. Wang, F. Costa, C. Tucker III, U. Gandhi, S. Mori, E. Wollan and D. Roland, *Predictive engineering tools for injection-molded long-carbon-fiber thermoplastic composites,* DoE, 2016.
16. A. P. R. Eberle, D. G. Baird, P. Wapperom and G. M. Velez-Garcia, "Using transient shear rheology to determine material parameters in fiber suspension theory," *J. Rheol.* **53** (3), 685 (2009).
17. T. Kitano, T. Kataoka and Y. Nagatsuka, "Shear flow rheological properties of vinylon- and glass-fiber reinforced polyethylene melts," *Rheol. Acta* **23** (1), 20 (1984).
18. M. A. Bibbo, S. M. Dinh and R. C. Armstrong, "Shear flow properties of semiconcentrated fiber suspensions," *J. Rheol.* **29** (6), 905 (1985).
19. M. Sepehr, G. Ausias and P. J. Carreau, "Rheological properties of short fiber filled polypropylene in transient shear flow," *J. Non-Newton. Fluid Mech.* **123** (1), 19 (2004).
20. A. P. R. Eberle, G. M. Vélez-García, D. G. Baird and P. Wapperom, "Fiber orientation kinetics of a concentrated short glass fiber suspension in startup of simple shear flow," *J. Non-Newton. Fluid Mech.* **165** (3–4), 110 (2010).
21. A. H. Wagner, D. M. Kalyon, R. Yazici and T. J. Fiske, "Uniaxial extensional flow behavior of a glass fiber-filled engineering plastic," *J. Reinf. Plast. Comp.* **22** (4), 327 (2003).
22. C. Mobuchon, P. J. Carreau, M.-C. Heuzey, M. Sepehr and G. Ausias, "Shear and extensional properties of short glass fiber reinforced polypropylene," *Polym. Compos.* **26** (3), 247 (2005).
23. P. Dumont, J.-P. Vassal, L. Orgéas, V. Michaud, D. Favier and J.-A. E. Månson, "Processing, characterisation and rheology of transparent concentrated fibre-bundle suspensions," *Rheol. Acta* **46** (5), 639 (2007).
24. M. Kompani and D. C. Venerus, "Equibiaxial extensional flow of polymer melts via lubricated squeezing flow. I. Experimental analysis," *Rheol. Acta* **39**, 444 (2000).
25. D. C. Venerus, M. Kompani and B. Bernstein, "Equibiaxial extensional flow of polymer melts via lubricated squeezing flow. Ii. Flow modeling," *Rheol. Acta* **39**, 574 (2000).
26. G. G. Lipscomb, M. M. Denn, D. U. Hur and D. V. Boger, "The flow of fiber suspensions in complex geometries," *J. Non-Newton. Fluid Mech.* **26** (3), 297 (1988).

27. J. L. Ericksen, "Transversely isotropic fluids," *Kolloid-Zeitschrift* **173** (2), 117 (1960).
28. S. M. Dinh and R. C. Armstrong, "A rheological equation of state for semiconcentrated fiber suspensions," *J. Rheol.* **28** (3), 207 (1984).
29. E. S. G. Shaqfeh and G. H. Fredrickson, "The hydrodynamic stress in a suspension of rods," *Phys. Fluids A* **2** (1), 7 (1990).
30. M. J. Cieslinski, P. Wapperom and D. G. Baird, "Fiber orientation evolution in simple shear flow from a repeatable initial fiber orientation," *J. Non-Newton. Fluid Mech.* **237**, 65 (2016).
31. S. M. Mazahir, G. M. Velez-Garcia, P. Wapperom and D. Baird, "Evolution of fibre orientation in radial direction in a center-gated disk: Experiments and simulation," *Composites Part A* **51**, 108 (2013).
32. S. M. Mazahir, G. M. Velez-Garcia, P. Wapperom and D. Baird, "Fiber orientation in the frontal region of a center-gated disk: Experiments and simulation," *J. Non-Newton. Fluid Mech.* **216**, 31 (2015).
33. K. J. Meyer, J. T. Hofmann and D. G. Baird, "Prediction of short glass fiber orientation in the filling of an end-gated plaque," *Composites Part A* **62**, 77 (2014).

Chapter 2: Literature Review

2.1: General Review

This section introduces the reader to general concepts that do not warrant intense scrutiny, but nonetheless merit brief discussion. Section 2.1.1 quickly reviews the industrial motivations behind the use of discontinuous fiber reinforcement and the importance of Brownian motion and fiber-matrix coupling agents. Section 2.1.2 reviews the two major classification schemes of polymer-fiber composites.

2.1.1: Fiber Reinforced Polymer Composites

Legislative pressure, in the form of increasingly stringent fuel economy and safety regulations, serves as a major source of inspiration for manufacturing processes in the automotive and aerospace industries. In particular, maximizing the strength-to-weight ratio of the various constituent parts in a car or airplane has become a key design point through the past few decades. Thermoplastic and thermoset parts reinforced with continuous fiber mats offer one solution, and these find extensive application in the aerospace industry. However, continuous fiber composites are limited to simple geometries.

Injection molding addresses these shortcomings.[1] Originally a machine for manufacturing unfilled polymer parts, injection molders can process polymer-fiber composites with no modification. The ability to fabricate geometrically complex parts is the major advantage of injection molding over laying up continuous-fiber-reinforced thermosets. This improved processability comes at the cost of control over fiber length and orientation, limiting injection-molded parts to applications requiring only modest mechanical properties. Figure 2.1.1 demonstrates the trade-off between processability and performance for a range of fiber reinforcement types.

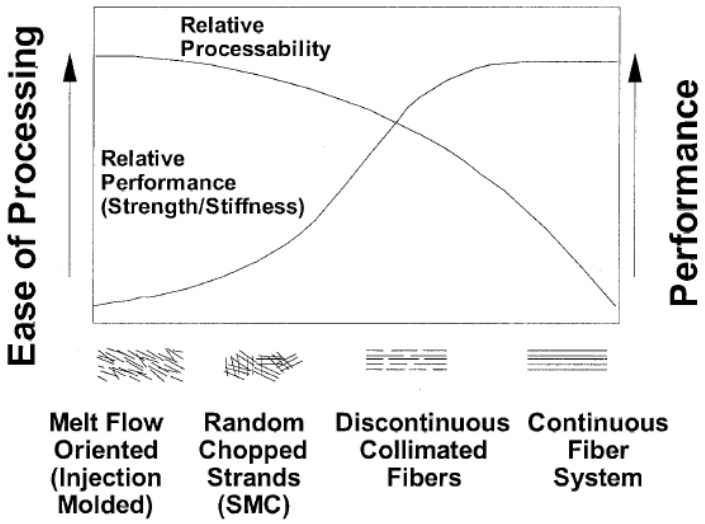

Fig. 2.1.1: Qualitative assessment of how the type of fiber reinforcement affects processability and part performance. Taken from Advani and Sozer.[1]

Simulation of injection molding requires orientation evolution equations. These models will be covered in more detail in subsequent sections, but a brief note will be made here on the importance of Brownian motion. The Péclet number describes the relative importance of the advective and diffusive rates of transport. In the case of fiber reinforcement, the Péclet number compares the rates of fiber motion through the matrix due to the flow of the matrix (advection) and thermally-induced molecular motion (diffusion), given by the following ratio:

$$Pe = \frac{\dot{\gamma}}{D_r} \tag{2.1.1}$$

in which $\dot{\gamma}$ is the shear rate and D_r is the fibers' coefficient of rotary diffusion. Earlier work in the field demonstrated that the Péclet number is much larger than unity in fiber suspensions of commercial interest[2, 3], thus all of the more recent orientation models ignore the influence of Brownian motion on the fibers. This makes the fiber evolution behavior a function of the kinematics, hydrodynamic interactions between the fibers, and direct interactions between fibers.

Regardless of how the fibers reinforce the polymer, achieving optimal interaction between them requires a surface treatment called sizing. Silanes form the basis for most common sizings. Plueddemann's [4] extensive review of silane coupling agents suggested sizing has an inconsistent effect on the rheological behavior of polymer-fiber suspensions. Sometimes sizing increased viscosity, sometimes it decreased viscosity. This seemed to be dependent on the specific formulation and application method. Unfortunately, manufacturers do not report the sizing used in their composites,

rendering fair comparisons between different products and matrix-fiber combinations nearly impossible.

2.1.2 Composite Classification

Fiber loading and length provide useful metrics with which to sort polymer-fiber composites. Classification by fiber loading focuses on the fibers' ability to move freely. In a dilute suspension, a fiber rotates without coming into direct contact with another fiber, and the perturbations in the matrix flow-field due to neighboring fibers fully dissipate before reaching the fiber. These hydrodynamic perturbations do not fully dissipate in semi-concentrated suspensions, but direct fiber contact still does not occur. Finally, fibers in concentrated suspensions experience both direct contact and hydrodynamic perturbations with neighboring fibers.

Doi and Edwards[5] provided rigorous bounds for these concentration regimes in their analysis of rod-like molecules. To meet the criteria for dilute suspensions, fibers must be separated by at least one fiber length. This leads to the limit:

$$n < L^{-3}, \tag{2.1.2}$$

where n is the fiber number density and L is the fiber length. In terms of the fiber volume fraction:

$$\varphi < a_r^{-2}, \tag{2.1.3}$$

in which a_r is the fiber aspect ratio L/D, D being the fiber's diameter.

Fibers in semi-concentrated suspensions lie within a fiber length of each other, but on average do not come any closer than a fiber diameter. This average spacing depends on the orientation state of the fibers. For highly aligned systems:

$$n \ll (D^2 L)^{-1}, \tag{2.1.4}$$

and for isotropic systems:

$$n \ll (DL^2)^{-1}, \tag{2.1.5}$$

which leads to:

$$\varphi < \frac{\pi}{4}, \tag{2.1.6}$$

$$\varphi < a_r^{-1}, \tag{2.1.7}$$

for highly aligned and isotropic systems respectively.

Classification by length is driven by mechanical properties. In glass-fiber systems, a fiber length of 1 mm separates "short" and "long" fibers. The modulus as a function of fiber length reaches a plateau while strength and impact resistance continue to increase, as shown by Fig. 2.1.2.

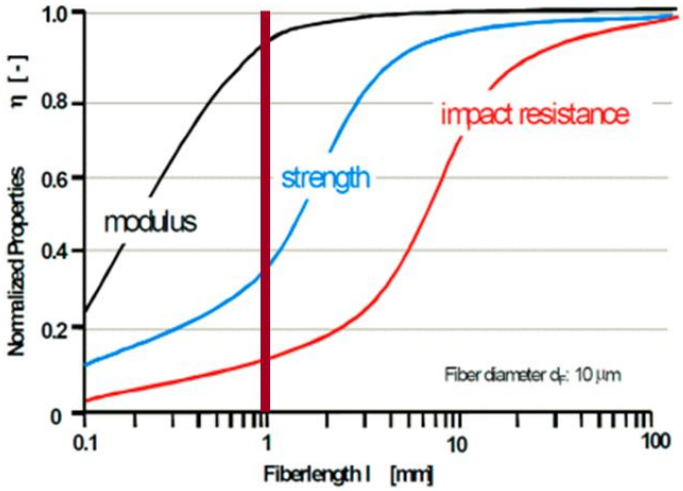

Fig. 2.1.2: Mechanical properties of wet-laid composites as a function of fiber length.

This length also seems to coincide with fiber flexibility, as fibers longer than 1 mm have been observed to flex under typical processing conditions.[6, 7] A metric due to Switzer and Klingenberg[8] estimates a fiber's effective stiffness based on the fiber's physical and mechanical properties:

$$S^{eff} = \frac{\pi E_Y}{\eta_m \dot{\gamma}} \left(\frac{1}{a_r^4} \right), \tag{2.1.8}$$

where E_Y is the fiber's Young's modulus, η_m is the matrix viscosity, and $\dot{\gamma}$ is the shear rate. Note the strong dependence on the fiber aspect ratio. Even small changes in fiber aspect ratio can lead to large changes in the flexibility of the fiber.

2.2 Orientation Measurement

Verification of models for mechanical properties, orientation evolution, and constitutive equations requires accurate orientation data. This section describes two experimental techniques developed to measure the orientation state of the suspended fibers. Section 2.2.1 covers in detail what has been dubbed the "method of ellipses", a stereographic technique, and section 2.2.2 briefly reviews micro-computed tomography.

2.2.1 Method of Ellipses

The relative ease, low cost, and automated nature of the method of ellipses (MOE) make it the method of choice for measuring orientation. At its core, the MOE is a stereographic technique in that it extrapolates the three-dimensional orientation state from two-dimensional micrographs. A group from Leeds[9] developed the concept into a semi-automated procedure, and Bay and Tucker[10] provided a thorough investigation of the data analysis.

Samples are extracted from a larger part with a band saw or water jets and encased in an epoxy plug. Figure 2.2.1 shows a schematic of a sample after extraction and before polishing. Note that a short buffer zone minimizes the influence of the high cutting forces on the orientation state at the desired observation plane.

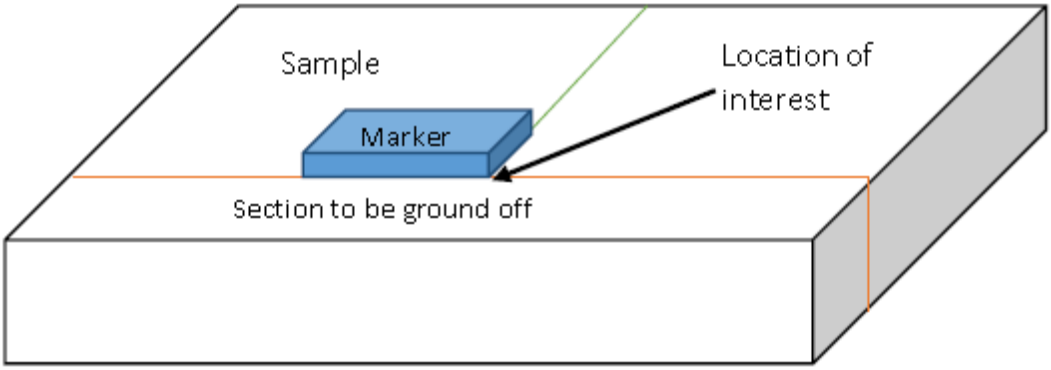

Fig. 2.2.1: Sample for polishing. Note the buffer region that will be eliminated during grinding and polishing.[11]

Once encased in the epoxy plug, the sample is ground down to the observation plane and subsequently polished for reflective microscopy. Plasma etching or gold-sputtering enhances the contrast between the matrix and the fibers and eats away a small layer of the matrix, resolving the ambiguity of the fibers' out-of-plane angle. Velez-Garcia[12] provided an extensive analysis of grinding, polishing, and etching conditions to aid in designing a sample preparation schedule for a particular fiber-matrix system. Polished and etched samples are then scanned with a microscope. A sample micrograph is shown in Fig. 2.2.2i, and Fig. 2.2.2ii demonstrates how etching reveals tails behind the ellipse that resolve ambiguity in the out-of-plane angle.

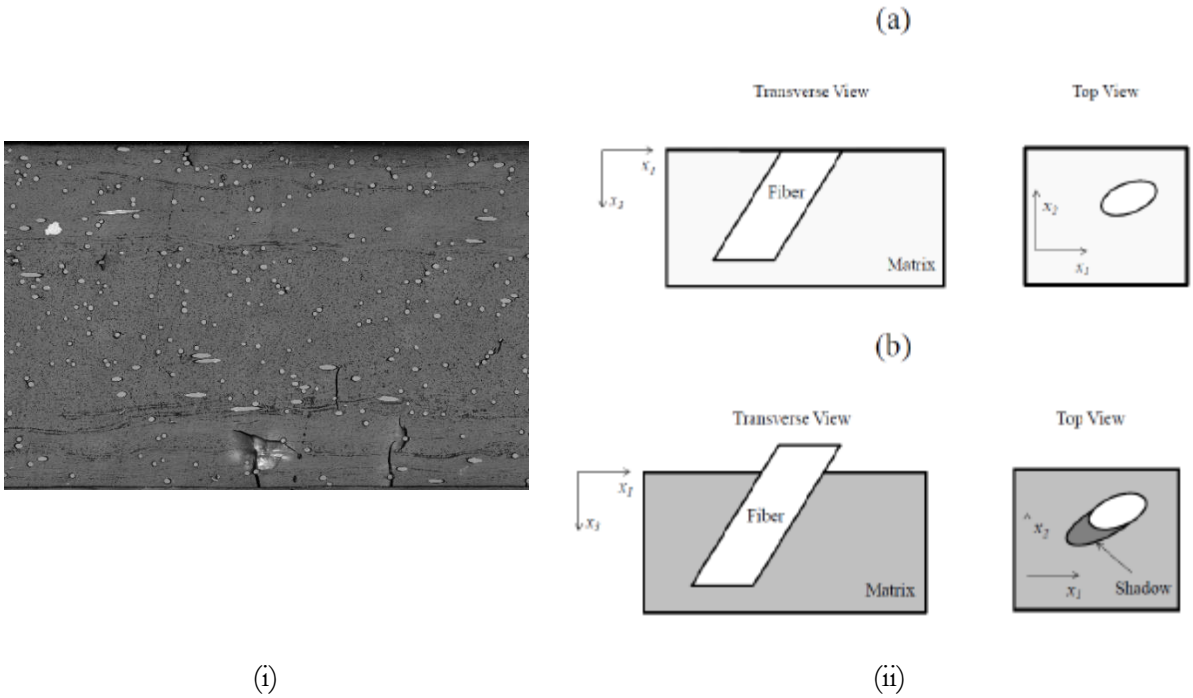

Figure 2.2.2: (i) demonstrates a typical micrograph of fiber orientation. (ii) shows how etching resolves the ambiguity of the out-of-plane angle (taken from Velez-Garcia[11])

Figure 2.2.3 provides a schematic demonstrating the logic behind the stereographic image analysis. Fibers that intersect the observation plane appear as ellipses, and geometric arguments (Eqs. 2.2.1-4) back out the three-dimensional orientation of the fiber:

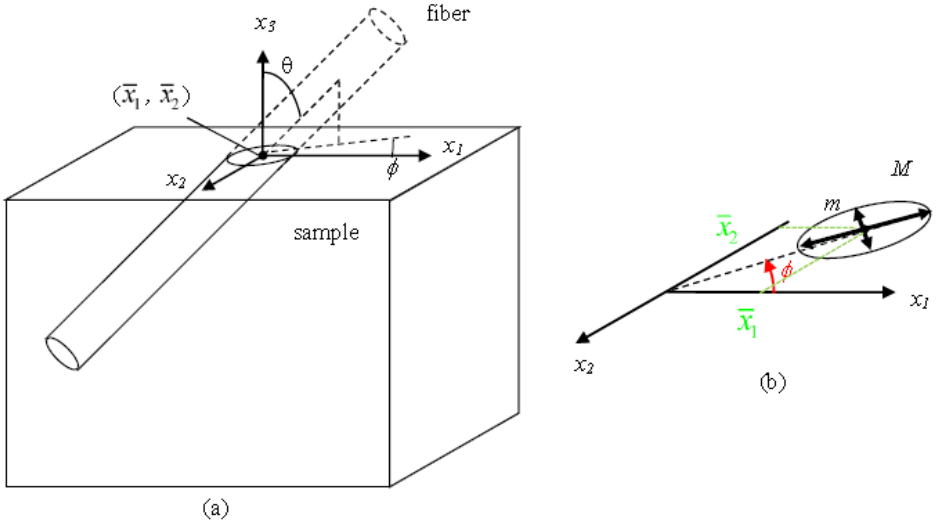

Figure 2.2.3: Calculation strategy behind the MOE. (a) shows the 3D projection of the elliptical footprint and the corresponding in- and out-of-plane angles. (b) demonstrates the determination of the in-plane angle from the observation plane. Taken from Velez-Garcia.[11]

$$\theta = \cos^{-1}\left(\frac{m}{M}\right), \tag{2.2.1}$$

$$p_1 = \sin\theta\cos\varphi, \tag{2.2.2}$$

$$p_2 = \sin\theta\sin\varphi, \tag{2.2.3}$$

$$p_3 = \cos\theta. \tag{2.2.4}$$

In this case, φ is the in-plane angle, which is measured directly; θ is the out-of-plane angle, which is calculated with the minor and major axes of the ellipse, m and M respectively; and the p_is are the components of $\boldsymbol{p}$ projected onto the Cartesian coordinate axes. These are subsequently used to calculate the components of $\boldsymbol{A}$:

$$A_{ij} = \frac{\sum_k \left(p_i p_j\right)_k L_k F_k}{\sum_k L_k F_k}, \tag{2.2.5}$$

such that L_k is the length of the k[th] fiber and F_k is a weighting function associated with fiber k.

Stereographic techniques introduce measurement bias. In the case of the MOE, fibers perpendicular to the observation plane are more likely to be observed than fibers parallel to the plane. Geometric arguments can account for this bias through the choice of weighting function. Konicek[13] proposed a weighting function (Eq. 2.2.6) that worked with partial objects, but only down to half of an ellipse. A later weighting function (Eq. 2.2.7) from Bay and Tucker[10] rectified this shortcoming using a cut-off angle:

$$F_k = \left(L_k\cos\theta_k + d_k\sin\theta_k\right)^{-1}, \tag{2.2.6}$$

$$F_k = \begin{cases} \left(L_k\cos\theta_k\right)^{-1}, & \theta_k \le \theta_c \\ d_k^{-1}, & \theta_k > \theta_c \end{cases}. \tag{2.2.7}$$

Here, θ_c is the cut-off angle defined as $\cos^{-1}(d/L)$. Bear in mind that the MOE cannot measure the length of each individual fiber, L_k. The average fiber length is used instead, which is a source of error fundamental to the MOE that cannot be rectified.

Being a statistical variable, $\boldsymbol{A}$ requires a fairly large population of fibers to generate reproducible data. Work on short fiber orientation suggested that $\sum_k F_k = 100 \pm 10$ fibers per mm creates a representative average of orientation in a specific region[14], which can be used to determine the necessary micrograph dimensions. An image width of 700 μm has proven to be a useful size for short-fiber composites (i.e. fibers shorter than 1 mm).[14]

Long fibers introduce two challenges to this analysis. First, highly parallel long fibers can extend beyond the boundaries of the micrograph, forcing the analysis to either extrapolate the orientation or to neglect the fiber completely. Second, typical processing conditions induce flexing in

long fibers, defying the assumption of rigid fibers inherent in the MOE. Hoffmann[6] addressed the first point by investigating wider micrographs, and ultimately found that a width of 5.5 mm generated reproducible results while keeping the micrograph area, and thus the computational effort, to a minimum. In reference to the second point, Bay and Tucker[10] suggest that if the length of the fiber is much longer than the fiber's radius of curvature, flexing doesn't adversely affect the orientation data, i.e.

$$\frac{L}{2r_c} \ll 1. \tag{2.8}$$

Hofmann provided experimental verification of this heuristic in his analysis of center-gated disks.[15]

In summary, the MOE is a simple, cost-effective method for measuring orientation in fiber reinforced plastic parts. The method, originally developed for short fiber reinforcement, has been extended to long fiber composites by increasing the width of the image to be analyzed provided fiber curvature falls below a threshold. Furthermore, weighting functions account for the error inherent in extrapolating 3D orientation data from 2D observations. The 2D nature of the method remains it's most significant shortcoming. Microcomputed tomography can provide a fully 3D analysis, yet it suffers from issues of its own, discussed in the following section.

2.2.2: Microcomputed Tomography

The major drawback of the method of ellipses is the 2D nature of the technique. This makes simultaneously measuring the orientation and length of individual fibers impossible, yet doing so is necessary to fully characterize the orientation state of the suspension. A 3D perspective also captures the flexed conformation of a fiber, something the method of ellipses cannot do. Micro-computed tomography (μ-CT) is currently the only technique capable of simultaneous length and orientation measurement,[16, 17, 18] as well as measuring the flexed conformation of the fibers.[19, 20]

Microcomputed tomography essentially takes snapshots of a sample from different angles, with X-ray radiation as the illuminating medium.[21] Figure 2.2.4 shows a schematic of a typical μ-CT setup. Samples are placed on a rotating stage and a movable X-ray source releases short bursts of radiation. Software composes the full three-dimensional rendering from these individual snapshots. Furthermore, μ-CT samples require much less processing before analysis compared to reflective microscopy, typically just extraction from the larger part. This reduces errors introduced by the polishing and etching processes. Shen et al.[22] first used μ-CT with fiber-reinforced parts, but the technique has only been slowly adopted since their work.

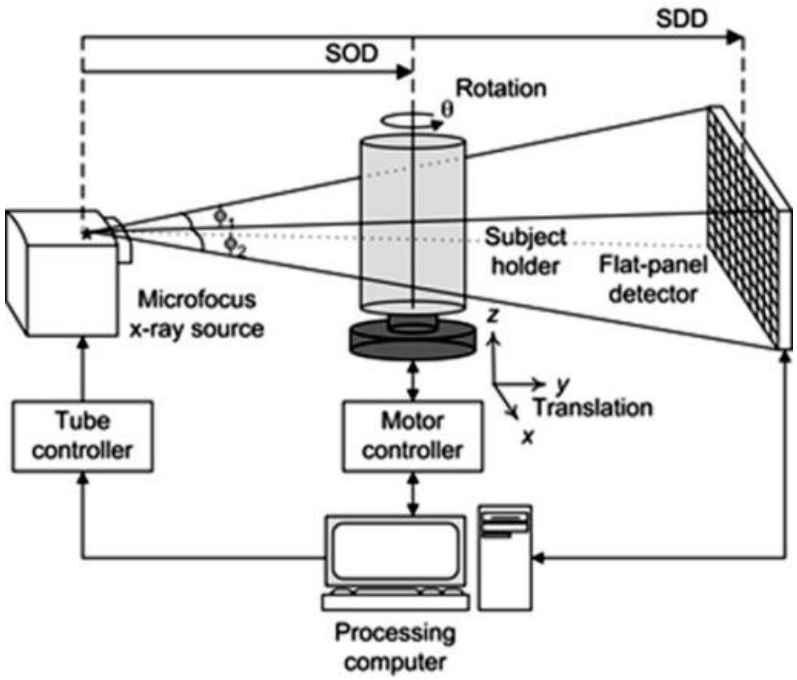

Figure 2.2.4: Schematic of μ-CT scanner, taken from Kim et al.[23] In this case, the x-ray source is stationary. Here, SOD means "source-object distance" and SDD "source-detector distance".

The analytical power of μ-CT comes with drawbacks. One critical shortcoming is the lack of significant contrast between carbon fibers and the polymer matrix.[24] Carbon dominates the molecular structure of both materials, giving them similar x-ray absorption capabilities. Powerful synchrotron beams can overcome this, but these are rare, expensive to use, and in high demand.[24, 25] The analysis of the resulting images also presents another non-trivial barrier to implementation. Several automated computational techniques have been developed,[16, 17, 18] but these either require powerful processors[21] or assume rigid fibers.[24] Finally, although samples require minimal preparation, penetration by the X-rays requires thin samples, typically no thicker than 2 mm.[26]

Bernasconi et al.[27] provided a useful comparison fiber orientation measurements from μ-CT and the MOE. In their study, they used both methods to measure the fiber orientation in a short-fiber-reinforced thermoplastic part. Good agreement was found between the methods except where fibers were highly perpendicular to the polished surface from the MOE. This corroborates the results from Bay and Tucker[10] who pointed out that measurement error would be larger for fibers highly perpendicular to the observation plane. Albrecht et al.[28] also compared orientation measurements using μ-CT and MOE and also found generally good agreement.

2.3: Suspension Rheology

The fiber microstructure in fiber suspensions influences the suspension's rheological behavior. Everything from the stress growth in startup of simple flows to steady-state viscosity curves provides insight into the fiber microstructure, which suggests that rheological tests could aid in understanding how fibers reorient during processing. A key objective of the proposed work is to identify a rheological test that can obtain fiber orientation model parameters that accurately predict fiber orientation during injection molding. To do this, one needs a thorough understanding of fiber suspension rheology.

Section 2.3.1 provides an overview of shear rheology of fiber suspensions. Workers in the field have used this flow extensively in various forms, primarily because most commercial rheometers are designed around imparting simple shear flow. This method does present some issues, as explored in section 2.3.2. Many processing flows feature extensional behavior in tandem with shear, so extensional rheology must be considered as well. Section 2.3.3 reviews rheological work using extensional flows, and section 2.3.4 reviews techniques used to impart extensional flows. Section 2.3.5 briefly reviews work on the effect of filler polydispersity.

2.3.1: Shear Rheology

Work with steady shear demonstrates that the presence of fibers increases the viscosity of the suspension.[29, 30, 31, 32, 33] Longer fibers and higher concentrations exacerbate this effect. Suspensions mostly differentiate themselves in the Newtonian and transition regions and end up converging in the power-law region. Some suspensions do not feature the Newtonian and transition regions[29, 31, 33], but whether this is evidence of a yield stress, or the fact that the Newtonian and transition regions lie below the limits of the apparatus used, remains an open question.

The steady-shear viscosity seems to reflect a steady fiber orientation state, so reserchers can only infer fiber reorientation by coupling a stress model with an orientation model. The complexity of the flow field, the lack of control over initial conditions, and the difficulty in obtaining direct observations of orientation in the capillary entry region in commercially available capillary rheometers all complicate experimental validation of the predicted fiber reorientation inferred through the viscosity curve. For these reasons, steady viscosity curves seem to be a non-ideal method for obtaining orientation model parameters. Oscillatory and startup flows, on the other hand, might capture orientation dynamics.

Material functions from oscillatory flow do not exhibit significant qualitative changes from the unfilled polymer matrix. Rather, they simply increase in magnitude with fiber concentration.[34, 35] Some

work suggests that fibers reorient during small and large amplitude oscillation. In particular, modeling work by Harlen and Koch[36] shows that a fiber in a weakly elastic Oldroyd-B fluid experiences orbital drift during oscillatory flow. Samples do not accumulate strain over multiple cycles during oscillatory tests, thus the matrix elasticity drives the orbital drift, which Petrich et al.[37] later corroborated. However, both worked with dilute suspensions of short fibers ($a_r < 100$, unspecified volume fraction). Elasticity-driven drift remains to be proven for concentrated suspensions. Commonly used orientation models would not capture this effect, however, as they neglect the matrix elasticity.

Startup of shear might better capture fiber reorientation. Work in this area suggests that fiber reorientation plays an unmistakable role in the stress growth by introducing a pronounced overshoot before settling on a steady state.[3, 34, 38, 39, 40, 41, 42, 43, 44, 45, 46] The unfilled matrix does not exhibit this stress overshoot. Sepehr et al.[46] demonstrated that changing the initial orientation changed this response, and this was corroborated by Cieslinski et al.[47] Shearing samples to a steady state and then reversing the flow direction delayed the stress overshoot, whereas unconditioned samples exhibit an immediate overshoot. This suggests fiber reorientation, not the mere presence of fibers, influenced the stress growth behavior. Eberle et al.[48] later verified this for short fiber systems, and Ortman et al.[49] demonstrated the same occurred in a long-fiber system, both by comparing fiber orientation evolution with the stress growth. Thus, startup of simple shear appears to be a viable method for tracking fiber reorientation due to flow through rheology, and superior to using steady shear viscosity or oscillatory material functions.

2.3.2: Methods for Obtaining Data in Startup of Simple Shear

Techniques for startup of shear thus far exclusively use drag flow between parallel plates or in a cone-and-plate fixture. Most work uses circular fixtures in conventional rheometers, giving rise to significant problems. Although the cone-and-plate fixture benefits from a shear rate that is independent of radial position, the fixture gap decreases from the rim to the center of the fixture. Close to the center, the gap is of the same order of magnitude as the length of the fiber reinforcement. This influences the fiber reorientation, and commonly used orientation models cannot account for the interaction between the fibers and walls. Maintaining the simple kinematics of the cone-and-plate fixture while avoiding wall effects requires modifications.

Two alternatives with the cone-and-plate have been proposed. Djalili-Moghaddam et al.[50] suggested a truncated cone-and-plate geometry, which left a relatively large gap between the upper cone and lower plate. Although this avoids wall interactions, it also results in the loss of the simple

kinematics that makes the cone-and-plate a desirable choice for shear flow. Eberle et al.[48] proposed a cone-and-donut sample in which a 25 mm plug was removed from the center of a 50 mm sample, making an annular sample. This method does not require a larger fixture gap, but the sample's viscosity must be large so that the sample does not flow into the center.

In lieu of making drastic changes to the cone-and-plate geometry to avoid wall interactions, other workers have used parallel plates because of the uniform thickness of the geometry. Keeping a gap about 3 times larger than the average fiber length reduces the influence of wall effects.[51, 52] The parallel plates do this at the cost of a non-uniform shear rate. Unlike the cone-and-plate fixture, the shear rate is a function of radial position in the parallel plates, making shear strain a function of radial position as well.

The sliding-plate rheometer presents an alternative method for simple shear that controls the gap thickness while imparting a uniform shear rate.[53, 54] Furthermore, this fixture avoids the curved streamlines in both the parallel plates and cone-and-plate fixtures. Most of the work with the sliding plate rheometer uses a localized shear stress transducer. This requires a small space surrounding the transducer face into which the suspension can flow, which can affect the force reading.[55]

2.3.3: Extensional Rheology

Extensional flows feature prominently in many polymer processing applications, such as fiber spinning, thermoforming, injection molding, and compression molding. Industry often subjects fiber-reinforced polymer composites to the same processes. Thus, process design requires understanding how fibers affect the stress growth, as well as understanding how fibers reorient, during extensional flow.

Bird et al. [56] provided the following mathematical definition of extensional (i.e. shear-free) flow:

$$u = -\frac{1}{2}(1+b)\dot{\varepsilon}x, \tag{2.3.1}$$

$$v = -\frac{1}{2}(1-b)\dot{\varepsilon}y, \tag{2.3.2}$$

$$w = \dot{\varepsilon}z, \tag{2.3.3}$$

such that the z direction is the primary stretching or compression direction. When $b = 0$ and $\dot{\varepsilon} > 0$, the sample undergoes simple extension, while $\dot{\varepsilon} < 0$ imparts biaxial compression. If $b = 1$, planar extension is attained.

Recall that in simple shear, the shear rate is the velocity gradient. This follows the definition of infinitesimal strains, so that large shear strain is simply the addition of many small shear strains. Extensional rheology uses a finite strain such that

$$\varepsilon = \ln(l/l_0), \tag{2.3.4}$$

in which l is the measured gauge length of the sample, and l_0 is the initial gauge length of the sample. This is often called Hencky strain. Hencky strain arises from the summation of infinite small strain steps. For an infinitesimal change in gauge length, dl:

$$\varepsilon = dl/l, \tag{2.3.5}$$

then the total strain for a finite deformation from l_0 to some arbitrary l is:

$$\varepsilon = \int_{l_0}^{l} \frac{dl}{l} = \ln(l/l_0), \tag{2.3.6}$$

as previously shown. Taking the time derivative of the Hencky strain yields the extensional strain rate:

$$\dot{\varepsilon} = \frac{d\varepsilon}{dt} = \frac{d}{dt}[\ln(l/l_0)] = \frac{1}{l}\frac{dl}{dt}, \tag{2.3.7}$$

and solution of this differential equation under the constraint of constant $\dot{\varepsilon}$ with l_0 as the initial condition reveals that

$$l = l_0 e^{\dot{\varepsilon} t}, \tag{2.3.8}$$

meaning that deformation at a constant rate of extension requires an exponential increase in the gauge length for the stretching case $(\dot{\varepsilon} > 0)$ and an exponential decrease in the gauge length for the compression case $(\dot{\varepsilon} < 0)$. This deformation profile presents a significant hurdle to the use of extensional rheology. One should also note that small Hencky strains result in very large deformations due to their logarithmic relationship, as shown in Fig. 2.3.1. For example, a Hencky strain of 5 requires a stretch of over 100 times the original filament length.

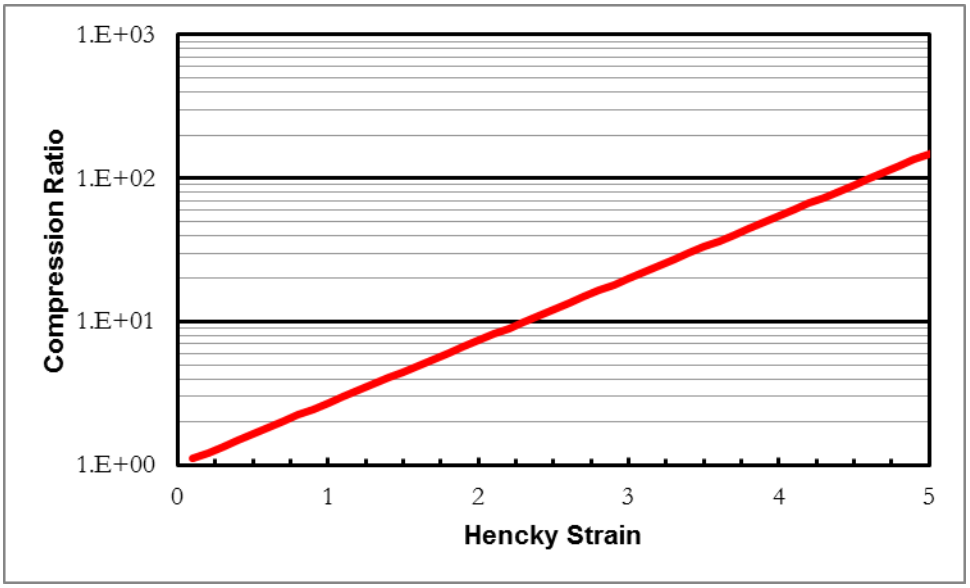

Figure 2.3.1: Demonstration of how compression ratio grows with Hencky strain. Typical extensional experiments only go to around 2 Hencky strain, or a compression ratio of 7.39.

Steady state values for extensional viscosity during uniaxial extension (hereafter referred to as simple extension) can be obtained from capillary rheometry by partitioning the pressure drop into extensional and shear contributions. Cogswell[57] provided the first approximation using a force balance, and Binding[58] updated the approach using an energy balance. Regardless of the method used, a variety of studies demonstrate that, as in shear, extensional viscosity experiences rate-thinning.[59, 60, 61, 62]

Mobuchon et al.[38] and Carneiro and Maia[42] extended the use of entry flow to the study of concentrated suspensions of polypropylene with short glass and carbon fiber reinforcement respectively. In both cases, the composite experienced the rate-thinning seen in the melt. Increasing fiber content increased the viscosity, however fiber attrition due to processing prevents any conclusions about the effect of fiber length. Contrary to what was seen in shear, the extensional viscosities do not converge at faster extension rates, however this could simply be a result of the limitation in the strain rates. Extension rates from entry flow do not usually exceed 100 s^{-1}, whereas capillary flow can attain several more decades of shear rates.

The use of steady flow to impart large extensional strains has also been applied to planar extension. Extensional viscosity under planar extension can be measured by flow birefringence using a cross-slot geometry.[63, 64, 65] As in simple extension, extensional viscosity experiences rate-thinning at higher extension rates. The studies cited focused on flow of LDPE and HDPE, mostly because the flow technique was developed to get around the strain-hardening of the material and dimensional limitations of typical transient extension measurements. As a result, researchers have neglected to

study simpler polymers (e.g. polypropylene and polystyrene) under planar extension. Unlike the case for simple extension, polymer-fiber suspensions have not been investigated in steady planar extension. Furthermore, the same criticisms leveled against using steady shear viscosity curves to obtain orientation model parameters apply to using steady extensional viscosity curves. Transient extensional viscosity measurements might be a better choice.

Depending on the number and size of branches, and the breadth of the molecular weight distribution, extensional flows can induce transient extensional stress growth behavior markedly different from that of transient shearing flow.[60, 62, 66, 67, 68, 69, 70, 71, 72] Low-density polyethylene (LDPE) often serves as a model system for a phenomenon called strain-hardening. Stress growth at the inception of flow will follow the linear viscoelastic predictions under slow strain rates (monotonic increase to a steady value), but beyond a critical strain rate stress dramatically increases above this limit. Although LDPE suggests this behavior is manifested through side branches on the polymer backbone, work with linear polymers such as polystyrene[72] and polypropylene[71] reveals that the presence of high molecular weight chains in the molecular weight distribution can also induce strain-hardening in systems that otherwise would not exhibit this behavior.

Transient extensional behavior of polymer-fiber suspensions under simple extension remains relatively unexplored when compared to shear. What work exists suggests that the viscosity decreases with strain rate somewhat and increases with fiber content.[39, 51, 73, 74, 75] Takahashi et al.[74] investigated the stress growth under uniaxial extension of concentrated suspensions of short fibers ($a_r = 23$, $\varphi = 0.20$) in LDPE. In this instance, the fibers suppressed the strain hardening behavior exhibited in the unfilled melt. Laun[39] found similar results in a comparable system ($a_r = 30$, 30 wt%), and also found that the same fibers and fiber loading induced strain softening in HDPE. Behavior at larger strains with polypropylene seems tied to the method used. Workers who employed filament stretching saw strain-softening,[51, 73] but others observed strain-hardening with sheet-stretching devices.[75, 76] Unfortunately, none of the studies discuss the quality of sample deformation in much detail. Filament stretching techniques in particular could be prone to necking, explaining the presence of the apparent softening.

Transient planar extension studies are much scarcer than those of simple extension. Hachmann[70] used a complicated sheet stretching device to investigate the stress growth of LDPE and HDPE, finding that they experienced strain-hardening in planar extension as well as simple extension. Khan and Larson[77] used a lubricated squeeze flow technique to investigate relaxation in linear and branched LDPEs after step strains in planar extension. They asserted that lubrication did not fail based

on the stress response: failure of lubrication resulted in an overload of the normal force transducer. To date, Hachmann's work remains the main trusted data set for planar extension of polymer melts, however the device that obtained this data apparently no longer exists.[78] Accordingly, planar extension of polymer-fiber suspensions has not been investigated.

Regardless of these shortcomings, transient extensional flow seems to be a viable alternative technique for obtaining orientation parameters. Tests have simple, well-defined kinematics and can be stopped at specific strain steps, allowing for direct observation of fiber orientation. This provides direct verification of predictions made through fitting a stress model coupled to an orientation model.

2.3.4: Methods for Measuring Transient Extensional Viscosity

Most work with extensional flows makes use of devices following one of two strategies to impart simple extension: sheet-stretching or filament-stretching. The latter can be performed in a Rheometrics Extensional Rheometer (RER) or the Rheotens apparatus. Testing in the RER involves stretching a cylinder at constant Hencky strain rate and is performed in a temperature-controlled oil bath. The oil can be selected to have a density matching (or close to) that of the polymer sample, reducing the effects of sagging. On the other hand, the Rheotens acts as a fiber spinning unit, using rotating drums to take up extrudate from a capillary rheometer.

Two obvious limitations of the Rheotens unit are the non-isothermal nature of the drawing process and the non-uniform extension rate along the spinline, both of which the RER rectifies. However, necking is a concern in both devices, which can give the appearance of strain-softening in the extensional viscosity data. Great care must be taken to minimize necking, and a detailed discussion of the deformation of the sample should always be reported, though seldom is.

Both devices also have poor control over the initial fiber orientation state. The Rheotens device requires an assumption of the orientation state at the capillary exit, typically flow-aligned. In the RER, polymeric suspensions with longer fiber reinforcement are also limited to a flow-aligned initial state by the dimensions of the samples. Based on the kinematics, the steady state in simple extension should be highly flow-aligned, so very little fiber reorientation would occur during the test in either device, meaning fiber reorientation could not be inferred through the stress response.

Sheet-stretching allows for the investigation of several initial conditions, but comes with other difficulties. Devices like those proposed by Meissner[66] and Sentmanat[79] stretch a thin polymer film. Meissner's device uses rotating clamps, and the sample is supported on a bed of inert gas that also acts as the heat transfer mechanism. An environmental chamber can also be employed to ensure

isothermal conditions. Sentmanat's device is a universal tool that can be installed in most readily-available rheometers. Samples are clamped to drums rotating in opposite directions. Note that this limits the deformation to a single drum circumference. Sample failure serves as the upper strain limit in Meissner's device, however reliable data beyond a Hencky strain of 3 have not been reported.

Both devices require thin samples to minimize sagging and to ensure an isothermal sample, and typical samples are about 2 mm thick, corresponding to a final thickness of 0.446 mm. This limits polymer-fiber suspensions to planar orientation by preventing out-of-plane motion, possibly biasing fiber reorientation. Thicker samples could avoid this, but the isothermal assumption becomes questionable, and polymer matrices used in commercial composites (i.e. polypropylene and polyamides) would likely sag. Necking also remains a concern.

As mentioned in the previous section, only two techniques exist for imparting transient planar extension. Hachmann's sheet stretching-device[70] involves a complicated set of rotating clamps and cutting devices. Samples are open to atmosphere and heated by a bed of nitrogen that also supports the sample. The authors report that samples were 2 mm thick and the maximum Hencky strain attained was 7 in equibiaxial extension, corresponding to a sample thickness of 1.82 μm. However, the planar extension samples experienced hazing and fracturing at a Hencky strain of about 5, or a thickness of about 13.5 μm. These are on the order of typical glass and carbon fiber diameters (around 16 μm and 6 μm respectively), so polymer-fiber suspensions will not be able to attain these high Hencky strains in this device unless thicker samples are used.

Hachmann used thin samples to minimize sagging and to ensure an isothermal sample. Sagging was also minimized by the high viscosity of the PE matrices. Typical commercial composites use polypropylene and polyamide matrices which would certainly sag under the reported testing conditions. Furthermore, the thin samples limit the fibers to a planar orientation and inhibit possible out-of-plane motion. Considering the complexity of the device and the required sample thickness, Hachmann's sheet-stretching technique does not appear to be a viable method for imparting planar extension.

Khan's and Larson's[77] lubricated squeeze flow technique seems a better choice. Loss of lubrication during the test places an upper limit on the maximum achievable strain however. Khan and Larson report that they used the stress response to verify lubrication at higher strains. A breakdown in lubrication resulted in an overload in the stress transducer. Venerus and co-workers[78, 80, 81] published an experimental and theoretical analysis of lubricated squeeze flow and agree that the onset of apparent strain-hardening in the stress-response actually signifies the breakdown of

lubrication. In their work with lubricated equibiaxial extension, a maximum Hencky strain of about 1 in the compression direction was attained. A later device[78] continuously pumped lubricant to the sample surface and extended the maximum Hencky strain to about 2.5.

Imparting transient planar extension through squeeze flow appears to be ideal for using extensional flow to obtain orientation model parameters. Thick samples allow fibers to move out of the horizontal plane and multiple initial conditions can be explored. The breakdown of lubrication can be identified through the stress response as long as the non-lubricated squeeze flow behavior is known.

2.3.5: Effect of Fiber Length Distribution

Fiber lengths in composite parts follow a broad distribution. This distribution is almost always lognormal in shape. Although composites are typically processed from pellets 13 mm long, the post-processing fiber length distribution (FLD) follows a lognormal trend with a mode around 1 mm, number average lengths rarely larger than about 2 mm, and a long tail going out to the original pellet length. In spite of this, every model for stress and orientation assumes that a population of fibers is uniform in length.

Work with suspensions of spherical particles provides some insight. The seminal work of Chong et al.[82] investigated the effect of a bimodal distribution of glass beads in polyisobutene near the maximum packing fraction (φ close to 0.61). Keeping the volume fraction of small spheres constant at 0.25, the diameter ratio and total solids volume fraction were varied and their effect on the relative viscosity was measured. Increasing the size ratio from $d/D = 0.138$ to 0.477 had two significant effects. First, increasing the size ratio at constant total solids volume fraction reduced the reduced viscosity. Second, increasing the size ratio increased the maximum packing fraction to a value greater than 0.70, higher than that of a monodisperse suspension, typically stated to be around 0.68. Both of these observations are almost assuredly due to the fact that, at the greatest size disparity, the small spheres were capable of fitting in the interstices between the larger spheres.

Later work by Poslinski et al.[83] took a similar approach investigating a bimodal suspension of glass beads in polybutene. This work held the size ratio constant at $d/D = 0.192$ and varied the total solids volume fraction and the fraction of small particles to probe their effect on the reduced viscosity and first normal stress coefficient, as well as the storage modulus and the dynamic viscosity. A complicated interaction between the two variables was revealed. Increasing the fraction of small beads had very little effect on any of the properties at lower volume fractions. The expected behavior of

increased reduced viscosity with increased solids content was observed. However, as the total solids content approached 0.60, the properties began to exhibit nonlinear behavior, going through a minimum at a small particle fraction of about 0.20, and then increasing with increasing small particle fraction. This behavior became much more pronounced as total solids fraction increased. Chang's and Powell's[84] work with poly(methyl methacrylate) and polystyrene beads in Dow Corning Fluid 200 corroborated this behavior.

Three different strategies have been employed to model this complicated behavior.[85] One strategy simply increases the maximum packing fraction. The crowding factor suggested by Mooney[86] is an alternative based on the idea that the spheres can only fit in a finite space. Farris[87] devised a third strategy that partitions the spheres into several fractions in such a way that particle interactions may be ignored. In other words, a polydisperse population of spheres could be modelled as a bi- or trimodal population. Farris's method in particular has had success in modelling experimental data for populations of spheres following a lognormal distribution.[85]

Unfortunately, the effect of polydispersity on the rheology and orientation dynamics of fiber suspensions in polymeric matrices has not been explored as extensively. To date, the only significant study of this nature has been carried out by Huq and Azaiez[30], in which the authors used chopped glass fibers 0.5 mm, 1.0 mm 1.5 mm, and 2.0 mm long suspended in an aqueous 3 wt% poly(ethylene oxide) solution. Bimodal distributions were mixed such that the number, weight, or Z average was equal to one of the unimodal lengths. For example, 0.5 mm and 2 mm fibers were mixed into three different bimodal populations, one with a number average length of 1.5 mm, another with a weight average length of 1.5 mm, and a final population with a Z average length of 1.5 mm. The steady shear viscosity of each population was compared against that for a unimodal suspension (e.g. a unimodal suspension with 1.5 mm fibers for the previously discussed case). Fiber orientation was not measured.

Bimodality had the largest effect in the low shear rate region. As the proportion of longer fibers increased, so did the zero-shear viscosity of the suspension. In contrast, the viscosity of the bimodal suspensions in the power law region converged to the same value as the unimodal suspension, irrespective of the ratio of long to short fibers. Both observations hold for a trimodal suspension that was also investigated.

The conclusions that can be drawn from the work are limited. The authors state that they investigated several total volume fractions, but only report data for 2 vol% suspensions. Only two fiber length ratios were investigated (0.5 mm to 2.0 mm and 1.0 mm to 2.0 mm). Furthermore, the ratio of short to long fibers was only controlled inasmuch as it gave the desired average length. Of

nine different bimodal distributions, only four had comparable ratios of short and long fibers so that the effect of length ratio could be isolated, and the data that could have been used for this was not reported. Finally, although the average lengths in this study do reflect average lengths measured in commercial composites, the fiber populations are composed of fairly short fibers. Commercial composites typically have small amounts of very long fibers, including those that match the original pellet length. The study by Huq and Azaiez can't provide insight on what effect, if any, these very long fibers have on viscosity.

2.4: Fiber Orientation Models

Models for fiber orientation evolution concern the following section. Section 2.4.1 reviews the fundamental mathematical formulation of orientation, taking a fiber to be a rigid rod and ultimately deriving the orientation tensor $\boldsymbol{A}$ commonly used in the orientation models. Section 2.4.2 explores the importance of the choice of closure approximation, and section 2.4.3 gives a summary of the Tucker family of models, starting with Folgar's and Tucker's extension of Jeffery's equation into semi-concentrated suspensions, and ending with the improved anisotropic rotary diffusion model. Section 2.4.4 considers the bead-rod model.

2.4.1: Fundamentals of Orientation Analysis

A common technique for modeling a rigid fiber uses a vector oriented along the fiber's major axis, typically $\boldsymbol{p}$ (Fig. 2.4.1).

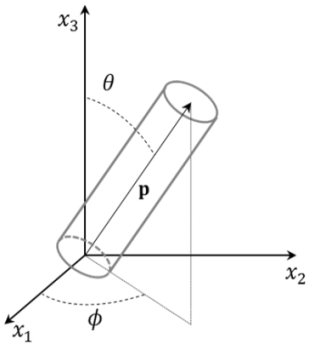

Fig. 2.4.1: Fiber orientation. The vector $\boldsymbol{p}$ is projected onto each of the coordinate axes and has a unit length.

Extending the technique to fiber suspensions necessitates the use of an orientation distribution function (ODF), $\psi(\boldsymbol{p}, \boldsymbol{x}, t)$, where $\boldsymbol{x}$ is the position vector and t is time. This function describes the probability of finding a fiber at some point $\boldsymbol{x}$ with an orientation between $\boldsymbol{p}$ and $\boldsymbol{p} + d\boldsymbol{p}$. Fibers are assumed to have fore-aft symmetry, thus the ODF in all of the applications in this work is symmetric, i.e. $\psi(-\boldsymbol{p}, \boldsymbol{x}, t) = -\psi(\boldsymbol{p}, \boldsymbol{x}, t)$. Moreover, the ODF must also be normalized such that:

$$\int \psi(\boldsymbol{p}, \boldsymbol{x}, t) d\boldsymbol{p} = 1. \tag{2.4.1}$$

Finally, a Smoluchowski equation describes the time evolution of the ODF under flow. For example, in the dilute suspension case:

$$\frac{D\psi}{Dt} = -\frac{\partial}{\partial \boldsymbol{p}} \cdot (\psi(\boldsymbol{p}, \boldsymbol{x}, t)\dot{\boldsymbol{p}}), \tag{2.4.2}$$

where D/Dt is the substantial derivative $\left(\frac{\partial}{\partial t} + v \cdot \nabla\right)$ and the dot above $\boldsymbol{p}$ represents its time derivative.

The ODF is a compact and complete description of the orientation state of the fibers.[88] However, solving the Smoluchowski equation directly requires two independent computational domains: the three-dimensional spatial domain of the problem (by way of the spatial derivatives in the substantial derivative) and the two-dimensional spherical orientation domain (by way of the unit sphere surface derivative $\partial/\partial \boldsymbol{p}$).[88] This double domain approach requires an unwieldy number of calculations in numerical simulations of injection molding.

Taking the second moment of $\psi(\boldsymbol{p}, \boldsymbol{x}, t)$ with respect to $\boldsymbol{p}$ yields a second-order tensor:

$$\boldsymbol{A} = \int \boldsymbol{pp}\psi(\boldsymbol{p}, \boldsymbol{x}, t) d\boldsymbol{p}. \tag{2.4.3}$$

Note that because the orientation distribution function is an even function due to the fore-aft symmetry of the rods, all odd-ordered moments of $\psi(\boldsymbol{p}, \boldsymbol{x}, t)$ are identically zero. This definition is used to convert the Smoluchowski equation to a tensor equation. For example, multiplication of Eq. 2.4.3 by $\boldsymbol{pp}$ and integrating over all possible orientation states yields the equivalent orientation evolution equation in tensor form, in this case Jeffery's model (Eq. 2.4.4 is only given as an illustration of the derivation of tensor models; these are described in detail in section 2.4.3):

$$\frac{D\boldsymbol{A}}{Dt} = (\boldsymbol{W} \cdot \boldsymbol{A} - \boldsymbol{A} \cdot \boldsymbol{W}) + \xi(\boldsymbol{D} \cdot \boldsymbol{A} + \boldsymbol{A} \cdot \boldsymbol{D} - 2\boldsymbol{D}\colon \boldsymbol{A_4}). \tag{2.4.4}$$

This conversion eliminates the orientation domain, making $\boldsymbol{A}$ defined solely on the spatial domain. However, the reduction in computational effort introduces a significant problem by introducing a new variable, $\boldsymbol{A_4}$, resulting in an under-specified set of equations.

This new tensor, $\boldsymbol{A_4}$, is defined as

$$\boldsymbol{A_4} = \int \boldsymbol{pppp}\psi(\boldsymbol{p}, t) d\boldsymbol{p}, \tag{2.4.5}$$

and could be calculated through a new evolution equation derived using a procedure similar to that used to derive Eq. 2.4.4. Doing so gives rise to a new tensor, $\boldsymbol{A_6}$, requiring yet another evolution equation. This process continues *ad infinitum* unless some alternate method for calculating the higher-order orientation tensor is used to close the set of equations. These aptly-named "closure approximations" will be discussed in detail in the following section. The series is typically closed with an approximation for $\boldsymbol{A_4}$, as most mechanical properties of interest are fourth-order tensors (e.g. stiffness, viscosity) and extending the series of evolution equations to include $\boldsymbol{A_6}$ requires considerably more computational effort.[88]

Both $\boldsymbol{A}$ and $\boldsymbol{A_4}$ are symmetric, and $\boldsymbol{A_4}$ contains all of the components of $\boldsymbol{A}$. Furthermore, the diagonal components of $\boldsymbol{A}$ sum to unity identically. These diagonal components describe the degree to which the fibers are aligned with respect to the coordinate axes, illustrated by Fig. 2.4.2. For example, perfect alignment in the x_1 direction results in $A_{11} = 1$ and $A_{22} = A_{33} = 0$, whereas the isotropic state is described by $A_{11} = A_{22} = A_{33} = 1/3$.

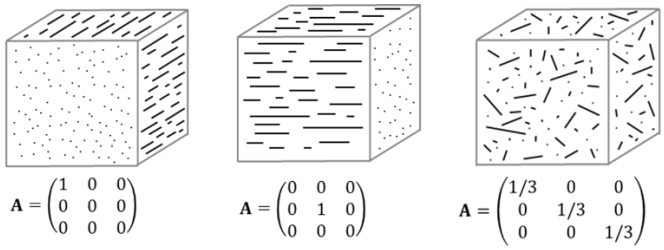

Fig. 2.4.2: Various orientation states as described by the orientation tensor. The diagonal components sum to unity in each case.

2.4.2 Closure approximations

Closing the infinite series of tensor evolution equations requires an approximation of the higher-order tensors. Past work has focused on approximating $\boldsymbol{A_4}$ in terms of the components of $\boldsymbol{A}$. Advani and Tucker determined the following criteria were the minimum required to approximate the correct fundamental behavior of $\boldsymbol{A_4}$ [89]:

1. $\boldsymbol{A_4}$ must be symmetric with respect to any pair of indices: $A_{ijkl} = A_{jikl}$ and $A_{ijkl} = A_{ijlk}$
2. The symmetry of the stiffness tensor requires: $A_{ijkl} = A_{klij}$
3. Maintaining $tr(\boldsymbol{A}) = 1$ with an incompressible fluid requires: $A_{iikl} = A_{kl} + sI_{kl}$ ($\boldsymbol{I}$ is the identity tensor in this case and s is an arbitrary scalar).

The first generation of approximations defined $\boldsymbol{A_4}$ in terms of linear and quadratic combinations of A_{ij}. Notable examples are Hand's linear approximation[90] and the quadratic

approximation.[91] The linear approximation yields the exact $\boldsymbol{A_4}$ when orientation is isotropic, and the quadratic approximation is exact for perfectly-aligned orientation. Hinch and Leal[92] and Advani and Tucker[89] developed composite approximations using the linear and quadratic results as asymptotic values and interpolating between the isotropic and aligned states.

No single approximation in the generation provided consistently superior approximations for general flows. Rather, the flow field under investigation dictated the closure approximation used. Subsequent generations used this as a cue and designed their approximations to give reasonable results over several types of flows rather than exactly recreating $\boldsymbol{A_4}$. Approximations from the second generation calculated $\boldsymbol{A_4}$ in terms of polynomial expressions of the components of $\boldsymbol{A}$. Each approximation differentiates itself in the method used to calculate the coefficients of its polynomial kernel. Cintra and Tucker[93] developed a family of approximations that makes the polynomial coefficients functions of the eigenvalues of $\boldsymbol{A}$. Verleye and Dupret[94] opted to use the invariants of $\boldsymbol{A}$, reducing the computational effort but introducing singularities in some flows. Chung and Kwon[95] addressed the singularities in their Invariant-Based Optimal Fitting (IBOF) approximation.

In each approximation, the coefficients are obtained by a least-squares fitting technique. A set of simple, homogeneous flow-fields are identified; the kinematics are plugged into the Smoluchowski equation; and the ODF is determined directly, allowing for an exact calculation of $\boldsymbol{A_4}$ through Eq. 2.4.5. The polynomial approximations are then fit to these results. Chung and Kwon used six different flow fields from simple shear and simple extension to superpositions of both, and their results were stable over a broad variety of flow fields and an acceptable range of rotary diffusion coefficients (see the Folgar-Tucker model in the following section).

2.4.3: Tucker Family of Orientation Models

Jeffery's model[96] serves as the starting point for all of the models discussed. In his analysis, Jeffery considered a single ellipsoidal particle in an incompressible Newtonian fluid in motion. So long as the velocity gradients occur over a scale longer than the fiber's dimensions, the fiber's centroid moves at the same velocity as the fluid would at that point (i.e. the fiber center does not move relative to the fluid). Moreover, Jeffery neglected the substantial derivative, justified by scaling arguments on the second order velocity terms as well as the time derivative. Bear in mind that creeping flow is not assumed, but is a necessary condition of the model. Solution of the equations of motion and continuity resulted in the following model:

$$\frac{D\boldsymbol{p}}{Dt} = \boldsymbol{W}\cdot\boldsymbol{p} + \xi(\boldsymbol{D}\cdot\boldsymbol{p} - \boldsymbol{D}\!:\!\boldsymbol{ppp}). \tag{2.4.6}$$

In this case, $\boldsymbol{W}$ is the vorticity tensor ($\boldsymbol{W} = 1/2[\boldsymbol{\nabla u} - (\boldsymbol{\nabla u})^t]$), ξ is a shape factor for a corresponding aspect ratio a_r ($\xi = (a_r^2 - 1)/(a_r^2 + 1)$), and $\boldsymbol{D}$ the rate-of-strain tensor ($\boldsymbol{D} = 1/2[\boldsymbol{\nabla u} + (\boldsymbol{\nabla u})^t]$). In defining the vorticity and rate-of-strain tensors, $\boldsymbol{u}$ is the velocity vector and $\boldsymbol{\nabla u} = \partial u_j/\partial x_i\, \boldsymbol{\delta_i}\boldsymbol{\delta_j}$, in which $\boldsymbol{\delta_i}$ is the unit vector in the i[th] direction. The D/Dt operator denotes the substantial derivative.

By inspection one can see that Jeffery's model predicts the fiber will rotate and translate with the fluid, with the $\boldsymbol{D}\!:\!\boldsymbol{ppp}$ term maintaining the unit length of $\boldsymbol{p}$. More specifically, Jeffery's model predicts a fiber will undergo periodic rotations under simple shear and will align in the primary extensional direction under simple extensional flow.

Strictly speaking, Jeffery's model is only valid for a fiber in a dilute suspension. The hydrodynamic perturbations caused by the fibers do not overlap in this regime, nor do the fibers come into direct contact. Experimental observations of fiber motion in semi-dilute suspensions by various groups demonstrate that hydrodynamic interactions influence fiber motion and that Jeffery's equation over-predicts the degree of alignment.[97, 98, 99, 100] Folgar and Tucker[101] developed an empirical model to account for the fiber interactions. Under the limit of large aspect ratios, a diffusion-like term was added to Jeffery's expression (see Eq. 2.4.7). This additional term functions much like Brownian motion in that it forces fibers away from alignment in the flow direction. This results in a steady orientation state for both simple shear and extensional flow. As the value of C_I increases, the final orientation state becomes more random. In $\boldsymbol{A}$ tensor form, the model is:

$$\frac{D\boldsymbol{A}}{Dt} = (\boldsymbol{W}\cdot\boldsymbol{A} - \boldsymbol{A}\cdot\boldsymbol{W}) + \xi(\boldsymbol{D}\cdot\boldsymbol{A} + \boldsymbol{A}\cdot\boldsymbol{D} - 2\boldsymbol{D}\!:\!\boldsymbol{A_4}) + 2C_I\dot{\gamma}(\boldsymbol{I} - 3\boldsymbol{A}). \tag{2.4.7}$$

All of the variables retain their original meanings. The final term introduces C_I, the coefficient of rotary diffusion, the scalar magnitude of the rate of strain tensor ($\dot{\gamma} = \sqrt{(1/2)\boldsymbol{D}\!:\!\boldsymbol{D}}$) and the identity tensor $\boldsymbol{I}$. Note that Folgar and Tucker use C_I as an empiricism, and in practice it is used as a fitting parameter. When $C_I = 0$ (i.e. hydrodynamic interactions are negligible), Jeffery's model is recovered.

Folgar's and Tucker's model predicted the orientation distribution function during simple shear in a Newtonian fluid. When Huynh[102] used the model to simulate injection molding of a thermoplastic reinforced with glass fibers, the Folgar-Tucker model over-predicted fiber alignment near the mold walls. Huynh reasoned that this might be due to several mechanisms that might retard fiber motion. These were modeled by multiplying the entire right-had side of Eq. 2.4.7 by a scaling

factor α, yielding Eq. 2.4.8. This parameter takes on a value between zero and unity and serves to slow down fiber orientation. In later rheological work with concentrated polypropylene/glass fiber suspensions, Sepehr et al.[46] used a similar "strain-scaling" approach to improve agreement between experimental and predicted stress-growth data during startup of steady shear. The model itself is:

$$\frac{D\boldsymbol{A}}{Dt} = \alpha[(\boldsymbol{W}\cdot\boldsymbol{A}-\boldsymbol{A}\cdot\boldsymbol{W}) + \xi(\boldsymbol{D}\cdot\boldsymbol{A}+\boldsymbol{A}\cdot\boldsymbol{D}-2\boldsymbol{D}:\boldsymbol{A_4}) + 2C_I\dot{\gamma}(\boldsymbol{I}-3\boldsymbol{A})]. \tag{2.4.8}$$

As convenient as this empiricism is, it violates material objectivity in that different Eulerian observers can obtain different results. This arises specifically due to the violation of the Jaumann derivative through the multiplication of the vorticity tensor. Wang et al.[103] resolved this by reconfiguring the $\boldsymbol{A}$ tensor in terms of its eigenvalues and eigenvectors, deriving the evolution equations for the eigenvectors, scaling the eigenvalues with κ, and recasting the resulting expressions back in terms of the orientation tensor $\boldsymbol{A}$. The resulting set of equations, known as the Reduced Strain Closure (RSC) model, follows:

$$\frac{D\boldsymbol{A}}{Dt} = (\boldsymbol{W}\cdot\boldsymbol{A}-\boldsymbol{A}\cdot\boldsymbol{W}) + \xi\left(\boldsymbol{D}\cdot\boldsymbol{A}+\boldsymbol{A}\cdot\boldsymbol{D}-2\boldsymbol{D}:\left(\boldsymbol{A}_4+(1-\kappa)(\boldsymbol{L}-\boldsymbol{M}:\boldsymbol{A}_4)\right)\right) + 2\kappa C_I\dot{\gamma}(\boldsymbol{I}-3\boldsymbol{A}), \tag{2.4.9}$$

$$\boldsymbol{L} = \sum_{i=1}^{3}\lambda_i\boldsymbol{e}_i\boldsymbol{e}_i\boldsymbol{e}_i\boldsymbol{e}_i, \tag{2.4.10}$$

$$\boldsymbol{M} = \sum_{i=1}^{3}\boldsymbol{e}_i\boldsymbol{e}_i\boldsymbol{e}_i\boldsymbol{e}_i. \tag{2.4.11}$$

Here, λ_i and $\boldsymbol{e_i}$ refer to the ith eigenvalue and eigenvector of $\boldsymbol{A}$, respectively. Note that revising Huynh's model affects two of the terms. First, the diffusion term is scaled by κ. Second, the $\boldsymbol{A_4}$ is modified to incorporate the new tensors based on the eigenvalues and eigenvectors of $\boldsymbol{A}$. Implementing the modification is practically equivalent to using a new closure approximation for $\boldsymbol{A_4}$, hence the name of the model.

Although the RSC model resolves the objectivity problem, it still assumes that the diffusive process introduced by Folgar and Tucker is isotropic. Practical experience fitting the RSC model to experimental orientation data from injection-molded parts reinforced by fibers longer than 1 mm revealed that the model is only capable of attaining an acceptable fit to one of the diagonal components of $\boldsymbol{A}$.[104] Anisotropic rotary diffusion was originally suggested in Folgar's and Tucker's work and several

attempts were made to incorporate this behavior, but those models were not explored in literature for various reasons.[105, 106, 107]

Phelps et al.[104] later approached the problem by building on work replacing the scalar rotary diffusion coefficient with a tensor. They started by revisiting diffusive flux as a vector equation, setting it proportional to the second invariant of the rate-of-strain tensor and an anisotropic diffusion tensor:

$$\boldsymbol{q} = -\dot{\gamma}\boldsymbol{D^r}\cdot\boldsymbol{\nabla}_s\psi, \tag{2.4.12}$$

making the corresponding Smoluchowski equation:

$$\frac{D\psi}{Dt} = -\frac{\partial}{\partial \boldsymbol{p}}\cdot(\psi(\boldsymbol{p},\boldsymbol{x},t)\dot{\boldsymbol{p}} + \boldsymbol{q}), \tag{2.4.13}$$

where $\boldsymbol{q}$ is the diffusivity vector, $\dot{\gamma}$ is the second invariant of the rate-of-strain tensor, $\boldsymbol{D^r}$ is a rotary diffusivity surface tensor, $\boldsymbol{\nabla}_s$ is the surface gradient operator defined in spherical coordinates, and ψ is the orientation distribution function. Folgar's and Tucker's isotropic model is recovered if $\boldsymbol{D^r}$ is replaced with the scalar C_I.

A subtle point here is that all of the quantities in Eqs. 2.4.12-13 are defined in orientation space, which is the surface of a unit sphere. In order to recast this expression in terms of the orientation tensor (a three-dimensional quantity), Phelps et al. reimagine $\boldsymbol{D^r}$ as a two-dimensional projection of some arbitrary three-dimensional tensor onto the two-dimensional orientation space. This new tensor was declared to be a quadratic function of orientation (through $\boldsymbol{pp}$) and was expressed as a symmetric global tensor $\boldsymbol{C}$ using a representation theorem due to Hand.[90] Plugging this expression into the Smoluchowski equation for the orientation distribution function and recasting this in terms of $\boldsymbol{A}$, Phelps et al. generated a nonlinear expression for the diffusive component of an arbitrary orientation evolution equation. Using various heuristics, the expression was significantly reduced to a single term, linear in $\boldsymbol{C}$, and proportional to $\dot{\gamma}$. Finally, a functional form for $\boldsymbol{C}$ was declared (again based on Hand's theorem) and the diffusive term was thus able to be incorporated into any orientation model by replacing the previous isotropic term. The result, which does not include the strain reduction factor κ, follows:

$$\begin{aligned}\frac{D\boldsymbol{A}}{Dt} = {} & (\boldsymbol{W}\cdot\boldsymbol{A} - \boldsymbol{A}\cdot\boldsymbol{W}) + \xi(\boldsymbol{D}\cdot\boldsymbol{A} + \boldsymbol{A}\cdot\boldsymbol{D} - 2\boldsymbol{D}\colon\boldsymbol{A_4}) \\ & + \dot{\gamma}(2\boldsymbol{C} - 2tr(\boldsymbol{C})\boldsymbol{A} - 5(\boldsymbol{C}\cdot\boldsymbol{A} + \boldsymbol{A}\cdot\boldsymbol{C}) + 10\boldsymbol{C}\colon\boldsymbol{A_4}),\end{aligned} \tag{2.4.14}$$

$$\boldsymbol{C} = b_1\boldsymbol{I} + b_2\boldsymbol{A} + b_3\boldsymbol{A}^2 + \frac{b_4}{\dot{\gamma}}\boldsymbol{D} + \frac{b_5}{\dot{\gamma}^2}\boldsymbol{D}^2. \tag{2.4.15}$$

Here, the b_is are taken to be scalar constants for use as fitting parameters. Incorporating the concepts behind the RSC model results in the following model:

$$\frac{D\boldsymbol{A}}{Dt} = (\boldsymbol{W}\cdot\boldsymbol{A} - \boldsymbol{A}\cdot\boldsymbol{W}) + \xi\left(\boldsymbol{D}\cdot\boldsymbol{A} + \boldsymbol{A}\cdot\boldsymbol{D} - 2\boldsymbol{D}\colon\left(\boldsymbol{A}_4 + (1-\kappa)(\boldsymbol{L} - \boldsymbol{M}\colon\boldsymbol{A}_4)\right)\right) + \dot{\gamma}\left(2(\boldsymbol{C} - (1-\kappa)\boldsymbol{C}\colon\boldsymbol{M}) - 2\kappa tr(\boldsymbol{C})\boldsymbol{A} - 5(\boldsymbol{C}\cdot\boldsymbol{A} + \boldsymbol{A}\cdot\boldsymbol{C}) + 10\boldsymbol{C}\colon\left(\boldsymbol{A}_4 + (1-\kappa)(\boldsymbol{L} - \boldsymbol{M}\colon\boldsymbol{A}_4)\right)\right), \tag{2.4.16}$$

where $\boldsymbol{C}$ is defined as above.

The combined ARD-RSC model requires six fitting parameters: the set of 5 b_is and κ. These parameters cannot be set arbitrarily. In fact, some combinations will lead to numerical instability or oscillations in the $\boldsymbol{A}$ components, even in simple flows. Although Phelps and Tucker[104] proposed a procedure for setting values of these parameters, the model's sensitivity remains a serious obstacle for implementation.

Tseng, Chang, and Hsu[108] addressed this by revisiting two key components of the ARD-RSC model: the treatment of strain reduction and the formulation of the anisotropic rotary diffusion tensor. In order to slow down the orientation kinetics, Tseng et al. reframed $\boldsymbol{A}$ by the similarity transformation in terms of a diagonal matrix and a rotational matrix:

$$\boldsymbol{A} = \boldsymbol{R}\cdot\boldsymbol{\Lambda}\cdot\boldsymbol{R}^{\boldsymbol{T}}, \tag{2.4.17}$$

where $\boldsymbol{R}$ is a 3-by-3 tensor made of the eigenvectors of $\boldsymbol{A}$, constructed in such a way that each column contains the three components of the eigenvector. The diagonal matrix $\boldsymbol{\Lambda}$ contains the eigenvalues of $\boldsymbol{A}$. Taking the substantial derivative of $\boldsymbol{A}$, Tseng et al. assumed Intrinsic Orientation Kinetics (IOK), meaning:

$$\frac{D\boldsymbol{A}}{Dt} = -\boldsymbol{R}\cdot\boldsymbol{\Lambda}^{IOK}\cdot\boldsymbol{R}^{\boldsymbol{T}}, \tag{2.4.18}$$

where $\boldsymbol{\Lambda}^{\mathrm{IOK}}$ is a formulation of $\boldsymbol{\Lambda}$ such that:

$$\sum_{i=1}^{3}\frac{D\lambda_i^{IOK}}{Dt} = \alpha\left[\sum_{i=1}^{3}\frac{D\lambda_i}{Dt} - \beta\left(\sum_{i=1}^{3}\frac{D\lambda_i}{Dt}\right)^2\right], \tag{2.4.19}$$

where parameters α and β are treated as fitting parameters. The specific form of Eq. 2.4.19 was selected because it satisfies the identity:

$$\sum_{i=1}^{3}\frac{D\lambda_i^{IOK}}{Dt} = 0, \tag{2.4.20}$$

which is derived from a similar identity for the regular eigenvalues. This modification was named the Retarding Principle Rate (RPR) and can be added as a correction to the isotropic model (Eq. 2.4.7) resulting in a simpler and more computationally efficient method than Eq. 2.4.9 for objectively introducing strain reduction. Tseng et al. implemented the RPR by first calculating $\boldsymbol{A}$ from the isotropic model at a time step, and using those results to calculate the RPR term at the same time step. In other words, the equations were solved separately.

Tseng et al. also revisited the development of the anisotropic diffusion tensor. Rather than adopt a general expression, Tseng et al. proposed the following form:

$$\boldsymbol{D}_r = C_I\left(\boldsymbol{I} - C_M\tilde{\boldsymbol{L}}\right). \tag{2.4.21}$$

Here, C_M is a new parameter called the fiber-rotary-resistance (FRR) coefficient, and $\tilde{\boldsymbol{L}}$ is called the fiber-rotary-resistance tensor, defined as:

$$\tilde{\boldsymbol{L}} = \frac{\boldsymbol{L}^T \cdot \boldsymbol{L}}{\boldsymbol{L}^T : \boldsymbol{L}}, \tag{2.4.21}$$

where $\boldsymbol{L}$ is simply the velocity gradient tensor $\boldsymbol{\nabla u}$. The trace of Eq. 2.4.21 is unity and the tensor is symmetric, however its definition through the velocity gradient renders the model non-objective. The advantage of using this anisotropic diffusion tensor is the significant reduction in fitting parameters.

Combining the IRD, FRR, and RPR models results in the following equations:

$$\frac{D}{Dt}\boldsymbol{A}^{iARD-RPR} = \frac{D}{Dt}\boldsymbol{A}^{\boldsymbol{HD}} + \frac{D}{Dt}\boldsymbol{A}^{\boldsymbol{iARD}}(C_I, C_M) + \frac{D}{Dt}\boldsymbol{A}^{\boldsymbol{RPR}}(\alpha, \beta), \tag{2.4.22}$$

$$\frac{D}{Dt}\boldsymbol{A}^{\boldsymbol{HD}} = (\boldsymbol{W}\cdot\boldsymbol{A} - \boldsymbol{A}\cdot\boldsymbol{W}) + \xi(\boldsymbol{D}\cdot\boldsymbol{A} + \boldsymbol{A}\cdot\boldsymbol{D} - 2\boldsymbol{A_4}:\boldsymbol{D}), \tag{2.4.23}$$

$$\frac{D}{Dt}\boldsymbol{A}^{\boldsymbol{iARD}} = 2\dot{\gamma}C_I(\boldsymbol{I} - 3\boldsymbol{A}) + 2\dot{\gamma}C_I C_M\left\{\left(\boldsymbol{A} - \tilde{\boldsymbol{L}}\right) + 5\left[\left(\boldsymbol{A}\cdot\tilde{\boldsymbol{L}}\right)_{symm} - \left(\boldsymbol{A_4}:\tilde{\boldsymbol{L}}\right)\right]\right\}, \tag{2.4.24}$$

$$\left(\boldsymbol{A}\cdot\tilde{\boldsymbol{L}}\right)_{symm} = \frac{1}{2}\left[\left(\boldsymbol{A}\cdot\tilde{\boldsymbol{L}}\right) + \left(\boldsymbol{A}\cdot\tilde{\boldsymbol{L}}\right)^T\right], \tag{2.4.24a}$$

$$\frac{D}{Dt}\boldsymbol{A}^{\boldsymbol{RPR}} = -\boldsymbol{R}\cdot\frac{D}{Dt}\boldsymbol{\Lambda}^{\boldsymbol{IOK}}\cdot\boldsymbol{R}^T, \tag{2.4.25}$$

$$\frac{D}{Dt}\Lambda_{ii}^{IOK} = \frac{D}{Dt}\lambda_i^{IOK} = \alpha\left[\frac{D\lambda_i}{Dt} - \beta\left(\left(\frac{D\lambda_i}{Dt}\right)^2 + \frac{D\lambda_j}{Dt}\frac{D\lambda_k}{Dt}\right)\right];\ \ i,j,k = 1,2,3. \tag{2.4.25a}$$

Note the modular nature of the improvements. Combined with the smaller number of parameters, the iARD-RPR model offers an improvement in computational efficiency over the ARD-RSC model. Furthermore, by setting $C_M = 0$, $\alpha = 1 - \kappa$, and $\beta = 0$, the ARD-RSC model can be recovered.

Tseng et al.[109] revisited their model to address the non-objectivity due to the use of $\boldsymbol{L}$. While looking at the analytical forms of $\boldsymbol{D^r}$ in simple shear and planar extension, they hypothesized recasting $\boldsymbol{D^r}$ in terms of the rate of deformation tensor, $\boldsymbol{D}$:

$$\boldsymbol{D^r} = C_I\left(\boldsymbol{I} - C_M\frac{\boldsymbol{D}\cdot\boldsymbol{D}}{\|\boldsymbol{D}\cdot\boldsymbol{D}\|}\right), \tag{2.4.26}$$

where $\|\boldsymbol{D}\cdot\boldsymbol{D}\| = \sqrt{(1/2)(\boldsymbol{D}\cdot\boldsymbol{D}):(\boldsymbol{D}\cdot\boldsymbol{D})}$. The rate of deformation tensor is objective by definition, making the new iARD formulation objective by extension. This redefinition of the FRR tensor makes no significant change to the evolution equations, and all instances of $\tilde{\boldsymbol{L}}$ may be replaced with the new definition.

Tseng and coworkers[110, 111] have recently made two incremental improvements to the iARD-RPR model. The first improvement involved reformulating the anisotropic rotary diffusion tensor $\boldsymbol{D_r}$ in terms of the eigenvalues of the $\boldsymbol{A}$ tensor as follows:

$$\boldsymbol{D_r} = \boldsymbol{R}\cdot\widehat{\boldsymbol{D}}_{\boldsymbol{r}}\cdot\boldsymbol{R^t}, \tag{2.4.27}$$

where $\boldsymbol{R}$ is defined the same as previously noted, and $\widehat{\boldsymbol{D}}_{\boldsymbol{r}}$ is a diagonal matrix in which

$$\widehat{\boldsymbol{D}}_{\boldsymbol{r}} = \begin{bmatrix} 1 & 0 & 0 \\ 0 & \Omega & 0 \\ 0 & 0 & 1-\Omega \end{bmatrix}, \tag{2.4.28}$$

where Ω is an empirical parameter. This new model, called the pARD model, provided only a modest improvement over the iARD model in predictions of orientation from an injection-molded plaque.[112] Note that, due to the modular nature of the iARD model, the pARD update only changed the anisotropic terms. The HD and RPR portions remain unchanged.

The second improvement to the iARD model was making α and C_I a function of the shear rate.[111] Empirical expressions were used to correlate the parameters with the shear rate:

$$C_I(\dot{\gamma}) = C_{I0}/(1 + (\dot{\gamma}/\dot{\gamma}_c)^2), \tag{2.4.29}$$

$$\alpha(\dot{\gamma}) = \alpha_0(1 - 1/(1 + (\dot{\gamma}/\dot{\gamma}_c)^2)), \tag{2.4.30}$$

where α_0 and C_{I0} are empirical fitting values, $\dot{\gamma}$ is the shear-rate (the authors give no indication whether this is the typical invariant shear rate $\dot{\gamma} = \sqrt{\boldsymbol{D}:\boldsymbol{D}/2}$ or some other quantity), and $\dot{\gamma}_c$ is a critical shear rate (the authors do not propose a physical interpretation of this parameter and treat it as another fitting parameter).

Tseng et al.[111] used the model to predict the gap-wise orientation profile in two separate end-gated plaques with different dimensions and made of different materials: one was 30 wt% short glass fiber in poly(butylene terephthalate) and one was 50wt% long carbon fiber in polypropylene. The

shear-rate dependence in the model made significantly better predictions in the core region of the plaques when compared with the constant-parameter version of the model. However, this comparison was only done for one location which was on the centerline of the plaque, halfway between the gate and the front of the plaque. A more rigorous validation effort looking at multiple locations in different geometries (say a CGD and EGP) made from the same material would give a better idea of how well the model performs.

In summary, the Tucker family of models represents the state of the art of orientation modeling. These models are currently employed in commercial simulation software and have been established as the basis of comparison for all other models. Even though these models are useful, they do suffer from several fundamental issues.

First, all of the empiricisms introduce more fitting parameters. Work in the field has obtained these by fitting to experimental data, typically from an injection-molded part. This couples the parameters to the mold design and molding conditions. A parameter-fitting technique independent of injection-molding has not been established. Because of this, the true predictive ability of the models is limited.

Second, the models are unable to track the conformation of the fibers during processing. The Tucker models all assume fibers remain rigid during processing, yet long fibers have been observed to flex.[7, 15] This might affect how fibers migrate as well as the mechanical properties of the molded part. Fiber attrition models might also need to incorporate flexing, as current attrition models assume fibers break exclusively under buckling.[113, 114]

Finally, fiber length is not explicitly included in the Tucker models. Observations of injection-molded parts suggest that, as fiber length increases, the gap-wise orientation profile becomes broader and flow-direction orientation is reduced near the mold walls when compared with short fibers.[115] In other words, fiber length seems to be an important variable that is not explicitly accounted for in the models.

2.4.4: The Bead-Rod Model

Although the Tucker family of models provides a sophisticated analysis, at its core this family of models works off the same paradigm as Jeffery: a micromechanical approach is used to analyze the orientation evolution of a population of rigid fibers. Two critical observations can be made. First, the micromechanical approach inevitably results in an intractable many-body problem that must be resolved through empiricisms, introducing an ever-growing list of fitting parameters. Although a

preponderance of fitting parameters yields acceptable predictions, they might obfuscate the effects of fundamental physics that the models don't directly address, such as the non-Newtonian behavior of the matrix and the broad distribution of fiber lengths. Second, and more specifically, fibers have been observed to flex under normal processing conditions. Flexing could affect the mechanical properties of an injection-molded part as well as the orientation evolution and spatial distribution of the fibers.

Noting its success in modeling flexible polymer chains, Strautins and Latz[116] adopted a bead-rod model to describe a single fiber (Fig 2.4.3).

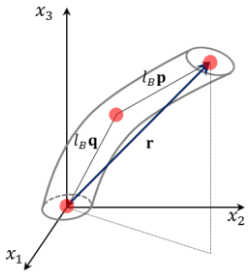

Fig. 2.4.3: Flexed fiber representation employed in the Bead-Rod model

Each rod is capable of moving independently around the center bead, but this motion is limited by the bending potential of the chain. Equation 2.4.27 gives the potential function used by Strautins and Latz:

$$U = \tilde{k}(1 + \boldsymbol{p} \cdot \boldsymbol{q}). \tag{2.4.27}$$

The $\tilde{k}$ here is a bending potential constant. Note that this particular form of the bending potential gives the fiber an aligned equilibrium state (i.e. $\boldsymbol{p} = -\boldsymbol{q}$).

The velocity field of the fluid in the neighborhood of the fiber is represented through a Taylor series expansion that incorporates the second order terms neglected by Jeffery's analysis. Solving the force and torque balances on each bead yields expressions for the linear and angular velocities of each bead, which are subsequently used in a Smoluchowski equation for the orientation distribution function $\psi(\boldsymbol{p}, \boldsymbol{q}, t)$. Notably, the diffusive terms of this equation were dropped so that the effects of flexibility could be isolated in the subsequent investigation.

To put the model in a more familiar and tractable form, Strautins and Latz used the moment formulation suggested by Advani and Tucker.[88] Note that the two-rod model allows the fiber to assume an asymmetric formulation. This causes the bead-rod orientation distribution function to lose the symmetry of its rigid-rod version, resulting in non-zero odd moments of the bead-rod orientation distribution $\psi(\boldsymbol{p}, \boldsymbol{q}, t)$. Limiting the model to the first and second moments of $\psi(\boldsymbol{p}, \boldsymbol{q}, t)$, the

Smoluchowski equation is used to generate the evolution equations, and clever use of closure approximations yields the set of equations:

$$\frac{D\boldsymbol{A}}{Dt} = (\boldsymbol{W}\cdot\boldsymbol{A}-\boldsymbol{A}\cdot\boldsymbol{W})+(\boldsymbol{D}\cdot\boldsymbol{A}+\boldsymbol{A}\cdot\boldsymbol{D}-2\boldsymbol{D}\colon\boldsymbol{A_4}) + \frac{l_B}{2}(\boldsymbol{Cm}+\boldsymbol{mC}-2(\boldsymbol{m}\cdot\boldsymbol{C})\boldsymbol{A})-2k\big(\boldsymbol{B}-\boldsymbol{A}tr(\boldsymbol{B})\big), \tag{2.4.28}$$

$$\frac{D\boldsymbol{B}}{Dt} = (\boldsymbol{W}\cdot\boldsymbol{B}-\boldsymbol{B}\cdot\boldsymbol{W})+(\boldsymbol{D}\cdot\boldsymbol{B}+\boldsymbol{B}\cdot\boldsymbol{D}-2(\boldsymbol{D}\colon\boldsymbol{A})\boldsymbol{B}) + \frac{l_B}{2}(\boldsymbol{Cm}+\boldsymbol{mC}-2(\boldsymbol{m}\cdot\boldsymbol{C})\boldsymbol{B})-2k\big(\boldsymbol{A}-\boldsymbol{B}tr(\boldsymbol{B})\big), \tag{2.4.29}$$

$$\frac{D\boldsymbol{C}}{Dt} = \nabla\boldsymbol{v}^t\cdot\boldsymbol{C}-(\boldsymbol{A}\colon\nabla\boldsymbol{v}^t)\boldsymbol{C}+\frac{l_B}{2}(\boldsymbol{m}-(\boldsymbol{m}\cdot\boldsymbol{C})\boldsymbol{C})-k\big(1-tr(\boldsymbol{B})\big)\boldsymbol{C}, \tag{2.4.30}$$

where:

$$\boldsymbol{A} = \int\int \boldsymbol{pp}\psi(\boldsymbol{p},\boldsymbol{q},t)d\boldsymbol{p}d\boldsymbol{q}, \tag{2.4.31}$$

$$\boldsymbol{B} = \int\int \boldsymbol{pq}(\boldsymbol{p},\boldsymbol{q},t)d\boldsymbol{p}d\boldsymbol{q}, \tag{2.4.32}$$

$$\boldsymbol{C} = \int\int \boldsymbol{p}\psi(\boldsymbol{p},\boldsymbol{q},t)d\boldsymbol{p}d\boldsymbol{q}, \tag{2.4.33}$$

$$\boldsymbol{m} = \sum_{i=1}^{3}\sum_{j=1}^{3}\sum_{k=1}^{3}\frac{\partial^2 v_i}{\partial x_j\partial x_k}A_{jk}\boldsymbol{\delta}_i, \tag{2.4.34}$$

noting that $\boldsymbol{\delta}_i$ refers to the basis vector pointing in the i[th] direction. The fourth-order orientation tensor, $\boldsymbol{A_4}$, is still present and requires a closure approximation.

The $\boldsymbol{B}$ and $\boldsymbol{C}$ tensors both contain information on the flexed state of the fibers. Note that in the perfectly straight case, $\boldsymbol{q}=-\boldsymbol{p}$. When this is true for the entire population of fibers, $\boldsymbol{B}=-\boldsymbol{A}$ and it follows that the trace of $\boldsymbol{B}$ is identically -1. Moreover, $\psi(\boldsymbol{p},\boldsymbol{q},t)$ becomes symmetric and $\boldsymbol{C}$ is identically $\boldsymbol{0}$. Thus, these two values taken in tandem describe the degree of flexing (the trace of $\boldsymbol{B}$) and its direction (through $\boldsymbol{C}$).

Ortman et al.[49] later extended the bead-rod model to concentrated suspensions by incorporating ideas from the Folgar-Tucker and Strain Reduction Factor models. First, the diffusion terms from the Smoluchowski terms are retained and the diffusion coefficient is given the form originally proposed by Folgar and Tucker. The bead-rod model was then re-derived with these terms. Second, the equations are multiplied by the strain reduction factor. The resulting equations follow:

$$\frac{D\boldsymbol{A}}{Dt} = \alpha\Bigg((\boldsymbol{W}\cdot\boldsymbol{A}-\boldsymbol{A}\cdot\boldsymbol{W})+(\boldsymbol{D}\cdot\boldsymbol{A}+\boldsymbol{A}\cdot\boldsymbol{D}-2\boldsymbol{D}\colon\boldsymbol{A_4}) + \frac{l_B}{2}(\boldsymbol{Cm}+\boldsymbol{mC}-2(\boldsymbol{m}\cdot\boldsymbol{C})\boldsymbol{A})+2C_I\dot{\gamma}-2k\big(\boldsymbol{B}-\boldsymbol{A}tr(\boldsymbol{B})\big)\Bigg), \tag{2.4.35}$$

$$\frac{D\boldsymbol{B}}{Dt} = \alpha\Bigg((\boldsymbol{W}\cdot\boldsymbol{B}-\boldsymbol{B}\cdot\boldsymbol{W})+(\boldsymbol{D}\cdot\boldsymbol{B}+\boldsymbol{B}\cdot\boldsymbol{D}-2(\boldsymbol{D}\colon\boldsymbol{A})\boldsymbol{B})-4C_I\dot{\gamma}\boldsymbol{B} + \frac{l_B}{2}(\boldsymbol{Cm}+\boldsymbol{mC}-2(\boldsymbol{m}\cdot\boldsymbol{C})\boldsymbol{B})-2k\big(\boldsymbol{A}-\boldsymbol{B}tr(\boldsymbol{B})\big)\Bigg), \tag{2.4.36}$$

$$\frac{D\boldsymbol{C}}{Dt} = \alpha\left(\nabla\boldsymbol{v}^t\cdot\boldsymbol{C}-(\boldsymbol{A}\colon\nabla\boldsymbol{v}^t)\boldsymbol{C}+\frac{l_B}{2}(\boldsymbol{m}-(\boldsymbol{m}\cdot\boldsymbol{C})\boldsymbol{C})-k\big(1-tr(\boldsymbol{B})\big)\boldsymbol{C}-2C_I\dot{\gamma}\boldsymbol{C}\right), \tag{2.4.37}$$

where $\boldsymbol{A}$, $\boldsymbol{B}$, $\boldsymbol{C}$, and $\boldsymbol{m}$ retain their original definitions.

2.5: Composite Stress Models

An accurate composite stress model linking the fiber microstructure to total stress in the composite would serve two purposes. First, the model could be used in tandem with rheological measurements to obtain orientation model parameters by fitting to stress growth data. This could be done as a time-saving alternative to fitting orientation data. Second, a constitutive equation would allow for full coupling between fiber orientation evolution and the velocity field. Current simulation software takes a decoupled approach, first calculating the flow field from the equations of continuity, momentum, and energy at each time step, and then updating the orientation state at the same time step. Tucker's[117] analysis of coupling between the stress and orientation demonstrates that coupling can have serious ramifications on the predicted flow field, so accounting for this through a constitutive equation might improve modeling accuracy.

In Section 2.5.1, attempts at modeling stress assuming a Newtonian matrix are reviewed. Section 2.5.2 expands on this, looking at models using a Non-Newtonian matrix. Section 2.5.3 rounds out the stress models with a look at non-lubricated squeeze flow and its corresponding models.

2.5.1 Newtonian Stress Models

Hand[90] and Giesekus[118] used Jeffery's results to obtain a constitutive equation for a dilute suspension of ellipsoids. This was done by evaluating the deviatoric stress acting on the ellipsoid, taking its volume average, and adding this to the fluid stress:

$$\boldsymbol{\sigma} = -P\boldsymbol{I}+2\eta_0\boldsymbol{D}+\varphi_0\sum\boldsymbol{\sigma_p}, \tag{2.5.1}$$

where $\boldsymbol{\sigma}$ is the total stress tensor, P is the hydrostatic pressure, $\boldsymbol{I}$ is the identity tensor, η_0 is the viscosity of the unfilled matrix, $\boldsymbol{D}$ is the rate of strain tensor ($1/2\,(\boldsymbol{\nabla v} + \boldsymbol{\nabla v^t})$), φ_0 is the volume fraction of a single fiber, and $\boldsymbol{\sigma_p}$ is the stress contribution of a single fiber.

Ericksen[119] proposed a phenomenological Transversely Isotropic Fluid (TIF) to address the non-objectivity of other stress models. The fluid is incompressible and local direction is described with a director, $\boldsymbol{p}$, at each point, giving the following expression:

$$\frac{D\boldsymbol{p}}{Dt} = \boldsymbol{W}\cdot\boldsymbol{p} + \xi(\boldsymbol{D}\cdot\boldsymbol{p} - \boldsymbol{D}\colon\boldsymbol{ppp}), \tag{2.5.2}$$

$$\boldsymbol{\sigma_{TIF}} = -P_0\boldsymbol{I} + 2\mu_0\boldsymbol{D} + (\mu_1 + \mu_2\boldsymbol{D}\colon\boldsymbol{pp})\boldsymbol{pp} + 2\mu_3(\boldsymbol{D}\cdot\boldsymbol{pp} + \boldsymbol{pp}\cdot\boldsymbol{D}), \tag{2.5.3}$$

where D/Dt signifies the substantial derivative, $\boldsymbol{W}$ is the vorticity tensor ($1/2\,(\boldsymbol{\nabla v} - \boldsymbol{\nabla v^t})$), ξ is a shape factor related to the particle aspect ratio a_r ($(a_r^2-1)/(a_r^2+1)$), P_0 is the equivalent TIF pressure, $\boldsymbol{I}$ is the identity tensor, and the μ_is are material constants. Equation 2.5.2 is Jeffery's equation for non-Brownian particles.

The material constants are key to this expression and directly couple the orientation state with the composite stress. Lipscomb et al.[91] noted that the stress from Eq. 2.5.3 should properly be set equal to $\boldsymbol{\sigma_p}$ from Eq. 2.5.1 for a single fiber. Using the expressions for the deviatoric stress from Jeffery and solving them in a coordinate system embedded in a fiber, Lipscomb et al. derived the following asymptotic expressions for the material constants under the limit of very long fibers:

$$\mu_0 = 2\eta_0, \tag{2.5.4}$$

$$\mu_1 = \mu_3 = 0, \tag{2.5.5}$$

$$\mu_2 = \left(\frac{a_r^2}{\ln a_r}\right)\eta_0, \tag{2.5.6}$$

$$\xi = 1, \tag{2.5.7}$$

thus making the TIF stress:

$$\boldsymbol{\sigma_{TIF}} = -P_0\boldsymbol{I} + 2\eta_0\boldsymbol{D} + \left(\frac{a_r^2}{\ln a_r}\right)\eta_0\boldsymbol{D}\colon\boldsymbol{pppp}. \tag{2.5.8}$$

Using Eq. 2.5.8 as the expression for $\boldsymbol{\sigma_p}$, volume averaging, and adopting the moment tensor formulation described in Section 2.4 gives:

$$\boldsymbol{\sigma} = -(P + \varphi P_0)\boldsymbol{I} + 2(1+2\varphi)\eta_0\boldsymbol{D} + \varphi\left(\frac{a_r^2}{\ln a_r}\right)\eta_0\boldsymbol{D}\colon\boldsymbol{A_4}, \tag{2.5.9}$$

along with the evolution equation:

$$\frac{D\boldsymbol{A}}{Dt} = \boldsymbol{W}\cdot\boldsymbol{A} - \boldsymbol{A}\cdot\boldsymbol{W} + \boldsymbol{D}\cdot\boldsymbol{A} + \boldsymbol{A}\cdot\boldsymbol{D} - 2\boldsymbol{D}\colon\boldsymbol{A_4}. \tag{2.5.10}$$

which is simply Jeffery's equation for long, non-Brownian fibers.

Bear in mind that these expressions are valid only in the dilute regime. Increasing the concentration of fibers makes hydrodynamic interactions important, and these effects must be incorporated into the stress model. Slender body theory has proved useful in this regard. Batchelor[120] first used this approach to predict the elongational stress of a suspension under simple extension. Dinh and Armstrong[121] later generalized Batchelor's results to arbitrary flows and orientation states by incorporating Batcehlor's expressions for the average inter-fiber spacing into an expression for the drag coefficient of the matrix acting on the fiber. In Batchelor's case:

$$\frac{\sigma_{p,11} - {}^{1}\!/_{2}\left(\sigma_{p,22} + \sigma_{p,33}\right)}{3\mu\dot{\varepsilon}} = \frac{4}{9}\frac{\varphi}{\ln\left({}^{\pi}\!/_{\varphi}\right)}a_r^2, \tag{2.5.11}$$

where 1 is the elongation direction, 2 and 3 are the compression directions, and $\dot{\varepsilon}$ is the extension rate. Dinh and Armstrong's general model gives the following expressions for the slip coefficient:

$$\zeta_p = \frac{4\pi L}{\ln(\pi/\varphi)}\eta_0, \qquad \text{aligned} \tag{2.5.12}$$

$$\zeta_p = \frac{2\pi L}{\ln(\pi/(2\varphi a_r))}\eta_0, \qquad \text{random} \tag{2.5.13}$$

which result in the following expressions for the constitutive equation:

$$\boldsymbol{\sigma} = -P\boldsymbol{I} + 2\eta_0\boldsymbol{D} + \left[\frac{4}{3}\frac{\varphi}{\ln(\pi/\varphi)}a_r^2\right]\eta_0\boldsymbol{D}\colon\boldsymbol{A_4}, \tag{2.5.14}$$

$$\boldsymbol{\sigma} = -P\boldsymbol{I} + 2\eta_0\boldsymbol{D} + \left[\frac{2}{3}\frac{\varphi}{ln(\pi D/2\varphi a_r)}a_r^2\right]\eta_0\boldsymbol{D}\colon\boldsymbol{A_4}, \tag{2.5.15}$$

for aligned and random orientations respectively. The disparity in the equations is a product of the expression used for the average inter-fiber spacing, as calculated by Batchelor. Close inspection reveals that in these models, μ_0, μ_1, and μ_3, are zero. This is due to the nature of slender-body analysis, which neglects the thickness of the particle under consideration,[117] although corrections can be made.[122]

Prompted by their previous success in modeling heat and mass transfer in fiber suspensions, Shaqfeh and Fredrickson[123] applied an alternative analysis based on the multiple-scattering expansion of the averaged Green's function. The alternate paradigm can treat hydrodynamic interactions more rigorously than the slender body analysis, and ultimately yields a stress tensor of the same form as that of Dinh and Armstrong, with:

$$\mu_2 = \frac{2a_r^2}{3(\ln(1/\varphi) + \ln(\ln(1/\varphi)) + C')}, \tag{2.5.16}$$

where C' is a factor than accounts for fiber orientation and shape. Incidentally, the values for randomly oriented and aligned rods are -0.6634 and 0.1585 respectively.[124]

The similarity in functional forms between the dilute and semi-dilute models from different analytical paradigms (Giesekus's exact solution, Ericksen's empiricism, Burger's slender body analysis, and Shaqfeh and Fredrickson's multiple scattering) has guided the development of stress tensors for the concentrated regime. Stress models in this regime adopt the form of Eq. 2.5.8 but treat μ_2 as a fitting parameter.

The simplicity of the Lipscomb-style Newtonian model has lent itself to extensive use in simulations of fiber suspensions in non-Newtonian matrices. Ausias et al.[40] investigated concentrated short-fiber-reinforced polypropylene (a_r = 25, loaded at 20 and 30 wt%) during shear creep. The suspension was modeled with a slightly modified Dinh-Armstrong model that treated the $\boldsymbol{D}:\boldsymbol{A_4}$ coefficient as a fitting parameter. This was fit to the stress-growth data from shear creep and coupled with Jeffery's model. Very good agreement was obtained for the overshoot peak value and the steady state stress, but the predicted overshoot breadth was too narrow.

Sepehr et al.[46] considered a similar system (polypropylene/glass fiber, a_r = 18.6, loaded at 5, 10, 20 and 30 wt%) during startup of shear. In this case, the Lipscomb model was coupled to the Folgar-Tucker model and the $\boldsymbol{D}:\boldsymbol{A_4}$ coefficient was treated as a fitting parameter. Strain was scaled by a factor α such that:

$$\gamma = \alpha\dot{\gamma}t, \tag{2.5.17}$$

to obtain better transient behavior from the predictions. Note that this scaling was not applied to the orientation model (as in Huynh[102] or Wang et al.[103]), but was used as an empiricism to "stretch" the predicted stress growth curve. The steady state values of the stress growth coefficient and the normal stress difference were predicted, but the transient behavior was in very poor agreement with empirical data. Wang et al.[103] would later introduce the strain reduction concept into the Folgar-Tucker model (in a way that would retain Eulerian objectivity) and couple it to the Lipscomb model.

2.5.2: Non-Newtonian Models

As suggested by Leal[125] and demonstrated by work from Mason and co-workers,[126, 127] the normal stresses present in non-Newtonian matrices (particularly polymer melts and suspensions) can have a profound effect on the orientation evolution of fibers. The Newtonian models of Lipscomb

and Dinh and Armstrong are fundamentally incapable of capturing these effects. This section looks at some efforts to account for the non-Newtonian behavior of the matrices. As will become clear, the resulting models are much more cumbersome than their Newtonian counterparts.

Goddard[128] started the efforts by following Batchelor's[120] slender body analysis for highly aligned fibers under simple extension and extending it to a power-law fluid. His result suggested that the stress introduced by the inclusion of fibers would be significantly smaller than that of the Newtonian case predicted by Batchelor. This effect arises from the shear-dominated flow between the fibers, in spite of the bulk extensional flow, which induces shear-thinning and thus a reduction in the bulk stress.

Wang et al.[129] later continued Dinh's and Armstrong's analysis in deriving a constitutive equation using the Ellis model. The main difference in the results was the form of the slip coefficient:

$$h\dot{\gamma}_0 = \frac{\tau_{1/2}}{\eta_0}\left[\left(\frac{h\dot{\gamma}_0}{2\pi\tau_{1/2}}\right)\ln(h^{-1})\zeta_s^{-1} + \frac{1}{m-1}\left(\frac{h\dot{\gamma}_0}{2\pi\tau_{1/2}}\right)^m (h^{1-m}-1)\zeta_s^{-m}\right], \tag{2.5.18}$$

where h is a dimensionless parameter correlating the inter-fiber spacing with the particle shape (equal to $\sqrt{\pi/\varphi}$ in the perfectly aligned limit), $\dot{\gamma}_0$ is the applied shear rate, $\tau_{1/2}$, m, and η_0 are the Ellis model parameters, and ζ_s is the slip coefficient. The constitutive equation is no different from Dinh's and Armstrong's result in form, and using their expression for the slip coefficient results in their model. The particle stress contribution is:

$$\boldsymbol{\sigma_p} = \frac{\varphi a_r^2}{3\pi\zeta_s}\boldsymbol{D}:\boldsymbol{A_4}. \tag{2.5.19}$$

The key result here is that the slip coefficient is now a function of the applied shear rate, allowing the model to capture the shear-thinning behavior of the matrix. Thomasset et al.[130] would later adopt a similar, simpler approach with the Carreau model.

One common trait between the works of Sepehr et al., Ausias et al., and Wang et al. is the fact that data were only generated at a limited number of slow shear rates. Thomasset et al.[130] greatly extended the analysis to higher and lower shear rates for yet another polypropylene/glass fiber composite (loaded from 7.3 to 17.4 vol%). Notably, composites were made from pultruding pellets of various initial lengths (1, 10, 15, and 20 mm) and breakage was noted, but the post-processing length distribution was not reported, nor was an average aspect ratio. The Lipscomb framework was adopted and modified to incorporate shear-thinning and an apparent yield stress. Specifically, the polymer viscosity was described by the Carreau model, and a yield stress term was added (see Eqs. 2.5.20-22).

$$\sigma_Y = GC\gamma, \tag{2.5.20}$$

$$\boldsymbol{\sigma} = GC\gamma_s + \eta_0\left(1 + \frac{\lambda^2}{2}\dot{\gamma}\right)^{\frac{n-1}{2}}\left[(1+2\varphi)\dot{\boldsymbol{\gamma}} + 15\mu_f \boldsymbol{A_4}\!:\dot{\boldsymbol{\gamma}}\right], \tag{2.5.21}$$

$$C = \frac{27}{6}(1 - 3\boldsymbol{A}\!:\boldsymbol{A} + 2\boldsymbol{A}\cdot\boldsymbol{A}\cdot\boldsymbol{A}). \tag{2.5.22}$$

In these equations, G is a proportionality constant; C is a constant used in the interpolation of the hybrid closure approximation for $\boldsymbol{A_4}$ and is a function of the orientation state; γ is the strain (γ_s being its value at the yield stress); η_0, λ, and n are the Carreau model constants; and μ_f is the coefficient coupling orientation and stress.

These modifications allowed the model to capture the shear-thinning behavior of the composites at fast shear rates and the apparent yield stress behavior at slow shear rates under both simple shear and simple extension. Close inspection of the model reveals that the Carreau model is rather crudely implemented, here simply replacing the Newtonian viscosity rather than the more rigorous slender body approach taken by Wang and Cheau[129] with the Ellis model. Thomasset et al.[130] found this model gave good agreement with steady state shear and simple extension viscosity, but they did not investigate startup of either flow.

Later work by Eberle et al.[52] would use parameters obtained from fitting a similar model to stress-growth data in order to predict orientation evolution. A poly(butylene terephthalate)/glass fiber composite (a_r = 28.2, loaded at ≤ 17.7 vol%) was subjected to startup of shear. The Lipscomb model with the Carreau viscosity model, coupled to the Folgar-Tucker model as modified by Huynh[102], was adopted, and μ_2, α, and C_I were used as fitting parameters. These were obtained by fitting to stress growth data at a shear rate of 6 s^{-1}. These parameters were then used to predict the stress-growth coefficient and first normal stress difference at 1 s^{-1} and 10 s^{-1} and the evolution of the A_{ii} components at 1 s^{-1}. Qualitative agreement was obtained in the stress growth and normal stress difference, however the shear rate dependence was not accurately captured. Orientation evolution at 1 s^{-1} was also qualitatively predicted, but flow-direction alignment was over-predicted.

Ortman et al.[49] extended this work into concentrated long fiber reinforced composites (a_r = 201, φ = 0.048 and 0.145) by making the coefficients functions of the invariants of $\boldsymbol{A}$. In this modified model:

$$\boldsymbol{\sigma_{mod}} = -P\boldsymbol{I} + \eta_m(\boldsymbol{D} + f_1\varphi\boldsymbol{D} + f_2\boldsymbol{A_4}\!:\boldsymbol{D}), \tag{2.5.23}$$

$$f_1 = \frac{c_1}{\dot{\gamma}_{min}^b} \quad \dot{\gamma} \leq \dot{\gamma}_{min}, \tag{2.5.24}$$

$$f_1 = \frac{c_1}{\dot{\gamma}^b} \quad \dot{\gamma} > \dot{\gamma}_{min}, \tag{2.5.25}$$

$$f_2 = c_2 I_A II_A III_A, \tag{2.5.26}$$

where

$$I_A = tr(\boldsymbol{A}), \tag{2.5.27}$$

$$II_A = \frac{1}{2}[tr(\boldsymbol{A})^2 - tr(\boldsymbol{A} \cdot \boldsymbol{A})], \tag{2.5.28}$$

$$III_A = \det(\boldsymbol{A}). \tag{2.5.29}$$

These empirical adjustments were made in an attempt to match the shear-thinning behavior of the composite (as opposed to just the matrix) and the stress overshoot. Model parameters were obtained by fitting to stress-growth data at some unspecified shear rate. The model with variable coefficients made improved predictions relative to the model with constant coefficients, particularly in matching the magnitude and breadth of the stress overshoot. Furthermore, the model parameters from the variable coefficient model made improved predictions of the A_{ii} evolution during startup of simple shear. No predictions or measurements were made of the normal stress difference.

One fundamental shortcoming of the models previously described is that they are still purely viscous models. Notable exceptions are the General Equation for Non-Equilibrium Reversible-Irreversible Coupling (GENERIC) template of Grmela and coworkers and the macroscopic model of Azaiez and coworkers.

Grmela and coworkers have composed a significant body of work[43, 131, 132, 133, 134] on fiber suspensions with viscoelastic matrices using a non-equilibrium thermodynamics perspective. Their models begin at the microscopic level. The suspension is described by the linear momentum of the polymer chains and the fibers, the configuration state of the polymer chains, the orientation state of the fibers, and sometimes the angular momentum of the fibers. Evolution equations of these quantities are postulated in terms of the matrix kinematics and a Hemlholtz free energy function, and coupled through a stress tensor involving an energy dissipation function.

All of the models explored at least approximate the GENERIC template.[135] This guarantees the evolution behavior will be in agreement with equilibrium thermodynamics, in other words that the free energy is at a minimum at the steady state. Although this guarantee is interesting from a fundamental perspective, its necessity in predicting stress growth and orientation evolution remains unclear. The model requires no small degree of customization for each application. Indeed the

GENERIC *structure* is retained in each application, but its *specific manifestation* can change a great deal. The experimentalist needs to identify the appropriate evolution equations for the polymer (e.g. FENE-P) and the fibers (e.g. Folgar-Tucker), and the appropriate analytical expression for the Helmholtz free energy and energy dissipation functions. Many combinations of these functions exist, so the experimentalist needs an extensive knowledge of these functions to best represent the system under study.

This high degree of customizability makes the GENERIC template difficult to evaluate. Efforts to match transient and steady state rheological data for a variety of systems of Newtonian[133] and non-Newtonian[43, 131, 132, 134] matrices with rigid[43, 131, 132, 133] and semi-flexible[134] fibers see reasonable qualitative agreement, but struggle to make quantitative predictions. Whether the GENERIC template or the specific evolution and energy functions selected are the source of quantitative failure is unclear.

Recent work by Azaiez[136] also attempts to incorporate the viscoelastic behavior of the polymer matrix with a stress tensor due to Giesekus[137] and two stress tensors based on the FENE-P[138] and FENE-CR[139] models, coupled with the Folgar-Tucker orientation model.[101] Note that the approach used with the polymer matrix resulted in a complex set of equations, given as follows:

$$\boldsymbol{\tau_c} = 2\eta_s \boldsymbol{D} + \boldsymbol{\tau_p} + \boldsymbol{\tau_f}, \tag{2.5.30}$$

Giesekus

$$\lambda\left[\frac{D\boldsymbol{\tau_p}}{Dt} - (\boldsymbol{\nabla u})^t \cdot \boldsymbol{\tau_p} - \boldsymbol{\tau_p} \cdot \boldsymbol{\nabla u}\right] + s\boldsymbol{\tau_p} - \frac{a\lambda}{\eta_0}(\boldsymbol{\tau_p} \cdot \boldsymbol{\tau_p}) + \frac{m(1-s)}{2}(\boldsymbol{A} \cdot \boldsymbol{\tau_p} + \boldsymbol{\tau_p} \cdot \boldsymbol{A}) = -2\eta_0 \boldsymbol{D}, \tag{2.5.31}$$

FENE-P

$$\lambda\left[\frac{D\boldsymbol{B}}{Dt} - (\boldsymbol{\nabla u})^t \cdot \boldsymbol{B} - \boldsymbol{B} \cdot \boldsymbol{\nabla u}\right] + Z\left[s\boldsymbol{B} + \frac{m(1-s)}{2}(\boldsymbol{A} \cdot \boldsymbol{B} + \boldsymbol{B} \cdot \boldsymbol{A})\right] = s\boldsymbol{I} + m(1-s)\boldsymbol{A}, \tag{2.5.32a}$$

$$\boldsymbol{\tau_p} = -\eta_0\left(\frac{Z\boldsymbol{B} - \boldsymbol{I}}{\lambda}\right), \tag{2.5.32b}$$

FENE-CR

$$\lambda\left[\frac{D\boldsymbol{B}}{Dt} - (\boldsymbol{\nabla u})^t \cdot \boldsymbol{B} - \boldsymbol{B} \cdot \boldsymbol{\nabla u}\right] + Z\left[s\boldsymbol{B} + \frac{m(1-s)}{2}(\boldsymbol{A} \cdot \boldsymbol{B} + \boldsymbol{B} \cdot \boldsymbol{A})\right] = Z[s\boldsymbol{I} + m(1-s)\boldsymbol{A}], \tag{2.5.33a}$$

$$\boldsymbol{\tau_p} = -\eta_0\left(\frac{Z\boldsymbol{B}}{\lambda}\right), \tag{2.5.33b}$$

Fiber Orientation Evolution

$$\frac{D\boldsymbol{A}}{Dt} = (\boldsymbol{W}\cdot\boldsymbol{A} - \boldsymbol{A}\cdot\boldsymbol{W}) + \xi(\boldsymbol{D}\cdot\boldsymbol{A} + \boldsymbol{A}\cdot\boldsymbol{D} - 2\boldsymbol{A_4}\colon\boldsymbol{D}) + 2C_I\dot{\gamma}(\boldsymbol{I} - 3\boldsymbol{A}), \tag{2.5.34}$$

Fiber Stress Contribution

$$\boldsymbol{\tau_f} = 2\varphi\eta(\dot{\gamma})[C\boldsymbol{D} + A\boldsymbol{D}\colon\boldsymbol{A_4}], \tag{2.5.35}$$

where λ is a force constant related to the dumbbell model, τ_p is the polymer contribution to the stress, s is a coupling parameter which tunes the influence of orientation on the polymer dumbbells, m is the dimensionality of the solution space (e.g. m = 3 for a 3D problem), a is a parameter related to the configuration-dependent mobility tensor, Z is a parameter that makes the spring force of the polymer dumbbell non-Hookean, and $\boldsymbol{B}$ is the end-to-end tensor which describes the orientation and degree of stretching exhibited by the polymer dumbbells. The equations presented here neglect the contribution of a Newtonian solvent included in the original model, which is a simple addition of $\eta\boldsymbol{D}$ to the composite stress (Eq. 2.5.30).

Two interesting observations can be made of Azaiez's and Grmela's models. First, that the fiber stress contribution is extremely similar to that proposed for Newtonian fluids, the only concession to the non-Newtonian behavior of the matrix being the use of a shear-rate-dependent viscosity. Given the general success of this style of fiber stress expression, this empiricism seems reasonable. Second, the orientation evolution model, like the stress tensor, is formally the same as that for a Newtonian matrix. The success of the Tucker family of models (all based on a Newtonian matrix) grants this empiricism credence. In spite of the success of the Newtonian stress and orientation models, their use does raise questions about logical consistency. Both Grmela and Azaiez take great pains to incorporate the elastic character of the matrix into the matrix stress response, but this same level of detail is not extended to the fiber stress and orientation evolution, in spite of experimental and theoretical evidence that matrix elasticity plays an influential role in both.

Models of the style proposed by Grmela and Azaiez, that is to say models that fully account for the matrix viscoelasticity, have seen far less development. As mentioned previously, the high degree of complexity and customizability of the GENERIC template makes its evaluation very difficult, and the non-equilibrium paradigm might act as a barrier for implementation by engineers. The model proposed by Azaiez,[136] though easier to envision, is still relatively unexplored compared to the Lipscomb-style model.

To date, only a handful of papers have investigated the Azaiez model. Huq and Azaiez[30] used it with an aqueous poly(ethylene oxide) solution loaded with unimodal glass fiber populations of aspect ratio ranging from 26.2 to 126. Fiber volume fraction varied between 2% and 7%, and long fiber suspensions were limited to lower loadings to minimize wall effects. The FENE-P model was fit to the steady-state shear viscosity data and the s and C_I parameters were used to fit the data. Notably, no single set of s and C_I could fit the entire shear rate range. The Newtonian plateau, transition and power law regions each required its own pair of parameters. Whether this is a failure of the model or a statement on the importance of fiber-matrix coupling in these regions is an open question. Recall that the model from Thomasset et al.[130] was able to predict both the shear and extensional viscosity curves of a polypropylene/glass fiber composite with a single set of parameters.

Kagarise et al.[140] applied the model to a polystyrene/carbon nanofiber (CNF) composite. They specifically used the decoupled version ($s = 1$) with a 5-mode Giesekus stress tensor. Stress tensor parameters were fit to the loss and storage moduli data of the unfilled resin from small amplitude oscillatory analysis, and C_I was obtained by minimizing error between the steady state value of A_{11} from both simple shear and simple extension. The model obtained very good agreement with the stress growth coefficient in simple shear for CNF loadings of 2, 5, and 10 wt%. Good agreement was also attained with the stress growth coefficient in simple extension at 2 wt% loading, but strain-hardening was over-predicted at the two higher loadings. Steady-state viscosity curves were not developed for either shear or simple extension.

2.5.3: Incorporating Fiber Bending

Several important composite part mechanical properties, such as impact toughness and fracture resistance, continue to improve as fiber length increases beyond 1 mm, and recent composite processing efforts have focused on minimizing fiber attrition to take advantage of these property enhancements. These long fibers are capable of flexing under processing conditions. Switzer and Klingenberg[8] quantified this ability to flex with the dimensionless parameter:

$$S^{eff} = \frac{\pi E_Y}{64\eta_m} a_r^{-4}, \tag{2.5.36}$$

in which E_Y is the Young's modulus and η_m is the matrix viscosity. As the value of S^{eff} increases, the fiber's ability to flex decreases. Noting the strong inverse relation to fiber aspect ratio, one sees that longer glass fibers can be expected to flex. This flexed state will introduce stresses and could affect the mechanical properties of an injection molded part as well as providing a mechanism for fiber

breakage. The orientation model of Strautins and Latz[116] was discussed in Section 2.4.4, so this section will focus on inclusion of flexibility in the stress model.

In addition to the modifications made to the Lipscomb-style stress tensor, Ortman et al.[49] suggested a term for fiber flexing:

$$\boldsymbol{\sigma_{bending}} = \frac{3}{4} k \varphi a_r \frac{tr(\boldsymbol{r})}{l_B^2} (\boldsymbol{A} - \boldsymbol{R}), \tag{2.5.37}$$

$$\boldsymbol{r} = l_B^2 \int \int (\boldsymbol{p} - \boldsymbol{q})\,(\boldsymbol{p} - \boldsymbol{q}) \psi(\boldsymbol{p}, \boldsymbol{q}, t) d\boldsymbol{p} d\boldsymbol{q}, \tag{2.5.38}$$

$$\boldsymbol{R} = \frac{\boldsymbol{r}}{tr(\boldsymbol{r})}, \tag{2.5.39}$$

where k is the fiber flexibility parameter, estimated as $(E_Y/64\eta_m)(d/l_B)^3$ in which d is the fiber diameter and l_B is the fiber half-length; $\boldsymbol{r}$ is the end-to-end tensor of a bent fiber; and $\boldsymbol{R}$ is the normalized end-to-end tensor. A population of unbent fibers yields $\boldsymbol{R} = \boldsymbol{A}$, nullifying the bending contribution. This study was a rather poor test of the model, as only a negligible degree of flexing was predicted.

Abisset-Chavanne et al.[141] took a different, more rigorous approach, extending the Taylor expansion of the velocity field in the neighborhood of the fiber to include the second gradient terms. They then systematically demonstrated that these were the minimum-order kinematics required to induce fiber flexing. Following through with this realization, fibers were modeled through their orientation vector $\boldsymbol{p}$ (still described through Jeffery's model) and a bending angle vector $\boldsymbol{\varphi}$, such that:

$$\dot{\boldsymbol{p}} = \boldsymbol{\nabla v} \cdot \mathbf{p} - \boldsymbol{\nabla v}\colon \mathbf{ppp}, \tag{2.5.40}$$

$$\dot{\boldsymbol{\varphi}} = \boldsymbol{\nabla \omega} \cdot \boldsymbol{p} L - \frac{\kappa}{\xi^R} \boldsymbol{\varphi}, \tag{2.5.41}$$

$$\boldsymbol{\omega} = \boldsymbol{\nabla} \times \mathbf{v}, \tag{2.5.42}$$

$$\kappa = \frac{E_Y I}{L}, \tag{2.5.43}$$

in which L is the fiber length, I is the moment of area, and ξ^r is a rotary friction coefficient.

Fried and Gurtin[142] proposed a second gradient formulation of the principle of internal power:

$$W_{int} = \int_\Omega \boldsymbol{\sigma}\colon \boldsymbol{\nabla v}\, d\boldsymbol{x} + \int_\Omega \boldsymbol{G}\colon \boldsymbol{\nabla \omega}\; d\boldsymbol{x}, \tag{2.5.44}$$

which gives rise to the momentum balance:

$$\rho \frac{D\boldsymbol{v}}{Dt} = \boldsymbol{\nabla} \cdot \boldsymbol{\sigma} + \boldsymbol{\nabla} \times (\boldsymbol{\nabla} \cdot \boldsymbol{G}), \tag{2.5.45}$$

$$\sigma = -P\boldsymbol{I} + 2\eta\boldsymbol{D} + 2\mu_2\eta\boldsymbol{D}:\boldsymbol{A_4}, \tag{2.5.46}$$

where $\boldsymbol{G}$ is called a hyper-stress. A constitutive equation for the hyper-stress was proposed:

$$\boldsymbol{G} = \boldsymbol{G^f} + \widetilde{\boldsymbol{G}}^{\boldsymbol{r}}, \tag{2.5.47}$$

$$\boldsymbol{G^f} = \eta\mathcal{L}_f(\boldsymbol{\nabla\omega} + \iota\boldsymbol{\nabla\omega^t}), \tag{2.5.48}$$

$$\widetilde{\boldsymbol{G}}^{\boldsymbol{r}} = \boldsymbol{G^r} + \zeta(\boldsymbol{G^r})^{\boldsymbol{t}}, \tag{2.5.49}$$

$$\boldsymbol{G^r} = \varrho\sum \boldsymbol{pM} = \varrho\sum \boldsymbol{p}(\kappa\boldsymbol{\varphi}), \tag{2.5.50}$$

where η is the matrix viscosity, $\mathcal{L}_f$ is a fluid gradient length, ι and ζ are constants that control the degree of symmetry or anti-symmetry of the fluid and rod contributions to the hyper-stress respectively, ϱ is a proportionality constant, and $\boldsymbol{M}$ is the bending moment acting of the ith fiber. The summation in Eq. 2.5.50 is over all fibers. Note that all of the fiber flexibility information is neatly contained in the rod contribution to the hyper-stress, $\boldsymbol{G^r}$.

Integrating Eqs. 2.5.47-50 over the orientation distribution function yields a moment tensor related to the fiber flexing:

$$\boldsymbol{g} = \int_S \int_C \boldsymbol{p\varphi\psi}(\boldsymbol{p},\boldsymbol{\varphi},t)\, d\boldsymbol{\varphi}d\boldsymbol{p}, \tag{2.5.51}$$

with a corresponding evolution equation:

$$\frac{D\boldsymbol{g}}{Dt} = \boldsymbol{\nabla v}\cdot\boldsymbol{g} - (\boldsymbol{\nabla v}:\boldsymbol{A})\boldsymbol{g} + L\boldsymbol{A}\cdot(\boldsymbol{\nabla\omega})^{\boldsymbol{t}} - \frac{\kappa}{\xi^R}\boldsymbol{g}, \tag{2.5.52}$$

that gives an evolution equation for the rod contribution to the hyper-stress:

$$\frac{D\boldsymbol{G^r}}{Dt} = \boldsymbol{\nabla v}\cdot\boldsymbol{G^r} - (\boldsymbol{D}:\boldsymbol{A})\boldsymbol{G^r} + E\mathcal{L}_r^2(\boldsymbol{A}\cdot\boldsymbol{\nabla\omega^t}) - T^{-1}\boldsymbol{G^r}, \tag{2.5.53}$$

in which $\mathcal{L}_r^2$ is a rod gradient length and $\boldsymbol{T}$ is a relaxation time related to the relaxation of elastic stress stored in the flexed fiber.

Equations 2.5.45-48, and 2.5.53 in addition to Jeffery's model constitute the system of equations for an arbitrary flow problem. The key feature of this model is the compartmentalization of the effects of orientation and flexing into the stress and hyper-stress respectively. Although the model itself is cumbersome and limited to dilute suspensions in Newtonian fluids, the compartmentalized nature of the stress contributions of orientation and flexing seems to corroborate the treatment by Ortman et al.[49] in which the flexing stress is a linear addition to the orientation and matrix contributions. However, the second-gradient model is much less easily used. Determining the initial condition for $\boldsymbol{G^r}$ isn't clear as it contains information on both the orientation and flexed state of the

fibers, and the authors provide no guidance. Further development of the model is necessary for implementation in rheological studies of polymer-fiber suspensions.

2.5.4: Non-Lubricated Squeeze Flow

Non-lubricated squeeze flow is a theoretically interesting flow for evaluating orientation models. On the one hand, it contains both shear and extensional flow. This could help identify when either extension or shear dominate the orientation dynamics, and how the interaction between the two flow types affects the orientation dynamics. This combination of shear and extension is also a key feature of injection-molding flows, so non-lubricated squeeze flow could serve as a useful, easily controlled analog for injection molding.

On the other hand, the kinematics could be useful for investigating fiber flexibility. The influence of fiber flexing on the fiber orientation dynamics remains poorly understood in spite of the prevalence of fiber flexing in long-fiber reinforced parts. Although Forgacs and Mason[143] observed fiber flexibility in suspensions of fibers inside Newtonian fluids during simple shear, the same has not been observed in suspensions of long glass fibers inside polymeric matrices during simple flows. Recent theoretical analyses by Abisset-Chevanne et al.[141] and Strautins and Latz[116] suggest that the origin of fiber flexibility lies in second-gradient influences in the velocity field close to an individual fiber's surface. Depending on the analysis used, the macroscopic flow field must be twice[116] or four-times[141] differentiable. This corroborates the lack of evidence for flexing in rheological flows despite observations of flexed fibers inside injection-molded parts., and suggests non-lubricated squeeze flow might provide a controlled method for producing a simple flow field (relative to injection molding) that nonetheless provides enough complexity to induce fiber flexing.

Several analytical expressions for the flow field in non-lubricated biaxial compression have been proposed. Ericsson et al.[144] made use of the divergence-free parabolic velocity field:

$$u = \dot{\gamma}_{11}^{0}\left(1 - 4\left(\frac{x_3}{h}\right)^2\right)x_1, \tag{2.5.54}$$

$$v = \dot{\gamma}_{22}^{0}\left(1 - 4\left(\frac{x_3}{h}\right)^2\right)x_2, \tag{2.5.55}$$

$$w = -(\dot{\gamma}_{11}^{0} + \dot{\gamma}_{22}^{0})\left(1 - 4\left(\frac{x_3}{h}\right)^2\right)x_2, \tag{2.5.56}$$

in which the subscripts 1, 2, and 3 refer to the horizontal plane directions (1 and 2) and the thickness direction (3); velocity components u, v, and w refer to the velocity in the 1, 2, and 3 directions respectively; $\dot{\gamma}_{ii}^{0}$ refers to the maximum through-thickness shear rate in the ith direction, and h is the

half-thickness of the sample. The authors coupled this flow field with the Lipscomb-style composite stress tensor and were able to predict anisotropic flow behavior in a wet-laid polypropylene-glass fiber composite.

Kotsikos et al.[145] combined a variational approach with a pseudo-power law stress model to give the following velocity profile:

$$u_r = \left(\frac{2n'+1}{n'+1}\right)\left(\frac{r}{2}\right)\bar{\dot{\varepsilon}}\left[1-\left(4\frac{z^2}{h^2}\right)^{\frac{n'+1}{2n'}}\right] \tag{2.5.57}$$

$$u_z = \left(\frac{2n'+1}{n'+1}\right)\bar{\dot{\varepsilon}}\left[\frac{z}{h}-\left(\frac{n'}{n'+1}\right)\left(\frac{z}{h/2}\right)^{\frac{2n'+1}{n'}}\right] \tag{2.5.58}$$

in which r and z refer to the radial and thickness directions respectively, u_r and u_z refer to the velocity in the r and z directions respectively, h is the thickness of the sample, $\bar{\dot{\varepsilon}}$ is the rate of compression, and n' is the value of the power law exponent that minimizes the dissipation of energy. The authors used this model to derive a closure force model that interpolated between pure extension and pure shear flow and was able to fit to experimental closure force data.

Even though the previous two examples apply strictly to biaxial compression, they suggest that squeeze flow should provide a flow field with kinematics that are complex enough to induce flexing. However, non-lubricated biaxial compression often fails to reorient fibers, which isn't ideal for evaluating models of fiber orientation dynamics. Ericsson et al.[144] found that when fibers were initially fully-oriented in a particular direction, the matrix flowed perpendicular to the fiber alignment direction rather than flowing freely. Thattaiparasarthy et al.[146] observed that fiber orientation did not change even when fibers where oriented randomly in the plane.

Work by Shuler and Advani[147] suggests that squeeze flow in a rectangular channel would not induce fiber reorientation or flexing either. However, the fibers in their work were as long as the sample was wide (5 cm) and were unidirectionally oriented in the width direction, so this behavior might not extend to shorter fiber systems. Furthermore, they used highly-loaded samples with volume fractions at and above 0.20, higher than typical injection-molded parts.

Dumont et al.[148] performed lubricated squeeze flow (constant linear closure rate) in a rectangular channel with a poly(methyl methacrylate) matrix reinforced with 13 mm long glass fiber bundles at 5, 10, and 15 vol% fiber bundles. They found that the fibers did indeed reorient during squeeze flow for all fiber loadings. Although they used lubrication, the stress growth during the test

suggests that lubrication failed at some point. Venerus an coworkers[80, 81] showed that a breakdown in lubrication would lead to a stress growth that exponentially increased in time, which was what Dumont et al. observed.

Preliminary work by Cieslinski[7] showed that fibers in a polypropylene-glass fiber composite extruded into a slit die did flex. This geometry is similar to that for squeeze flow in a rectangular channel, and like the slit die, squeeze flow in a rectangular channel is pressure-driven. Non-lubricated squeeze flow in the rectangular channel would have a more complex flow field than the biaxial case owing to the side walls, thus the kinematics should satisfy the criteria for flow-induced flexing.

The force required to close the platens during squeeze flow would also be measured, so squeeze flow could be used to validate a suspension stress model. Engmann et al.[149] published an extensive general review of work investigating lubricated and non-lubricated biaxial squeeze flow, and Servais et al.[150] provided a short review of biaxial squeeze flow of fiber reinforced plastics in particular. Researchers have proposed various models for predicting the closure force, including those based on a Carreau fluid[147, 150], a power law fluid[145, 146, 151], a Bingham fluid[152], and even Dinh's and Armstrong's composite tensor (under the assumption that orientation did not change from the initial state).[144]

All of these models assume fibers do not reorient during flow, which is a valid assumption for biaxial squeeze flow, but might not hold for squeeze flow in a rectangular channel. Nor do these models offer a method to account for fiber flexing. Ortman et al.[49] suggested such a term, but the model was evaluated in startup of shear where only a very small amount of flexing would be expected. Rajabian et al.[134] suggested an alternative model for incorporating fiber flexibility, but again only evaluated this model in startup of shear. The theoretical analyses from Strautins and Latz[116] and Abisset-Chevanne et al.[141] suggest flexing should not be significant in simple shear.

To conclude, non-lubricated squeeze flow in a rectangular channel seems to be a potential method of investigating the influence of fiber flexibility on orientation evolution and the composite stress. Work with biaxial compression suggests the kinematics should be sufficiently complex for inducing fiber flexing, but not so complex that analytical expressions for the flow field can't be proposed, reducing the need for fully 3D simulations. Furthermore, preliminary observations of pressure-driven flow of a polypropylene-glass fiber composite through a slit die suggest that squeeze flow in a rectangular channel, which is similar in a number of aspects, should be able to induce flexing as well. Finally, non-lubricated squeeze flow should provide a method for directly measuring the influence of fiber flexing on closure force, and thus also a method for evaluating a stress model that can account for fiber flexing.

2.6: Summary of Previous Group Work

This section summarizes previous efforts from members of the Baird group to provide context for the proposed work. Very little work outside of the group has correlated fiber orientation evolution and stress growth behavior with experimental data. Furthermore, most outside work obtained orientation model parameters from fitting to orientation data in an injected-molded part rather than from rheological experiments. Evaluating orientation model parameters from fitting to data from rheological experiments (either from orientation data directly or through a stress tensor) in their ability to predict orientation evolution during injection molding of model geometries has been a recurring theme throughout the group's work and is unique in the field.

Eberle[153] began by investigating short glass fiber reinforced poly(butylene terephthalate). In this work, he pioneered the use of a cone-and-donut sample to investigate the stress growth and fiber orientation evolution of the composite under startup of simple shear. He obtained orientation model parameters by fitting a stress model to stress-growth coefficient and normal stress data, and these made predictions that compared favorably with experimental observations of the orientation evolution. Mazahir and coworkers[154, 155] and Velez-Garcia et al.[14] later used these parameters in simulations of injection molding of a center-gated disk (CGD). The parameters yielded orientation predictions that were reasonable where shear dominated the flow, but made worse predictions where extensional flow becomes important, such as the core of the part and the advancing front. Meyer et al.[156] later found that these same orientation model parameters did not make acceptable predictions of orientation in an end-gated plaque (EGP).

Ortman et al.[49] extended Eberle's analysis to long-glass-fiber reinforcement in polypropylene using the sliding plate rheometer. They also made extensive changes to the stress model used by Eberle to account for the rate-thinning behavior seen in the stress-growth coefficient and fiber flexibility, and suggested a method for making the model coefficients functions of the invariants of the orientation tensor. This modified tensor was used to obtain orientation model parameters by fitting exclusively to stress growth data. Later work demonstrated that these parameters made reasonable predictions of orientation in an injection-molded CGD[154, 157], but again only where shear dominated the flow.

In addition to the failure in the EGP, several common themes occur throughout the previous efforts. First, both direct observation of orientation evolution[49, 158] and stress growth under flow reversal[52] suggest orientation evolution appears to be independent of strain rate, at least within the range investigated. Second, the typical method for incorporating orientation effects in a stress model through the fourth-order orientation tensor does not sufficiently capture the influence of fiber

reorientation. Cieslinski et al.[47] demonstrated this through direct measurement of the fourth-order tensor components. Finally, all of the work suggested exploring extensional flows, both for fundamental interest and, considering the failures in the EGP simulations, to determine if the orientation model parameters are dependent on the flow field.

References

1. S. G. Advani and E. M. Sozer, *Process modeling in composites manufacturing*. Marcel-Dekker, Inc.: New York, NY, 2003; Vol. 59.
2. J. Burgers, *Second report on viscosity and plasticity*. North Holland Publishing Co.: Amsterdam, 1938.
3. E. Ganani and R. L. Powell, "Rheological properties of rodlike particles in a newtonian and a non-newtonian fluid," *J. Rheol.* **30** (5), 995 (1986).
4. E. P. Plueddemann, Chemistry of silane coupling agents. In *Silane coupling agents*, Springer: 1991; pp 31.
5. M. Doi and S. F. Edwards, *The theory of polymer dynamics*. Oxford University Press: 1988; Vol. 73.
6. J. T. Hofmann, G. M. Vélez-Garcia, D. G. Baird and A. R. Whittington, "Application and evaluation of the method of ellipses for measuring the orientation of long, semi-flexible fibers," *Polym. Compos.* **34** (3), 390 (2013).
7. M. J. Cieslinski. *Using a sliding plate rheometer to obtain material parameters for simulating long fiber orientation in injection molded composites*, PhD Thesis. Virginia Tech, 2015.
8. L. H. Switzer III and D. J. Klingenberg, "Rheology of sheared flexible fiber suspensions via fiber-level simulations," *J. Rheol.* **47** (3), 759 (2003).
9. A. Clarke, N. Davidson and G. Archenhold, "A multitransputer image analyser for 3d fibre orientation studies in composites," *Trans. Royal Microscopical Soc.* **1**, 305 (1990).
10. R. S. Bay and C. L. Tucker III, "Stereological measurements and error estimates for three-dimensional fiber orientation," *Polym. Eng. Sci.* **32** (4), 240 (1992).
11. G. Velez-Garcia. *Experimental evaluation and simulations of fiber orientation in injection molding of polymers containing short glass fibers*, PhD Thesis. Virginia Tech, 2012.
12. G. M. Velez-Garcia, P. Wapperom, V. Kunc, D. Baird and A. Zink-Sharp, "Sample preparation and image acquisition using optical-reflective microscopy in the measurement of fiber orientation in thermoplastic composites," *J. Microsc.* **248**, 23 (2012).
13. T. S. Konicek. *A method to determine three-dimensional fiber orientation in fiber reinforced polymers*, Masters Thesis. University of Illinois at Urbana-Champaign, 1987.
14. G. M. Vélez-García, P. Wapperom, D. G. Baird, A. O. Aning and V. Kunc, "Unambiguous orientation in short fiber composites over small sampling area in a center-gated disk," *Composites Part A* **43** (1), 104 (2012).
15. J. Hofmann, G. M. Velez-Garcia, D. Baird and A. R. Whittington, "Application and evaluation of the method of ellipses for measuring the orientation of long, semi-flexible fibers," *Polym. Compos.* **34** (3), 390 (2013).
16. M. Teßmann, S. Mohr, S. Gayetskyy, U. Haßler, R. Hanke and G. Greiner, "Automatic determination of fiber-length distribution in composite material using 3d ct data," *EURASIP J. Adv. Signal Process* **2010** (1), (2010).
17. J. Tan, J. Elliott and T. Clyne, "Analysis of tomography images of bonded fibre networks to measure distributions of fibre segment length and fibre orientation," *Adv. Eng. Mater.* **8** (6), 195 (2006).
18. D. Salaberger, K. A. Kannappan, J. Kastner, J. Reussner and T. Auinger, "Evaluation of computed tomography data from fibre reinforced polymers to determine fibre length distribution," *Int. Polym. Proc.* **26** (3), 283 (2011).
19. G. Requena, G. Fiedler, B. Seiser, P. Degischer, M. Di Michiel and T. Buslaps, "3d-quantification of the distribution of continuous fibres in unidirectionally reinforced composites," *Composites Part A* **40** (2), 152 (2009).

20. M. Krause, J.-M. Hausherr, B. Burgeth, C. Herrmann and W. Krenkel, "Determination of the fibre orientation in composites using the structure tensor and local x-ray transform," *J. Mater. Sci.* **45** (4), 888 (2010).
21. S. R. Stock, *Microcomputed tomography: Methodology and applications*. CRC press: Boca Raton, FL, 2008.
22. H. Shen, S. Nutt and D. Hull, "Direct observation and measurement of fiber architecture in short fiber-polymer composite foam through micro-ct imaging," *Compos. Sci. Technol.* **64** (13), 2113 (2004).
23. J. G. Kim, S. O. Jin, M. H. Cho and S. Y. Lee, "Inter-plane artifact suppression in tomosynthesis using 3d ct image data," *Biomed. Eng. Online* **10** (106), (2011).
24. F. Cosmi, A. Bernasconi and N. Sodini, "Phase contrast micro-tomography and morphological analysis of a short carbon fibre reinforced polyamide," *Compos. Sci. Technol.* **71** (1), 23 (2011).
25. J. Martin-Herrero and C. Germain, "Microstructure reconstruction of fibrous c/c composites from x-ray microtomography," *Carbon* **45** (6), 1242 (2007).
26. S. Stock, "X-ray microtomography of materials," *Int. Mater. Rev.* **44** (4), 141 (1999).
27. A. Bernasconi, F. Cosmi and P. J. Hine, "Analysis of fibre orientation in short fibre reinforced polymers: A comparison between optical and tomographic methods," *Compos. Sci. Technol.* **72** (16), 2002 (2012).
28. K. Albrecht, E. Baur, H.-J. Endres, R. Gente, N. Graupner, M. Koch, M. Neudecker, T. Osswald, P. Schmidtke, S. Wartzack, K. Webelhaus and J. Mussig, "Measuring fiber orientation in sisal fibre-reinforced, injection molded polypropylene - pros and cons of the experimental methods to validate injection moulding simulation," *Composites Part A* **95**, 54 (2017).
29. M. Chaouche and D. L. Koch, "Rheology of non-brownian rigid fiber suspensions with adhesive contacts," *J. Rheol.* **45** (2), 369 (2001).
30. A. M. A. Huq and J. Azaiez, "Effects of length distribution on the steady shear viscosity of semiconcentrated polymer-fiber suspensions," *Polym. Eng. Sci.* **45** (10), 1357 (2005).
31. C. D. Han and K. W. Lem, "Rheology of unsaturated polyester resins. I. Effects of filler and low-profile additive on the rheological behavior of unsaturated polyester resin," *J. Appl. Polym. Sci.* **28** (2), 743 (1983).
32. S. Goto, H. Nagazono and H. Kato, "The flow behavior of fiber suspensions in newtonian fluids and polymer solutions," *Rheol. Acta* **25** (3), 246 (1986).
33. B. Mary, C. Dubois, P. J. Carreau and P. Brousseau, "Rheological properties of suspensions of polyethylene-coated aluminum nanoparticles," *Rheol. Acta* **45** (5), 561 (2006).
34. M. Keshtkar, M. C. Heuzey and P. J. Carreau, "Rheological behavior of fiber-filled model suspensions: Effect of fiber flexibility," *J. Rheol.* **53** (3), 631 (2009).
35. J. P. Greene and J. O. Wilkes, "Steady-state and dynamic properties of concentrated fiber-filled thermoplastics," *Polym. Eng. Sci.* **35** (21), 1670 (1995).
36. O. G. Harlen and D. L. Koch, "Orientational drift of a fibre suspended in a dilute polymer solution during oscillatory shear flow," *J. Non-Newton. Fluid Mech.* **73** (1), 81 (1997).
37. M. P. Petrich, M. Chaouche, D. L. Koch and C. Cohen, "Oscillatory shear alignment of a non-brownian fiber in a weakly elastic fluid," *J. Non-Newton. Fluid Mech.* **91** (1), 1 (2000).
38. C. Mobuchon, P. J. Carreau, M.-C. Heuzey, M. Sepehr and G. Ausias, "Shear and extensional properties of short glass fiber reinforced polypropylene," *Polym. Compos.* **26** (3), 247 (2005).
39. H. M. Laun, "Orientation effects and rheology of short glass fiber-reinforced thermoplastics," *Colloid Polym. Sci.* **262** (4), 257 (1984).
40. G. Ausias, J.-F. Agassant, M. Vincent, P. Lafleur, P.-A. Lavoie and P. Carreau, "Rheology of short glass fiber reinforced polypropylene," *J. Rheol.* **36** (4), 525 (1992).
41. S. E. Barbosa, D. R. Ercoli, M. A. Bibbó and J. Kenny, "Special issue advances in fiber reinforced composites technology rheology of short-fiber composites: A systematic approach," *Compos. Struct.* **27** (1), 83 (1994).
42. O. S. Carneiro and J. M. Maia, "Rheological behavior of (short) carbon fiber/thermoplastic composites. Part i: The influence of fiber type, processing conditions and level of incorporation," *Polym. Compos.* **21** (6), 960 (2000).

43. A. S. A. Ramazani, A. Ait-Kadi and M. Grmela, "Rheology of fiber suspensions in viscoelastic media: Experiments and model predictions," *J. Rheol.* **45** (4), 945 (2001).
44. M. Sepehr, P. J. Carreau, M. Moan and G. Ausias, "Rheological properties of short fiber model suspensions," *J. Rheol.* **48** (5), 1023 (2004).
45. M. Rajabian, G. Naderi, M. H. Beheshty, P. G. Lafleur, C. Dubois and P. J. Carreau, "Experimental study and modeling of flow behavior and orientation kinetics of layered silicate/polypropylene nanocomposites in start-up of shear flows," *Int. Polym. Proc.* **23** (1), 110 (2008).
46. M. Sepehr, G. Ausias and P. J. Carreau, "Rheological properties of short fiber filled polypropylene in transient shear flow," *J. Non-Newton. Fluid Mech.* **123** (1), 19 (2004).
47. M. J. Cieslinski, D. Baird and P. Wapperom, "Obtaining repeatable initial fiber orientation for the transient rheology of fiber suspensions in simple shear flow," *J. Rheol.* **60**, 161 (2016).
48. A. P. R. Eberle, G. M. Vélez-García, D. G. Baird and P. Wapperom, "Fiber orientation kinetics of a concentrated short glass fiber suspension in startup of simple shear flow," *J. Non-Newton. Fluid Mech.* **165** (3–4), 110 (2010).
49. K. Ortman, D. Baird, P. Wapperom and A. Whittington, "Using startup of steady shear flow in a sliding plate rheometer to determine material parameters for the purpose of predicting long fiber orientation," *J. Rheol.* **56** (4), 955 (2012).
50. M. Djalili-Moghaddam and S. Toll, "Fibre suspension rheology: Effect of concentration, aspect ratio and fibre size," *Rheol. Acta* **45** (3), 315 (2006).
51. M. R. Kamal, A. T. Mutel and L. A. Utracki, "Elongational behavior of short glass fiber reinforced polypropylene melts," *Polym. Compos.* **5** (4), 289 (1984).
52. A. P. R. Eberle, D. G. Baird, P. Wapperom and G. M. Velez-Garcia, "Using transient shear rheology to determine material parameters in fiber suspension theory," *J. Rheol.* **53** (3), 685 (2009).
53. J. M. Dealy and S. S. Soong, "A parallel plate melt rheometer incorporating a shear stress transducer," *J. Rheol.* **28** (4), 355 (1984).
54. J. G. Oakley and A. J. Giacomin, "A sliding plate normal thrust rheometer for molten plastics," *Polym. Eng. Sci.* **34** (7), 580 (1994).
55. C. Kolitawong, A. J. Giacomin and L. M. Johnson, "Invited article: Local shear stress transduction," *Rev. Sci. Instrum.* **81** (2), 021301-1 (2010).
56. R. B. Bird, R. C. Armstrong and O. Hassager, *Dynamics of polymeric liquids*. 2 ed.; Wiley: New York, NY, 1987; Vol. 1.
57. F. N. Cogswell, "Converging flow of polymer melts in extrusion dies," *Polym. Eng. Sci.* **12** (1), 64 (1972).
58. D. Binding, "An approximate analysis for contraction and converging flows," *J. Non-Newton. Fluid Mech.* **27** (2), 173 (1988).
59. M. Padmanabhan, C. W. Macosko and M. Padmanabhan, "Extensional viscosity from entrance pressure drop measurements," *Rheol. Acta* **36** (2), 144 (1997).
60. D. A. Gotsis and A. Odriozola, "The relevance of entry flow measurements for the estimation of extensional viscosity of polymer melts," *Rheol. Acta* **37** (5), 430 (1998).
61. H. M. Laun and H. Schuch, "Transient elongational viscosities and drawability of polymer melts," *J. Rheol.* **33** (1), 119 (1989).
62. J. Aho, V. H. Rolón-Garrido, S. Syrjälä and M. H. Wagner, "Extensional viscosity in uniaxial extension and contraction flow—comparison of experimental methods and application of the molecular stress function model," *J. Non-Newton. Fluid Mech.* **165** (5–6), 212 (2010).
63. D. Auhl, D. M. Hoyle, D. Hassell, T. D. Lord, O. G. Harlen, M. R. Mackley and T. C. B. McLeish, "Cross-slot extensional rheometry and the steady-state extensional response of long chain branched polymer melts," *J. Rheol.* **55** (4), 875 (2011).
64. D. M. Hoyle, Q. Huang, D. Auhl, D. Hassell, H. K. Rasmussen, A. L. Skov, O. G. Harlen, O. Hassager and T. C. B. McLeish, "Transient overshoot extensional rheology of long-chain branched polyethylenes:

Experimental and numerical comparisons between filament stretching and cross-slot flow," *J. Rheol.* **57** (1), 293 (2013).
65. W. M. H. Verbeeten, G. W. M. Peters and F. P. T. Baaijens, "Viscoelastic analysis of complex polymer melt flows using the extended pom–pom model," *J. Non-Newton. Fluid Mech.* **108** (1–3), 301 (2002).
66. J. Meissner, "Development of a universal extensional rheometer for the uniaxial extension of polymer melts," *T. Soc. Rheol.* **16** (3), 405 (1972).
67. M. Padmanabhan, L. J. Kasehagen and C. W. Macosko, "Transient extensional viscosity from a rotational shear rheometer using fiber-windup technique," *J. Rheol.* **40** (4), 473 (1996).
68. M. H. Wagner, P. Ehrecke, P. Hachmann and J. Meissner, "A constitutive analysis of uniaxial, equibiaxial and planar extension of a commercial linear high-density polyethylene melt," *J. Rheol.* **42** (3), 621 (1998).
69. H. M. Wagner, H. Bastian, P. Hachmann, J. Meissner, S. Kurzbeck, H. Münstedt and F. Langouche, "The strain-hardening behaviour of linear and long-chain-branched polyolefin melts in extensional flows," *Rheol. Acta* **39** (2), 97 (2000).
70. P. Hachmann and J. Meissner, "Rheometer for equibiaxial and planar elongations of polymer melts," *J. Rheol.* **47** (4), 989 (2003).
71. H. Munstedt, "Dependence of the elongational behavior of polystyrene melts in molecular weight and molecular weight distribution," *J. Rheol.* **24** (6), 847 (1980).
72. S. Kurzbeck, F. Oster, H. Munstedt, T. Q. Nguyen and R. Gensler, "Rheological properties of two polypropylenes with different molecular structure," *J. Rheol.* **43** (2), 359 (1999).
73. Y. Chan, J. L. White and Y. Oyanagi, "A fundamental study of the rheological properties of glass-fiber-reinforced polyethylene and polystyrene melts," *J. Rheol.* **22** (5), 507 (1978).
74. T. Takahashi, J.-i. Takimoto and K. Koyama, "Uniaxial elongational viscosity of various molten polymer composites," *Polym. Compos.* **20** (3), 357 (1999).
75. J. Ferec, M. C. Heuzey, J. Perez-Gonzalez, L. Vargas, G. Ausias and P. Carreau, "Investigation of the rheological properties of short glass fiber-filled polypropylene in extensional flow," *Rheol. Acta* **48** (1), 59 (2009).
76. A. H. Wagner, D. M. Kalyon, R. Yazici and T. J. Fiske, "Uniaxial extensional flow behavior of a glass fiber-filled engineering plastic," *J. Reinf. Plast. Comp.* **22** (4), 327 (2003).
77. S. A. Khan and R. G. Larson, "Step planar extension of polymer melts using a lubricated channel," *Rheol. Acta* **30** (1), 1 (1991).
78. D. C. Venerus, T.-Y. Shiu, T. Kashyap and J. Hosttetler, "Continuous lubricated squeezing flow: A novel technique for equibiaxial elongational viscosity measurements on polymer melts," *J. Rheol.* **54** (5), 1083 (2010).
79. M. L. Sentmanat, "Miniature universal testing platform: From extensional melt rheology to solid-state deformation behavior," *Rheol. Acta* **43** (6), 657 (2004).
80. M. Kompani and D. C. Venerus, "Equibiaxial extensional flow of polymer melts via lubricated squeezing flow. I. Experimental analysis," *Rheol. Acta* **39**, 444 (2000).
81. D. C. Venerus, M. Kompani and B. Bernstein, "Equibiaxial extensional flow of polymer melts via lubricated squeezing flow. Ii. Flow modeling," *Rheol. Acta* **39**, 574 (2000).
82. J. Chong, E. Christiansen and A. Baer, "Rheology of concentrated suspensions," *J. Appl. Polym. Sci.* **15** (8), 2007 (1971).
83. A. J. Poslinski, M. E. Ryan, R. K. Gupta, S. G. Seshadri and F. J. Frechette, "Rheological behavior of filled polymeric systems ii. The effect of a bimodal size distribution of particulates," *J. Rheol.* **32** (8), 751 (1988).
84. C. Chang and R. L. Powell, "Effect of particle size distributions on the rheology of concentrated bimodal suspensions," *J. Rheol.* **38** (1), 85 (1994).
85. P. M. Mwasame, N. J. Wagner and A. N. Beris, "Modeling the effects of polydispersity on the viscosity of noncolloidal hard sphere suspensions," *J. Rheol.* **60** (2), 225 (2016).
86. M. Mooney, "The viscosity of a concentrated suspension of spherical particles," *J. Coll. Sci.* **6** (2), 162 (1951).

87. R. J. Farris, "Prediction of the viscosity of multimodal suspensions from unimodal viscosity data," *T. Soc. Rheol.* **12** (2), 281 (1968).
88. S. G. Advani and C. L. Tucker III, "The use of tensors to describe and predict fiber orientation in short fiber composites," *J. Rheol.* **31** (8), 751 (1987).
89. S. G. Advani and C. L. Tucker, "Closure approximations for three-dimensional structure tensors," *J. Rheol.* **34** (3), 367 (1990).
90. G. L. Hand, "A theory of anisotropic fluids," *J. Fluid Mech.* **13** (01), 33 (1962).
91. G. G. Lipscomb, M. M. Denn, D. U. Hur and D. V. Boger, "The flow of fiber suspensions in complex geometries," *J. Non-Newton. Fluid Mech.* **26** (3), 297 (1988).
92. E. Hinch and L. Leal, "Constitutive equations in suspension mechanics. Part 2. Approximate forms for a suspension of rigid particles affected by brownian rotations," *J. Fluid Mech.* **76** (01), 187 (1976).
93. J. S. Cintra Jr and C. L. Tucker III, "Orthotropic closure approximations for flow-induced fiber orientation," *J. Rheol.* **39** (6), 1095 (1995).
94. F. Dupret and V. Verleye, "Modelling the flow of fiber suspensions in narrow gaps," *Rheology Series*, 1347 (1999).
95. D. H. Chung and T. H. Kwon, "Invariant-based optimal fitting closure approximation for the numerical prediction of flow-induced fiber orientation," *J. Rheol.* **46** (1), 169 (2002).
96. G. B. Jeffery, "The motion of ellipsoidal particles in a viscous fluid," *Proc. R. Soc. London, Ser. A* **102** (715), 161 (1922).
97. A. Okagawa, R. G. Cox and S. G. Mason, "The kinetics of flowing dispersions. Vi. Transient orientation and rheological phenomena of rods and discs in shear flow," *J. Colloid Interf. Sci.* **45** (2), 303 (1973).
98. J. P. Bell, "Flow orientation of short fiber composites," *J. Compos. Mater.* **3** (2), 244 (1969).
99. P. F. Bright, R. J. Crowson and M. J. Folkes, "A study of the effect of injection speed on fibre orientation in simple mouldings of short glass fibre-filled polypropylene," *J. Mater. Sci.* **13** (11), 2497 (1978).
100. R. J. Crowson, M. J. Folkes and P. F. Bright, "Rheology of short glass fiber-reinforced thermoplastics and its application to injection molding i. Fiber motion and viscosity measurement," *Polym. Eng. Sci.* **20** (14), 925 (1980).
101. F. Folgar and C. L. Tucker III, "Orientation behavior of fibers in concentrated suspensions," *J. Reinf. Plast. Compos.* **3** (2), 98 (1984).
102. H. M. Huynh. *Improved fiber orientation predictions for injection-molded composites*, Masters Thesis. University of Illinois at Urbana-Champaign, 2001.
103. J. Wang, J. F. O'Gara and C. L. Tucker III, "An objective model for slow orientation kinetics in concentrated fiber suspensions: Theory and rheological evidence," *J. Rheol.* **52** (5), 1179 (2008).
104. J. H. Phelps and C. L. Tucker III, "An anisotropic rotary diffusion model for fiber orientation in short- and long-fiber thermoplastics," *J. Non-Newton. Fluid Mech.* **156** (3), 165 (2009).
105. S. Ranganathan and S. G. Advani, "Fiber–fiber interactions in homogeneous flows of nondilute suspensions," *J. Rheol.* **35** (8), 1499 (1991).
106. X. Fan, N. Phan-Thien and R. Zheng, "A direct simulation of fibre suspensions," *J. Non-Newton. Fluid Mech.* **74** (1–3), 113 (1998).
107. N. Phan-Thien, J. Dudek, D. V. Boger and V. Tirtaatmadja, "Squeeze film flow of ideal elastic liquids," *J. Non-Newton. Fluid Mech.* **18** (3), 227 (1985).
108. H.-C. Tseng, R.-Y. Chang and C.-H. Hsu, "Phenomenological improvements to predictive models of fiber orientation in concentrated suspensions," *J. Rheol.* **57** (6), 1597 (2013).
109. H.-C. Tseng, R.-Y. Chang and C.-H. Hsu, "An objective tensor to predict anisotropic fiber orientation in concentrated suspensions," *J. Rheol.* **60** (2), 215 (2016).
110. H.-C. Tseng, R.-Y. Chang and C.-H. Hsu, "The use of principal spatial tensor to predict the anisotropic fiber orientatino in concentrated fiber suspensions," *J. Rheol.* **62** (1), 313 (2018).

111. H.-C. Tseng, R.-Y. Chang and C.-H. Hsu, "The use of shear-rate-dependent parameters to improve fiber orientation predictions for injection molded fiber composites," *Composites Part A* **104**, 81 (2018).
112. H.-C. Tseng, R.-Y. Chang and C.-H. Hsu, "The use of principal strain tensor to predict anisotropic fiber orientation in concentrated fiber suspensions," *J. Rheol.* **62** (1), 313 (2018).
113. J. H. Phelps, A. I. Abd El-Rahman, V. Kunc and C. L. Tucker III, "A model for fiber length attrition in injection-molded long-fiber composites," *Composites Part A* **51**, 11 (2013).
114. A. Durin, P. De Micheli, J. Ville, F. Inceoglu, R. Valette and B. Vergnes, "A matricial approach of fibre breakage in twin-screw extrusion of glass fibres reinforced thermoplastics," *Composites Part A* **48**, 47 (2013).
115. J. Hofmann. *Extension of the method of ellipses to determining the orientation of long, semi-flexible fibers in model 2- and 3-dimensional geometries*, PhD Thesis. Virginia Tech, 2013.
116. U. Strautins and A. Latz, "Flow-driven orientation dynamics of semiflexible fiber systems," *Rheol. Acta* **46** (8), 1057 (2007).
117. C. L. Tucker, "Flow regimes for fiber suspensions in narrow gaps," *J. Non-Newton. Fluid Mech.* **39** (3), 239 (1991).
118. H. Giesekus, "Elasto-viskose flüssigkeiten, für die in stationären schichtströmungen sämtliche normalspannungskomponenten verschieden groß sind," *Rheol. Acta* **2** (1), 50 (1962).
119. J. L. Ericksen, "Transversely isotropic fluids," *Kolloid-Zeitschrift* **173** (2), 117 (1960).
120. G. K. Batchelor, "The stress generated in a non-dilute suspension of elongated particles by pure straining motion," *J. Fluid Mech.* **46**, 813 (1971).
121. S. M. Dinh and R. C. Armstrong, "A rheological equation of state for semiconcentrated fiber suspensions," *J. Rheol.* **28** (3), 207 (1984).
122. M. A. Bibbo, S. M. Dinh and R. C. Armstrong, "Shear flow properties of semiconcentrated fiber suspensions," *J. Rheol.* **29** (6), 905 (1985).
123. E. S. G. Shaqfeh and G. H. Fredrickson, "The hydrodynamic stress in a suspension of rods," *Phys. Fluids A* **2** (1), 7 (1990).
124. M. B. Mackaplow and E. S. Shaqfeh, "A numerical study of the rheological properties of suspensions of rigid, non-brownian fibres," *J. Fluid Mech.* **329**, 155 (1996).
125. L. G. Leal, "The slow motion of slender rod-like particles in a second-order fluid," *J. Fluid Mech.* **69** (02), 305 (1975).
126. E. Bartram, H. L. Goldsmith and S. G. Mason, "Particle motions in non-newtonian media," *Rheol. Acta* **14** (9), 776 (1975).
127. F. Gauthier, H. Goldsmith and S. Mason, "Particle motions in non-newtonian media. Ii. Poiseuille flow," *T. Soc. Rheol.* **15** (2), 297 (1971).
128. J. D. Goddard, "Tensile stress contribution of flow-oriented slender particles in non-newtonian fluids," *J. Non-Newton. Fluid Mech.* **1** (1), 1 (1976).
129. M. L. Wang and T. C. Cheau, "A constitutive approach for studying concentrated suspensions of rigid fibers in a non - newtonian ellis fluid," *JCIE* **14** (5), 483 (1991).
130. J. Thomasset, P. J. Carreau, B. Sanschagrin and G. Ausias, "Rheological properties of long glass fiber filled polypropylene," *J. Non-Newton. Fluid Mech.* **125** (1), 25 (2005).
131. A. Ait-Kadi and M. Grmela, "Modelling the rheological behaviour of fibre suspensions in viscoelastic media," *J. Non-Newton. Fluid Mech.* **53**, 65 (1994).
132. M. Grmela, A. Ait-Kadi and P. G. Lafleur, "Suspensions of fibers in viscoelastic fluids: Rheology," *J. Chem. Phys.* **109** (16), 6973 (1998).
133. M. Sepehr, P. J. Carreau, M. Grmela, G. Ausias and P. Lafleur, "Comparison of rheological properties of fiber suspensions with model predictions," *J. Polym. Eng.* **24** (6), 579 (2004).
134. M. Rajabian, C. Dubois and M. Grmela, "Suspensions of semiflexible fibers in polymeric fluids: Rheology and thermodynamics," *Rheol. Acta* **44** (5), 521 (2005).

135.M. Grmela, "Why generic?," *J. Non-Newton. Fluid Mech.* **165** (17–18), 980 (2010).
136.J. Azaiez, "Constitutive equations for fiber suspensions in viscoelastic media," *J. Non-Newton. Fluid Mech.* **66** (1), 35 (1996).
137.H. Giesekus, "A simple constitutive equation for polymer fluids based on the concept of deformation-dependent tensorial mobility," *J. Non-Newton. Fluid Mech.* **11** (1-2), 69 (1982).
138.R. B. Bird, C. F. Curtiss, R. C. Armstrong and O. Hassager, *Dynamics of polymeric liquids*. 2 ed.; John Wiley & Sons: USA, 1987; Vol. 2.
139.M. D. Chilcott and J. M. Rallison, "Creeping flow of dilute polymer solutions past cylinders and spheres," *J. Non-Newton. Fluid Mech.* **29**, 381 (1988).
140.C. Kagarise, K. Miyazono, M. Mahboob, K. W. Koelling and S. E. Bechtel, "A constitutive model for characterization of shear and extensional rheology and flow induced orientation of carbon nanofibers/polystyrene melt composites," *J. Rheol.* **55** (4), 781 (2011).
141.E. Abisset-Chavanne, J. Férec, G. Ausias, E. Cueto, F. Chinesta and R. Keunings, "A second-gradient theory of dilute suspensions of flexible rods in a newtonian fluid," *Arch. Comp. Meth. Eng.* **22** (3), 511 (2014).
142.E. Fried and M. E. Gurtin, "Tractions, balances, and boundary conditions for nonsimple materials with application to liquid flow at small-length scales," *Arch. Ration. Mech. An.* **182** (3), 513 (2006).
143.O. Forgacs and S. Mason, "Particle motions in sheared suspensions: X. Orbits of flexible threadlike particles," *J. Coll. Sci.* **14** (5), 473 (1959).
144.K. A. Ericsson, S. Toll and J.-A. E. Månson, "The two-way interaction between anisotropic flow and fiber orientation in squeeze flow," *J. Rheol.* **41** (3), 491 (1997).
145.G. Kotsikos and A. G. Gibson, "Investigation of the squeeze flow behaviour of sheet moulding compounds (smc)," *Composites Part A* **29** (12), 1569 (1998).
146.K. B. Thattaiparthasarthy, S. Pillay and U. K. Vaidya, "Rheological characterization of long fiber thermoplastics – effect of temperature, fiber length and weight fraction," *Composites Part A* **40** (10), 1515 (2009).
147.S. F. Shuler and S. G. Advani, "Transverse squeeze flow of concentrated aligned fibers in viscous fluids," *J. Non-Newton. Fluid Mech.* **65** (1), 47 (1996).
148.P. Dumont, J.-P. Vassal, L. Orgéas, V. Michaud, D. Favier and J.-A. E. Månson, "Processing, characterisation and rheology of transparent concentrated fibre-bundle suspensions," *Rheol. Acta* **46** (5), 639 (2007).
149.J. Engmann, C. Servais and A. S. Burbidge, "Squeeze flow theory and applications to rheometry: A review," *J. Non-Newton. Fluid Mech.* **132** (1), 1 (2005).
150.C. Servais, A. Luciani and J.-A. E. Månson, "Squeeze flow of concentrated long fibre suspensions: Experiments and model," *J. Non-Newton. Fluid Mech.* **104** (2-3), 165 (2002).
151.A. G. Gibson and S. Toll, "Mechanics of the squeeze flow of planar fibre suspensions," *J. Non-Newton. Fluid Mech.* **82** (1), 1 (1999).
152.G.-P. Picher-Martel, A. Levy and P. Hubert, "Compression moulding of carbon/peek randomly-oriented strands composites: A 2d finite element model to predict the squeeze flow behaviour," *Composites Part A* **81**, 69 (2016).
153.A. P. R. Eberle. *The dynamic behavior of a concentrated composite fluid containing non-brownian glass fibers in rheometrical flows*, PhD Thesis. Virginia Polytechnic Institute and State University, 2008.
154.S. M. Mazahir, G. M. Velez-Garcia, P. Wapperom and D. Baird, "Evolution of fibre orientation in radial direction in a center-gated disk: Experiments and simulation," *Composites Part A* **51**, 108 (2013).
155.S. M. Mazahir, G. M. Velez-Garcia, P. Wapperom and D. Baird, "Fiber orientation in the frontal region of a center-gated disk: Experiments and simulation," *J. Non-Newton. Fluid Mech.* **216**, 31 (2015).
156.K. J. Meyer, J. T. Hofmann and D. G. Baird, "Prediction of short glass fiber orientation in the filling of an end-gated plaque," *Composites Part A* **62**, 77 (2014).
157.K. Ortman, D. Baird, P. Wapperom and A. Aning, "Prediction of fiber orientation in the injection molding of long fiber suspensions," *Polym. Compos.* **33** (8), 1360 (2012).

158. M. J. Cieslinski, P. Wapperom and D. G. Baird, "Influence of fiber concentration on the startup of shear flow behavior of long fiber suspensions," *J. Non-Newton. Fluid Mech.* **222**, 163 (2015).

Chapter 3: Evaluating Rigid and Semi-Flexible Fiber Orientation Evolution Models in Simple Flows

Gregory M. Lambert, Donald G. Baird
Department of Chemical Engineering, Virginia Tech, Blacksburg, VA, USA 24060
Macromolecules Innovation Institute, Virginia Tech, Blacksburg, VA, USA, 24060

3.1 Abstract

As American vehicle fuel efficiency requirements have become more stringent due to the CAFE standards, the auto industry has turned to fiber reinforced polymer composites as replacements for metal parts to reduce weight while simultaneously maintaining established safety standards. Furthermore, these composites may be easily processed using established techniques such as injection molding and compression molding. The mechanical properties of these composites are dependent on, among other variables, the orientation of the fibers within the part.

Several models have been proposed to correlate fiber orientation with the kinematics of the polymer matrix during processing, each using various strategies to account for fiber interactions and fiber flexing. However, these all require the use of empirical fitting parameters. Previous work has obtained these parameters by fitting to orientation data at a specific location in an injection-molded part. This ties the parameters to the specific mold design used. Obtaining empirical parameters is not a trivial undertaking and adds significant time to the entire mold design process. Considering that new parameters must be obtained any time some aspect of the part or mold is changed, an alternative technique that obtains model parameters independent of the mold design could be advantageous.

This paper continues work looking to obtain empirical parameters from rheological tests. During processing, the fiber-polymer suspension is subjected to a complex flow with both shear and extensional behavior. Rather than use a complex flow, this study seeks to isolate and compare the effects of shear and extension on two orientation models. To this end, simple shear and planar extension are employed and the evolution of orientation from a planar random initial condition is tracked as a function of strain.

Simple shear was imparted using a sliding plate rheometer designed and fabricated in-house. A novel rheometer tool was developed and fabricated in-house to impart planar extension using a lubricated squeeze flow technique, where a low viscosity Newtonian lubricant is applied to the solid boundaries to minimize the effect of shearing due to the no-slip boundary condition. The Folgar-Tucker model[1] with a strain reduction factor is used as a rigid fiber model and compared against a

Bead-Rod model (a semi-flexible model) proposed by Ortman et al.[2] Both models are capable of predicting the data, with the Bead-Rod model performing slightly better. Orientation occurs at a much faster rate under startup of planar extension, and also attains a much higher degree of flow alignment when compared with startup of steady shear.

3.2 Introduction

The "lightweighting" strategy currently pursued by the auto industry (i.e. the replacement of metallic components in the frame and interior of a vehicle with lighter weight materials) has brought fiber reinforced polymer composites into favor as a construction material. The greatest advantage of these composites is their ability to be melt-processed with established manufacturing techniques such as injection molding. Fiber length and orientation strongly affect the mechanical properties of these composites. Composites with long (>1mm) fibers have improved mechanical properties over short (<1mm) fiber reinforcement,[3, 4, 5] and these long fibers have been observed to flex when subjected to processing conditions.[6, 7]

Several models have been proposed to predict fiber orientation during processing.[1, 8, 9, 10, 11] All of these rely on empirical parameters, and most assume the fibers are rigid. One common technique for obtaining the empirical parameters is fitting the model of choice to experimental orientation data at some point in an injection molded part.[11] However, the resulting parameters are coupled to the mold design in this case. One potential alternative is using simple flows – such as simple shear – to obtain the empirical parameters independently of the mold design.

The type of flow used to obtain the parameters is an important consideration. Although simple shear is rather straight-forward to implement, the parameters obtained therein can struggle to accurately predict orientation within parts.[12, 13] A stronger flow, such as extensional flow, might better reflect the flow within the molds. Producing this type of flow is much more difficult. A new rheometer fixture that attempts to realize planar extension is used in this paper, and the orientation evolution between startup of steady planar extension and startup of steady shear is compared.

3.2.1 Orientation

The simplest way to describe the orientation of a single fiber is to use a unit vector aligned with the fiber's longest axis (Fig. 3.1). In order to reduce the computational demand of tracking a very large population of fibers (such as what is seen in thermoplastic-fiber composite materials), the orientation state at a point may be described by a tensor formed by taking the second moment of the unit vector:

$$\boldsymbol{A} = \oint \boldsymbol{pp}\psi(\boldsymbol{p}, t)d\boldsymbol{p}, \tag{3.1}$$

where $\psi(\boldsymbol{p}, t)$ is the orientation distribution function describing the probability of a fiber having an orientation between $\boldsymbol{p}$ and $\boldsymbol{p} + d\boldsymbol{p}$, and the integral is taken over all possible orientations. This $\boldsymbol{A}$ tensor serves as a compact description of the orientation state.[14] Although similar to the stress tensor from kinetic theories for polymer chains, this parallel is strictly to exploit the mathematical properties of the orientation tensor.

Jeffery[15] first developed an equation describing the orbit of a single fiber in a homogeneous flow field. Later, Folgar and Tucker[1] extended the model to the semi-dilute regime by accounting for the hydrodynamic fiber interactions with a phenomenological term. This term takes a form similar to that employed for rotary diffusion of Brownian motion. Thus, the new term forces fibers away from perfect alignment with the flow direction and broadens the orientation distribution. Folgar's and Tucker's model takes the following form in the limit of long fibers:

$$\frac{D\boldsymbol{A}}{Dt} = \boldsymbol{W}\cdot\boldsymbol{A} - \boldsymbol{A}\cdot\boldsymbol{W} + \boldsymbol{D}\cdot\boldsymbol{A} + \boldsymbol{A}\cdot\boldsymbol{D} - \boldsymbol{2D}\colon\boldsymbol{A}_4 + 2C_I D(\boldsymbol{I} - 3\boldsymbol{A}), \tag{3.2}$$

where $\boldsymbol{W}$ is the vorticity tensor, $\boldsymbol{D}$ is the rate of strain tensor, C_I is the isotropic coefficient of rotary diffusion, D is the scalar magnitude of the rate of strain tensor, and $\boldsymbol{A_4}$ is the fourth moment of the orientation vector $\boldsymbol{p}$.

Work with highly-loaded industrially relevant composites later found that fibers tend to reorient much slower than predicted by Eq. 3.2. Sepehr et al.[16] and Huynh[9] proposed that this retardation could be attributed to direct contacts between fibers and proposed a strain reduction factor. Huynh's model follows:

$$\frac{D\boldsymbol{A}}{Dt} = \alpha[\boldsymbol{W}\cdot\boldsymbol{A} - \boldsymbol{A}\cdot\boldsymbol{W} + \boldsymbol{D}\cdot\boldsymbol{A} + \boldsymbol{A}\cdot\boldsymbol{D} - 2\boldsymbol{D}\colon\boldsymbol{A}_4 + 2C_I D(\boldsymbol{I} - 3\boldsymbol{A})], \tag{3.3}$$

where the only change to the Folgar-Tucker model is the introduction of α, the so-called strain reduction factor. This is the rigid model used in the current study. Thus, the empirical parameters to be fit to the orientation data are C_I and α.

The modification of the vorticity tensor by the scalar strain reduction factor makes the model non-objective, specifically because it violates the Jaumann corotational derivative. Wang et al.[8] corrected this in the Reduced Strain Closure (RSC) model. However, comparisons between orientation predictions and experimental data in model injection molding geometries suggest that objectivity provides only a modest improvement in accuracy.[17]

Simple flows were employed in this study. Under planar extension the vorticity tensor is identically zero, suggesting that simulations for lubricated squeeze flow do not require an objective model. Although this is not the case for simple shear, the authors point to the above works and suggest that the considerable decrease in the velocity field complexity makes the objective treatment unnecessary within experimental error.

Many industrially relevant materials have fiber reinforcement longer than 1 mm, and these fibers have been observed to flex during injection molding.[18] Rigid models might not be capable of accurately predicting orientation of these long fibers. A semi-flexible model for dilute suspensions was developed to account for this. The fiber is now described by two orientation vectors, $\boldsymbol{p}$ and $\boldsymbol{q}$, as shown in Fig. 3.2. Strautins and Latz[10] worked out two new tensors to further describe the orientation state. The tensor $\boldsymbol{B}$ is the mixed second moment of the distribution, and the tensor $\boldsymbol{C}$ is the first moment of the distribution. These new tensors are in addition to the $\boldsymbol{A}$ tensor, which has a slightly different definition in the semi-flexible model.

$$\boldsymbol{A} = \oint \boldsymbol{pp}\psi(\boldsymbol{p},\boldsymbol{q},t)d\boldsymbol{p}d\boldsymbol{q}, \tag{3.4}$$

$$\boldsymbol{B} = \oint \boldsymbol{pq}\psi(\boldsymbol{p},\boldsymbol{q},t)d\boldsymbol{p}d\boldsymbol{q}, \tag{3.5}$$

$$\boldsymbol{C} = \oint \boldsymbol{p}\psi(\boldsymbol{p},\boldsymbol{q},t)d\boldsymbol{p}d\boldsymbol{q}. \tag{3.6}$$

Ortman et al.[2] extended the model to industrially relevant composites by introducing the rotary diffusion-like term from the Folgar-Tucker model and the strain reduction factor. The following model results:

$$\begin{aligned}\frac{D\boldsymbol{A}}{Dt} = \alpha\Big[&\boldsymbol{W}\cdot\boldsymbol{A} - \boldsymbol{A}\cdot\boldsymbol{W} + \boldsymbol{D}\cdot\boldsymbol{A} + \boldsymbol{D}\cdot\boldsymbol{A} - 2\boldsymbol{D}\colon\boldsymbol{A}_4 + 2C_I D(\boldsymbol{I} - 3\boldsymbol{A}) \\ &+ \frac{l_B}{2}(\boldsymbol{Cm} + \boldsymbol{mC} - 2(\boldsymbol{m}\cdot\boldsymbol{C})\boldsymbol{A}) - 2k\big(\boldsymbol{B} - \boldsymbol{A}tr(\boldsymbol{B})\big)\Big],\end{aligned} \tag{3.7}$$

$$\begin{aligned}\frac{D\boldsymbol{B}}{Dt} = \alpha\Big[&\boldsymbol{W}\cdot\boldsymbol{B} - \boldsymbol{B}\cdot\boldsymbol{W} + \boldsymbol{D}\cdot\boldsymbol{A} + \boldsymbol{A}\cdot\boldsymbol{D} - 2\boldsymbol{D}\colon\boldsymbol{A}_4 + 2C_I D\boldsymbol{B} \\ &+ \frac{l_B}{2}(\boldsymbol{Cm} + \boldsymbol{mC} - 2(\boldsymbol{m}\cdot\boldsymbol{C})\boldsymbol{B}) - 2k\big(\boldsymbol{A} - \boldsymbol{B}tr(\boldsymbol{B})\big)\Big],\end{aligned} \tag{3.8}$$

$$\frac{D\boldsymbol{C}}{Dt} = \alpha\Big[(\boldsymbol{\nabla v})^t\cdot\boldsymbol{C} - (\boldsymbol{A}\colon(\boldsymbol{\nabla}\mathbf{v})^t)\boldsymbol{C} - 2C_I D\boldsymbol{C} + \frac{l_B}{\boldsymbol{2}}\big(\boldsymbol{m} - (\boldsymbol{m}\cdot\boldsymbol{C})\boldsymbol{C} - k\big(1 - tr(\boldsymbol{B})\big)\boldsymbol{C}\big)\Big], \tag{3.9}$$

$$\boldsymbol{m} = \left(\frac{\partial^2 v_i}{\partial x_j \partial x_k}\right) A_{jk}\boldsymbol{\delta_i}, \tag{3.10}$$

where l_B is the fiber half-length and the parameter k describes the flexibility of the fiber. As its value increases, it becomes more rigid. Note that the repeated indices in Eq. 3.10 imply summation, and $\boldsymbol{\delta}_i$ is the ith base vector of the coordinate system. The vectors $\boldsymbol{p}$ and $\boldsymbol{q}$ can be used to determine the end-to-end vector $\boldsymbol{p} - \boldsymbol{q}$, and this can be used to describe the orientation of a flexed fiber.

3.3 Experimental

3.3.1 Composite Characterization

Samples in this study consisted of a high viscosity polypropylene matrix loaded at 10 wt% with glass fibers. The raw material was a commercially available composite (Verton, SABIC) in the form of 13 mm pultruded pellets loaded at 30 wt% glass fiber. Although the raw material had a uniform fiber length distribution, the fibers were poorly wetted by the matrix. Raw pellets were fed through an extruder (Killion, KLB100) with pellets of the neat resin for dilution and fiber dispersion. Figure 3.3 presents the resulting fiber length distribution. The original fiber length of 13 mm was not retained, and significant fiber breakage was observed.

Fiber length was determined as follows. Three strands of the extrudate were wrapped in aluminum foil and ashed in a convection oven (Vulcan, A-550) at 400°C for two hours. The fibers were placed on a glass slide and scanned (Canon, CanoScan 8400F) at 1200 dpi resolution. Fiber length was measured from the scans using ImageJ (NIH). Over 9,000 fibers were measured. Number average fiber length was 1.55 mm, weight average fiber length was 3.59 mm, and number average diameter was 14.0 μm. The resulting fiber length distribution, shown in Fig. 3.3, followed a lognormal trend which has been observed previously in extruded and injection molded composite materials.

Although typical industrial composites are reinforced at 30 wt% and higher loadings, the 10 wt% used in this study was chosen out of necessity. The stresses developed during compression of 30 wt% material resulted in overloading the transducer in the ARES-G2 rheometer used in the squeeze flow tests. A new fixture, discussed in the future work section, has been designed for use with an Instron testing platform so that the stress growth behavior of composites with industrially relevant loadings can be explored.

3.3.2 Sample Fabrication

All of the samples used in this study were compression molded. Strands of the extrudate were placed in the sample molds with the intention of imparting a planar random initial orientation state. Cone and donut samples were prepared by molding 50 mm disks, then boring a 25 mm hole in the center. These samples were used to measure the stress response in startup of steady shear. Sliding

plate samples were prepared by molding a single ply 1.5 mm thick. Orientation data under startup of steady shear was collected from these samples. Finally, planar extension samples were prepared by molding four 2 mm thick plies and consolidating them into a single 8 mm thick sample. Both orientation and stress growth data were collected from these samples. A Carver laboratory press, equipped with a platen temperature control system (Omega), was used, and all samples were pressed at 180°C for 20 minutes under 1 metric ton of force. Table 3.I shows the dimensions of each sample.

3.3.3 Rheological Tests

Constant Shear

Two methods were employed to impart shear deformation on the samples: the sliding plate proposed by Giacomin,[19] and the cone and donut proposed by Eberle.[20] All tests were performed at a shear rate of 0.1 s^{-1} at 200°C. The sliding plate geometry has proven useful for obtaining orientation data for fiber composites under simple shear as the sample thickness is constant and can be controlled.[2] Furthermore, the fibers are not forced to conform to curved streamlines seen in the more conventional parallel plate and cone and plate geometries for polymer melts. A detailed description of the setup used in this study may be found elsewhere.[2] The geometry is mounted vertically on an Instron testing platform (model 4204) inside of a convection oven. A constant shear rate can be set by programming a constant crosshead speed. Shear stress is measured at a single location with a capacitance probe. The samples used in this study did not generate a sufficient signal for measuring stress growth data, therefore only orientation data could be obtained from the sliding plate samples. Stress growth was measured using the cone and donut geometry. This setup maintains the cone and plate fixture's advantage of a constant shear rate along the radius of the plate, while avoiding gap effects at the center of the plate. While this setup has worked for short-fiber-reinforced samples, significant voids and edge fracture are observed for samples with long-fiber reinforcement. The stress growth data from these samples were treated as qualitative and used only as an aid in determining at what strain a steady orientation state might have been reached. All of the cone and donut tests were run in a Rhemoetrics strain-controlled rheometer (RMS 800).

Constant Planar Extension

The planar extension velocity field is, by definition, shear free. In order to ensure this occurred, a new fixture was developed in-house (Fig. 3.4). The bottom tool's channel was 31.75 mm square with walls 29.8 mm tall, and the upper tool was rectangular, measuring 31.75 mm wide by 28.3 mm long.

A low viscosity silicone lubricant (DCF 203, Dow Corning) was applied to all of the solid boundaries to induce slip and reduce shear in the melt. Significant fundamental and experimental work has been performed to test the limits of lubricated equibiaxial squeeze flow.[21, 22] The results of this work suggest that the relative magnitudes of the melt and lubricant viscosity and layer thickness are key experimental variables. Work by Kompani et al.[22] suggest a viscosity ratio of 10^{-5} to 10^{-4} lubricant to melt, and a thickness ratio of 0.02 to 0.06 lubricant to melt.

A strain sweep from 10 s^{-1} to 50 s^{-1} was run in an ARES G2 using a 25 mm diameter cone and plate to determine the viscosity of the lubricant at the test temperature (200°C). The cone angle was 0.1 rad. Lubricant viscosity was thus found to be 0.054 Pa.s. The zero-shear viscosity of the matrix was measured with a frequency sweep from 0.1 Hz to 100 HZ at 5% strain using the same cone and plate fixture at the same temperature. Matrix zero shear viscosity was found to be 1494 Pa.s, yielding a lubricant to viscosity ratio of $3.61 \cdot 10^{-5}$. Lubricant layer thickness could not be controlled well due to the low viscosity of the lubricant. It is thus impossible to determine if the amount of lubricant used in this study resulted in lubricant layer thickness within the ideal range.

The effect of lubrication was gauged by the stress growth behavior. Non-lubricated samples featured a distinct behavior, whereby the stress grew until the transducer was overloaded. An adequate amount of lubricant resulted in stress growth that stayed below the limits of the transducer and attained a maximum value.

Planar extension tests were run at 200°C at a constant Hencky strain rate of 0.05 s^{-1} in compression. Samples had a room temperature thickness of 8 mm. Lubricant was applied to the bottom tool with a syringe, and then the sample was placed on top and allowed to melt at the test temperature of 200°C. After the sample had melted, lubricant was placed on the sample with a syringe and the upper fixture was brought into contact with the lubricant. A rest period of two minutes was allowed so that the freshly applied lubricant could reach the test temperature before the test began.

3.3.4 Orientation Measurement

Fiber orientation was measured at several strain values. The observation plane of all of the samples was the xz plane, where x was the flow direction and z the through-thickness direction. A detailed description of the sample preparation for the observation planes may be found elsewhere.[23] Essentially, the samples are mounted inside of epoxy pucks, and traditional metallographic sanding and polishing techniques are used to prepare the samples for reflective microscopy. Plasma etching is then used to improve the contrast between the matrix and the fibers. Micrographs of the observation

planes were taken with an optical microscope (Nikon Eclipse LV100) equipped with a motorized stage at 20x magnification. Image-stitching software (NIS-Elements Basic Research) was used to scan and ultimately produce the micrographs.

The subsequent analysis of the micrographs is known as the method of ellipses[24], so-called because the analysis calculates the orientation of individual fibers based on geometric arguments from the appearance of the elliptical footprint each fiber leaves on the observation plane. In-plane and out-of-plane angles (θ and φ respectively) and the components of the $\boldsymbol{p}$ vector are calculated as follows in Cartesian coordinates:

$$p_1 = \sin\theta\cos\varphi \tag{10}$$

$$p_2 = \sin\theta\sin\varphi \tag{11}$$

$$p_3 = \cos\theta \tag{12}$$

$$\theta = \cos^{-1}\left(\frac{m}{M}\right) \tag{13}$$

and the resulting population of fibers can be used to calculate the orientation tensor $\boldsymbol{A}$ by taking their dyadic products and applying a weighting function:

$$\langle \boldsymbol{pp} \rangle = \frac{\sum_k (\boldsymbol{pp})_k L_k F_k}{\sum_k L_k F_k} \tag{14}$$

where $\langle \boldsymbol{pp} \rangle$ is the ensemble average of the dyadic product $\boldsymbol{pp}$, the orientation tensor $\boldsymbol{A}$; $(\boldsymbol{pp})_k$is the dyadic product of fiber k; L_k is the length of fiber k; and F_k is a weighting function for fiber k which accounts for bias from the choice of investigation plane. Several weighting functions have been proposed, and the specific weighting function used in this work is that proposed by Bay and Tucker.[6] This weighting function incorporates partial objects in the orientation measurements:

$$F_k = (L_k \cos\theta_k)^{-1} \qquad \theta_k < \theta_c \tag{15}$$

$$F_k = \theta_k^{-1} \qquad \theta_k > \theta_c \tag{16}$$

where $\theta_c = \cos^{-1}\left(\frac{d_k}{L_k}\right)$ is a cut-off angle and d_k is the fiber diameter. Note that, in this work, L_n is substituted for L_k, as the method this work employs to obtain fiber orientation cannot determine the length of any individual fiber. Micrographs are analyzed with code developed in-house in MATLab.

The remaining tensors of the Bead-Rod model, $\boldsymbol{B}$ and $\boldsymbol{C}$, where not calculated directly. Rather, initial values were set assuming initially straight fibers. This means the $\boldsymbol{B}$ tensor is set to the negative of the $\boldsymbol{A}$ tensor, and the $\boldsymbol{C}$ tensor is a zero tensor. The values are subsequently calculated from the model. Experimental values for the components of $\boldsymbol{B}$ must be calculated from $\boldsymbol{p}$ and $\boldsymbol{q}$ vectors from

each fiber. This data is difficult to obtain using the stereographic techniques used in this study. More importantly, the calculations used to obtain the $\boldsymbol{p}$ vectors assumed the fibers were rigid.

While the previous point might seem to invalidate the results of the Bead-Rod model, using the rigid assumption is justified for rheometric flows by theoretical treatments of bending. Strautins and Latz,[10] in their seminal paper on the Bead-Rod model, correlated fiber flexing to the second derivative of the velocity field. A more recent development by Abisset-Chavanne et al.[25] correlates fiber flexing to the fourth derivative of the velocity field. At the macroscopic scale, the velocity fields employed in this study are homogeneous, and flexibility due to hydrodynamic forces would seem to be negligible.

Moreover, Batchelor's[26] shear cell model for Newtonian matrices and Goddard's[27] subsequent extension to non-Newtonian matrices suggest that the velocity field between the fibers can be approximated as rheometric. In other words, the first order derivatives of the inner velocity field are larger in magnitude relative to the higher order derivatives. Thus even accounting for velocity field coupling at the microscopic scale, fiber flexing might be negligible, at least in the limit of highly aligned fibers.

Flexing due to inter-fiber contacts might be expected in the concentrated regime. However, the majority of the fibers in the suspension in this study are shorter than 1 mm, the heuristic length threshold for glass fiber flexing due to hydrodynamic or mechanical forces. This suggests that the fibers are not flexed and the rigid assumption used in the analysis holds. The authors grant that the analysis could use refinement and improvements are suggested in the future work section.

3.3.5 Model Fitting

All of the models require two empirical parameters: the strain reduction factor ($\boldsymbol{\alpha}$) and the isotropic coefficient of rotary diffusion (C_I). Models were fit to orientation data by eye. First, C_I was used to ensure the steady state of A_{xx} was fit. The strain reduction factor was then used to shift the curve to fit the remaining data points on the A_{xx} curve.

The Bead-Rod model also requires a third parameter, the fiber flexibility parameter k, which can be estimated based on a three-point bending analysis, resulting in the following expression:

$$k = \frac{E_Y}{64\eta_m}\left(\frac{d}{L}\right)^3 \tag{17}$$

where E_Y is the Young's modulus of the fiber (taken to be 80 GPa in this work), η_m is the matrix viscosity (measured to be 1494 Pa.s), and d and L are the fiber diameter and half-length (measured to be 14.0 μm and 0.775 mm respectively).[2]

Several methods may be used to calculate k. The number and weight average lengths could be used, or the number and weight averages of k itself could be used. Table 3.II shows the values for the different choices. Using the number and weight average length yields small values of k, suggesting that the fibers are very flexible. However, experimental observation suggests that, in the conditions used in this study, fibers do not flex very much. The direct number and weight average values of k thus seem more appropriate, and the number average value was used in this study. Using the weight average value resulted in convergence issues in the simulations.

3.4 Results and Discussion

3.4.1 Stress Growth

Figures 3.5a and 3.5b show the stress growth behavior of the composite under startup of steady shear and startup of constant planar extension respectively. The stress growth behavior between the two tests is markedly different. On the one hand, the shear stress growth goes through an overshoot before settling on a steady value. On the other hand, the extensional stress growth increases almost monotonically to either a maximum or steady state value.

Data for a similar composite has been reported for startup of steady shear, and the current data follows the expected behavior.[2, 28] Although planar extension has never been performed on a composite, previous work reporting stress growth during uniaxial extension with a short-fiber-reinforced composite in a polypropylene matrix has been reported by Ferec al.[29], and qualitatively agrees with the present data. Notably, there is a small toe region at the beginning of the stress growth which might be due to the compression of the lubricant layer.

3.4.2 Orientation Evolution

The evolution of the diagonal components of the $\boldsymbol{A}$ tensor under startup of steady shear and startup of constant planar extension are shown in Fig. 3.6. Under startup of steady shear, the fibers approach a steady state. This agrees with previous work, as do the magnitudes of the fitting parameters.[2, 20, 23] Very similar behavior is also seen under startup of constant planar extension, however this occurs on a much faster time scale. Furthermore, the degree of flow alignment is much higher than that seen in shear. Both observations agree with the point that extensional flow is a

stronger flow than shear. Notably, the value of C_I is very similar between the different tests when comparing the same model. The value of the strain reduction factor is nearly an order of magnitude different between the tests, but considering the difference in the strength of the flows, this is reasonable.

Previous work on orientation evolution during startup of steady shear has suggested that there is a correlation between a steady state orientation and a steady stress state.[2, 20] This is observed in the current shear tests, and also appears to hold for the startup of constant planar extension as well.

3.5 Conclusions and Future Work

Both the rigid and semi-flexible orientation models were capable of tracking the fiber reorientation during the two tests used in this study. However, the fitting parameters were different between the two tests. Although the isotropic coefficient of rotary diffusion was similar between shear and extension, the strain reduction factor differed by an order of magnitude. This suggests that this parameter is confounded by the test method used to obtain it. Further work needs to be done comparing how well the two sets of fitting parameters predict orientation during injection molding of a real part. Relatively simple geometries, such as the center-gated disk or end-gated plaque, might be good geometries to explore.

Additional work also needs to be done to improve the lubricated squeeze flow technique. Poor control of the lubricant layer thickness is a crucial shortcoming of the current technique. A continuously lubricated device, similar to what Venerus[30] has proposed for equibiaxial extension, may remedy this problem.

Future work should also consider an alternative sample fabrication technique. The current method of extruding pellets results in a non-uniform fiber length distribution, obfuscating the effects of fiber length. A wet-laying technique similar to that employed during paper-making might reduce fiber attrition while maintaining good dispersion of fibers within the matrix.

Refinements to the analysis of experimental orientation data are warranted as well. First, an alternative inspection plane could be employed to verify that bending is insignificant. Considering that the fibers are oriented in the xz plane, a supplemental analysis in this plane could be used. This technique was pioneered by Hofmann[7] for center-gated disks, but was neglected from the current study due to time constraints and the previously mentioned theoretical considerations.

Second, bearing in mind that Strautins and Latz developed their model in the semi-flexible limit, the $\boldsymbol{q}$ vector is approximately the negative of the $\boldsymbol{p}$ vector. This assumption could be

incorporated into the current analysis technique and would provide a useful first approximation for experimental values of the components of the $\boldsymbol{B}$ tensor.

As a final note, the notion of fiber flexibility brings up several fundamental questions, particularly in how to account for the effects of flexing. The ability to model the actual flexed state of the fiber would be useful for predictions of mechanical properties in parts, where the flexed state would bear a load differently than a straight fiber. Flexing could also affect the quality of fiber dispersion, as flexed fibers might be more likely to form flocs. Finally, flexing provides another mechanism for breaking in addition to the buckling proposed by Phelps et al.[31]

Two approaches have been taken to model the flexed state. First is the bead-rod method proposed by Strautins and Latz.[10] Abisset-Chavanne et al.[25] recently proposed a different approach by using a single orientation vector and then directly tracking the fiber bending angle directly. Although the Bead-Rod model is a more intuitive approach, extracting information on the average flexed state of the fibers isn't straightforward, as both the $\boldsymbol{B}$ and $\boldsymbol{C}$ tensors contain relevant information. The Abisset-Chevanne approach is more direct, but utilizes a non-standard form of the stress tensor and has never been implemented, which might discourage further exploration.

Coupling these models to a fiber center diffusion model to track fiber inhomogeneity or a fiber failure model that allows for bending could improve existing models as improvements in processing technology result in longer fiber distributions. How to do so is, of course, an open question and one worth further study.

3.6 Acknowledgments

The authors would like to thank Michael Vaught of the Chemical Engineering machine shop for his assistance in designing and fabricating the planar extension fixture. This work was partially funded through a grant from the American Chemistry Council (458405) and a fellowship from Eastman Chemical Company (441201).

3.7 Nomenclature

$\boldsymbol{A}$	Orientation tensor (second moment)
$\boldsymbol{A_4}$	fourth-order orientation tensor
$\boldsymbol{B}$	Orientation tensor (mixed second moment)
$\boldsymbol{C}$	Orientation Tensor (first moment)
C_I	isotropic coefficient of rotary diffusion
$\boldsymbol{D}$	Rate of Strain Tensor
$\boldsymbol{e_i}$	base vector of i^{th} coordinate axis
F_k	Weighting function for fiber k
$\boldsymbol{I}$	Identity tensor
L_k	Length of fiber k
$\boldsymbol{m}$	Second order velocity derivative vector
M	Major axis
m	Minor axis
$\boldsymbol{p}$	orientation vector
$\boldsymbol{q}$	orientation vector
t	time
$\boldsymbol{W}$	Vorticity tensor
α	strain reduction factor
$\mathbf{\nabla v}$	velocity gradient tensor
θ	out-of-plane angle
θ_k	out-of-plane angle of fiber k
θ_c	critical out-of-plane angle
φ	in-plane angle
ψ	orientation distribution function

References

1. F. Folgar and C. L. Tucker III, "Orientation behavior of fibers in concentrated suspensions," *J. Reinf. Plast. Compos.* **3** (2), 98 (1984).
2. K. Ortman, D. Baird, P. Wapperom and A. Whittington, "Using startup of steady shear flow in a sliding plate rheometer to determine material parameters for the purpose of predicting long fiber orientation," *J. Rheol.* **56** (4), 955 (2012).
3. J. L. Thomason and M. A. Vlug, "Influence of fibre length and concentration on the properties of glass fibre-reinforced polypropylene: 1. Tensile and flexural modulus," *Composites Part A* **27** (6), 477 (1996).
4. J. L. Thomason, "The influence of fibre length and concentration on the properties of glass fibre reinforced polypropylene: 5. Injection moulded long and short fibre pp," *Composites Part A* **33** (12), 1641 (2002).
5. J. L. Thomason, "The influence of fibre length and concentration on the properties of glass fibre reinforced polypropylene. 6. The properties of injection moulded long fibre pp at high fibre content," *Composites Part A* **36** (7), 995 (2005).
6. R. S. Bay and C. L. Tucker III, "Stereological measurements and error estimates for three-dimensional fiber orientation," *Polym. Eng. Sci.* **32** (4), 240 (1992).
7. J. T. Hofmann, G. M. Vélez-Garcia, D. G. Baird and A. R. Whittington, "Application and evaluation of the method of ellipses for measuring the orientation of long, semi-flexible fibers," *Polym. Compos.* **34** (3), 390 (2013).
8. J. Wang, J. F. O'Gara and C. L. Tucker III, "An objective model for slow orientation kinetics in concentrated fiber suspensions: Theory and rheological evidence," *J. Rheol.* **52** (5), 1179 (2008).
9. H. M. Huynh. *Improved fiber orientation predictions for injection-molded composites*, Masters Thesis. University of Illinois at Urbana-Champaign, 2001.
10. U. Strautins and A. Latz, "Flow-driven orientation dynamics of semiflexible fiber systems," *Rheol. Acta* **46** (8), 1057 (2007).
11. J. H. Phelps and C. L. Tucker III, "An anisotropic rotary diffusion model for fiber orientation in short- and long-fiber thermoplastics," *J. Non-Newton. Fluid Mech.* **156** (3), 165 (2009).
12. K. J. Meyer, J. T. Hofmann and D. G. Baird, "Prediction of short glass fiber orientation in the filling of an end-gated plaque," *Composites Part A* **62**, 77 (2014).
13. K. Ortman, D. Baird, P. Wapperom and A. Aning, "Prediction of fiber orientation in the injection molding of long fiber suspensions," *Polym. Compos.* **33** (8), 1360 (2012).
14. S. G. Advani and C. L. Tucker III, "The use of tensors to describe and predict fiber orientation in short fiber composites," *J. Rheol.* **31** (8), 751 (1987).
15. G. B. Jeffery, "The motion of ellipsoidal particles in a viscous fluid," *Proc. R. Soc. London, Ser. A* **102** (715), 161 (1922).
16. M. Sepehr, G. Ausias and P. J. Carreau, "Rheological properties of short fiber filled polypropylene in transient shear flow," *J. Non-Newton. Fluid Mech.* **123** (1), 19 (2004).
17. S. M. Mazahir, G. M. Velez-Garcia, P. Wapperom and D. Baird, "Evolution of fibre orientation in radial direction in a center-gated disk: Experiments and simulation," *Composites Part A* **51**, 108 (2013).
18. R. S. Bay and C. L. Tucker, "Fiber orientation in simple injection moldings. Part i: Theory and numerical methods," *Polym. Compos.* **13** (4), 317 (1992).
19. J. G. Oakley and A. J. Giacomin, "A sliding plate normal thrust rheometer for molten plastics," *Polym. Eng. Sci.* **34** (7), 580 (1994).
20. A. P. R. Eberle, D. G. Baird, P. Wapperom and G. M. Velez-Garcia, "Using transient shear rheology to determine material parameters in fiber suspension theory," *J. Rheol.* **53** (3), 685 (2009).
21. M. Kompani and D. C. Venerus, "Equibiaxial extensional flow of polymer melts via lubricated squeezing flow. I. Experimental analysis," *Rheol. Acta* **39**, 444 (2000).
22. D. C. Venerus, M. Kompani and B. Bernstein, "Equibiaxial extensional flow of polymer melts via lubricated squeezing flow. Ii. Flow modeling," *Rheol. Acta* **39**, 574 (2000).

23. G. M. Velez-Garcia, P. Wapperom, V. Kunc, D. Baird and A. Zink-Sharp, "Sample preparation and image acquisition using optical-reflective microscopy in the measurement of fiber orientation in thermoplastic composites," *J. Microsc.* **248**, 23 (2012).
24. M. Vincent, T. Giroud, A. Clarke and C. Eberhardt, "Description and modeling of fiber orientation in injection molding of fiber reinforced thermoplastics," *Polymer* **46**, 6719 (2005).
25. E. Abisset-Chavanne, J. Férec, G. Ausias, E. Cueto, F. Chinesta and R. Keunings, "A second-gradient theory of dilute suspensions of flexible rods in a newtonian fluid," *Arch. Comp. Meth. Eng.* **22** (3), 511 (2014).
26. G. K. Batchelor, "The stress generated in a non-dilute suspension of elongated particles by pure straining motion," *J. Fluid Mech.* **46**, 813 (1971).
27. J. D. Goddard, "Tensile stress contribution of flow-oriented slender particles in non-newtonian fluids," *J. Non-Newton. Fluid Mech.* **1** (1), 1 (1976).
28. M. J. Cieslinski, P. Wapperom and D. G. Baird, "Influence of fiber concentration on the startup of shear flow behavior of long fiber suspensions," *J. Non-Newton. Fluid Mech.* **222**, 163 (2015).
29. J. Ferec, M. C. Heuzey, J. Perez-Gonzalez, L. Vargas, G. Ausias and P. Carreau, "Investigation of the rheological properties of short glass fiber-filled polypropylene in extensional flow," *Rheol. Acta* **48** (1), 59 (2009).
30. D. C. Venerus, T.-Y. Shiu, T. Kashyap and J. Hosttetler, "Continuous lubricated squeezing flow: A novel technique for equibiaxial elongational viscosity measurements on polymer melts," *J. Rheol.* **54** (5), 1083 (2010).
31. J. H. Phelps, A. I. Abd El-Rahman, V. Kunc and C. L. Tucker III, "A model for fiber length attrition in injection-molded long-fiber composites," *Composites Part A* **51**, 11 (2013).

Tables and Figures

Table 3.I: Sample Dimensions

	Length		*Width*		*Thickness*	
Planar Extension	23.8	mm	31.8	mm	8	mm
Sliding Plate	152.6	mm	51.5	mm	1.5	mm
	Outer Diameter		*Inner Diameter*		*Thickness*	
Cone and Donut	50	mm	25	mm	0.05	mm

Table 3.II: Values for the flexibility parameter using different methods

Number Average Length	Weight Average Length	Number Average k	Weight Average k
5.02 s^{-1}	0.460 s^{-1}	1,040 s^{-1}	39,990 s^{-1}

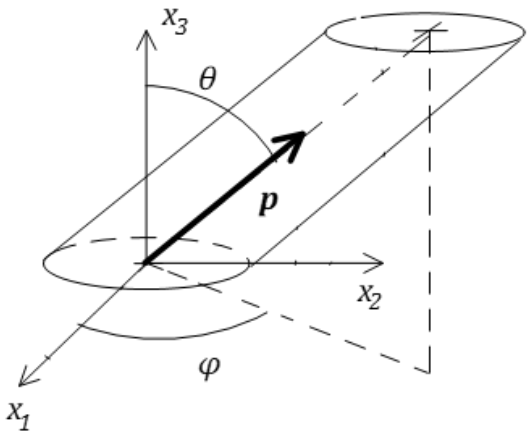

Fig. 3.1: Using the $\boldsymbol{p}$ vector to describe a rigid fiber's orientation

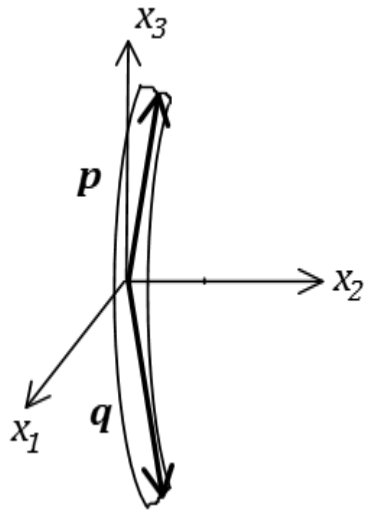

Fig. 3.2: Describing fiber orientation using the two vectors $\boldsymbol{p}$ and $\boldsymbol{q}$.

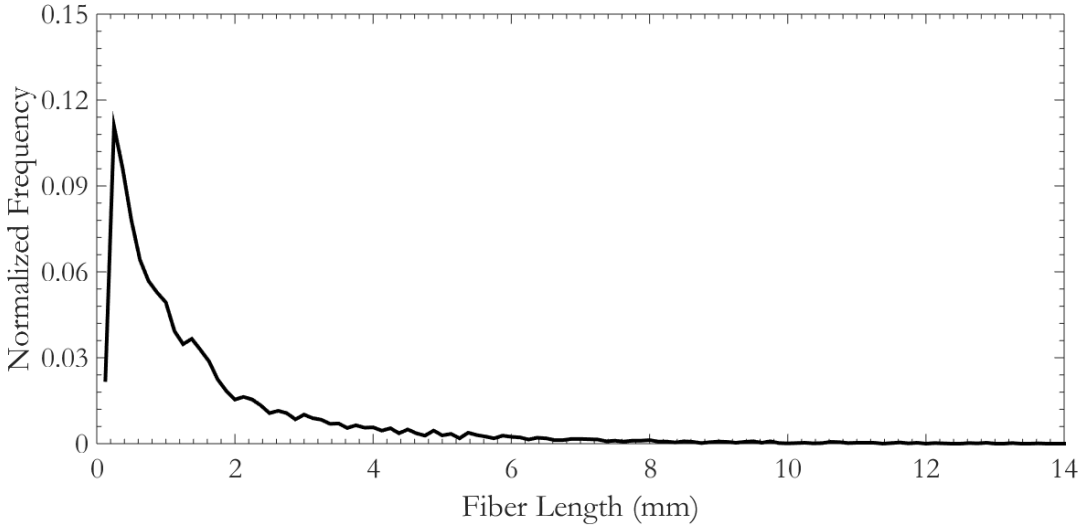

Fig. 3.3: Fiber length distribution in the composite used in this study.

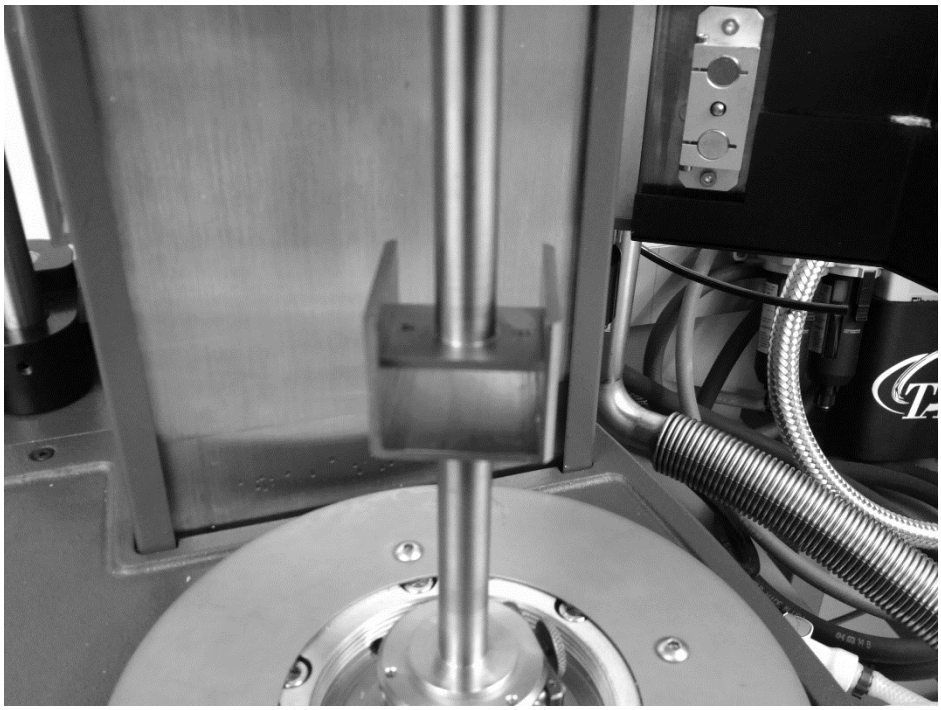

Fig. 3.4: Fixture used for startup of constant planar extension

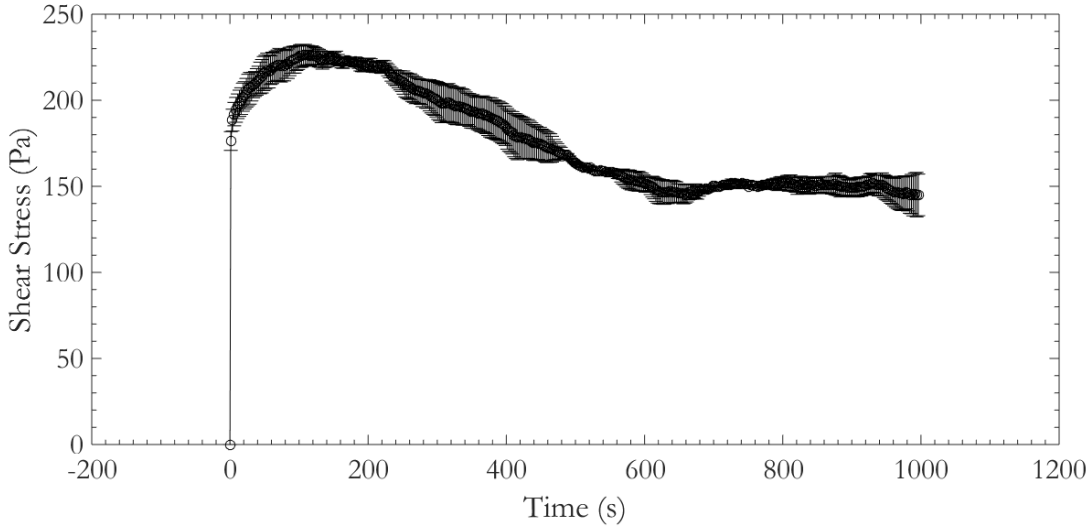

(a)

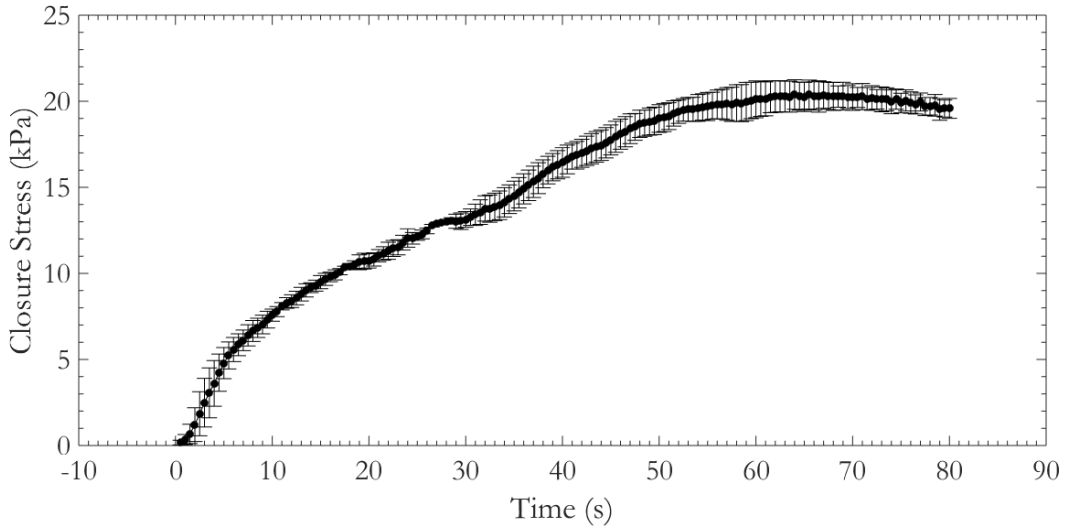

(b)

Fig. 3.5: Stress growth under startup of steady shear (a) and startup of steady planar extension (b). Shear rate used was 0.1 s^{-1} and the Hencky strain rate used was 0.05 s^{-1} in compression. Error bars are the standard deviation.

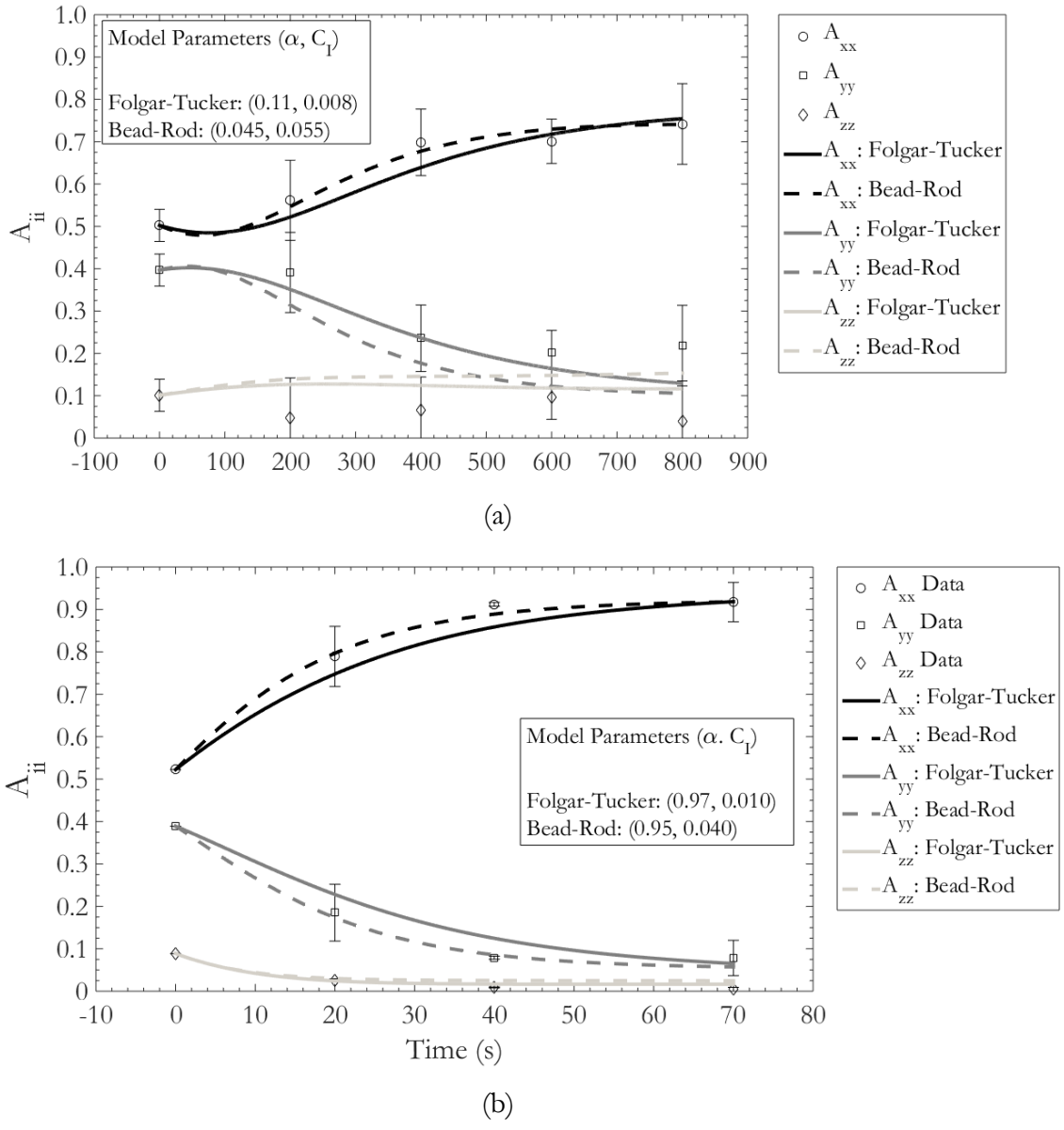

Fig. 3.6: Orientation evolution under startup of steady shear (a) and startup of constant planar extension (b). Shear rate used was 0.1 s^{-1} and the Hencky strain rate used was 0.05s^{-1} in compression. Error bars are the standard deviation. Solid lines correlate to predictions of the Folgar-Tucker model, and dashed lines correlate to predictions by the Bead-Rod model.

Chapter 4: Obtaining short-fiber orientation model parameters using non-lubricated squeeze flow

Gregory Lambert,[1,2] Peter Wapperom,[3] and Donald Baird,[1,2]

1) Department of Chemical Engineering, Virginia Tech, 24061 Blacksburg, VA, USA

2) Macromolecules Innovation Institute, Virginia Tech, 24061 Blacksburg, VA, USA

2) Department of Mathematics, Virginia Tech, 24061 Blacksburg, VA, USA

4.1 Abstract

Accurate models of fiber orientation dynamics during the processing of polymer-fiber composites are needed for the design work behind important automobile parts. All of the existing models utilize empirical parameters, but a standard method for obtaining them independent of processing does not exist. This study considers non-lubricated squeeze flow through a rectangular channel as a solution. A two-dimensional finite element method simulation of the kinematics and fiber orientation evolution along the centerline of a sample is developed as a first step towards a fully three-dimensional simulation. The model is used to fit to orientation data in a short-fiber-reinforced polymer composite after squeezing. Fiber orientation model parameters obtained in this study do not agree well with those obtained for the same material during startup of simple shear. This is attributed to the vastly different rates at which fibers orient during shearing and extensional flows. A stress model is also used to try to fit to experimental closure force data. Although the model can be tuned to the correct magnitude of the closure force, it does not fully recreate the transient behavior.

4.2 Introduction

Replacing metallic components with lighter materials, also known as "lightweighting," is a common practice in the automotive and aerospace industries, primarily with the aim of improving fuel economy. Many of the necessary vehicle parts require complex shapes and must be made by injection molding the material. This results in significant fiber attrition and a complex fiber orientation state throughout the part. Therefore, to design injection-molded parts, models that accurately predict fiber attrition and the evolution of orientation during injection molding are necessary. This study focuses on the flow behavior of fiber-reinforced polymer suspensions and its relation to fiber orientation.

A fiber's orientation can be described using a single vector of unit length, often dubbed $\boldsymbol{p}$, aligned with the fiber's longest axis (Fig. 4.1). Typical fiber-reinforced polymer composite parts contain thousands of fibers, and modeling the motion of each individual fiber would be extremely

demanding from a computational standpoint. A more compact method would be to track the orientation distribution function, $\boldsymbol{\psi(p,t)}$ through a Fokker-Planck equation.[1] Solving this equation requires two separate solution domains: first, the physical processing space and second, a spherical orientation domain at each point in the physical space. Again, this is computationally intensive for modeling fiber-reinforced polymer composite flow and processing.

Advani and Tucker[1] addressed this by introducing a series of tensors based on even-ordered moments of the orientation distribution function. The first two tensors are defined by:

$$\boldsymbol{A} = \int \boldsymbol{pp}\psi(\boldsymbol{p},t)d\boldsymbol{p}, \tag{4.1}$$

$$\boldsymbol{A_4} = \int \boldsymbol{pppp}\psi(\boldsymbol{p},t)d\boldsymbol{p}. \tag{4.2}$$

The evolution equations for all of the tensors require a solution only on the physical processing space, yet retain all of the information contained in the orientation distribution function. However, using the tensors results in an infinite series of evolution equations (i.e. the equation for $\boldsymbol{A}$ involves $\boldsymbol{A_4}$, whose equation involves $\boldsymbol{A_6}$, ad infinitum). The series must be closed with an approximation of the highest rank tensor, often $\boldsymbol{A_4}$. This study uses the Invariant-Based Optimal Fitting approximation introduced by Chung and Kwong[2] which was developed to give a good approximation of $\boldsymbol{A_4}$ in a variety of homogeneous and inhomogeneous flow fields.

In Jeffery's[3] seminal work an equation was derived that predicted the orientation of a dilute suspension of fibers in a Newtonian fluid:

$$\frac{D\boldsymbol{A}}{Dt} = \boldsymbol{W}\cdot\boldsymbol{A} - \boldsymbol{A}\cdot\boldsymbol{W} + \xi(\boldsymbol{D}\cdot\boldsymbol{A} + \boldsymbol{A}\cdot\boldsymbol{D} - 2\boldsymbol{A_4}\colon\boldsymbol{D}), \tag{4.3}$$

in which D/Dt is the substantial derivative, $\boldsymbol{W}$ is the vorticity tensor $(1/2)[(\boldsymbol{\nabla u})^{\boldsymbol{t}} - \boldsymbol{\nabla u}]$, and $\boldsymbol{D}$ is the rate-of-strain tensor $(1/2)[(\boldsymbol{\nabla u})^{t} + \boldsymbol{\nabla u}]$. The shape factor ξ is defined as $(1 - a_r^2)/(1 + a_r^2)$ in which $a_r = L/d$, the fiber aspect ratio, in which L is the fiber length and d is the fiber diameter. Notable results from this model are that a slender fiber ($\xi = 1$) reaches an orientation perfectly aligned in the principal straining direction during extensional flow and lies in the planes of shear during simple shear flow.

Folgar and Tucker[4] introduced a rotary diffusion term after observing fiber interactions in semi-concentrated suspensions (i.e. $a_r^{-2} < \varphi < a_r^{-1}$, in which φ is the fiber volume fraction):

$$\frac{D\boldsymbol{A}}{Dt} = \boldsymbol{W}\cdot\boldsymbol{A} - \boldsymbol{A}\cdot\boldsymbol{W} + \xi(\boldsymbol{D}\cdot\boldsymbol{A} + \boldsymbol{A}\cdot\boldsymbol{D} - 2\boldsymbol{A_4}\colon\boldsymbol{D}) + 2C_I D(\boldsymbol{I} - 3\boldsymbol{A}), \tag{4.4}$$

in which D is the scalar magnitude of the rate-of-strain tensor ($D = \sqrt{2\boldsymbol{D}:\boldsymbol{D}}$) and C_I is the fiber-fiber interaction coefficient. Note that Jeffery's model is recovered if C_I is set to zero. The most important result from this model is that fiber orientation becomes less aligned with the flow direction as C_I increases.

While attempting to model the injection molding of a fiber-reinforced polymer composite, Huynh[5] found that the fiber orientation evolution was much slower than that predicted by Eq. 4.4. He multiplied the right hand side of Eq. 4.4 by a factor α which takes a value between 0 and 1:

$$\frac{D\boldsymbol{A}}{Dt} = \alpha[\boldsymbol{W}\cdot\boldsymbol{A} - \boldsymbol{A}\cdot\boldsymbol{W} + \xi(\boldsymbol{D}\cdot\boldsymbol{A} + \boldsymbol{A}\cdot\boldsymbol{D} - 2\boldsymbol{A_4}:\boldsymbol{D}) + 2C_I D(\boldsymbol{I} - 3\boldsymbol{A})]. \quad (4.5)$$

A similar technique was used with rheological experiments by Sepehr et al.[6] to improve agreement between the predicted and experimental stress growth during startup of simple shear by multiplying the shear strain with a strain reduction factor which also took a value between 0 and 1. This model will be referred to as the Strain Reduction Factor (SRF) model. Objectivity is violated by the SRF model. This has been addressed by the Reduced Strain Closure (RSC) model by Wang et al.[7]:

$$\frac{D\boldsymbol{A}}{Dt} = \boldsymbol{W}\cdot\boldsymbol{A} - \boldsymbol{A}\cdot\boldsymbol{W} + \xi(\boldsymbol{D}\cdot\boldsymbol{A} + \boldsymbol{A}\cdot\boldsymbol{D} - 2[\boldsymbol{A_4} + (1-\kappa)(\boldsymbol{L} - \boldsymbol{M}:\boldsymbol{A_4})]:\boldsymbol{D}) + 2\kappa C_I D(\boldsymbol{I} - 3\boldsymbol{A}), \quad (4.6)$$

$$\boldsymbol{L} = \sum_{i=1}^{3} \lambda_i \boldsymbol{e}_i\boldsymbol{e}_i\boldsymbol{e}_i\boldsymbol{e}_i, \quad (4.7)$$

$$\boldsymbol{M} = \sum_{i=1}^{3} \boldsymbol{e}_i\boldsymbol{e}_i\boldsymbol{e}_i\boldsymbol{e}_i, \quad (4.8)$$

in which $\boldsymbol{L}$ and $\boldsymbol{M}$ are fourth-order tensors based on the eigenvalues, λ_i, and eigenvectors, $\boldsymbol{e}_i$, of $\boldsymbol{A}$. In Eq. 4.6, κ is the strain reduction factor, which takes a value between 0 and 1 and slows the rate of fiber orientation, specifically by slowing the rate of change of the eigenvalues of $\boldsymbol{A}$. Orientation predictions from the SRF and RSC models are used in this study.

The fiber orientation evolution equations include empirical parameters (α, κ, and C_I) which are typically found by fitting to fiber orientation data. The value of C_I is determined by fitting to a steady orientation state. This can be determined for injection molded parts by looking at orientation near the mold walls. Here, the flow can be approximated as simple shear and the composite is assumed to accumulate a shear strain large enough to reach a steady orientation state.[8] The remaining parameter (α or κ) can be determined by fitting to orientation data while using the value of C_I determined by fitting to the steady state orientation.[8] For injection molded parts, this typically consists of selecting a

value of α or κ to fit the core region of the through-thickness orientation profile in the part.[8, 9, 10, 11] This procedure ties the fiber orientation model parameters to the processing conditions, so part design can be an iterative process that might generate suboptimal (but still acceptable) parts due to time and material constraints. A method that can be used to determine the fiber orientation model parameters independently of processing could remedy this.

Rheological testing of fiber-reinforced polymer suspensions could be useful in this regard. Past work has looked at obtaining fiber orientation model parameters by fitting to the fiber orientation evolution during simple shear in a cone-and-donut geometry.[12] These parameters were subsequently used to model the injection molding of center-gated disks and produced reasonable agreement with experimental data.[13]

However, those studies utilized reinforcing fibers that were short (average length less than 1 mm), whereas more recent industrial composites use long fibers (average length greater than 1 mm). Fiber orientation model parameters obtained from startup of simple shear flow of these long-fiber suspensions in a sliding plate rheometer produced mixed results. Predictions for injection-molded center-gated disks were reasonable[14], but predictions were very poor for end-gated plaques.[10] Recent work by Lambert and Baird[15] compared fiber orientation evolution between simple shear (in a sliding plate) and planar extension (by lubricated squeeze flow through a square channel) and found that the strain reduction factor changed by an order of magnitude between the two flows, suggesting that the relative magnitudes of shearing and extension during injection molding have a significant impact on fiber orientation evolution.

Fiber flexing might also play an important role in fiber orientation evolution, as long fibers have been observed to flex during processing.[16] Fiber buckling due to the stress along the fiber's longest axis is one potential mechanism, however this is unlikely to occur during simple shear for short-glass-fiber-reinforced polymer suspensions in the range of shear rates possible in a typical rheometer.[17] Orientation models from Strautins and Latz[18] and Abisset-Chevanne et al.[19] propose that flexing could also be driven by the gradient of the velocity field. For this mechanism to be relevant, the velocity field must have a non-zero Hessian, meaning rheometric flows like simple shear and planar extension cannot induce flexing through this mechanism either.[19]

These points offer a potential explanation for why fiber orientation model parameters for long-fiber suspensions obtained from simple shear yielded poor predictions for the end-gated plaque. First, injection molding features both shear and extensional flow, so parameters fit to orientation data from simple shear do not reflect the influence of the extensional flow on the orientation evolution.

Second, the shear stress experienced by the fibers during injection molding is much higher than the shear stress during simple shear in a typical rheometer, therefore fiber flexing due to the buckling mechanism is important. Third, although the velocity field in the center-gated disk can be approximated as a two-dimensional flow, the velocity field of the end-gated plaque is much more complex and suggests that the gradient-driven flexing mechanism should also be considered. Therefore, the conditions in the end-gated plaque might not have been sufficiently replicated by simple shear. Non-lubricated squeeze flow through a rectangular channel, such as that used in this study, might be a better analog for injection molding flows. Both shearing and extension are present in the squeeze flow velocity field, and the velocity field should also be able to induce fiber flexing through the gradient-driven flexing mechanism.

Although fiber orientation model parameters can be obtained by fitting directly to fiber orientation data, obtaining this data is a laborious process. Fitting to stress growth data through a stress model that includes contributions from the fiber orientation might be an alternative technique that would save substantial time. Lipscomb et al.[20] developed the following model for dilute $(a_r^{-2} < \varphi)$ fiber suspensions:

$$\boldsymbol{\sigma} = -P\boldsymbol{I} + 2\eta\boldsymbol{D} + 2\eta N_p \boldsymbol{A_4} : \boldsymbol{D}, \tag{4.9}$$

in which P is the hydrostatic pressure, $\boldsymbol{I}$ is the identity tensor, η is the solvent viscosity, and N_p is a coefficient called the particle number which has the analytical form $N_p = a_r^2/\ln(a_r)$. This model was able to predict streamlines during contraction flow of a Boger fluid with glass fibers. Later work by Dinh and Armstrong[21] and Shaqfeh and Frederickson[22] extended the model to semi-concentrated suspensions $(a_r^{-2} < \varphi < a_r^{-1})$ using slender-body and scattering theory respectively. In spite of the disparate analytical methods their models take a form similar to Eq. 4.9, differentiated only by the analytical form of N_p. Work with concentrated fiber suspensions has retained a model of this form, but treats N_p as a fitting parameter.[12, 23] One objective of this study is to determine if Eq. 4.9 can be used to obtain fiber orientation model parameters by fitting to force growth data during non-lubricated squeeze flow. Therefore, N_p is treated as a fitting parameter in this work as well.

In summary, a standardized method for obtaining fiber orientation model parameters for long-fiber-reinforced polymer suspensions independent of processing conditions is desired. Doing so with flows that could be relatively simple to implement, measure, and model in the lab would be ideal. Fiber orientation model parameters would be obtained from either fitting to measured force or stress data using a stress model such as Eq. 4.9 in conjunction with a fiber orientation model such as the SRF or

RSC models, or fitting to fiber orientation data at some location in the sample. At first glance, non-lubricated squeeze flow through a rectangular channel has potential. Its inhomogeneous velocity field could induce fiber flexing, and its combination of shearing and extensional flows makes it an easily-controlled analogue to injection molding. In order to determine if non-lubricated squeeze flow would be useful in this regard, it must first be developed with a simpler system than a semi-flexible long-fiber-reinforced suspension.

The objective of this study is to investigate the fiber orientation evolution in non-lubricated squeeze flow. This flow is relevant to fiber-reinforced polymer composite processing because, like injection molding, it features both shearing and extension, therefore fiber orientation model parameters obtained from non-lubricated squeeze flow might better represent fiber orientation dynamics during injection molding. As this is the first step in developing fully three-dimensional simulations, a short-fiber-reinforced polymer composite from an earlier study[24] is used to eliminate confounding effects from fiber flexibility and to provide a basis of comparison for the empirical parameters. Simple two-dimensional kinematics are derived using the lubrication approximation, and a two-dimensional finite element method solution for the velocity and pressure fields is used as well. The predicted through-thickness fiber orientation profile at one location is then compared against experimental data. A stress model, Eq. 4.9, is also used to predict and fit to the closure force, to determine if this is a viable alternative method for obtaining fiber orientation model parameters.

4.3 Experimental

4.3.1 Fiber length measurement

Non-lubricated squeeze flow samples were created by compression molding nozzle purge with a fiber length distribution similar to that used by Cieslinski et al.[24] Raw material came in the form of 13 mm long pellets of SABIC's Verton composite (MV006S GYLTNAT), which consisted of polypropylene loaded with 30 wt% glass fiber. These pellets were mixed with 1 wt% of a green pigment and then fed into an Arburg Allrounder injection molder (model 221-55-250) and injected into the atmosphere rather than into a mold. This material was collected, cut into pellets roughly 8 mm long, and fed back into the injection molder. The resulting twice-extruded material was subsequently used in compression molding thenon-lubricated squeeze flow (NLSF) samples. In both steps, the four zones of the barrel temperature profile were set at 190°C, 210°C, 210°C, and 210°C with a screw back pressure of 0 bar. The screw speed during the first extrusion was 50 rpm, and 100 rpm during the second extrusion.

Fiber length was measured using a procedure based on that used by Kunc et al.[25] with modification. In the original method an epoxy plug was injected into a bed of glass fibers after the matrix had been calcined using a moving stage to make a cylinder of epoxy through the bed. This was supposed to generate a cylinder with a uniform cross section, but in practice the plug cross section can change significantly through the bed thickness. In this work, a syringe needle (BD PrecisionGlide, 20G; D = 0.9 mm) was instead coated with a quick setting epoxy to ensure a uniform diameter. Scans of the fibers were taken by placing them directly onto an Epson Perfection V800 Photo scanner; all scans were at 6400 dpi. Fiber length was measured using ImageJ (National Institutes of Health). This method was applied to samples from Cieslinski et al.[24] as well as the nozzle purge from this study to verify that the fiber length distributions were similar. Number average fiber lengths are 0.347 mm and 0.309 for the old and current material, respectively, and the weight average lengths are 0.531 mm and 0.515 mm, respectively, and the distributions are compared in Fig. 4.2a.

4.3.2 Squeeze Flow Experiments

Non-lubricated squeeze flow samples were created by compression molding the nozzle purge material. Strands of the purge were broken into pieces roughly 13 mm long and placed in a mold 254 mm long by 50.8 mm wide. The material was compressed in a Carver laboratory press (model 2602) with heated platens (controlled by an Omega CN 7800 temperature controller) at 200°C for 20 minutes with a compression force of 0.75 metric tons. The press was not able to maintain the compression force over the whole time period, thus the force was increased to 0.75 metric tons every 5 minutes. The mold was then placed in a cooling press for 20 minutes. This procedure resulted in plies that were about 2 mm thick, and four plies were compressed using the same procedure to create a single 8 mm thick plaque. A band saw (Delta) was subsequently used to cut out two 88.9 mm long by 50.8 mm wide sections. A major reason for making samples through compression molding was to impart a planar random initial orientation state to the fibers. The samples did have a consistently planar orientation state (i.e. very small degree of orientation out of the horizontal plane), but each sample exhibited significant variation in the plane (see section 4.5.1).

A custom device built in-house was used for the squeeze flow experiments. The device consists of a rectangular channel 88.9 mm wide mounted on the bottom fixture, and an upper fixture equipped with an 88.9 mm wide by 50.8 mm long compression head. Note that this means that the sample area under the compression head is constant throughout the squeeze flow. A picture of the fixtures is given in Fig. 4.3, and a schematic of the test is presented in Fig. 4.4. Both fixtures were

mounted on an Instron 5969 equipped with an environmental chamber (Instron. 3119-609). All tests were run at 200°C at a constant Hencky strain rate $\left(\dot{\varepsilon} = \dot{H}/H\right)$ of -0.50 s^{-1} (where the negative sign indicates compression) for 2 s to a strain of 1.0 $(\varepsilon = \dot{\varepsilon}t)$. Note that in the definition of $\dot{\varepsilon}$, H is the time-dependent thickness of the sample, and $\dot{H}$ is the closure rate of the platens, dH/dt, which is also time-dependent.

4.3.3 Fiber Orientation Measurement

Fiber orientation was measured using the method of ellipses.[26] With this technique, a small portion of the squeeze flow sample was extracted and polished on the xz plane. Fibers intersecting this plane appeared as ellipses, and their orientation was calculated based on geometric arguments around their minor and major axes. Orientation measurements were taken along the centerline of the samples at $x = L/2$ in the flow direction, seen in Fig. 4.5. Samples were cut with a band saw (Delta) employing a 2 mm buffer between the cut surface and the desired observation plane, and these strips were then mounted in an epoxy plug for polishing. The plugs were created by first placing the strips inside a 6.35 mm inner diameter high density polyethylene ring (McMaster-Carr) with the desired orientation plane facing down and pouring a thermosetting epoxy from Precision Surfaces, Inc., consisting of a 5:1 (w/w) mixture of resin (PSI-233-4R) to hardener (PSI-233-4H), over the strips. All of the plugs were allowed to cure for 24 hours.

Once the epoxy plugs had cured, they were sanded and polished using a Buehler AutoMet 250 following a routine suggested by Velez-Garcia.[27] This routine consisted of sanding down to the desired observation plane with increasingly fine grades of sandpaper, then polishing the surface with alumina slurries with increasingly fine particles (5 μm to 0.3 μm). Once the samples had been polished, they were plasma etched with oxygen for 30 minutes (Plasma Prep II, Structure Probe, Inc.). Doing so improves the contrast between the fiber and matrix and also allows for unambiguous measurement of a fiber's out-of-plane angle.[28] Micrographs of the observation planes were taken and analyzed using the procedure by Velez-Garcia et al.[29] The micrographs were 1 mm wide and taken through the thickness of the sample, and the image analysis included a weighting function from Bay and Tucker[30] to account for measurement bias from using a two-dimensional plane.

4.4 Numerical Solution

4.4.1 Governing Equations

Samples were modeled in a rectangular coordinate system with x corresponding to the primary flow direction, y to the width or neutral direction, and z to the time-dependent thickness direction (see Fig. 4.5). The governing equations were solved on the xz plane where $y = 0$ (i.e. halfway between the walls). Due to the motion of the top platen, the domain changes with time, specifically through $H(t)$. With this in mind, the solution domain is [0, L]x[0, $H(t)$]. The SRF and RSC models were used to simulate the fiber orientation evolution. Both the approximate solution and the finite element solution were solved starting with Eqs. 4.10 and 4.11:

$$\boldsymbol{\nabla \cdot u} = 0, \tag{4.10}$$

$$\mathbf{0} = -\boldsymbol{\nabla} P + 2\eta \nabla^2 \boldsymbol{u} + 2\eta N_p \boldsymbol{\nabla \cdot} (\boldsymbol{A_4} \boldsymbol{:} \boldsymbol{D}). \tag{4.11}$$

Both one- and two-way coupling solutions were considered. In the one-way case, the equations of motion and continuity were solved independently of the fiber orientation equation to determine the velocity and pressure fields (i.e. as though N_p was set to 0). The two-way coupling simulations solved Eqs. 4.10 and 4.11 as they are, along with the SRF and RSC models. The closure force was calculated by integrating $-\sigma_{zz}$ from Eq. 4.9 over the top platen ($z = H(t)$):

$$F_z = \int_{-L}^{L} \int_{-W/2}^{W/2} P - 2\eta D_{zz} - 2\eta N_p [D_{xx} A_{xxzz} + D_{zz} A_{zzzz} + 2D_{xz} A_{xzzz}] dy dx. \tag{4.12}$$

4.4.2. Approximate 2D Solution

The derivation for the velocity and pressure fields follows that from Bird et al.[31] for squeeze flow between parallel disks. The analysis takes place on the xz plane at $y = 0$. To start, let u, v, and w be the x, y, and z components of the velocity, $\boldsymbol{u}$, respectively, and let P be the hydrostatic pressure. Assuming symmetry across the xz plane, then $v = 0$, and u, w, and P are independent of y. Furthermore, the fiber contribution to the total stress is assumed to be negligible (i.e. $N_p = 0$). Under these assumptions, Eqs. 4.10 and 4.11 for an incompressible Newtonian fluid under creeping flow reduce to:

$$\frac{\partial u}{\partial x} + \frac{\partial w}{\partial z} = 0, \tag{4.13}$$

$$\frac{\partial P}{\partial x} = \eta \left[\frac{\partial^2 u}{\partial x^2} + \frac{\partial^2 u}{\partial z^2} \right], \tag{4.14}$$

$$\frac{\partial P}{\partial z} = \eta\left[\frac{\partial^2 w}{\partial x^2} + \frac{\partial^2 w}{\partial z^2}\right]. \tag{4.15}$$

A non-dimensional form of Eqs. 4.13-15 can be derived using the following definitions:

$$x = L\bar{x}, \qquad z = H\bar{z},$$

$$w = \dot{H}\bar{w}, \qquad u = \frac{\dot{H}}{H}L\bar{u}, \qquad P = \eta\left(\frac{L}{H}\right)^2\left(\frac{\dot{H}}{H}\right)\bar{P}.$$

Considering that $L \gg H$, the rate at which u and w change with respect to z dominates their rate of change with respect to x, suggesting $\partial^2 u/\partial x^2 \ll \partial^2 u/\partial z^2$ and $\partial^2 w/\partial x^2 \ll \partial^2 w/\partial z^2$, and simplifying Eqs. 4.13-15 to:

$$\frac{\partial u}{\partial x} + \frac{\partial w}{\partial z} = 0, \tag{4.16}$$

$$\frac{\partial P}{\partial x} = \eta\frac{\partial^2 u}{\partial z^2}, \tag{4.17}$$

$$\frac{\partial P}{\partial z} = \eta\frac{\partial^2 w}{\partial z^2}. \tag{4.18}$$

These suggest that $u = xf(z,t)$ and $P = P_x(x,t) + P_z(z,t)$. Using the boundary conditions $u|_{z=0} = 0, u|_{z=H} = 0, w|_{z=0} = 0$, and, $w|_{z=H} = \dot{H}$, the velocity and pressure fields are:

$$u(x,z,t) = -6\frac{\dot{H}}{H}x\left[\frac{z}{H} - \frac{z^2}{H^2}\right], \tag{4.19}$$

$$w(z,t) = \dot{H}\left[3\frac{z^2}{H^2} - 2\frac{z^3}{H^3}\right], \tag{4.20}$$

$$P(x,z,t) = 6\eta\frac{\dot{H}}{H}\left[\frac{x^2}{H^2} + \frac{z}{H} - \frac{z^2}{H^2}\right] + P_a. \tag{4.21}$$

In Eq. 4.21, P_a is ambient pressure which is arbitrarily set to 0.

4.4.3 2D Finite Element Solution

The finite element technique used to solve Eqs. 4.10 and 4.11 with the SRF (Eq. 4.5) and RSC (Eq. 4.6) fiber orientation models is described in detail by Mazahir et al.[32] and incorporates the moving upper boundary ($z = H(t)$) through the Arbitrary Lagrangian/Eulerian method.[33] The results were obtained on a 16x16 quadrilateral mesh with a continuous biquadratic velocity, continuous bilinear pressure, and discontinuous biquadratic orientation and extra stress. At the lower platen ($z = 0$), $u = w = 0$, and the fluid moves with the upper platen ($z = H(t)$) so that $u = 0$ and $w = dH(t)/dt$. The top platen was closed at a constant Hencky strain rate, therefore $H(t) = H_0\exp(\dot{\varepsilon}t)$ where H_0 is the

initial sample thickness (8 mm) and $\dot{\varepsilon}$ is the Hencky strain rate (-0.5 s^{-1}). Symmetry was assumed at x = 0. At the outlet, $x = L$, velocity was prescribed according to Eqs. 4.19 and 4.20. A time step of 0.01 s was used for all simulations to ensure that results were indistinguishable on the scale of the plots. In all simulations, the initial fiber orientation condition was set to $A_{xx} = A_{yy} = 0.45$, and $A_{zz} = 0.1$, which was uniform throughout the domain.

4.5 Results and Discussion

4.5.1 Fiber Orientation Evolution

The measured initial through-thickness fiber orientation profile at $x = L/2$ averaged over three samples, is shown in Fig. 4.6. The initial state averages out to a close-to-planar-random state, where to $A_{xx} = A_{yy} = 0.45$, and $A_{zz} = 0.1$, but the large error bars reveal significant variation in the A_{xx} and A_{yy} components between samples. The through-thickness fiber orientation profile at the same location after a Hencky strain of 1.0, averaged over three samples, is shown in Fig. 4.7. The fibers became more flow-aligned, as evidenced by the increase in A_{xx}. This generally agrees with findings from Dumont et al.[34] for long-glass-fiber-bundle reinforced PMMA in planar squeeze flow. Furthermore, x-direction alignment is stronger towards the center of the samples where extensional flow dominates shear flow, consistent with findings by Lambert and Baird[15] that planar extension has a stronger effect on fiber orientation than shear. Note that the z-direction orientation is small throughout the thickness of the sample, regardless of proximity to the platens. This suggests that the platens do not significantly influence the out-of-xy -plane rotation of the fibers.

Predictions from the SRF model using fiber orientation model parameters obtained by Cieslinski et al.[24] are given in Fig. 4.7a. In this case, α was determined to be 0.25 and C_I was determined to be 0.005 when Eq. 4.5 was fit to fiber orientation evolution data during startup of simple shear. In non-lubricated squeeze flow, these parameters result in fiber orientation profiles that under predict A_{xx} and over predict A_{yy}, although A_{zz} is well-predicted. In Fig. 4.7b, fiber orientation model parameters were used to fit the SRF model to the fiber orientation data. In this case, α was 1.0 and C_I was 0.020. These parameters better capture the shape of the fiber orientation profile around $z = H/2$. In particular, the value of C_I is comparable to that used by Song et al.[35] to model the compression molding of a hat section part from a 40 wt% glass fiber-polypropylene composite.

However, one detail to consider in the future is the method used to obtain the orientation data. Albrecht et al.[36] recently found that, for sisal-reinforced polypropylene, μCT and analysis of

microtomed slices yielded different results in the measured fiber orientation distribution toward the center of an injection molded plaque, while the methods agreed towards the walls of the plaque. Near the center of the plaques, microtomes suggested the fibers were in a planar random orientation, while measurements from μCT suggested the fibers were aligned in the flow direction. This discrepancy was attributed to the varying fiber content within the plaques. It was reported that the fibers were more concentrated in the center of the plaque, where the two orientation measurement methods diverged, than near the walls, where the orientation measurement methods agreed. The number of fibers measured through the thickness of the samples in this study was not found to change significantly through the thickness of the part, therefore the observed orientation profile is expected to be accurate.

One major difference between the parameter sets is the magnitude of α. Lambert and Baird[15] found similar results when comparing fiber orientation evolution between startup of simple shear and startup of planar extension in a glass-fiber-reinforced polypropylene suspension. In that case, fibers oriented at a much slower rate during simple shear than they did during planar extension. Considering that non-lubricated squeeze flow features both extensional and shear kinematics, an examination of the through-thickness shear and extensional strain profile might provide context for the shape of the orientation profile.

Shear and extensional strain can be calculated by integrating the analytical expressions for $\partial u/\partial z$ and $\partial u/\partial x$ respectively, and the shear and extensional strain profiles at $x = \mathrm{L}/2$ at a Hencky strain of 1 are shown in Fig. 4.8. A shear strain of about 16 was attained near the upper and lower platens. Cieslinski et al.,[24] using the same material as this study but in startup of simple shear, observed that the measured flow-direction fiber orientation decreased from its initial value at a shear strain of 16 and had not reached a steady state even after a shear strain of 100. However, an α of 0.25 (obtained from startup of simple shear[24]) predicts the fiber orientation near the walls fairly well in non-lubricated squeeze flow. Notably, the same parameters actually over predicted flow-direction orientation at low shear strains in simple shear. Based on the measured fiber orientation evolution data during startup of simple shear,[24] flow-direction fiber orientation near the platens would decrease slightly from the initial condition after 16 shear strain units, but this was not observed in the NLSF samples. Rather, the small amount of extensional strain near the platens seems to cause the flow-direction fiber orientation to increase.

The center of the sample is dominated by planar extension and reaches a Hencky strain of around 1.5, as calculated by integrating the expression for $\partial u/\partial x$. Results from Lambert and Baird[15] and Dumont et al.[37] suggest that fibers reorient very quickly in planar extension, and even a small

extensional strain results in a large change in fiber orientation. An α of 1.0 (similar to previously reported values for lubricated squeeze flow[15]) fits the orientation near the center and over predicts the rate of fiber reorientation in the shear-dominated region, as the fibers reorient much more slowly during simple shear than the SRF model predicts. Considering the SRF model uses only a single parameter to control the rate of fiber orientation, and that the rate of fiber orientation during simple shear and planar extension are very different, it appears that the SRF model is fundamentally incapable of accurately predicting fiber orientation in a mixed flow. Improvements to the fiber orientation model need some mechanism through which it can differentiate between shear and extensional flow.

Two-way coupling can influence the velocity field. Predictions of the orientation profile from one- and two-way coupling should be compared to determine if changes to the velocity field result in significantly different fiber orientation predictions. As Fig. 4.9 shows, two-way coupling makes only a small change in the fiber orientation predictions. Only the A_{xx} component of the fiber orientation is shown, but the general trend is similar for both A_{yy} and A_{zz}. Here, predictions are made using α = 1.0 and C_I = 0.020, and N_p = 159 is used with the two-way coupling simulation, which was calculated with the expression due to Shaqfeh and Fredrickson[22] using a_r = 23.2 and φ = 0.133. The fiber orientation predictions are only differentiated near the center of the sample, and one-way coupling results in a very slightly broader profile.

Notably, the SRF model is not objective except when α is 1. Orientation model parameters obtained by fitting an objective model to orientation data from startup of simple shear might yield better predictions when used to predict orientation evolution during other flows. Cieslinski et al.[24] obtained the RSC model parameters by fitting to the same fiber orientation data from startup of simple shear used for the non-objective model, and determined that κ was 0.20 and C_I was 0.005. With these parameters, the objective model predicts less flow-direction orientation around $z = H/2$ and greater flow-direction orientation near the platens than the non-objective model, as seen in Fig. 4.10a. Predictions for the RSC model using the SRF model parameters (i.e. $\kappa = \alpha$ = 0.25) are also shown in Fig. 4.10a to demonstrate that the difference in the model predictions is not simply due to the different values of α and κ obtained from fitting to orientation data. With the matched parameters, the RSC model predicts greater flow-direction orientation than the SRF model for all points except the very center. Two-way coupling does not significantly alter the predictions from the RSC model either, as shown in Fig. 4.10b where the trends overlap on the scale of the plot. Therefore, it appears that model objectivity alone cannot reconcile the difference between fiber orientation model predictions and data.

4.5.2 Closure Force

Although fiber orientation model parameters can be obtained by fitting to fiber orientation data, this requires significant time and effort. Using the fiber orientation model parameters to fit to force or stress data would be much faster, provided an accurate stress model is used. Stress models such as Eq. 4.9 have been used in the past to obtain fiber orientation model parameters for concentrated short-fiber-reinforced polymer suspensions.[6, 12] Unlike those cases, in which the stress model was fit to viscosity or normal stress difference data, pressure contributes to the closure stress in non-lubricated squeeze flow. Furthermore, the pressure gradients are dependent on the fiber orientation state. Therefore, simulations with two-way coupling are required when predicting or fitting to the closure force.

The measured closure force, averaged over three samples, is shown in Fig. 4.11a alongside a prediction of the closure force from evaluating Eq. 4.9 using the fiber orientation and stress model parameters from Cieslinski et al.[24] for both the SRF and RSC fiber orientation models. In that case, α was 0.25, C_I was 0.005, and N_p was 174 for the SRF model, and $\kappa = 0.20$, $C_I = 0.005$, and $N_p = 174$ for the RSC model. The experimental data is consistent with the closure force growth observed during equibiaxial squeeze flow of short-glass-fiber-bundle-reinforced polypropylene by Servais et al.,[38] and long-glass-fiber-bundle-reinforced PMMA by Dumont et al.[34] In this study, the closure force increases rapidly during the first 0.30 s, followed by a longer period during which the closure force increases at a much slower rate. However, Eq. 4.9 not only over predicts the closure force, but also fails to reproduce the two distinct periods of closure force growth seen in the experimental data. Closure force predictions using Eq. 4.9 and fiber orientation model parameters from Sec. IV A are shown alongside the closure force data in Fig. 4.11b for values of $N_p = 0$, 20, 40, and 159. The last value was calculated using the analytical expression from Shaqfeh and Frederickson[22] using $a_r = 23.2$ and $\varphi = 0.133$. Again, the stress model is not capable of replicating the two closure force growth periods, but decreasing the value of N_p does bring the predicted closure force within the correct magnitude, particularly towards the end of the test.

4.5.3 Discussion

One goal of this study is to investigate fiber orientation dynamics in a flow that is analogous to injection molding, but much easier to control and simulate. The empirical parameters from the fiber orientation models are presumably determined by the details of the suspension, such as the fiber volume fraction, the fiber aspect ratio, and the rheological behavior of the matrix. Therefore, the

empirical parameters are ostensibly valid for all flow fields. However, previous work comparing fiber orientation dynamics during startup of simple shear and startup of planar extension showed that the rate of fiber orientation was very different between the two flows, and a single set of fiber orientation model parameters could not be used to predict the fiber orientation dynamics during both flows.[15] This seems to be the case in this study as well. Fiber orientation model parameters obtained by fitting to fiber orientation data during startup of simple shear[24] reasonably predicted the fiber orientation near the platens, where shear dominates the flow field, but under predicted flow-direction fiber orientation, and over predicted neutral-direction fiber orientation, around $z = H/2$. The fiber orientation model parameters could be used to fit to the fiber orientation at $z = H/2$, but these parameters were markedly different from fiber orientation model parameters obtained from simple shear (Table 4.I).

If non-lubricated squeeze flow is to be used to obtain orientation model parameters, improvements to the fiber orientation model in this study must be made to reconcile the inconsistency with the parameters from startup of simple shear. A major point of contention seems to be the disparity in the rate of reorientation between shear and extension. Fibers appear to reorient very quickly under extension, but much more slowly during shear, and both flows are prominent in non-lubricated squeeze flow. Fiber orientation models must account for this. Phelps and Tucker8 improved upon the RSC model by generalizing the rotary diffusion coefficient into a tensor and allowing it to become a function of $\boldsymbol{D}$ and $\boldsymbol{A}$. Doing so improved fiber orientation predictions in an injection molded part.8 However, the application of strain reduction is similar to that employed by the SRF and RSC models in that no distinction is made between shear and extension; strain is reduced equally in both types of flows. Another model proposed by Ferec et al.39 incorporated fiber-fiber interactions through an analysis of the forces acting on the fibers, providing a mechanism for both rotary diffusion and the slowed rate of orientation during shear. The model was able to predict the delayed overshoot in viscosity and the difference between the first and second normal stress differences during startup of simple shear, as well as the steady state viscosity profile of a polybutylene-glass fiber suspension.[40] However, Ferec et al.[39] demonstrated in their Appendix A that the model has a form similar to Eq. 4.6, and strain reduction is applied equally to shear and extension. Neither the Phelps and Tucker[8] nor the Ferec et al.[39] models would be expected to reconcile the different sets of parameters.

Modifications to the boundary conditions might also improve predictions. Work with equibiaxial compression of glass-fiber-reinforced polypropylene suggests the presence of yield stresses

and partial slip at the platens.[38] Yield stress does not seem to be important for the material in this study and is addressed later in this section. Partial slip, on the other hand, might play a role in the distinct decrease in the rate of the experimental closure force growth data.

Another goal of the study was to evaluate the performance of a stress model, Eq. 4.9, in predicting or fitting closure force data so that orientation model parameters may be obtained by fitting to force data rather than orientation data. This model has been used successfully with startup of simple shear,[6, 12] however it seems incapable of predicting the two closure force growth regions during non-lubricated squeeze flow. According to Eq. 4.9, the only contributions to the closure force are the hydrostatic pressure, the suspending matrix, and the hydrodynamic stress on the fibers. However, the suspension in this study falls in the concentrated regime, where fiber-fiber interactions should be important. Servais et al.[38] provided a brief review of stress models for predicting the closure force for compression molding concentrated fiber-reinforced suspensions and found that most researchers incorporate yield stresses and partial slip, and proposed that fiber-fiber interactions were the source of these phenomena. However, the model they developed is limited to equibiaxial squeeze flow, as it assumes that the fiber orientation does not change. This is reasonable for equibiaxial squeeze flow,[37] but clearly not for the planar squeeze flow used in this study.

Ferec et al.[39] also considered the effect of fiber interactions on the total stress of a concentrated fiber suspension. Fiber-fiber interactions introduce a new term to Eq. 4.9 which explicitly accounts for the contribution of the interactions on the total stress. The initial period of rapid increase in the force seen in Fig. 4.11 might be the result of compressing a network of fibers.[38] As squeeze flow continues, fiber orientation becomes more flow-aligned and the number of fiber contact points decreases,[39] which might partially explain why the rate of force growth decreases after the initial period. This feature could be captured by the model proposed by Ferec et al.[39] as the fiber interactions are weighted by $\left|\boldsymbol{p}^{\alpha} \times \boldsymbol{p}^{\beta}\right|$ (where $\boldsymbol{p}^{\alpha}$ and $\boldsymbol{p}^{\beta}$ refer to distinct, contacting fibers) which decreases as the fibers become aligned. However, their stress model is tied to their orientation model, which isn't expected to accurately capture the difference in the rates of fiber reorientation between shear and extension.

More recent work by Picher-Martel et al.[41] suggests incorporating a yield stress might be useful for predicting the closure force as well. Their model considers the composite to be a homogeneous continuum following a model by Papanastasiou[42] that rectifies the discontinuous nature of the Herschel-Bulkley model. Accounting for the yield stress let the model reasonably predict the shape of the advancing front and the sample thickness as a function of time of a PEEK/carbon fiber composite

during creep flow in a geometry similar to that used in this study. As the sample was modeled as a homogeneous continuum, it could not directly couple the composite stress and fiber orientation state.

However, a direct comparison with their work is not straightforward. Their experiments were essentially creep tests, during which the closure force is constant and the Hencky strain rate changes with time. Picher-Martel et al. do not report the Hencky strain rate, but their plots of sample thickness with time suggest the Hencky strain rates in their experiments are much slower than that in the current study (a constant -0.50 s^{-1}). The model they developed to predict the sample thickness with time suggests that the yield stress of the suspension dominates the deformation of the composite at slow Hencky strain rates, while the viscosity of the suspension dominates the deformation at the faster Hencky strain rates during the early portion of the tests. The Hencky strain rate during this stage is closer to that in this work, suggesting that the viscous (as opposed to viscoplastic) model used in this work, Eq. 4.9, is reasonable for the chosen Hencky strain rate.

4.6. Conclusions

Fiber orientation model parameters obtained from startup of simple shear[24] fairly predicted the fiber orientation near the platens, where shear dominates the kinematics, but could not predict the orientation state towards the center of the sample. Even so, the SRF and RSC models could still be fit to orientation data at $z = H/2$, where the sample experiences planar extension, by setting α or $\varkappa$ to 1. Due to the great disparity between the observed rates of fiber reorientation during shear and extensional flow, the SRF and RSC models were not capable of describing the fiber orientation state during non-lubricated squeeze flow, which includes both shear and extensional kinematics, with a single set of fiber orientation model parameters. Implicit in the orientation models is the idea that the empirical parameters are determined by the characteristics of the suspension (e.g. fiber volume fraction, fiber length, and matrix rheology), yet it appears that the parameters, in particular α and $\varkappa$, are dependent on the local kinematics as well. Improvements to the fiber orientation modeling need to account for this difference in fiber reorientation rates.

The stress model, Eq. 4.9, could be tuned to the correct magnitude by changing the value of N_p, but could not predict the two distinct periods in the closure force growth data. This means that Eq. 4.9 might be useful for obtaining model parameters as it has elsewhere,6, 12 but improvements should be made. Work that considered fiber-fiber interactions suggests that this is due to the absence of a term in Eq. 4.9 that directly considers fiber-fiber interactions.39 The need for including a yield stress remains unclear. Work modeling the compression molding of fiber-reinforced polymer

composites suggests it plays a role in how the composites deform.38, 41 However, comparison with the work by Picher-Martel et al.41 suggests the Hencky strain rate used in this work is too fast for the yield stress to influence the deformation of the samples, and comparison with the work by Servais et al.38 suggests that the yield stress influence on the stress growth is rather small considering the small aspect ratios of the fibers in this study.

Future work will also extend the analysis to polymer suspensions with long, semi-flexible fibers. The flow field in non-lubricated squeeze flow seems to be complex enough to induce fiber flexing[18, 19] and would provide a better test for models of fiber flexibility than rheometric flows. This will be necessary to understand the influence of fiber flexibility on the fiber orientation dynamics, which should improve injection molding simulations of long-fiber-reinforced polymer composites. A consideration of yield stress in these suspensions is also warranted.

4.7 Acknowledgements

The authors thank Michael Vaught from the Virginia Tech Chemical Engineering machine shop for his efforts in assisting with the design and construction of the non-lubricated squeeze flow fixture. The authors also thank Junwei Luo for assisting with the image analysis. This work was partially funded by General Motors Company.

References

1. S. G. Advani and C. L. Tucker III, "The use of tensors to describe and predict fiber orientation in short fiber composites," *J. Rheol.* **31** (8), 751 (1987).
2. D. H. Chung and T. H. Kwon, "Invariant-based optimal fitting closure approximation for the numerical prediction of flow-induced fiber orientation," *J. Rheol.* **46** (1), 169 (2002).
3. G. B. Jeffery, "The motion of ellipsoidal particles in a viscous fluid," *Proc. R. Soc. London, Ser. A* **102** (715), 161 (1922).
4. F. Folgar and C. L. Tucker III, "Orientation behavior of fibers in concentrated suspensions," *J. Reinf. Plast. Compos.* **3** (2), 98 (1984).
5. H. M. Huynh. *Improved fiber orientation predictions for injection-molded composites*, Masters Thesis. University of Illinois at Urbana-Champaign, 2001.
6. M. Sepehr, G. Ausias and P. J. Carreau, "Rheological properties of short fiber filled polypropylene in transient shear flow," *J. Non-Newton. Fluid Mech.* **123** (1), 19 (2004).
7. J. Wang, J. F. O'Gara and C. L. Tucker III, "An objective model for slow orientation kinetics in concentrated fiber suspensions: Theory and rheological evidence," *J. Rheol.* **52** (5), 1179 (2008).
8. J. H. Phelps and C. L. Tucker III, "An anisotropic rotary diffusion model for fiber orientation in short- and long-fiber thermoplastics," *J. Non-Newton. Fluid Mech.* **156** (3), 165 (2009).
9. J. Wang. *Improved fiber orientation kinetics for injection molded composites*, PhD Thesis. University of Illinois, 2007.
10. K. J. Meyer, J. T. Hofmann and D. G. Baird, "Prediction of short glass fiber orientation in the filling of an end-gated plaque," *Composites Part A* **62**, 77 (2014).
11. H.-C. Tseng, R.-Y. Chang and C.-H. Hsu, "An objective tensor to predict anisotropic fiber orientation in concentrated suspensions," *J. Rheol.* **60** (2), 215 (2016).

12. A. P. R. Eberle, D. G. Baird, P. Wapperom and G. M. Velez-Garcia, "Using transient shear rheology to determine material parameters in fiber suspension theory," *J. Rheol.* **53** (3), 685 (2009).
13. S. M. Mazahir, G. M. Velez-Garcia, P. Wapperom and D. Baird, "Evolution of fibre orientation in radial direction in a center-gated disk: Experiments and simulation," *Composites Part A* **51**, 108 (2013).
14. K. Ortman, D. Baird, P. Wapperom and A. Aning, "Prediction of fiber orientation in the injection molding of long fiber suspensions," *Polym. Compos.* **33** (8), 1360 (2012).
15. G. M. Lambert and D. G. Baird, "Evaluating rigid and semiflexible fiber orientation evolution models in simple flows," *J. Man. Sci. Eng.* **139** (3), 031012-1 (2017).
16. M. J. Cieslinski. *Using a sliding plate rheometer to obtain material parameters for simulating long fiber orientation in injection molded composites*, PhD Thesis. Virginia Tech, 2015.
17. A. Durin, P. De Micheli, J. Ville and F. Inceoglu, "A matricial approach of fibre breakage in twin-screw extrusion of glass fibres reinforced thermoplastics," *Composites Part A* **48**, 47 (2013).
18. U. Strautins and A. Latz, "Flow-driven orientation dynamics of semiflexible fiber systems," *Rheol. Acta* **46** (8), 1057 (2007).
19. E. Abisset-Chavanne, J. Férec, G. Ausias, E. Cueto, F. Chinesta and R. Keunings, "A second-gradient theory of dilute suspensions of flexible rods in a newtonian fluid," *Arch. Comp. Meth. Eng.* **22** (3), 511 (2014).
20. G. G. Lipscomb, M. M. Denn, D. U. Hur and D. V. Boger, "The flow of fiber suspensions in complex geometries," *J. Non-Newton. Fluid Mech.* **26** (3), 297 (1988).
21. S. M. Dinh and R. C. Armstrong, "A rheological equation of state for semiconcentrated fiber suspensions," *J. Rheol.* **28** (3), 207 (1984).
22. E. S. G. Shaqfeh and G. H. Fredrickson, "The hydrodynamic stress in a suspension of rods," *Phys. Fluids A* **2** (1), 7 (1990).
23. K. Ortman, D. Baird, P. Wapperom and A. Whittington, "Using startup of steady shear flow in a sliding plate rheometer to determine material parameters for the purpose of predicting long fiber orientation," *J. Rheol.* **56** (4), 955 (2012).
24. M. J. Cieslinski, P. Wapperom and D. G. Baird, "Fiber orientation evolution in simple shear flow from a repeatable initial fiber orientation," *J. Non-Newton. Fluid Mech.* **237**, 65 (2016).
25. V. Kunc, B. J. Frame, B. N. Nguyen, C. L. Tucker III and G. Velez-Garcia, *Fiber length distribution measurement for long glass and carbon fiber reinforced injection molded thermoplastics*, In: Proceedings of the 7th annual society of plastic engineers automotive composites conference and exposition, Troy, MI, 2007.
26. P. J. Hine, N. Davidson, R. A. Duckett and I. M. Ward, "Measuring the fibre orientation and modelling the elastic properties of injection-moulded long-glass-fibre-reinforced nylon," *Compos. Sci. Technol.* **53** (2), 125 (1995).
27. G. Velez-Garcia. *Experimental evaluation and simulations of fiber orientation in injection molding of polymers containing short glass fibers*, PhD Thesis. Virginia Tech, 2012.
28. G. M. Vélez-García, P. Wapperom, D. G. Baird, A. O. Aning and V. Kunc, "Unambiguous orientation in short fiber composites over small sampling area in a center-gated disk," *Composites Part A* **43** (1), 104 (2012).
29. G. M. Velez-Garcia, P. Wapperom, V. Kunc, D. Baird and A. Zink-Sharp, "Sample preparation and image acquisition using optical-reflective microscopy in the measurement of fiber orientation in thermoplastic composites," *J. Microsc.* **248**, 23 (2012).
30. R. S. Bay and C. L. Tucker III, "Stereological measurements and error estimates for three-dimensional fiber orientation," *Polym. Eng. Sci.* **32** (4), 240 (1992).
31. R. B. Bird, R. C. Armstrong and O. Hassager, *Dynamics of polymeric liquids*. 2 ed.; Wiley: New York, NY, 1987; Vol. 1.
32. S. M. Mazahir, G. M. Velez-Garcia, P. Wapperom and D. Baird, "Fiber orientation in the frontal region of a center-gated disk: Experiments and simulation," *J. Non-Newton. Fluid Mech.* **216**, 31 (2015).
33. T. J. R. Hughes, W. K. Liu and T. K. Zimmermann, "Lagrangian-Eulerian finite element formulation for incompressible viscous flows," *Comput. Method. Appl. M.* **29**, 329 (1981).

34. P. Dumont, J.-P. Vassal, L. Orgéas, V. Michaud, D. Favier and J.-A. E. Månson, "Processing, characterisation and rheology of transparent concentrated fibre-bundle suspensions," *Rheol. Acta* **46** (5), 639 (2007).
35. Y. Song, U. Gandhi, C. Perez, T. Osswald, S. Vallury and A. Yang, "Method to account for the fiber orientation of the initial charge on the fiber orientation of finished part in compression molding simulation," *Composites Part A* **100**, 244 (2017).
36. K. Albrecht, E. Baur, H.-J. Endres, R. Gente, N. Graupner, M. Koch, M. Neudecker, T. Osswald, P. Schmidtke, S. Wartzack, K. Webelhaus and J. Mussig, "Measuring fiber orientation in sisal fibre-reinforced, injection molded polypropylene - pros and cons of the experimental methods to validate injection moulding simulation," *Composites Part A* **95**, 54 (2017).
37. T. Laurencin, L. Orgéas, P. J. J. Dumont, S. Rolland du Roscoat, P. Laure, S. Le Corre, L. Silva, R. Mokso and M. Terrien, "3d real-time and in situ characterisation of fibre kinematics in dilute non-newtonian fibre suspensions during confined and lubricated compression flow," *Compos. Sci. Technol.* **134**, 258 (2016).
38. C. Servais, A. Luciani and J.-A. E. Månson, "Squeeze flow of concentrated long fibre suspensions: Experiments and model," *J. Non-Newton. Fluid Mech.* **104** (2-3), 165 (2002).
39. J. Férec, G. Ausias, M. C. Heuzey and P. J. Carreau, "Modeling fiber interactions in semiconcentrated fiber suspensions," *J. Rheol.* **53** (1), 49 (2009).
40. G. Natale, G. Ausias, J. Férec, M. Heuzey and P. Carreau, "Modeling interactions in carbon nanotube suspensions: Transient shear flow," *J. Rheol.* **60** (6), 1069 (2016).
41. G.-P. Picher-Martel, A. Levy and P. Hubert, "Compression moulding of carbon/peek randomly-oriented strands composites: A 2d finite element model to predict the squeeze flow behaviour," *Composites Part A* **81**, 69 (2016).
42. T. C. Papanastasiou and A. G. Boudouvis, "Flows of viscoplastic materials: Models and computations," *J. Rheol.* **31** (5), 385 (1987).

Tables and Figures

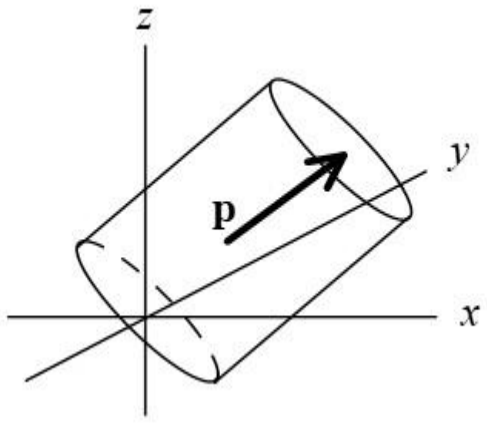

Fig. 4.1: Describing the orientation of a single fiber with a unit vector $\boldsymbol{p}$.

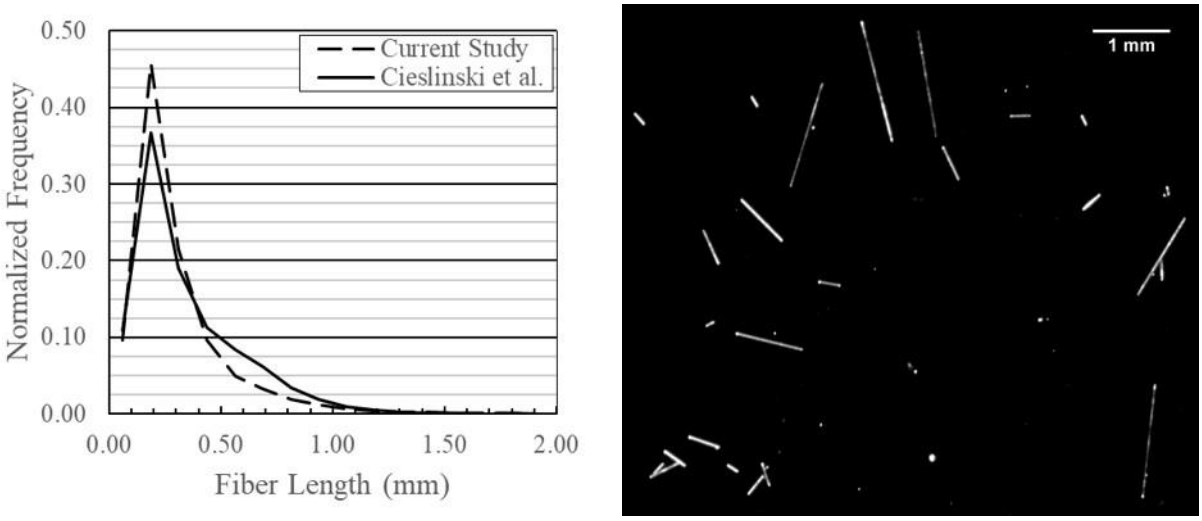

(a) (b)

Fig. 4.2: (a) Comparison of fiber length distributions (FLDs) from material used by Cieslinski et al.[24] and the nozzle purge used in this study. Both FLDs shown were measured using the technique in this study. Number average length was 0.347 mm and 0.309 mm for the material in Cieslinski et al. and the current study respectively. Weight average length was 0.531 mm and 0.515 mm for the material in Cieslinski et al. and the current study respectively. (b) Representative portion of a scan used to measure the FLD.

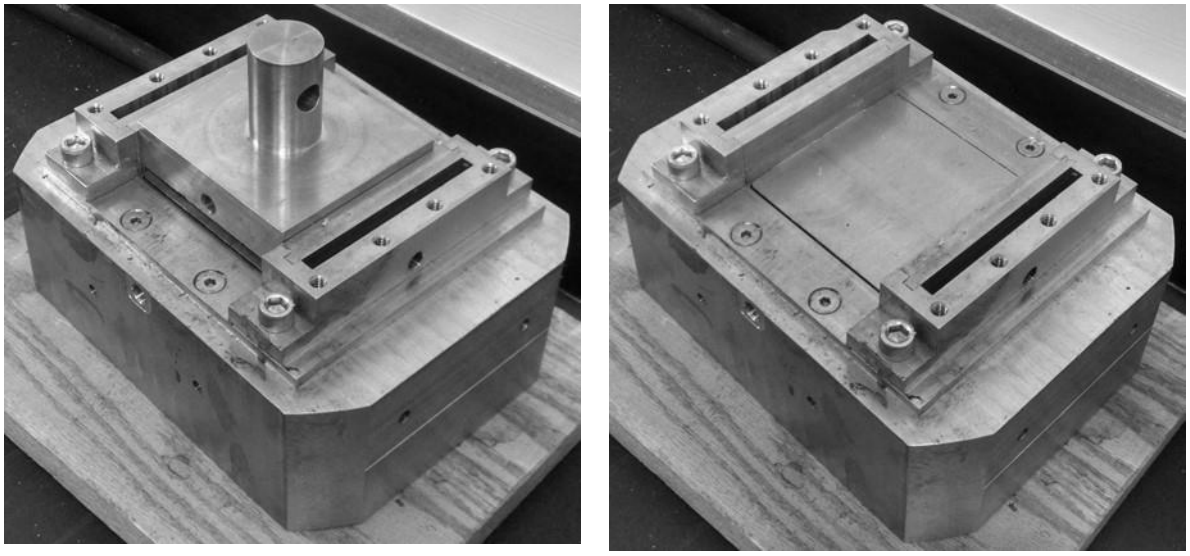

(a) (b)

Fig. 4.3: Isometric view of the non-lubricated squeeze flow tool. (a) shows the tool with both fixtures, and (b) the bottom fixture for a clear view of the channel.

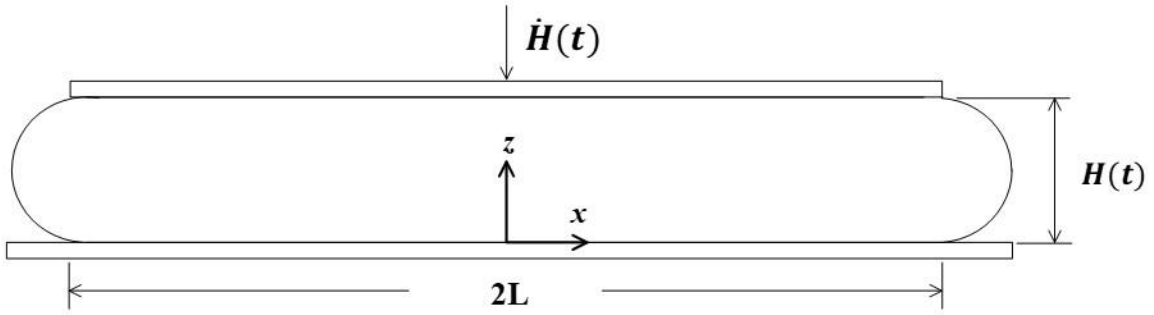

Fig. 4.4: Schematic of the non-lubricated squeeze flow device. The fluid flow is symmetric about $x = 0$. Both the sample thickness, H, and the rate of closure for the top platen, $\dot{H}$, are time-dependent. The channel has a length 2L = 50.8 mm and an initial thickness $H(0)$ of 8 mm.

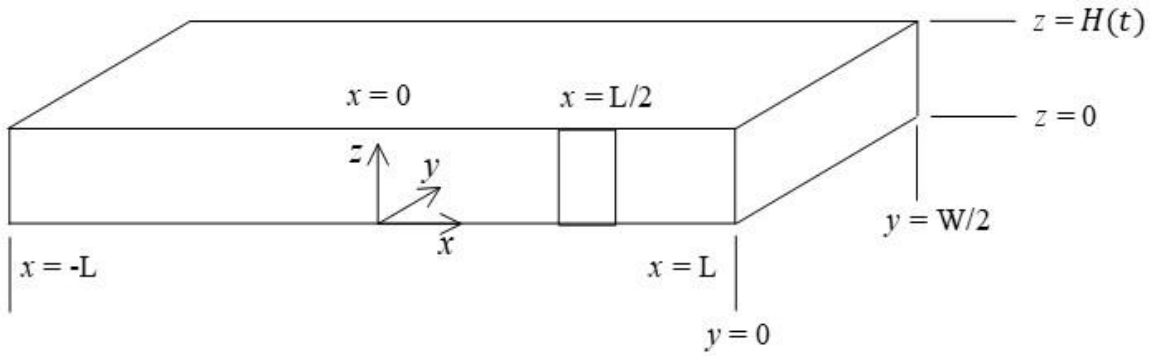

Fig. 4.5: Location of orientation measurements identified in the box at x = L/2. Note that this is one-half of the sample, and the observation plane is along the xz plane at $y = 0$. Sample dimensions are L = 25.4 mm, W = 88.9 mm, and H = 8.0 mm or 2.94 mm for the initial state and at 1 Hencky strain respectively. The width of the micrograph taken at x = L/2 was 1 mm. Flow is symmetric about $x = 0$, with fluid moving in the positive x-direction for positive x positions.

Table 4.I: Comparison of parameters for the SRF model from Cieslinski et al.[24] and this study

Parameter	Cieslinski et al.	Decoupled	Coupled
α	0.20	1.00	1.00
C_I	0.005	0.020	0.020
N_p	174[a]		159[b]

[a]Value was obtained by fitting to shear stress growth during startup of simple shear
[b]Value was calculated using the expression proposed by Shaqfeh and Frederickson[22]

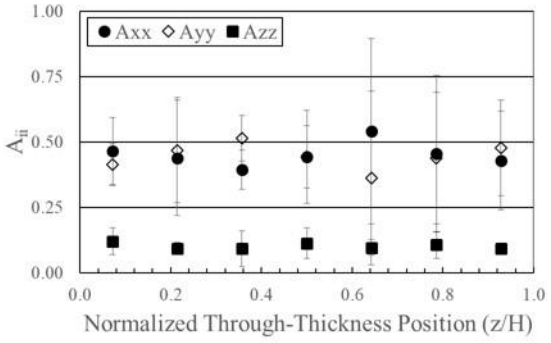

FIG. 4.6: Initial fiber orientation state at x = L/2. Note that A_{xx} refers to flow-direction alignment, A_{yy} to neutral-direction alignment, and A_{zz} to thickness-direction alignment. Error bars are 95% confidence intervals.

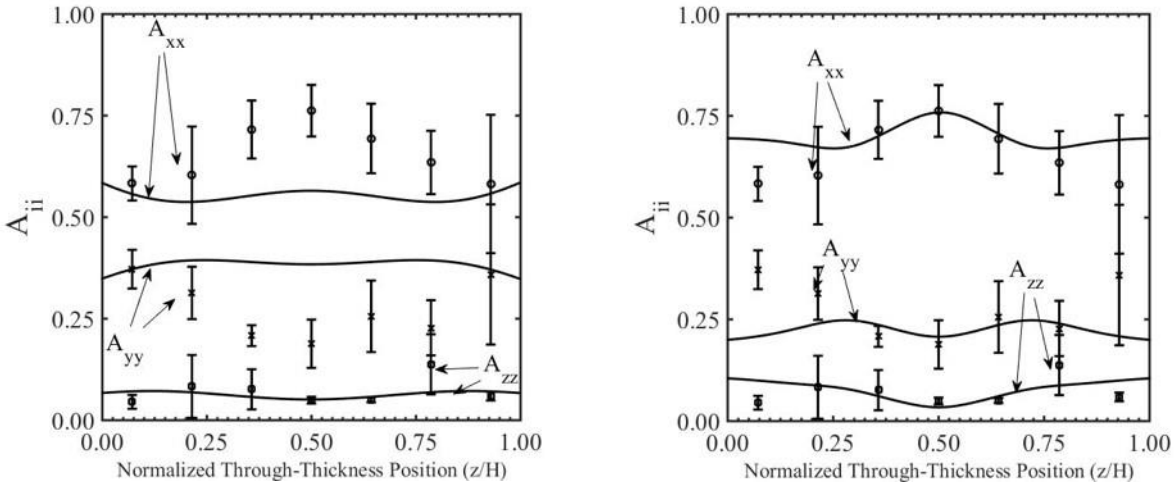

Fig. 4.7: Through-thickness fiber orientation profile at x = L/2 after a Hencky strain of 1.0 at a constant Hencky strain rate of -0.5 s^{-1}. Note that A_{xx}, A_{yy}, and A_{zz} refer to flow-, neutral-, and thickness-direction orientation respectively. (a) Solid lines correspond to predictions from the SRF model using fiber orientation model parameters determined in Cieslinski et al.[24] by fitting to fiber orientation evolution during startup of simple shear. Model parameters were α = 0.25 and C_I = 0.005. (b) Solid lines correspond to fits of the SRF models to the orientation data. Model parameters are α = 1.0 and C_I= 0.020. All simulations were run with one-way coupling. Error bars are 95% confidence intervals.

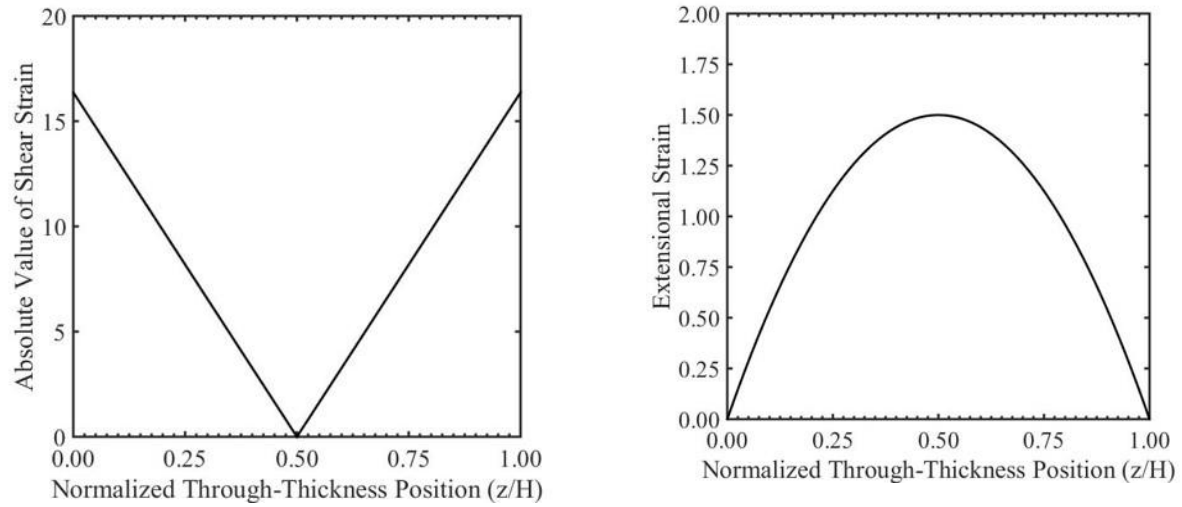

(a) (b)

Fig 4.8: (a) Shear strain through the thickness of the sample at x = L/2. Shear strain was calculated by integrating $\partial u/\partial z$ using Eq. 19 with respect to time to 2 s, corresponding to a Hencky strain of 1. (b) Extensional strain through the thickness of the sample at x = L/2. Extensional strain was calculated by integrating $\partial u/\partial x$ using Eq. 19 with respect to time to 2 s, corresponding to a Hencky strain of 1.

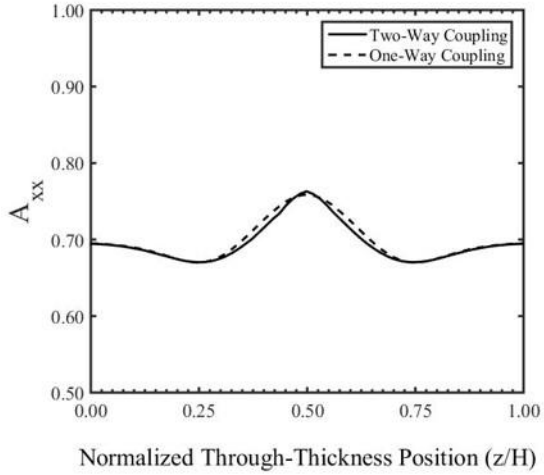

Fig. 4.9: Comparison between two- and one-way coupling on A_{xx} at x = L/2. Fiber orientation model parameters for the SRF model were α = 1.0, C_I = 0.020, and N_p = 159. Solid lines are predictions from two-way coupling, and dashed lines are predictions from one-way coupling.

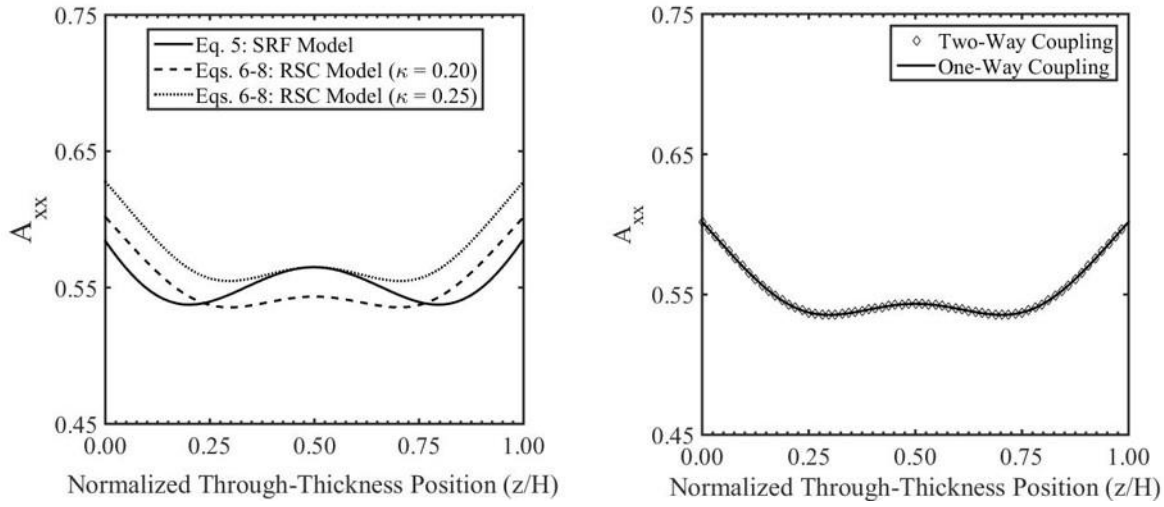

Fig. 4.10: (a) Comparison of A_{xx} predictions between Eq. 5 (non-objective, solid line) and Eqs. 6-8 (objective, dashed and dotted lines). Parameters for the SRF model are $\alpha = 0.25$ and $C_I = 0.005$. Parameters for the RSC model are $C_I = 0.005$ and either $\kappa = 0.20$ or 0.25. (b) Comparison of predictions of A_{xx} using one- and two-way coupling with the RSC model from Eqs. 6-8 with $\kappa = 0.20$, $C_I = 0.005$, and $N_p = 174$.

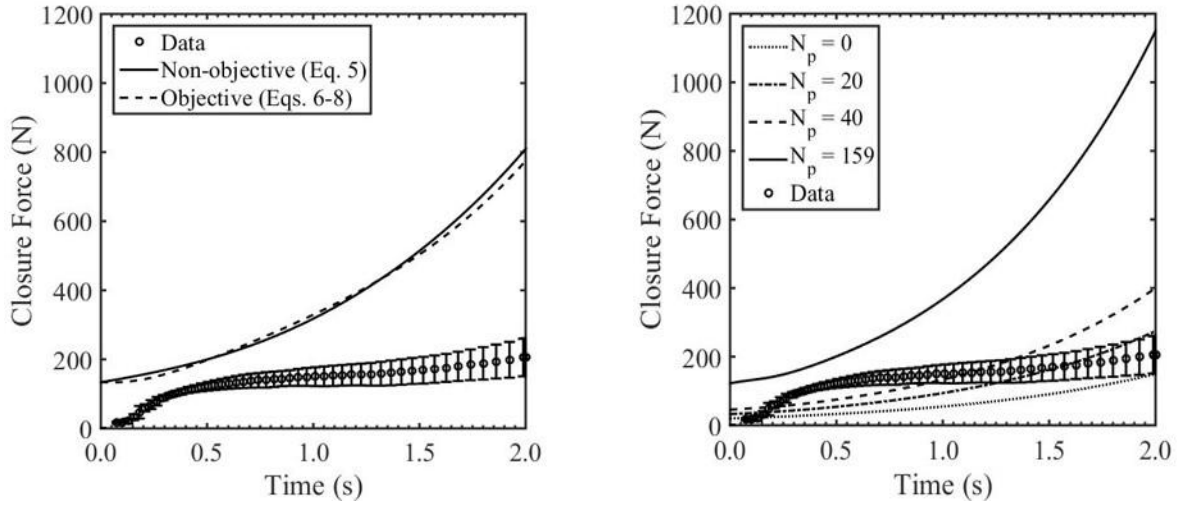

(a) (b)

Fig. 4.11 Closure force as a function of time. Closure rate was a constant Hencky strain rate of -0.50 s^{-1}. Circles are averages over three samples, and error bars are 95% confidence intervals. (a) Solid line is the prediction from evaluating Eq. 9 and using parameters from Cieslinski et al.[24] for the SRF model: $\alpha = 0.25$, $C_I = 0.005$, and $N_p = 174$. Dashed line is the prediction from Eq. 9 using parameters from Cieslinski et al.[24] for the RSC model: $\kappa = 0.20$, $C_I = 0.005$, and $N_p = 174$. (b) Lines are predictions from evaluating Eq. 9 using fiber orientation model parameters from fitting to fiber orientation data from non-lubricated squeeze flow using the SRF model: $\alpha = 1.0$, $C_I = 0.020$, and $N_p = 0$, 20, 40, and 159. The last value is calculated from the analytical expression from Shaqfeh and Fredrickson.[22]

Table 4.I: Comparison of parameters for the SRF model from Cieslinski et al.[24] and this study

Parameter	Cieslinski et al.	Decoupled	Coupled
α	0.20	1.00	1.00
C_I	0.005	0.020	0.020
N_p	174[a]		159[b]

[a]Value was obtained by fitting to shear stress growth during startup of simple shear
[b]Value was calculated using the expression proposed by Shaqfeh and Frederickson[22]

Chapter 5: Comparing fiber orientation evolution between shear and non-lubricated squeeze flow

Gregory Lambert,[1,2] Peter Wapperom,[3] and Donald Baird,[1,2]

1) Department of Chemical Engineering, Virginia Tech, 24061 Blacksburg, VA, USA

2) Macromolecules Innovation Institute, Virginia Tech, 24061 Blacksburg, VA, USA

2) Department of Mathematics, Virginia Tech, 24061 Blacksburg, VA, USA

5.1 Abstract

Lightweighting has become an integral part of vehicle design in the transportation industry. This strategy makes extensive use of fiber-reinforced thermoplastics, which can be injection molded into very complicated shapes. Proper composite design work requires knowledge of the complex orientation state throughout a part to predict properties like stiffness and strength. Although evolution models for the orientation state have been developed for this, each model requires empirical parameters, and no standard method for obtaining these exists. This work continues efforts to find such a test. Here, a glass-fiber-reinforced polypropylene loaded with 30, 40, and 50 wt% fiber is subjected to startup of shear and non-lubricated squeeze flow (NLSF). In both cases, fibers were initially oriented perpendicular to the flow and gap-wise directions. The orientation evolution is reported for both flows and an attempt was made at fitting several orientation models to the data. The measured orientation evolution from startup of shear was slower than expected, and this slower evolution appears to be a result of the initial orientation state and the fiber concentration. Furthermore, a steady orientation state was not observed at any fiber concentration for up to 100 shear strain units. On the other hand, the measured orientation profile from NLSF was found to be essentially independent of fiber concentration. However, the measured orientation profile could not be replicated with any combination of parameters, which suggests the parameters are a function of the local flow type. The apparent dependence of the empirical parameters on the local flow type and initial orientation state suggests shortcomings in the orientation models, which currently assume that the empirical parameters are only dependent on the characteristics of the suspension, such as the fiber aspect ratio and volume fraction.

5.2 Introduction

Over the past several decades, the transportation industry has adopted a strategy known as "lightweighting" to reduce vehicle weight and improve fuel economy. This entails replacing dense

materials (e.g. steel alloys) with less-dense materials such as aluminum alloys and plastics. The thermosetting and thermoplastic resins commonly used are reinforced with fiber fillers to improve the mechanical and thermal properties of the final parts, and this property enhancement is determined in large part by the orientation of the fibers.[1, 2] Composites with thermoplastic resins are of particular interest because they can be injection molded into complex shapes. However, this results in a complex orientation state throughout the part, and so the ability to predict the final orientation state accurately is key to predicting the mechanical and thermal properties of a proposed part.

Various models have been proposed, stemming from Jeffery's[3] pioneering analysis for a dilute suspension of fibers in a Newtonian matrix, that relate the evolution of the fiber orientation state to the deformation of the matrix during processing. Tucker and co-workers[4, 5, 6], as well as Tseng and co-workers[7, 8, 9, 10] in more recent times, developed models for semi-concentrated and concentrated suspensions of rigid fibers. These models account for fiber interactions by introducing phenomenological terms that adjust the rate of orientation evolution and control the steady orientation state. Strautins and Latz[11] developed a model for dilute suspensions of semi-flexible fibers which was later modified for concentrated suspensions by Ortman et al.[12] by adapting the phenomenological terms from the orientation models for concentrated suspensions of rigid fibers. All of these models use empirical fitting parameters, yet a standard method for obtaining these parameters independent of fitting to data from an injection molded part does not currently exist. This necessitates an iterative part design methodology, as manufacturers can't truly predict orientation in a proposed part. The part in question must be made first.

Eberle et al.[13] and Ortman et al.[12] demonstrated that fiber orientation model parameters could be obtained by fitting to orientation data from the startup of simple shear. With this method, a composite sample with a known initial orientation state is deformed at a constant shear rate, and the deformation is stopped at a set strain. The fiber orientation state is measured at each strain and a profile tracking the evolution of the fiber orientation as a function of shear strain is constructed. The orientation models can be fit to this data, and the resulting parameters can be used to predict orientation in injection molded parts. Shear-fitted parameters have been successful in predicting the orientation profile in a center-gated disk with both short- and long-glass fiber reinforcement in the shear-dominated regions near the mold walls, but these parameters did not make good predictions in regions where extensional flow dominates, such as the center of the part and the advancing front.[14, 15] Nor did shear-fitted parameters provide even qualitative predictions of the orientation state in an end-gated plaque.[16]

One potential shortcoming of the shear-fitting method is that it assumes shearing and extension have a comparable influence on orientation. Hence, the fiber orientation dynamics during startup of shear should be representative of a shear-dominated processing flow. Lambert and Baird[17] demonstrated that, apparently, fiber orientation is significantly faster under extension compared to shearing. This would suggest that even relatively low extension rates could have a significant influence on fiber orientation even in the presence of relatively high shear rates. Considering that typical injection molding flows contain both shearing and extensional deformation, it stands to reason that a rheological test that incorporates both might yield orientation model parameters that are applicable to a broad range of geometries.

Lambert et al.[18] addressed this by proposing non-lubricated squeeze flow (NLSF), which contains both shearing (due to the no-slip boundary condition) and extension (by virtue of the squeezing). They demonstrated that shear-fitted orientation model parameters could not predict the resulting orientation profile, but the orientation model could still be fit somewhat with a different set of parameters. Therefore, it would seem that shear-fitted orientation model parameters are unsuitable for predicting orientation in mixed shearing and extension flow fields.

With this in mind, the present study seeks to address this by measuring the orientation profiles of a long-glass-fiber-reinforced polypropylene during both startup of steady shear and NLSF, and obtaining orientation model parameters by fitting to the resulting orientation profiles. These parameter sets would ultimately be used with injection molding simulations to determine which fitting test gives the best predictions.

5.3 Experimental

5.3.1 Sample Preparation

Samples for startup of shear and non-lubricated squeeze flow (NLSF) were made from a commercial glass-fiber-reinforced polypropylene available from SABIC (Verton, MV006S GYLTNAT). The raw material came in the form of 13 mm long pellets, and these were fed into an injection molder (BOY, 35E) to produce strands of nozzle purge. These strands were subsequently compression molded into samples for either startup of shear or NLSF. Three fiber concentrations were used: 30, 40, and 50 wt%. The 30 and 50 wt% pellets were processed as-is, but the 40 wt% material was made by mixing equal masses of the 30 and 50 wt% pellets.

The injection molder consisted of a five-zone barrel with a 32 mm diameter screw. The temperature profile along the barrel was set at 200°C, 215°C, 220°C, 220°C, and 220°C. During the

plastication phase, the screw was rotated at 200 rpm against a back pressure of 0 bar. Material was injected into the atmosphere at a flowrate of 4.8 cm^3/s, and the resulting strands were collected and allowed to cool to room temperature before being cut by hand to strands roughly 50 mm long. As is typical of injection molded composites, severe fiber length attrition occurred during processing.

Fiber length was measured following a procedure proposed by Kunc et al.[19] with modifications. Details can be found elsewhere[18], but the procedure involves calcinating several strands of the nozzle purge in an oven and collecting the leftover glass fibers with an epoxy-coated needle. Fibers were removed from the needle with a second, shorter calcination, and the fibers were scanned with a desktop scanner. Fiber length was then measured from the images. The resulting fiber lengths were reported in Table 5.I for each concentration. Considering that the number averages were all around 1 mm and the weight averages were significantly longer, we classified the fibers as long fibers.

Nozzle purge strands were compression molded into plies approximately 1.5 mm thick. A Carver laboratory press (model 2602) with heated platens (controlled by an Omega CN 7800 temperature controller) was used, with a temperature of 200°C. The cut strands were placed in a 254 mm long by 50.8 mm wide rectangular mold. A compression force of 0.75 metric tons was used, but the press was not able to maintain this force. Rather, this force was reapplied every 5 minutes over the course of 20 minutes, after which the mold was removed from the press and placed in a cooling press for 20 minutes.

Startup-of-shear samples were made by laying the nozzle purge strands oriented in the width direction of the mold and compression molded. This resulted in samples with fibers initially oriented perpendicular to the flow direction. These samples consisted of a single ply. Cieslinski et al.[20] observed that compression molded samples can be problematic in that the sign of the A_{xz} component of $\boldsymbol{A}$ can change from sample to sample, and this inconsistency can influence the orientation dynamics. Care was taken to ensure that ensure strands were laid down with the same orientation (see Fig. 5.1) to mitigate the effects of the inconsistent sign of the off-diagonal components of $\boldsymbol{A}$. This method was chosen in spite of the drawback to keep the initial orientation state consistent between startup of shear and NLSF.

Samples for NLSF were created by slowly building up a sample over repeated compressions. In these samples, the first ply was made by laying the nozzle purge oriented along the length of the mold and then compression molded. After cooling, this ply was removed from the mold to cut off excess material, then placed back in the mold and another layer of nozzle purge was placed on top of it, again oriented along the length of the mold. The combination of pellets laid on a ply was then

compression molded using the same procedure, resulting in a single, thicker plaque. This process of building samples one layer at a time was repeated until the samples were 6.5 mm thick. The resulting 254 mm by 50.8 mm by 6.5 mm bars were then cut with a bandsaw (Delta) into two 88.9 mm by 50.8 mm by 6.5 mm samples for NLSF. Samples were made in this way to impart an initial orientation state perpendicular to the main flow direction and to reduce void content in the NLSF samples.

5.3.2 Rheological Tests

Startup-of-shear tests were run in a sliding plate rheometer. Details of the device can be found elsewhere.[21] The device itself was mounted in a convection oven (Russels Technical Products, RB2-340), and the displacement of the sliding plate was controlled by an Instron universal testing platform (model 4204). All tests were run at 200°C, with temperature measured by a thermocouple which was situated between the plates and remained between the plates throughout the test. The fixture was initially heated by placing the thermocouple on the bottom moving plate and securing the stationary top plate by tightening the securing screws by hand, ensuring that the thermocouple was in contact with both plates as the fixture was heated. Once the plates had reached 200°C, the oven was opened, the top plate was removed, and a sample was placed on the bottom plate. The upper plate was then secured to the bottom plate by tightening the screws by hand. The oven was closed and the sample was allowed to melt for 20 min, after which the upper plate was fully secured by opening the oven again and tightening the screws with a hex key. Shearing was started after closing the oven and allowing the fixture to return to 200°C. A shear rate of 1 s^{-1} was used with a gap of 1.5 mm.

Nonlubricated squeeze flow tests were run in a custom feature, the details of which can be found in Lambert et al.[18] The fixture is mounted in a convection oven (Instron, 3119-609) on an Instron testing platform (model 5969). All tests were run at 200°C at a constant Hencky strain rate ($\dot{\varepsilon} = \dot{H}/H$) of -0.50 s^{-1} for 2 s to give a maximum Hencky strain of 1. Note that $\dot{\varepsilon}$ is the Hencky strain rate, H is the (time-dependent) sample thickness, and $\dot{H}$ is time derivative of the sample thickness.

5.3.3 Fiber Orientation Measurement

Fiber orientation was measured using the method of ellipses.[22] This is a destructive method through which a small portion of a sample is extracted, and one surface is polished. This surface is micrographed. In the picture, fibers appear as ellipses, and the orientation of the fibers can be calculated from geometric relationships.

Samples for orientation analysis were cut out from the larger sample by a bandsaw (Delta), leaving a 2 mm buffer zone between the cut surface and the surface to be analyzed. These smaller

samples were encased in an epoxy plug. The plug was formed by setting the sample in the center of a 6.35 mm diameter high-density polyethylene ring, pouring in a 5:1 (w/w) mixture of a resin (Precision Surfaces, PSI-231-4R) and hardener (Precision Surfaces, PSI-231-4H), and allowing the plug to cure for 24 hours at ambient conditions. After curing, the plugs were sanded and polished using a Buehler AutoMet 250 polisher following a routine suggested by Velez-Garcia.[23] The plugs were then plasma etched (Structure Probe, Plasma Prep II) with oxygen gas for 30 minutes to improve the visual contrast between the matrix and fibers and to remove a thin layer of the matrix to unambiguously measure the out-of-plane angle of the fibers.[24] Micrographs were taken with a Nikon Eclipse LV100 microscope equipped with a movable stage and controlled with NIS Elements Basic Research Version 3.2 (Nikon) software. All micrographs were 1 mm wide. Micrographs of startup-of-shear samples were 1.5 mm tall, and micrographs of NLSF samples were either 6.5 mm tall for the initial orientation measurements, or 2.93 mm tall for the 1 Hencky strain orientation measurements.

Micrographs were taken of the xz-plane, where x is the flow direction (in shear) or stretching direction (in NLSF), and z is the gap-wise direction. Samples from startup of shear were taken from the center of the sample, the region directly under the shear stress transducer. Figure 5.2 shows the location of the samples from NLSF, as well as the plane from which orientation was measured.

The centroid coordinates, major and minor axes, and the in-plane and out-of-plane angles of each fiber were measured using MATLab code developed in-house.[24] Notably, this analysis incorporates a weighting function due to Bay and Tucker[25] to account for the inherent bias towards measuring fibers that are more perpendicular to the xz plane. All orientation data reported here were calculated as an average of three samples, and error bars correspond to the 95% confidence interval associated with the average values.

5.4 Numerical Simulations

5.4.1 Orientation Evolution Equations

One widely used method for representing the orientation of a fiber is with a unit vector, $\boldsymbol{p}$, pointing along the fiber's longest axis. An orientation distribution function, $\psi(\boldsymbol{p})$, then describes the probability of finding a fiber with orientation between $\boldsymbol{p}$ and $\boldsymbol{p} + d\boldsymbol{p}$. The local orientation state of a suspension of fibers can be described using the even-ordered moments of this distribution function:

$$\boldsymbol{A} = \int \boldsymbol{pp}\psi(\boldsymbol{p})d\boldsymbol{p}, \tag{5.1}$$

$$\boldsymbol{A_4} = \int \boldsymbol{pppp}\psi(\boldsymbol{p})d\boldsymbol{p}. \tag{5.2}$$

These tensor quantities represent a compact description of the orientation state[26], and several empirical evolution models have been proposed for describing how orientation changes as the suspension flows. In deriving evolution equations for $\boldsymbol{A}$, one finds that a closure approximation is needed for the higher-order tensors. This work uses the IBOF[27] closure for $\boldsymbol{A_4}$.

Equation 5.3 is known as the Strain Reduction Factor (SRF) model, so-called because the scalar α, which takes a value between 0 and 1, effectively slows down the rate of orientation by reducing the total strain accrued by the sample. This was first proposed by Huynh.[28]

$$\frac{D\boldsymbol{A}}{Dt} = \alpha[\boldsymbol{W}\cdot\boldsymbol{A} - \boldsymbol{A}\cdot\boldsymbol{W} + \xi(\boldsymbol{D}\cdot\boldsymbol{A} + \boldsymbol{A}\cdot\boldsymbol{D} - 2\boldsymbol{A_4}\colon\boldsymbol{D}) + 2C_I D(\boldsymbol{I} - 3\boldsymbol{A})]. \tag{5.3}$$

In this equation, $\boldsymbol{D}$ and $\boldsymbol{W}$ are the rate-of-strain and vorticity tensor, respectively, and D is the scalar magnitude of the rate-of-strain tensor (i.e. $D = \sqrt{\boldsymbol{D}\colon\boldsymbol{D}/2}$). The scalar ξ is a function of the fiber aspect ratio (i.e. $\xi = (r^2-1)/(r^2+1)$), and approaches unity in the limit of long fibers. Consequently, ξ was set to 1 in the simulations in this work. The parameters α and C_I are fitting parameters used to slow down the rate of orientation and adjust the steady orientation state, respectively. Obtaining these parameters by fitting to orientation data is the main thrust of this study.

Wang et al.[29] later pointed out that the SRF model was not objective because the scalar α modified the vorticity terms, violating the Jaumann corotational derivative. They rectified this with Eqs. 5.4-6:

$$\begin{aligned}\frac{D\boldsymbol{A}}{Dt} = \boldsymbol{W}\cdot\boldsymbol{A} - \boldsymbol{A}\cdot\boldsymbol{W} + \boldsymbol{\xi}(\boldsymbol{D}\cdot\boldsymbol{A} + \boldsymbol{A}\cdot\boldsymbol{D} - 2[\boldsymbol{A_4} + (1-\kappa)(\boldsymbol{L} - \boldsymbol{M}\colon\boldsymbol{A_4})]\colon\boldsymbol{D}) \\ + 2\kappa C_I D(\boldsymbol{I} - 3\boldsymbol{A}),\end{aligned} \tag{5.4}$$

$$\boldsymbol{L} = \lambda_{\boldsymbol{i}}\boldsymbol{e_i}\boldsymbol{e_i}\boldsymbol{e_i}\boldsymbol{e_i}, \tag{5.5}$$

$$\boldsymbol{M} = \boldsymbol{e_i}\boldsymbol{e_i}\boldsymbol{e_i}\boldsymbol{e_i}. \tag{5.6}$$

Eqs. 5.4-6 are the Reduced Strain Closure (RSC) model, so-called because the implementation of the strain reduction phenomenon results in a modification to the $\boldsymbol{A_4}$ terms that functions as a sort of closure relationship for $\boldsymbol{A_4}$. Note that although κ is used in place of α, it maintains the same function of reducing the strain accrued by the sample. The strain reduction phenomenon is achieved in this model by slowing down the time evolution of the eigenvalues (but not the eigenvectors) of $\boldsymbol{A}$, given by λ_i and $\boldsymbol{e_i}$, respectively.

Equations 5.4-6 were developed for use with short-fiber reinforcement, which is expected to stay rigid. Strautins and Latz[11] modified the analysis to account for the limited flexibility of longer fibers. This was done by using two vectors to describe the fiber orientation, $\boldsymbol{p}$ and $\boldsymbol{q}$, which modifies the orientation distribution function to $\psi(\boldsymbol{p},\boldsymbol{q})$. Their model was limited to dilute suspensions, but Ortman et al.[12] introduced the strain reduction and isotropic rotary diffusion phenomena to extend the model to concentrated suspensions, given by Eqs. 5.7-13:

$$\frac{D\boldsymbol{A}}{Dt} = \alpha\Big[\boldsymbol{W}\cdot\boldsymbol{A} - \boldsymbol{A}\cdot\boldsymbol{W} + \boldsymbol{D}\cdot\boldsymbol{A} + \boldsymbol{D}\cdot\boldsymbol{A} - 2\boldsymbol{D}\colon\boldsymbol{A}_4 + 2C_I D(\boldsymbol{I} - 3\boldsymbol{A}) + \frac{l_B}{2}(\boldsymbol{C}\boldsymbol{m} + \boldsymbol{m}\boldsymbol{C} - 2(\boldsymbol{m}\cdot\boldsymbol{C})\boldsymbol{A}) - 2k\big(\boldsymbol{B} - \boldsymbol{A}tr(\boldsymbol{B})\big)\Big], \tag{5.7}$$

$$\frac{D\boldsymbol{B}}{Dt} = \alpha\Big[\boldsymbol{W}\cdot\boldsymbol{B} - \boldsymbol{B}\cdot\boldsymbol{W} + \boldsymbol{D}\cdot\boldsymbol{A} + \boldsymbol{A}\cdot\boldsymbol{D} - 2\boldsymbol{D}\colon\boldsymbol{A}_4 + 2C_I D\boldsymbol{B} + \frac{l_B}{2}(\boldsymbol{C}\boldsymbol{m} + \boldsymbol{m}\boldsymbol{C} - 2(\boldsymbol{m}\cdot\boldsymbol{C})\boldsymbol{B}) - 2k\big(\boldsymbol{A} - \boldsymbol{B}tr(\boldsymbol{B})\big)\Big], \tag{5.8}$$

$$\frac{D\boldsymbol{C}}{Dt} = \alpha\Big[(\boldsymbol{\nabla v})^t\cdot\boldsymbol{C} - (\boldsymbol{A}\colon(\boldsymbol{\nabla}\mathbf{v})^t)\boldsymbol{C} - 2C_I D\boldsymbol{C} + \frac{l_B}{\mathbf{2}}\big(\boldsymbol{m} - (\boldsymbol{m}\cdot\boldsymbol{C})\boldsymbol{C} - k\big(1 - tr(\boldsymbol{B})\big)\boldsymbol{C}\big)\Big], \tag{5.9}$$

$$\boldsymbol{m} = \left(\frac{\partial^2 v_i}{\partial x_j \partial x_k}\right) A_{jk}\boldsymbol{\delta_i}. \tag{5.10}$$

$$\boldsymbol{A} = \int\int \boldsymbol{p}\boldsymbol{p}\psi(\boldsymbol{p},\boldsymbol{q},t)d\boldsymbol{p}d\boldsymbol{q}, \tag{5.11}$$

$$\boldsymbol{B} = \int\int \boldsymbol{p}\boldsymbol{q}\psi(\boldsymbol{p},\boldsymbol{q})d\boldsymbol{p}d\boldsymbol{q}, \tag{5.12}$$

$$\boldsymbol{C} = \int\int \boldsymbol{p}\psi(\boldsymbol{p},\boldsymbol{q})\,d\boldsymbol{p}d\boldsymbol{q}. \tag{5.13}$$

In Eq. 5.10, $\boldsymbol{\delta_i}$ is the unit vector pointing in the i[th] direction. Note that the Bead-Rod (BR) model uses two parameters that are dependent on the fibers: l_B and k. The former is simply half the length of the fiber. The latter is a bending potential constant, which can be estimated by Eq. 5.14 using a three-point bending analysis:

$$k = \frac{E_Y}{64\eta_m}\left(\frac{d}{l_B}\right)^3. \tag{5.14}$$

Note that E_Y is the Young's modulus of the fiber, taken to be 80 GPa; d is the fiber diameter, taken to be 14 μm; and l_B is the fiber half-length, taken from either the number or weight average length. The matrix viscosity, η_m, was measured with a 25 mm diameter cone-and-plate fixture in an ARES G2 rheometer (TA Instruments) at a shear rate of 1 s^{-1} at 200°C and found to be 940 Pa-s. Simulations

of startup-of-shear used the value of k corresponding to the number average length of the fibers in the suspension. The NLSF simulations presented here used a k of 44.3 s^{-1}, which corresponds to the number average length of the 50 wt% samples. All of the Bead-Rod simulations used assumed initial values for the $\boldsymbol{B}$ and $\boldsymbol{C}$ tensors, where $\boldsymbol{B} = -\boldsymbol{A}$ and $\boldsymbol{C} = \boldsymbol{0}$. These settings correspond to the limiting case of straight fibers.

5.4.2 Startup of Shear

Simulations of startup of simple shear were performed in MATLab using the "ode23s" differential equation solver with the measured initial orientation state:

$$\boldsymbol{A}(t=0) = \begin{bmatrix} 0.155 & 0.0263 & 0.0017 \\ 0.0263 & 0.822 & 0.0088 \\ 0.0017 & 0.0088 & 0.0228 \end{bmatrix}.$$

This was measured from the 40 wt% samples according to the procedure laid out previously and averaged over three samples. The initial orientation of the 40 wt% samples was assumed to be a representative case for the 30 and 50 wt% samples because they were all made using the same compression molding procedure. Note that the x-direction is taken to be the flow direction, the y-direction is the vorticity axis, and the z-direction is the gap-wise direction. The initial condition shown above, therefore, represents an initial state highly aligned with the vorticity axis. A schematic of the coordinate system and velocity profile is shown in Fig. 5.3.

5.4.3 Non-Lubricated Squeeze Flow

Simulations of NLSF were run using a finite element technique based on the Arbitrary Lagrangian/Eulerian method.[30] Mazahir et al.[31] provide a more thorough description of the method as applied to simulating fiber orientation dynamics. A schematic of the coordinate system and the location of the orientation measurement is shown in Fig 1. The sample domain was [0,L]x[0,$H(t)$], discretized into a 16x16 quadrilateral mesh. Symmetry was assumed about $x = 0$. In these simulations, continuous biquadratic polynomials were used for velocity, and continuous linear polynomials were used for pressure. Discontinuous biquadratic polynomials were used for orientation in all of the models. At the lower platen $z = 0$, $\boldsymbol{u} = \boldsymbol{0}$. At the upper platen, $z = H(t)$, $\boldsymbol{u} = \left(0,0,\dot{H}(t)\right)$, where the dot represents the time derivative d/dt. The upper platen was closed at a constant Hencky strain rate, meaning

$$H(t) = H_0 e^{\dot{\varepsilon} t} \tag{5.15}$$

in which H_0 is the initial sample thickness (6.5 mm in this work) and $\dot{\varepsilon}$ is the Hencky strain rate (-0.5 s^{-1} in this work). Furthermore, the velocity profile derived by Lambert et al.[18] was prescribed for $\boldsymbol{u}$ at x = L.

The measured initial orientation state from the 40 wt% material was used as the initial condition:

$$\boldsymbol{A}(t=0) = \begin{bmatrix} 0.306 & 0.045 & 0.014 \\ 0.045 & 0.654 & -0.007 \\ 0.014 & -0.007 & 0.040 \end{bmatrix}.$$

Note that the x-direction is the stretching direction, the y-direction is the neutral direction, and the z-direction is the gap- wise direction. Again, this data was taken using the procedure outlined previously and averaged over three samples.

Two-dimensional simulations of NLSF at the center-plane of the sample were performed. In addition to the orientation equations, the continuity and Navier-Stokes equations, given by Eqs. 5.16 and 17, were also solved:

$$\boldsymbol{\nabla} \cdot \mathbf{u} = 0, \tag{5.16}$$

$$-\boldsymbol{\nabla} P + 2\eta \boldsymbol{\nabla^2 u} = 0. \tag{5.17}$$

Here, $\boldsymbol{u}$ is the velocity vector ($\boldsymbol{u} = (u, v)$) and P is the hydrostatic pressure. Note that Eq. 5.17 implies one-way coupling between the velocity gradients and orientation. This means that, at each time step, Eqs. 5.16 and 5.17 were solved independently of the orientation equation to determine the velocity and pressure fields. These values were then used to calculate orientation at the same time step. The one-way coupling approach was used because Lambert et al.[18] demonstrated that two-way coupling had a minimal influence on the orientation evolution during NLSF. Recall that the solution domain is limited to the xz plane, so only 2D simulations were performed.

5.5 Results and Discussion

5.5.1 Startup of Shear

The evolution of flow-direction orientation is plotted as a function of shear strain for all three fiber concentrations in Fig. 5.4. The reported data is an average between three samples, and the 95% confidence intervals are reported alongside the average values. Only a small change in orientation occurred in the 40 and 50 wt% samples, while reorientation was stronger in the 30 wt% samples. The reorientation behavior of the 30 wt% material is comparable with that reported by Ortman et al.[12] for

a similar suspension and initial orientation. However, fiber orientation slows down significantly in the 40 and 50 wt% material

The apparently slower orientation is reflected in the fitting parameters for both the SRF and BR models, in particular the value of α. Several attempts to fit the SRF model to the orientation data from the 30 wt% material are shown in Fig. 5.5. When a typical value of $\alpha = 0.20$ is used, the rate of orientation evolution is over-predicted. This apparent slowing of the orientation evolution is even more pronounced with the 40 and 50 wt% samples, as shown in Fig. 5.6. A value of $\alpha = 0.06$ had to be used to ensure that the orientation evolution wasn't over-predicted.

Another interesting point is the lack of an observed steady state in the orientation profiles. According to Phelps et al.,[6] the parameter C_I should be determined by fitting to steady state data. This is reasonable considering that the rotary diffusion term was added to the models specifically to adjust the steady state orientation.[4] Without a steady state for fitting, a series of values of C_I between 0.001 and 0.010 were used to determine the value of C_I that gave the best fit to the data. The results in Fig. 5.5 suggest a $C_I = 0.005$ gave the best fit to the orientation evolution data for the 30 wt% material. However, no combination of α and C_I could give a good fit to all of the orientation evolution data for the 40 and 50 wt% material. The value of C_I was therefore determined by its ability to come close to the A_{xx} data at 75 and 100 shear strain.

Note that the 95% confidence intervals of the 40 and 50 wt% samples overlap, meaning that there is no statistically significant difference between their orientation evolution behavior. Therefore, only one set of α and C_I was used for the two fiber concentrations. With this limitation in mind, the best value of C_I was found to be 0.005 for the 40 and 50 wt% samples. Interestingly, although the values of α are much lower than usual, the values of C_I fall within the expected range. The fitted model parameters and their corresponding A_{xx} trends from the SRF model are shown alongside the orientation evolution data for the 30, 40, and 50 wt% samples in Fig. 5.7. The model predictions are reasonable, but they all under-predict the orientation at 25 shear strain.

Similar results are obtained when fitting the BR model to the orientation evolution data. Using an $\alpha = 0.10$ was necessary to fit to the orientation evolution data for the 30 wt% material (Fig. 5.8), but this low value still over-predicted the rate of orientation evolution in the 40 and 50 wt% samples. These required an $\alpha = 0.040$, as shown in Fig. 5.9. The same method for obtaining C_I for the SRF model was adopted for the BR model, and the results can be seen in Figs. 5.8 and 5.9. Reasonable fits were obtained with $C_I = 0.001$ for the 30 wt% material and $C_I = 0.008$ for the 40 and 50 wt% samples.

Figure 5.10 plots the BR model trends using the fitted parameters alongside the orientation evolution data for all three fiber concentrations. Again, the fits are reasonable.

As with the SRF model, the same set of BR model parameters was used for both the 40 and 50 wt% samples. This was done not only because of the overlapping confidence intervals, but because the predictions from the BR were negligibly different when using the corresponding k and l_B values. This can be seen in Fig. 5.10 where the corresponding values of k and l_B are used in conjunction with the fitted parameters for the 40 and 50 wt% samples, and the A_{xx} trends completely overlap.

5.5.2 Non-Lubricated Squeeze Flow

Stretch-direction orientation starts from a state primarily aligned in the neutral direction (Fig. 5.11), and after 1 Hencky strain the profile features high stretch-direction alignment near the center and low stretch-direction alignment near the walls (Fig. 5.12). The shape of the profile itself agrees well with that reported by Lambert et al.[18] for a short-fiber composite. It appears that, unlike the orientation dynamics in shear, the orientation dynamics in NLSF are independent of fiber concentration, and especially good agreement is found between the 30 and 50 wt% material.

Attempts at fitting the SRF, RSC, and BR models to the orientation profile are shown in Figs. 5.13 and 5.14. Apparently no one set of parameters can fully capture the shape of the profile. The models can be fit to data either near the walls, where shearing dominates, or near the center, where extension dominates. Notably, both parameter sets are the same as those used by Lambert et al.[18] In their work, the parameter set used in Fig. 5.14 came from fitting to orientation evolution data from startup of shear, while the parameter set used in Fig. 5.13 came from fitting to the "mountain peak" shape of the profile. One curious point with the current fitting efforts is that the "mountain peak" shape can't be replicated as it was in Lambert et al.[18] This is most likely due to the change in the initial orientation state.

It is difficult to obtain fitting parameters from the NLSF data. Firstly, and most importantly, it appears that no combination of parameters can actually fit to the profile. Shear-like parameters can predict the orientation near the walls, and extension-like parameters can predict orientation at the center, but the general shape of the orientation profile cannot be replicated. Secondly, there is only a single time point for fitting α. The α parameter was introduced specifically to tune the transient behavior of the model and, therefore, the orientation profile at several Hencky strain units is needed to ensure that the correct transient behavior is captured. Finally, it isn't clear if a steady state is achieved

at any point in the profile. A rigorous C_I value can't be obtained without steady state data, and orientation profiles at multiple Hencky strain units would help establish this.

5.6 Conclusions

One peculiar feature of the orientation evolution from startup of shear is the significantly slower orientation dynamics relative to previously reported work using long-glass-fiber reinforced polypropylene from Ortman et al.[12] and Cieslinski et al.[32] It would appear that the slower dynamics are due to the initial condition used in this study. Indeed, Ortman et al.[12] found that evolution from the vorticity axis-aligned state was notably slower than the evolution from an initial orientation state that was random in the plane perpendicular to the velocity gradient. This was made clear by the fact that the value of α used in both the SRF and BR models in their work, which was obtained by fitting to orientation evolution from the planar random state, over-predicted orientation from the vorticity-axis-aligned state.

A drastic reduction in the rate of the orientation evolution was observed when increasing fiber content from 30 to 40 wt%, which is different from the data reported by Cieslinski et al.[32] Their work was limited to an initial orientation state that was random in the plane perpendicular to the velocity gradient, but they reported very little concentration dependence on the orientation evolution when looking at suspensions with 10 to 40 wt% long glass fibers. It would seem from the data reported in this study that the combination of the fiber content and the initial fiber orientation worked together to significantly slow down fiber orientation. Precisely why this might be the case would have to be established with further work comparing orientation evolution from different initial orientation states and fiber concentrations.

Supposing the above points hold true in a closer analysis of the interaction between fiber content and initial orientation on the rate of fiber orientation, then the method in which the orientation models account for the strain reduction phenomenon needs to be reconsidered. Strain reduction is currently controlled by a single scalar, α or κ, which is assumed to be a unique property of the suspension and should be independent of the orientation state, yet this work suggests that α and κ are at least dependent on the initial orientation state. A first step could be to incorporate fiber interactions into the orientation model, such as the model put forth by Ferec and coworkers.[33, 34] The model is intriguing because ξ and C_I become a function of the orientation state. However, the model, crucially, lacks a mechanism for the strain reduction phenomenon. Wang et al.[29] noted that reducing

the value of ξ from 1 (the long-fiber limit) predicted oscillations in the orientation evolution during startup of shear that are not observed in fiber suspensions, so varying ξ with orientation would not be a useful method for making the strain reduction phenomenon orientation-dependent.

The interaction model is also based on slender body theory, which predicts that fibers essentially stop interacting with each other when they are highly aligned. The current work suggests that when fibers are initially highly aligned, the orientation evolution is considerably slower than if they start in a more random initial orientation state. This is seen in the lower-than-expected values for α from startup of shear. If fiber interactions are indeed one cause of the strain reduction phenomenon, and if the strain reduction effect increases as the intensity of fiber interactions increases, then the current work suggests that highly-aligned fibers interact with each other more strongly than randomly-oriented fibers. This is exactly the opposite of what is predicted by slender body theory.

An analysis that accounts for an interaction area might yield a model with different behavior. This might include considering a small volume of lubricating fluid between neighboring fibers.[35, 36] In this case, fiber interactions would be modeled with lubrication forces rather than direct mechanical contacts. This volume of fluid would be maximized when fibers are highly aligned and minimize when fibers are perpendicular. Therefore, in the case of fibers that are initially highly aligned, interactions between the fibers would be at their largest.

Another interesting feature of the orientation evolution data is that a steady orientation state was not observed in the strain range considered in this work. The orientation data reported by Ortman et al.[12] and Cieslinski et al.[32] suggest that 100 shear strain is a reasonable window for establishing a steady state, yet one was not attained in startup of shear. The steady state is needed for fitting C_I. Future work with startup of shear will need to consider going out to larger shear strains or starting with a different initial condition closer to the steady state, say a planar random or flow-direction-aligned state. Although this would not address the problems with the strain reduction phenomenon, changing the initial condition ensures the fibers will attain a steady state within the strain limits of the sliding plate rheometer. Figures 5.15 and 5.16 suggest that a Hencky strain between 2 and 3 could be used to establish the steady state in NLSF. This happens because the shear rate near the upper and lower platens grows large enough to accrue a significant amount of shear strain, even though NLSF lasts only a few seconds. This would need to be validated with future work that looks at the orientation profile at several Hencky strains, not just the single point in this study.

Obtaining a rigorous value of α or κ from NLSF would require an orientation profile at multiple Hencky strain units. This would increase confidence that the chosen value accurately captures

the reorientation dynamics. However, in light of the NLSF orientation data presented by Lambert et al.[18] and in this study, it seems clear that α and κ are incapable of capturing the orientation dynamics in a flow with both shearing and extension as it is currently implemented. One possible solution is to make α or κ a function of some metric that distinguishes between shear and extensional flow and then interpolating between shear-like and extension-like values, say 0.20 and 1.0, respectively. NLSF provides an ideal test case for the idea, not only because it combines shearing and extension in a rather simple experimental setup, but it is also much simpler to simulate than injection molding. Developing the idea with injection molded samples would be problematic, as one would have to account for non-isothermal effects (e.g. solidification near the mold walls, changes in viscosity) and the advancing front.

5.7 Acknowledgements

The authors thank Michael Vaught and Kevin Holshouser for their help in designing and constructing the NLSF fixture. They also thank Dr. Michael Bortner for access to the Instron used in the NLSF experiments.

References

1. L. A. Carlson, *Thermoplastic composite materials: Composite materials series, vol. 7*. Elsevier: NY, 1991; Vol. 7.
2. M. W. Hyer, *Stress analysis of fiber-reinforced composite materials*. 2 ed.; DEStech Publications: Lancaster, PA, 2009.
3. G. B. Jeffery, "The motion of ellipsoidal particles in a viscous fluid," *Proc. R. Soc. London, Ser. A* **102** (715), 161 (1922).
4. F. Folgar and C. L. Tucker III, "Orientation behavior of fibers in concentrated suspensions," *J. Reinf. Plast. Compos.* **3** (2), 98 (1984).
5. J. Wang. *Improved fiber orientation kinetics for injection molded composites*, PhD Thesis. University of Illinois, 2007.
6. J. H. Phelps and C. L. Tucker III, "An anisotropic rotary diffusion model for fiber orientation in short- and long-fiber thermoplastics," *J. Non-Newton. Fluid Mech.* **156** (3), 165 (2009).
7. H.-C. Tseng, R.-Y. Chang and C.-H. Hsu, "Phenomenological improvements to predictive models of fiber orientation in concentrated suspensions," *J. Rheol.* **57** (6), 1597 (2013).
8. P. H. Foss, H.-C. Tseng, J. Snawerdt, Y.-J. Chang, W.-H. Yang and C.-H. Hsu, "Prediction of fiber orientation distribution in injection molded parts using moldex3d simulation," *Polym. Compos.* **35** (4), 671 (2014).
9. H.-C. Tseng, R.-Y. Chang and C.-H. Hsu, "An objective tensor to predict anisotropic fiber orientation in concentrated suspensions," *J. Rheol.* **60** (2), 215 (2016).
10. H.-C. Tseng, R.-Y. Chang and C.-H. Hsu, "The use of principal spatial tensor to predict the anisotropic fiber orientatino in concentrated fiber suspensions," *J. Rheol.* **62** (1), 313 (2018).
11. U. Strautins and A. Latz, "Flow-driven orientation dynamics of semiflexible fiber systems," *Rheol. Acta* **46** (8), 1057 (2007).
12. K. Ortman, D. Baird, P. Wapperom and A. Whittington, "Using startup of steady shear flow in a sliding plate rheometer to determine material parameters for the purpose of predicting long fiber orientation," *J. Rheol.* **56** (4), 955 (2012).
13. A. P. R. Eberle, D. G. Baird, P. Wapperom and G. M. Velez-Garcia, "Using transient shear rheology to determine material parameters in fiber suspension theory," *J. Rheol.* **53** (3), 685 (2009).
14. S. M. Mazahir, G. M. Velez-Garcia, P. Wapperom and D. Baird, "Evolution of fibre orientation in radial direction in a center-gated disk: Experiments and simulation," *Composites Part A* **51**, 108 (2013).

15. K. Ortman, D. Baird, P. Wapperom and A. Aning, "Prediction of fiber orientation in the injection molding of long fiber suspensions," *Polym. Compos.* **33** (8), 1360 (2012).
16. K. J. Meyer, J. T. Hofmann and D. G. Baird, "Prediction of short glass fiber orientation in the filling of an end-gated plaque," *Composites Part A* **62**, 77 (2014).
17. G. M. Lambert and D. G. Baird, "Evaluating rigid and semiflexible fiber orientation evolution models in simple flows," *J. Man. Sci. Eng.* **139** (3), 031012-1 (2017).
18. G. Lambert, P. Wapperom and D. Baird, "Obtaining short-fiber orientation model parameters using non-lubricated squeeze flow," *Phys. Fluids* **29** (12), 121608-1 (2017).
19. V. Kunc, B. J. Frame, B. N. Nguyen, C. L. Tucker III and G. Velez-Garcia, *Fiber length distribution measurement for long glass and carbon fiber reinforced injection molded thermoplastics*, In: Proceedings of the 7th annual society of plastic engineers automotive composites conference and exposition, Troy, MI, 2007.
20. M. J. Cieslinski, D. Baird and P. Wapperom, "Obtaining repeatable initial fiber orientation for the transient rheology of fiber suspensions in simple shear flow," *J. Rheol.* **60**, 161 (2016).
21. N. Agarwal. *Transient shear flow rheology of concentrated long glass fiber suspensions in a sliding plate rheometer*, Masters Thesis. Virginia Polytechnic Institute and State University, 2009.
22. P. J. Hine, N. Davidson, R. A. Duckett and I. M. Ward, "Measuring the fibre orientation and modelling the elastic properties of injection-moulded long-glass-fibre-reinforced nylon," *Compos. Sci. Technol.* **53** (2), 125 (1995).
23. G. Velez-Garcia. *Experimental evaluation and simulations of fiber orientation in injection molding of polymers containing short glass fibers*, PhD Thesis. Virginia Tech, 2012.
24. G. M. Vélez-García, P. Wapperom, D. G. Baird, A. O. Aning and V. Kunc, "Unambiguous orientation in short fiber composites over small sampling area in a center-gated disk," *Composites Part A* **43** (1), 104 (2012).
25. R. S. Bay and C. L. Tucker III, "Stereological measurements and error estimates for three-dimensional fiber orientation," *Polym. Eng. Sci.* **32** (4), 240 (1992).
26. S. G. Advani and C. L. Tucker III, "The use of tensors to describe and predict fiber orientation in short fiber composites," *J. Rheol.* **31** (8), 751 (1987).
27. D. H. Chung and T. H. Kwon, "Invariant-based optimal fitting closure approximation for the numerical prediction of flow-induced fiber orientation," *J. Rheol.* **46** (1), 169 (2002).
28. H. M. Huynh. *Improved fiber orientation predictions for injection-molded composites*, Masters Thesis. University of Illinois at Urbana-Champaign, 2001.
29. J. Wang, J. F. O'Gara and C. L. Tucker III, "An objective model for slow orientation kinetics in concentrated fiber suspensions: Theory and rheological evidence," *J. Rheol.* **52** (5), 1179 (2008).
30. T. J. R. Hughes, W. K. Liu and T. K. Zimmermann, "Lagrangian-Eulerian finite element formulation for incompressible viscous flows," *Comput. Method. Appl. M.* **29**, 329 (1981).
31. S. M. Mazahir, G. M. Velez-Garcia, P. Wapperom and D. Baird, "Fiber orientation in the frontal region of a center-gated disk: Experiments and simulation," *J. Non-Newton. Fluid Mech.* **216**, 31 (2015).
32. M. J. Cieslinski, P. Wapperom and D. G. Baird, "Influence of fiber concentration on the startup of shear flow behavior of long fiber suspensions," *J. Non-Newton. Fluid Mech.* **222**, 163 (2015).
33. J. Férec, G. Ausias, M. C. Heuzey and P. J. Carreau, "Modeling fiber interactions in semiconcentrated fiber suspensions," *J. Rheol.* **53** (1), 49 (2009).
34. G. Natale, G. Ausias, J. Férec, M. Heuzey and P. Carreau, "Modeling interactions in carbon nanotube suspensions: Transient shear flow," *J. Rheol.* **60** (6), 1069 (2016).
35. S. Le Corre, P. Dumont, L. Orgeas and D. Favier, "Rheology of highly concentrated planar fiber suspensions," *J. Rheol.* **49** (5), 1029 (2005).
36. C. Servais, J.-A. E. Manson and S. Toll, "Fiber-fiber interaction in concentrated suspensions: Disperse fibers," *Journal of Rheology* **43** (4), 991 (1999).

Tables and Figures

Table 5.I: Number and weight average lengths corresponding to each fiber concentration. The half-length and bending potential constant from the Bead Rod model were calculated using the number average length.

Fiber Concentration	Number Average Length mm	Weight Average Length mm	Fiber Half Length l_B mm	Bending Potential Constant k s^{-1}
30 wt%	1.14	3.40	0.570	19.7
40 wt%	0.986	2.68	0.493	30.4
50 wt%	0.870	2.42	0.435	44.3

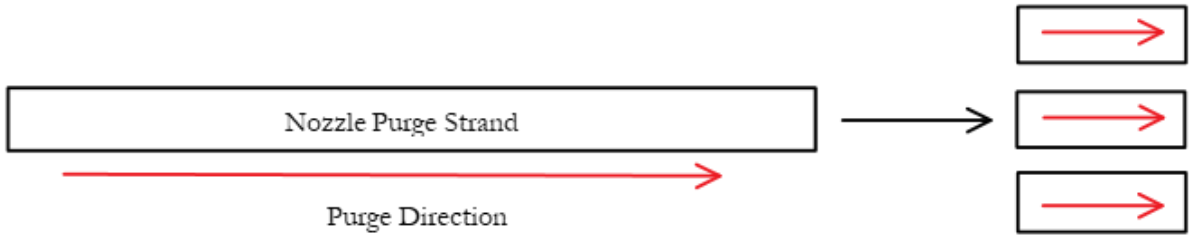

Fig. 5.1: Illustration of how nozzle purge strands were laid into the mold. "Purge direction" refers to the direction the strand flowed out of the injection molder when the nozzle purge was generated.

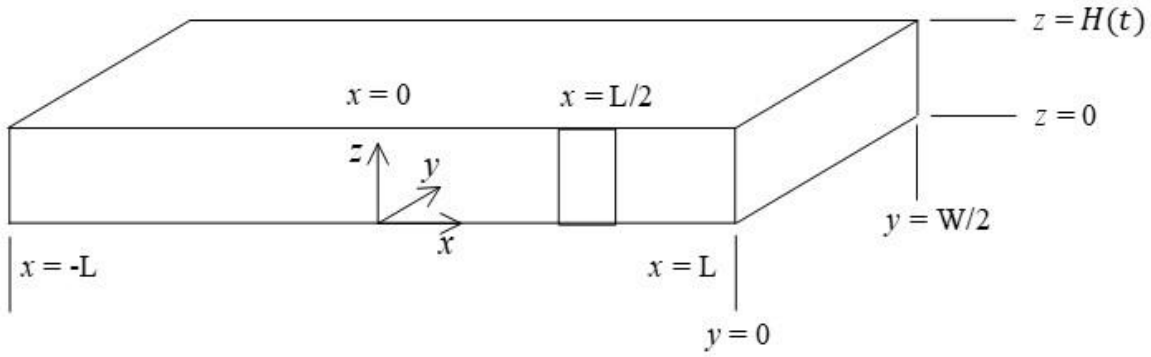

Fig. 5.2: Location of orientation measurements identified in the box at x = L/2. Note that this is one-half of the sample, and the observation plane is along the xz plane at y = 0. Sample dimensions are L = 25.4 mm, W = 88.9 mm, and H_0 = 6.5 mm or H = 2.39 mm for the initial state and at 1 Hencky strain, respectively. The micrograph taken at x = L/2 was 1 mm wide and through the thickness of the sample. Flow is symmetric about x = 0, with fluid moving in the positive x-direction for positive x positions.

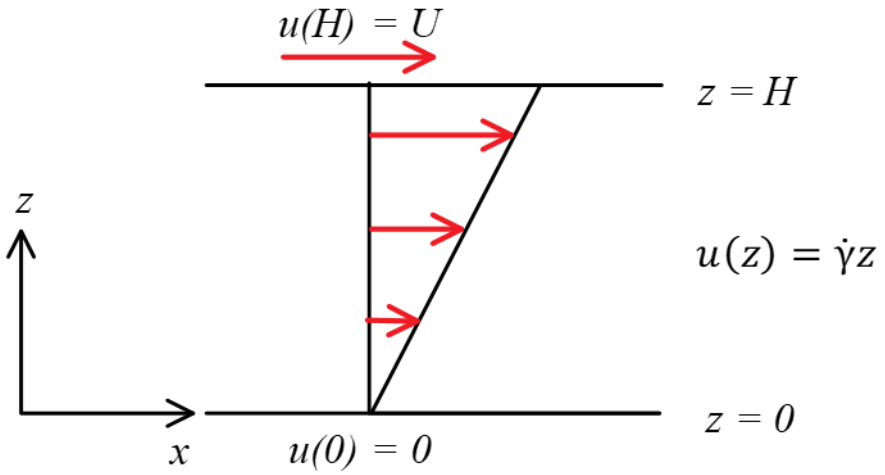

Fig. 5.3: Schematic of the sliding plate. In this work, H is a constant 1.5 mm, and $\dot{\gamma} = U/H$ is a constant 1.0 s^{-1}. Note that flow is in the x-direction and the velocity is changing in the z-direction.

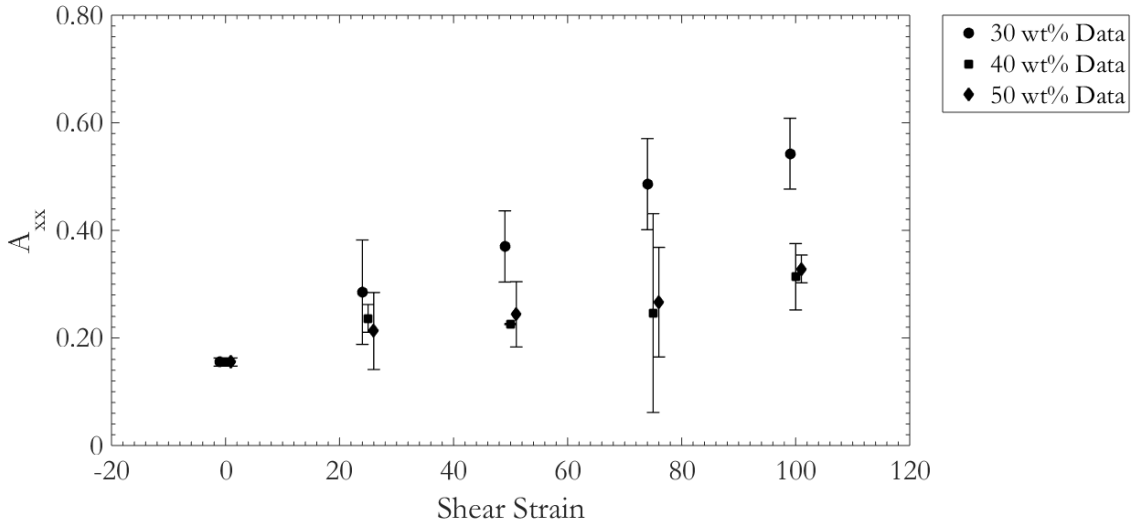

Fig. 5.4: Flow-direction fiber orientation evolution during startup of shear. A shear rate of 1.0 s^{-1} was applied. Data points are an average over three samples and the error bars correspond to 95% confidence intervals. Samples were subjected to a constant shear rate of 1.0 s^{-1}. Orientation was measured at 0, 25, 50, 75, and 100 shear strain units. The 30 and 50 wt% markers are offset by -1 and +1 shear strain unit respectively to make distinguishing which error bars are associated with which data set easier.

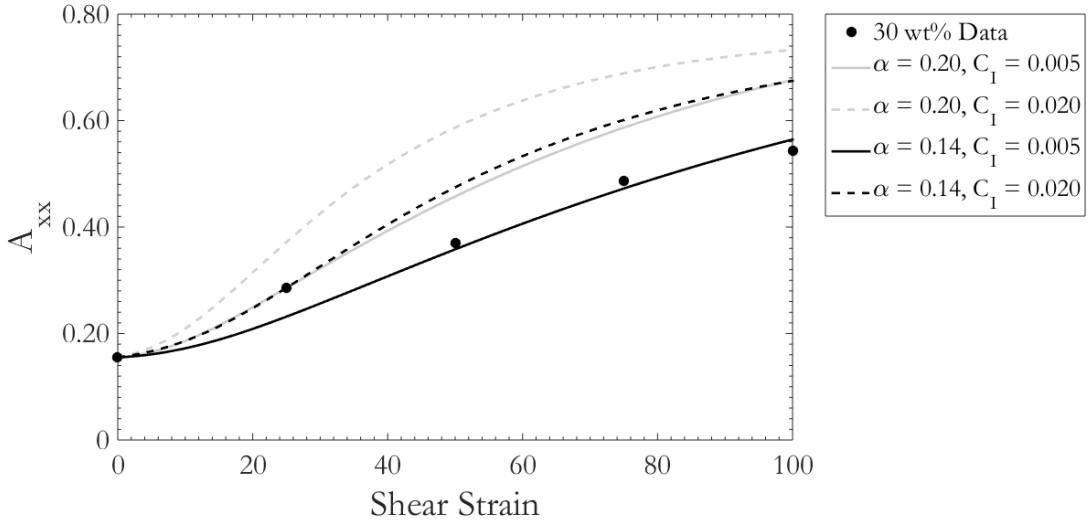

Fig. 5.5: Plot of several attempts to fit the SRF model to the orientation data from startup of shear for the 30 wt% material averaged over three samples. The fitting attempts with $\alpha = 0.20$ use typical values of the model parameters, but these over-predict the rate of orientation evolution. Ultimately, the attempt setting $\alpha = 0.14$ and $C_I = 0.005$ was deemed to give the best fit. Samples were subjected to a constant shear rate of 1.0 s^{-1}.

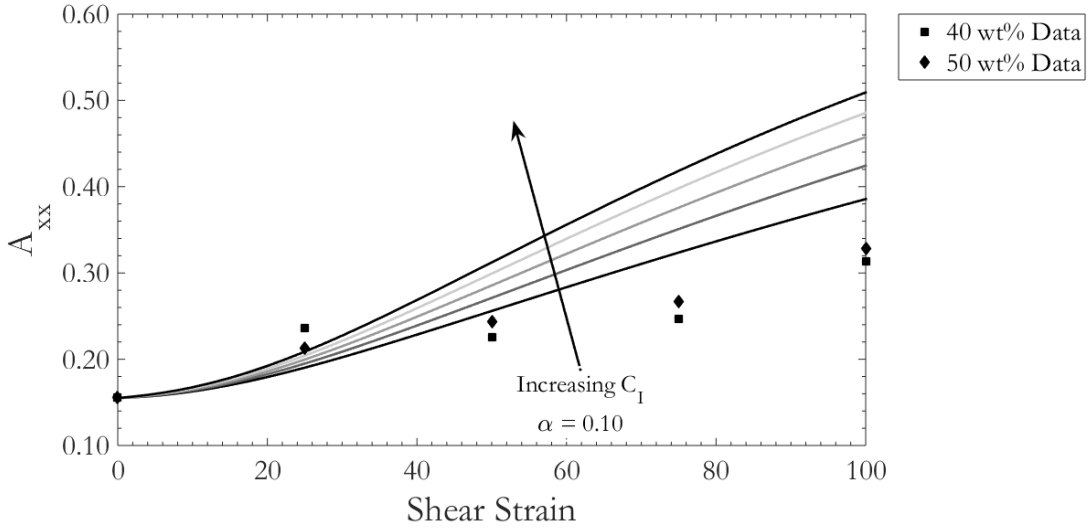

(a)

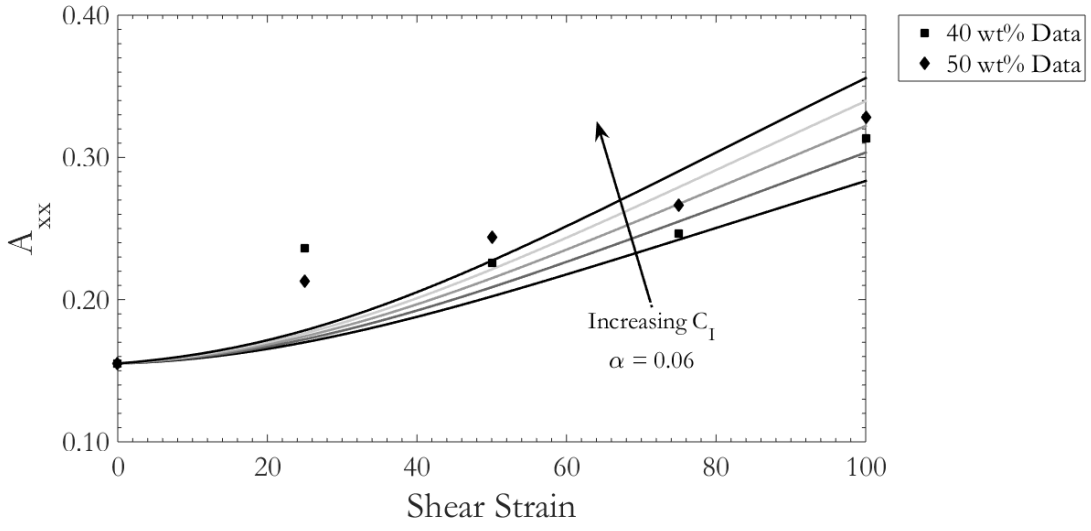

(b)

Fig. 5.6: Plot of several attempts to fit the SRF model to the orientation data from startup of shear for the 40 and 50 wt% samples. Data was averaged over three samples for each fiber concentration. The same range of C_I values are used in both (a) and (b), spanning from 0.001 to 0.009 in increments of 0.002. Together, (a) and (b) demonstrate that the Folgar-Tucker model could not fit the entire evolution profile. The parameter pair $\alpha = 0.06$ and $C_I = 0.005$ was chosen as it seemed to split the 40 and 50 wt% data at 100 strain fairly well. Note that the 95% confidence intervals for the 40 and 50 wt% material overlap, meaning that the difference in the 40 and 50 wt% orientation data was not statistically significant. Therefore, only one set of parameters was used to fit to the data. Samples were subjected to a constant shear rate of 1.0 s^{-1}.

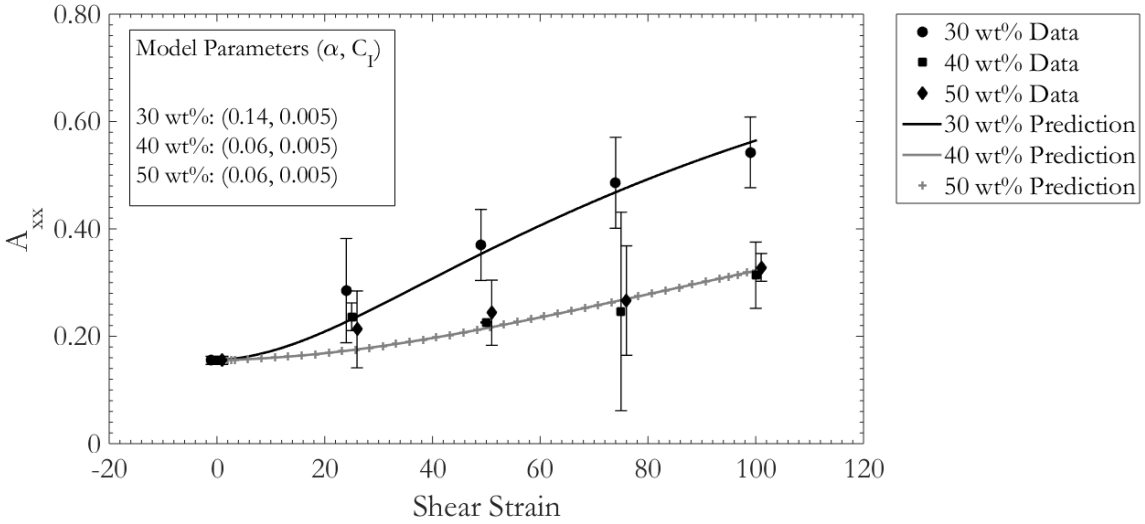

Fig. 5.7: Trends from the SRF model predicted by the fitted model parameters. Only x-direction orientation is shown. Samples were subjected to a constant shear rate of 1.0 s^{-1}. Orientation was measured at 0, 25, 50, 75, and 100 shear strain units. The 30 and 50 wt% markers are offset by -1 and +1 shear strain unit respectively to make distinguishing which error bars are associated with which data set easier.

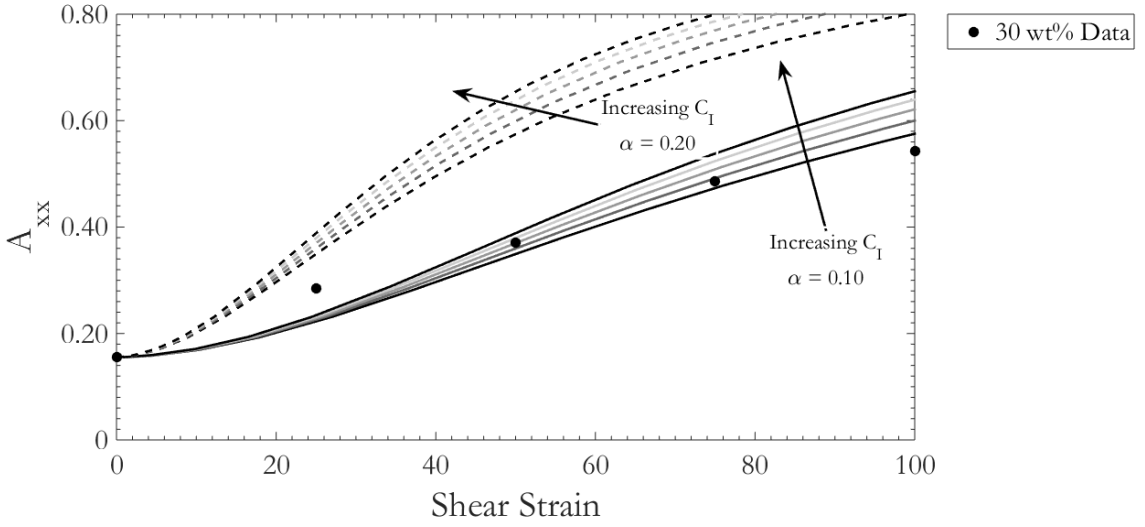

Fig. 5.8: Plot of several attempts to fit the Bead-Rod model to the orientation data from startup of shear for the 30 wt% material averaged over three samples. The same range of C_I values was used with both values of α, spanning from 0.001 to 0.009 in increments of 0.002. The parameter pair α = 0.10 and C_I = 0.001 was chosen as it seemed to come close to the most points while not over-predicting the orientation at 100 shear strain too much. Values for k and l_B corresponding to the 30 wt% material were used (see Table 5.I). Samples were sheared at a constant shear rate of 1.0 s^{-1}.

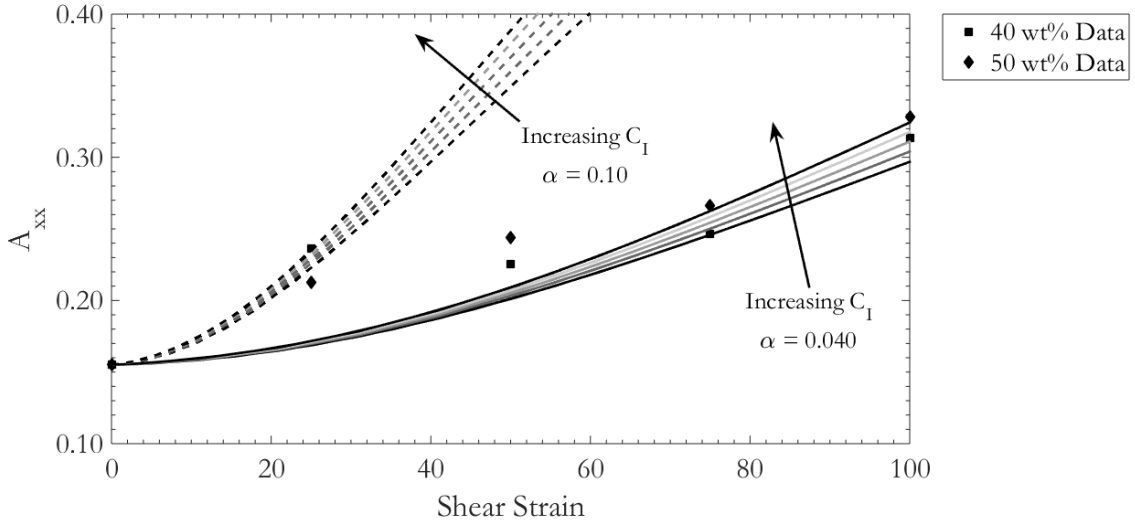

Fig. 5.9: Plot of several attempts to fit the Bead-Rod model to the orientation data from startup of shear for the 40 and 50 wt% material averaged over three samples for each fiber concentration. Values for k and l_B corresponding to the 50 wt% material were used (see Table 5.I). Predictions using the values of k and l_B corresponding to the 40 wt% material were not noticeably different from predictions using the corresponding 50 wt% values, therefore only the values for the 50 wt% material were used in obtaining fitting parameters. The same range of C_I values was used for both values of α, spanning from 0.001 to 0.09 in increments of 0.002. The parameter set $\alpha = 0.040$ and $C_I = 0.008$ was used as these seemed to split the 40 and 50 wt% data. Recall that the 95% confidence intervals overlap, thus the difference in the orientation data for the 40 and 50 wt% material was not statistically significant. Therefore, only one set of parameters was to fit the data. Samples were subjected to a constant shear rate of 1.0 s^{-1}.

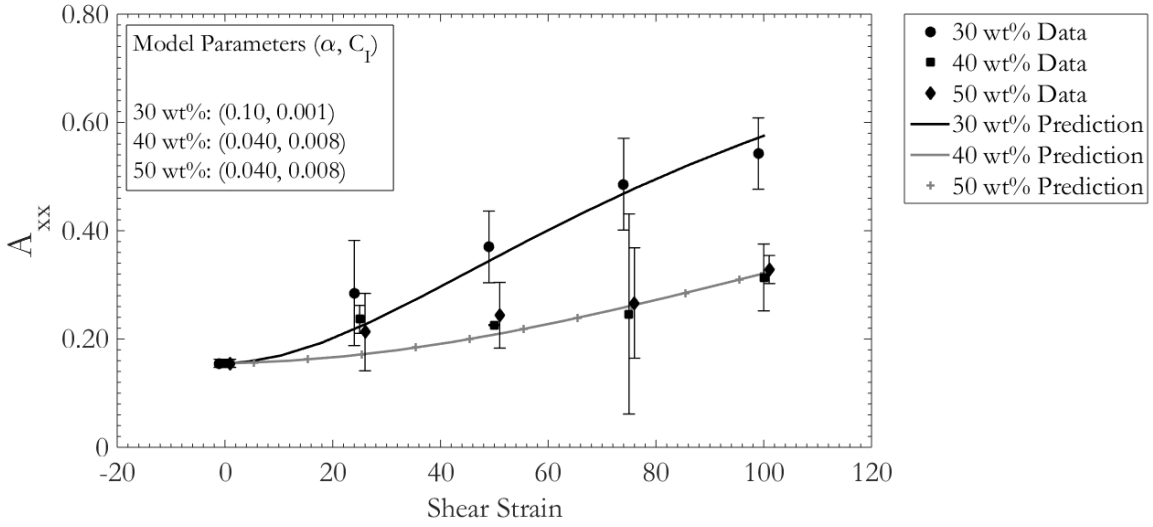

Fig. 5.10: Fitting the Bead-Rod model to the orientation data from startup of shear averaged over three samples. Only x-direction orientation is shown. Different values of k and l_B were used for each concentration, corresponding to the number average fiber length in the suspension (See Table 5.I for values). Samples were subjected to a constant shear rate of 1.0 s^{-1}. The 30 and 50 wt% markers are offset by -1 and +1 shear strain unit respectively to make distinguishing which error bars are associated with which data set easier.

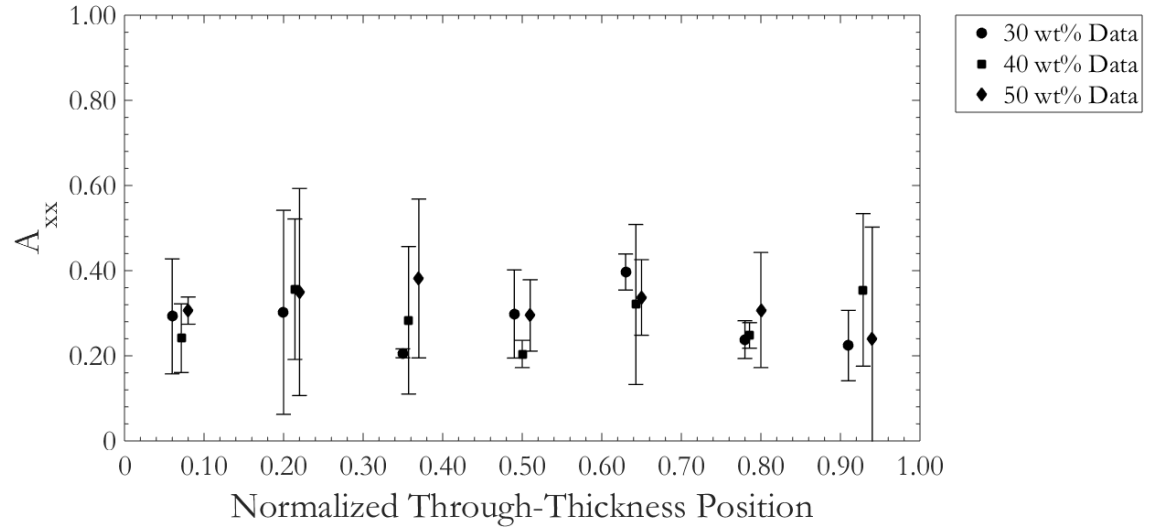

Fig. 5.11: Initial stretching-direction orientation state for NLSF samples. Data is averaged over three samples and the error bars are 95% confidence intervals. All data was measured at the same through-thickness locations: 0.07, 0.21 0.36, 0.50, 0.64, 0.79, and 0.92. Data from the 30 and 50 wt% samples are offset by -0.01 and +0.01 respectively to make distinguishing which error bars correspond to which data set easier.

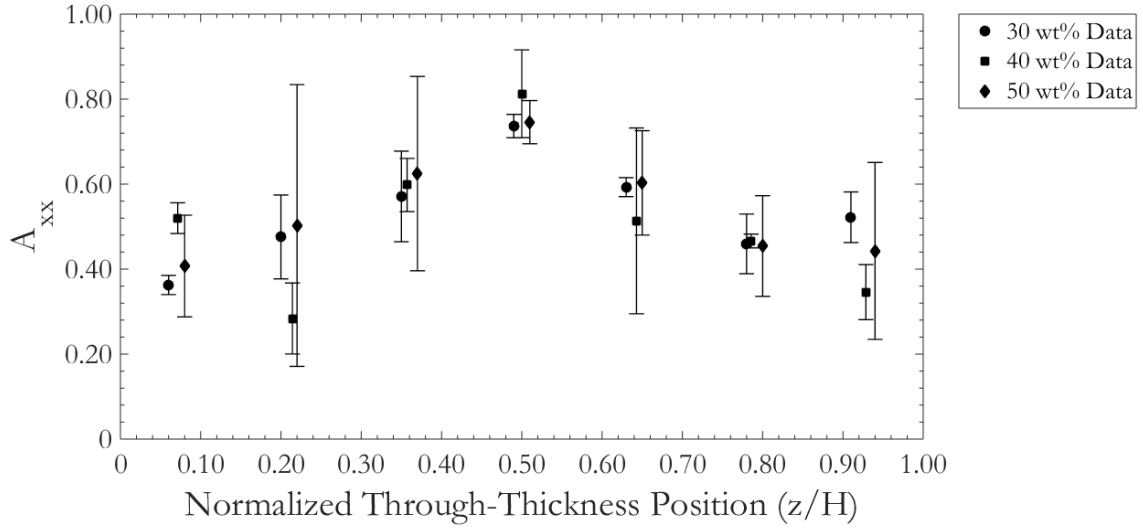

Fig. 5.12: Flow-direction orientation in NLSF at 1 Hencky strain. The sample was compressed at a constant Hencky strain rate of -0.50 s^{-1}. Note that this means the sample thickness decreased exponentially in time. Data is averaged over three samples for each fiber concentration and the error bars are 95% confidence intervals. All data was measured at the same through-thickness locations: 0.07, 0.21 0.36, 0.50, 0.64, 0.79, and 0.92. Data from the 30 and 50 wt% samples are offset by -0.01 and +0.01 respectively to make distinguishing which error bars correspond to which data set easier.

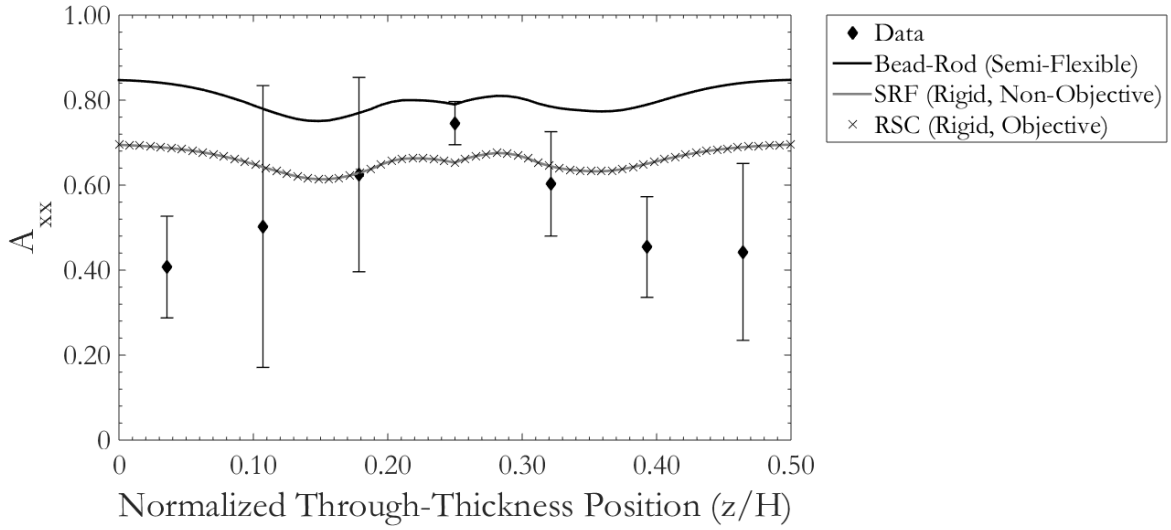

Fig. 5.13: Simulation results for the Bead-Rod, Strain Reduction Factor, and Reduced Strain Closure models using α = 1.0 (SRF and BR) or κ = 1.0 (RSC) and C_I = 0.020 after 1 Hencky strain at a constant Hencky strain rate of -0.50 s^{-1}. Data is from the 50 wt% samples and averaged over three samples. Error bars are 95% confidence intervals. Table 5.I gives the values for the corresponding physical parameters in the Bead-Rod model. Note that when $\kappa = \alpha = 1.0$, the SRF and RSC models are identical, hence the overlapping trendlines.

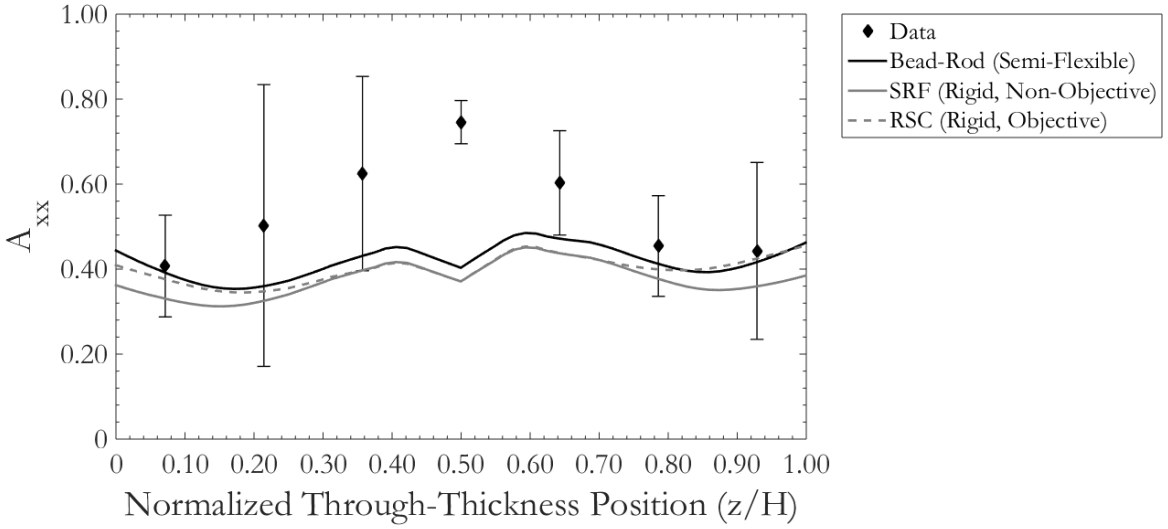

Fig. 5.14: Simulation results for the Bead-Rod, Strain Reduction Factor, and Reduced Strain Closure models using $\alpha = \kappa = 0.20$ and $C_I = 0.005$ after 1 Hencky strain at a constant Hencky strain rate of -0.50 s^{-1}. Data is from the 50 wt% material and averaged over three samples. Error bars are 95% confidence intervals. Table 5.I gives the values of the corresponding physical parameters in the Bead-Rod model.

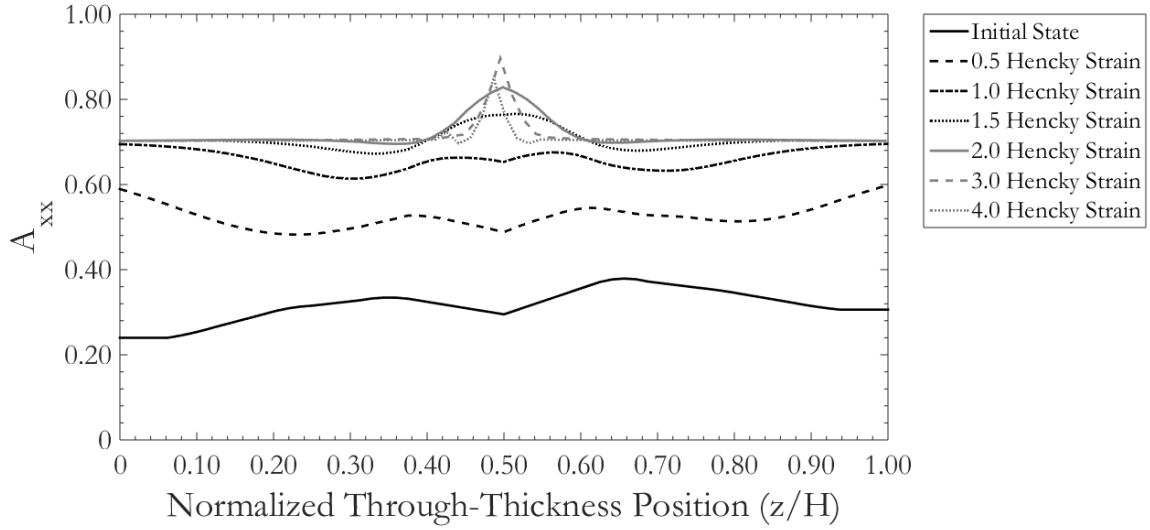

Fig. 5.15: Simulation of stretching-direction orientation through the thickness of the sample after the listed Hencky strain units. Only results from the Strain Reduction Factor (Rigid, Non-Objective) model are shown, with $\alpha = 1.0$ and $C_I = 0.020$. The maximum Hencky strain attained in the NLSF experiments was 1.0 at a constant Hencky strain rate of -0.50 s^{-1}.

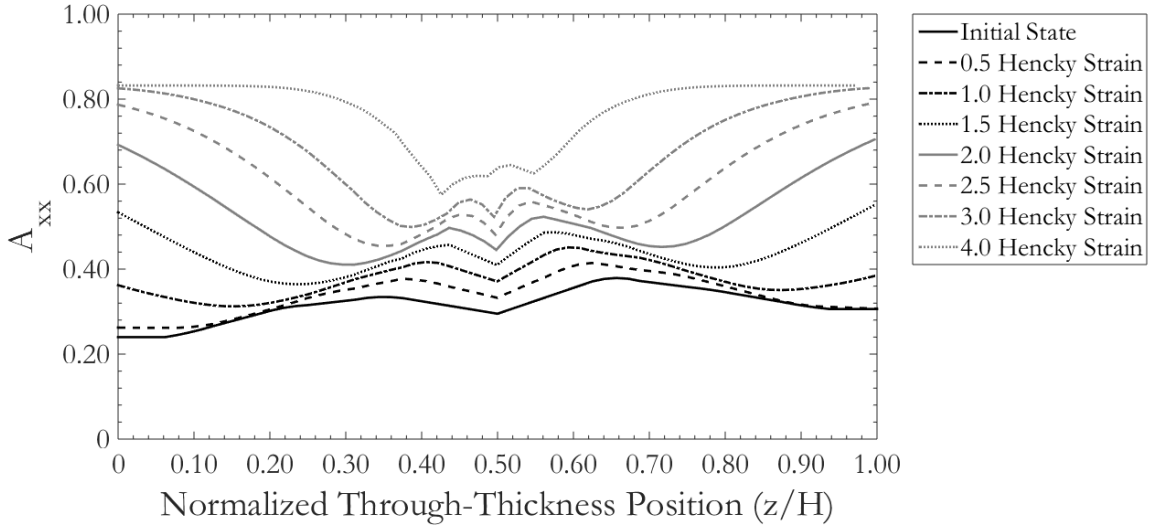

Fig. 5.16: Simulation of stretching-direction orientation through the thickness of the sample after the listed Hencky strain units. Only results from the Strain Reduction Factor (Rigid, Non-Objective) model are shown, with $\alpha = 0.20$ and $C_I = 0.005$. The maximum Hencky strain attained in the NLSF experiments was 1.0 at a constant Hencky strain rate of -0.50 s^{-1}.

Chapter 6: Conclusions Recommendations for Future Work

6.1 Conclusions

The work presented in this dissertation investigating the objectives stated in Ch. 1 leads to the conclusions that:

1. The empirical orientation model parameters are apparently not independent of the flow type used to obtain them. When comparing the orientation dynamics between startup of shear and planar extension, it was found that the value of the strain reduction factor α was roughly it's maximum value of 1 in planar extension and significantly smaller in startup of shear. Furthermore, no single set of empirical parameters could fit the entire gap-wise orientation profile from non-lubricated squeeze flow, where the relative magnitude of shear and extension changes through the sample thickness.

2. Two tests incorporating extensional flow were used in this work: planar extension and non-lubricated squeeze flow. Planar extension is a shear-free rheometric flow and was realized using lubricated squeeze flow in a parallel plate fixture. Orientation models could be fit to the orientation data from planar extension rather well, but the corresponding values of the empirical parameters changed depending on the test. Non-lubricated squeeze flow has both shearing and extensional flow and was also realized in a newly-designed fixture. Orientation models could not be fit to the entire gap-wise profile from non-lubricated squeeze flow. However, parameters with values typical of startup of shear did predict orientation near the top and bottom platens (where shear dominates), and parameters could also fit to the data near the center of the sample (where extension dominates) using an α of 1, similar to what was found for planar extension.

3. Interesting results were found when comparing the orientation dynamics between startup of shear and non-lubricated squeeze flow of a long-fiber composite. Three fiber concentrations were used: 30, 40, and 50 wt% fiber. The orientation dynamics during non-lubricated squeeze flow seemed to be independent of fiber concentration, yet the orientation dynamics during startup of shear slowed down significantly when increasing fiber loading from 30 to 40 and 50 wt%. All tests were performed using an initial fiber orientation state perpendicular to the flow

direction and lying in the plane with a normal perpendicular to the gap-wise direction. This seemed to result in orientation dynamics that were significantly slower than previous work in startup of shear, which used an initial orientation state that was random in the plane with a normal perpendicular to the gap-wise direction. With all of this in mind, it would appear that the initial orientation state and fiber concentration interact to change the fiber orientation dynamics in a way that the orientation models cannot reflect without using different parameters for every combination of flow type, initial orientation state, and fiber concentration. Therefore, it seems that the models are missing some fundamental behavior, perhaps in how the fibers interact with each other.

6.2 Further Work Investigating NLSF

The non-lubricated squeeze flow test will be a useful method for investigating how the interaction between shear and extensional flow influences fiber orientation. Unlike injection molding, the experiments are isothermal, the deformation rates can be controlled to a much greater degree, and the initial orientation state is much easier to control. This will allow us to minimize confounding effects like phase changes, viscosity temperature-dependence, assuming initial conditions, and modeling an advancing front. Having said this, more needs to be done to establish NLSF as a parameter fitting test.

Most importantly, we need data on how the orientation profile changes with Hencky strain. This will accomplish two goals: establishing the transient behavior of the orientation profile and verifying the existence of a steady state in the orientation profile. The first point is important because α should be obtained by fitting to data from several time points. This parameter was developed to tune the evolution of orientation, so data at multiple time points will improve our confidence in the fitted value. The second point will improve our confidence in the fitted value of C_I, which was introduced to adjust the steady state orientation.

Absolute sample dimensions play a crucial role in determining the limits of the NLSF experiments. A sample cannot be too thin. On one hand, a sample can be ripped apart if too much void space is in the sample. Based on my experience, squeeze flow will actually make these larger rather than close them, and as their size approaches the sample dimensions the sample inevitably breaks up. This was the primary reason samples were limited to 1 Hencky strain in this work. Recall that a constant Hencky strain rate requires an exponential displacement. This poses a significant problem, as even "small" Hencky strains actually require large linear displacements. Figure 6.1 shows

the sample thickness as a function of Hencky strain during the course of NLSF for several initial sample thicknesses. Ending a test with a sample roughly 1 mm thick might be acceptable if void content in the sample is minimal. For the sake of this discussion, we'll treat 1 mm as the limiting case.

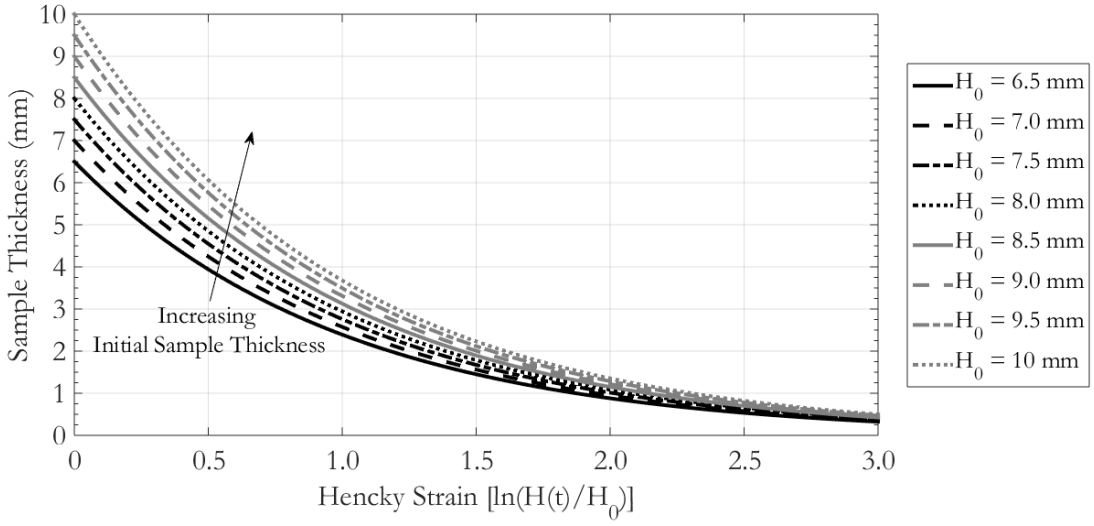

Fig. 6.1: Sample thickness as a function of the Hencky strain applied during NLSF. Several initial thickness values are used.

Another point to consider is that thin samples limit the spatial resolution we can achieve with the orientation analysis. The through-thickness orientation profiles are obtained by breaking each micrograph into some number of bins. These bins must be large enough to capture a statistically significant number of fibers because the orientation tensors are calculated from a statistical distribution. Void spaces exacerbate this problem by significantly reducing the number of fibers in a bin.

Yet another point to consider is the matter of a steady state, which is necessary to fit C_I. While a steady state through-thickness profile might not be achievable due to the dimensional constraints mentioned above, we could consider the limiting cases of planar extension and shear, both of which are present in NLSF. Chapter 4 suggests that a steady orientation state might be achieved in the neighborhood of 2 Hencky strain units during planar extension. Using the velocity field derived in Ch. 4, we can calculate the amount of extensional strain accrued through the thickness of the NLSF sample, and this is plotted in Fig. 6.2. Bear in mind that in this specific figure Hencky strain refers to the bulk deformation of the sample ($ln\, H/H_0$) and extensional strain is the flow-direction velocity derivative integrated through time. A total extensional strain of 3 is attained at the center of the sample (z/H = 0.5) after 2 Hencky strain, which ought to be enough to establish a steady orientation state at the sample center. This is independent of the initial sample thickness. Furthermore, Figs. 5.14 and

5.15 from Ch. 5 suggest that a steady state is achieved after 2-3 Hencky strain units in the shear-dominated regions near the top and bottom platens.

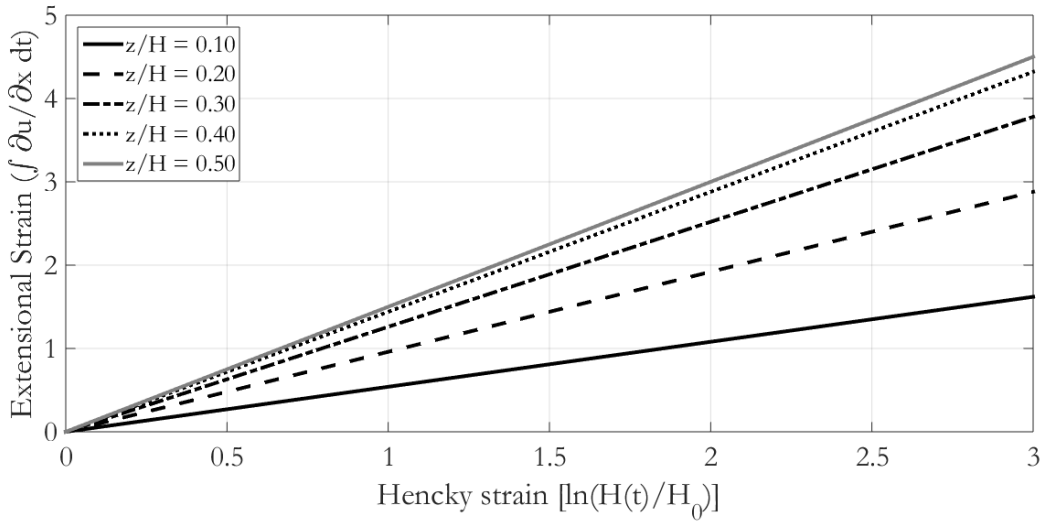

Fig. 6.2: Extensional strain as calculated by the velocity profile in Ch. 4 at several normalized thickness locations. These are plotted against the bulk Hencky strain applied to the sample during NLSF.

Considering the above points, taking the NLSF test out to 2 Hencky strain units appears promising, so long as the samples start thick enough. An initial sample thickness of 8 to 8.5 mm should work. This would balance sample preparation time (thicker samples would take considerably longer to make) with ensuring the samples end the test thicker than 1 mm.

6.2 Variable α

Chapter 3 strongly suggests that a single value of α cannot accurately capture the orientation dynamics in a mixed shear/extensional flow, and this is further supported by Chps. 4 and 5. Making α a function of the local flow field could help rectify this. In short, the value of α could be tuned to a shear-like value (say 0.20) and an extension-like value (say 1.0) based on the value of some metric that quantifies a flow's "type". This metric would have to be invariant to ensure that the results are independent of the coordinate system. Some function dependent on the eigenvalues/eigenvectors or the invariant quantities of the kinematic tensors (namely the rate-of-strain tensor and the vorticity tensor) would be a good place to start. Non-lubricated squeeze flow would be a useful test for this technique due to its combination of shear and extensional flow.

6.3 Stress Model

Directly measuring fiber orientation is labor-intensive. The time needed to cut samples, mount them into epoxy pucks, grind and polish them for microscopy, take the micrographs, and prepare the micrographs for the image analysis, takes much more time than running the actual experiments. Coupling fiber orientation with stress growth through a stress model would provide an alternative, and much faster, method for obtaining model parameters by allowing us to fit to stress-growth data. That being said, there are problems with existing suspension stress models.

Cieslinski et al.[1] demonstrated that the commonly-used Lipscomb[2] stress tensor had trouble predicting the stress growth during startup of shear when a repeatable initial orientation state was used. If values of $\boldsymbol{A_4}$ calculated by the $\boldsymbol{A}$ values predicted by the orientation models are used with the stress model, then the stress model could predict the experimentally observed stress overshoot. However, the stress model was not able to reproduce the stress overshoot in startup of shear when measured values of $\boldsymbol{A_4}$ were used to calculate the stress. It would then seem that the stress model can predict the correct behavior, but using an incorrect mechanism. Cieslinski[3] also looked at a stress model that incorporates direct interactions between fibers, and the results suggested that including these interactions would not improve the model's accuracy. In spite of this tension between the theoretical treatment of suspension stress and the experimental data, it remains a fact that the overshoot in the stress-growth was not observed with the unfilled resin. Although the overshoot seems to be driven by some interaction between the fibers and matrix, the precise mechanism for the stress overshoot during startup of shear remains unclear.

As Ch. 4 demonstrates, the Lipscomb model does not perform well in NLSF either. Model parameters obtained from fitting to startup-of-shear stress-growth data over-predict the stress growth during NLSF. The predicted stress can be tuned to the same magnitude as the experimental data, but the qualitative transient behavior (rapid increase in the beginning, followed by a slow increase for the duration of the test) is not predicted very well.

A common feature in the stress growth during both planar extension and NLSF is that stress grows from an initially unstressed state. Bird et al.[4] note this is the case even with NLSF of unfilled resins and attributed this to the elastic nature of the polymers. The Lipscomb model is a purely viscous stress model, and, therefore, it is fundamentally incapable of capturing the rapid increase from the unstressed state, or any other elastic behavior.

One potential avenue for modifying the stress tensor would be to attempt a viscoelastic model. Accounting for elasticity would likely help in fitting to the small-strain stress-growth data in NLSF.

Elastic effects might also be important in the stress growth during startup of shear as well. Fiber fillers induce elasticity in otherwise Newtonian matrices[5], so this induced elasticity might contribute to the overshoot in stress growth. Ramazani et al.[6] attempted to use the FENE model within Grmela's[7] GENERIC framework to predict viscosity and the first normal stress coefficient during the startup of shear of two viscoelastic matrices reinforced with glass fibers. The model made qualitative predictions for the data, and earlier theoretical work by Ait-Kadi et al.[8] suggests matrix elasticity contributes to the predicted overshoot. A continuum-level viscoelastic model such as Gieskus's[9] model or the FENE[10] model, which are non-linear in stress, might also be useful.

References

1. M. J. Cieslinski, P. Wapperom and D. G. Baird, "Fiber orientation evolution in simple shear flow from a repeatable initial fiber orientation," *J. Non-Newton. Fluid Mech.* **237**, 65 (2016).
2. G. G. Lipscomb, M. M. Denn, D. U. Hur and D. V. Boger, "The flow of fiber suspensions in complex geometries," *J. Non-Newton. Fluid Mech.* **26** (3), 297 (1988).
3. M. J. Cieslinski. *Using a sliding plate rheometer to obtain material parameters for simulating long fiber orientation in injection molded composites*, PhD Thesis. Virginia Tech, 2015.
4. R. B. Bird, R. C. Armstrong and O. Hassager, *Dynamics of polymeric liquids*. 2 ed.; Wiley: New York, NY, 1987; Vol. 1.
5. M. Sepehr, P. J. Carreau, M. Moan and G. Ausias, "Rheological properties of short fiber model suspensions," *J. Rheol.* **48** (5), 1023 (2004).
6. A. S. A. Ramazani, A. Ait-Kadi and M. Grmela, "Rheology of fiber suspensions in viscoelastic media: Experiments and model predictions," *J. Rheol.* **45** (4), 945 (2001).
7. M. Grmela, "Why generic?," *J. Non-Newton. Fluid Mech.* **165** (17–18), 980 (2010).
8. A. Ait-Kadi and M. Grmela, "Modelling the rheological behaviour of fibre suspensions in viscoelastic media," *J. Non-Newton. Fluid Mech.* **53**, 65 (1994).
9. H. Giesekus, "A simple constitutive equation for polymer fluids based on the concept of deformation-dependent tensorial mobility," *J. Non-Newton. Fluid Mech.* **11** (1-2), 69 (1982).
10. R. B. Bird, C. F. Curtiss, R. C. Armstrong and O. Hassager, *Dynamics of polymeric liquids*. 2 ed.; John Wiley & Sons: USA, 1987; Vol. 2.

Appendix A

FLD data for the material from Ch. 3.

Bin mm	Normalized Frequency -		Bin mm	Normalized Frequency -		Bin mm	Normalized Frequency -
0.125	0.022234		4.875	0.00455		9.625	0.00031
0.25	0.110858		5	0.002896		9.75	0.000827
0.375	0.09607		5.125	0.003413		9.875	0.000207
0.5	0.07818		5.25	0.001861		10	0.000103
0.625	0.064219		5.375	0.003826		10.125	0.000207
0.75	0.056774		5.5	0.002999		10.25	0.00031
0.875	0.05274		5.625	0.002482		10.375	0.000103
1	0.049328		5.75	0.001861		10.5	0.000207
1.125	0.039297		5.875	0.002792		10.625	0.00062
1.25	0.034747		6	0.002378		10.75	0.000517
1.375	0.036608		6.125	0.002172		10.875	0.000207
1.5	0.032782		6.25	0.001448		11	0.00031
1.625	0.028749		6.375	0.002068		11.125	0.00031
1.75	0.022441		6.5	0.001861		11.25	0.00031
1.875	0.018407		6.625	0.001241		11.375	0
2	0.015408		6.75	0.001241		11.5	0.000207
2.125	0.016339		6.875	0.001655		11.625	0.000414
2.25	0.015408		7	0.001655		11.75	0.000103
2.375	0.01334		7.125	0.001551		11.875	0.00031
2.5	0.010651		7.25	0.001448		12	0
2.625	0.011479		7.375	0.000827		12.125	0.000207
2.75	0.010651		7.5	0.001034		12.25	0.000103
2.875	0.00848		7.625	0.000724		12.375	0
3	0.010134		7.75	0.001034		12.5	0
3.125	0.008893		7.875	0.001034		12.625	0.000207
3.25	0.008376		8	0.001241		12.75	0.000103
3.375	0.006929		8.125	0.000724		12.875	0.00031
3.5	0.007032		8.25	0.000724		13	0
3.625	0.005481		8.375	0.000414		13.125	0
3.75	0.006412		8.5	0.000827		13.25	0.000207
3.875	0.005584		8.625	0.00062		13.375	0
4	0.005688		8.75	0.000207		13.5	0
4.125	0.00455		8.875	0.000517		13.625	0.000103
4.25	0.005377		9	0.000724		13.75	0
4.375	0.003619		9.125	0.00062		13.875	0
4.5	0.004964		9.25	0.00031		14	0

4.625	0.003619		9.375	0.00062			
4.75	0.002792		9.5	0.000827			

Stress growth data from startup of shear for the material in Ch. 3. Note that this was recorded from the RMS 800 using a cone-and-donut sample.

Time s	Strain -	Stress Pa	SD Pa
0	0	0	0
1.25	0.125	176.3373	5.451953
3.75	0.375	188.4805	6.332756
6.25	0.625	191.9498	6.805843
8.75	0.875	194.4453	7.236473
11.25	1.125	196.517	7.128647
13.75	1.375	198.2395	7.588256
16.25	1.625	199.4983	7.776951
18.75	1.875	201.7944	8.179277
21.25	2.125	202.8416	7.962277
23.75	2.375	204.3289	8.356516
26.25	2.625	205.9524	9.110624
28.75	2.875	206.9606	9.199581
31.25	3.125	207.8043	8.234538
33.75	3.375	208.8792	7.395517
36.25	3.625	209.5039	7.218278
38.75	3.875	210.692	7.675864
41.25	4.125	211.7797	7.953516
43.75	4.375	212.9887	9.175994
46.25	4.625	213.9565	9.724558
48.75	4.875	215.4903	9.901124
51.25	5.125	216.3098	9.849906
53.75	5.375	217.2344	10.12486
56.25	5.625	216.7512	9.543276
58.75	5.875	217.4642	8.310016
61.25	6.125	218.8133	9.126798
63.75	6.375	219.1894	8.319451
66.25	6.625	219.742	8.79119
68.75	6.875	220.36	8.812081
71.25	7.125	220.5082	9.589776
73.75	7.375	220.025	9.443537
76.25	7.625	220.2933	8.943494
78.75	7.875	220.2077	8.992689

81.25	8.125	220.7973	8.037755
83.75	8.375	221.2219	8.54319
86.25	8.625	222.4902	8.226451
88.75	8.875	223.2807	7.58556
91.25	9.125	223.4795	7.814016
93.75	9.375	223.6365	7.811995
96.25	9.625	224.4634	7.179191
98.75	9.875	224.6299	6.73643
101.25	10.125	225.6178	6.615126
103.75	10.375	225.8719	6.673756
106.25	10.625	226.287	6.189887
108.75	10.875	226.1078	6.373191
111.25	11.125	226.2904	5.592127
113.75	11.375	226.1159	5.665583
116.25	11.625	225.7014	5.827996
118.75	11.875	226.2641	5.329975
121.25	12.125	225.7014	5.263257
123.75	12.375	225.7398	4.809714
126.25	12.625	225.1124	4.775345
128.75	12.875	224.4601	5.127127
131.25	13.125	223.9209	4.868344
133.75	13.375	223.183	5.073888
136.25	13.625	223.7093	4.791518
138.75	13.875	223.6851	4.49904
141.25	14.125	223.8704	4.249019
143.75	14.375	223.9843	3.366867
146.25	14.625	224.1689	2.686216
148.75	14.875	223.768	2.17202
151.25	15.125	224.4351	3.452454
153.75	15.375	224.6932	3.843997
156.25	15.625	223.5065	3.092585
158.75	15.875	222.6203	2.738781
161.25	16.125	221.8298	3.045411
163.75	16.375	221.9066	3.43628
166.25	16.625	222.6365	2.799433
168.75	16.875	223.1466	1.347151
171.25	17.125	223.2949	1.779803
173.75	17.375	222.0488	1.83439
176.25	17.625	222.1303	1.814847
178.75	17.875	221.9632	2.180107
181.25	18.125	222.6789	2.444281
183.75	18.375	222.0144	2.763715
186.25	18.625	220.7178	2.161238

188.75	18.875	219.7851	2.76102
191.25	19.125	219.9192	3.310259
193.75	19.375	220.1713	3.675519
196.25	19.625	220.3337	3.541411
198.75	19.875	220.606	3.736845
201.25	20.125	220.767	3.682258
203.75	20.375	220.8277	3.299476
206.25	20.625	219.5857	3.277237
208.75	20.875	219.403	3.078433
211.25	21.125	219.0553	2.946346
213.75	21.375	219.2366	2.92815
216.25	21.625	218.9764	2.952411
218.75	21.875	219.2035	3.542084
221.25	22.125	219.403	3.790084
223.75	22.375	219.4927	3.420106
226.25	22.625	218.6469	3.00565
228.75	22.875	217.4803	3.285324
231.25	23.125	216.2788	3.250954
233.75	23.375	214.879	3.744932
236.25	23.625	213.7287	3.707867
238.75	23.875	213.3466	4.309671
241.25	24.125	212.8587	4.399975
243.75	24.375	212.2063	4.99841
246.25	24.625	211.6005	5.559779
248.75	24.875	211.0539	5.948626
251.25	25.125	210.2755	6.779561
253.75	25.375	209.0214	7.005321
256.25	25.625	208.5119	7.230408
258.75	25.875	207.9917	7.254669
261.25	26.125	207.865	7.482451
263.75	26.375	206.8676	7.529625
266.25	26.625	206.2759	7.454147
268.75	26.875	205.7475	7.742582
271.25	27.125	205.4631	7.270843
273.75	27.375	205.2616	7.220299
276.25	27.625	204.8431	7.220973
278.75	27.875	204.2885	7.925212
281.25	28.125	204.1295	7.868603
283.75	28.375	203.7885	8.328212
286.25	28.625	203.3693	8.059994
288.75	28.875	202.9003	9.069515
291.25	29.125	202.1172	9.417254
293.75	29.375	201.5774	9.72658

296.25	29.625	201.0268	9.77308
298.75	29.875	200.6278	10.35804
301.25	30.125	199.6527	10.74823
303.75	30.375	198.974	10.86212
306.25	30.625	198.0407	11.04745
308.75	30.875	198.2415	11.19975
311.25	31.125	197.8904	10.63299
313.75	31.375	198.5407	10.84797
316.25	31.625	198.6297	11.09193
318.75	31.875	197.9531	10.68354
321.25	32.125	197.6431	10.56358
323.75	32.375	197.1403	10.46384
326.25	32.625	196.5918	10.54875
328.75	32.875	196.3909	10.61614
331.25	33.125	196.6834	10.83988
333.75	33.375	196.2743	10.51708
336.25	33.625	196.0546	10.54134
338.75	33.875	195.6773	10.21651
341.25	34.125	195.1348	9.710406
343.75	34.375	194.9804	9.084342
346.25	34.625	194.3806	9.549341
348.75	34.875	193.4904	9.574276
351.25	35.125	193.5005	9.782515
353.75	35.375	193.1002	9.484646
356.25	35.625	192.6716	9.092428
358.75	35.875	192.2625	9.374798
361.25	36.125	192.3683	9.948297
363.75	36.375	192.1001	10.29738
366.25	36.625	192.0698	10.45036
368.75	36.875	191.4255	10.34254
371.25	37.125	190.968	10.35264
373.75	37.375	190.5717	11.04543
376.25	37.625	190.0514	11.41473
378.75	37.875	189.6289	11.53671
381.25	38.125	189.0722	11.14719
383.75	38.375	188.7488	11.23884
386.25	38.625	188.2575	11.19773
388.75	38.875	188.0472	11.30556
391.25	39.125	187.2271	11.2321
393.75	39.375	186.5842	11.40327
396.25	39.625	185.6959	11.03127
398.75	39.875	185.0544	11.33993
401.25	40.125	183.3858	11.76449

403.75	40.375	182.2839	11.84604
406.25	40.625	181.5932	11.90736
408.75	40.875	181.0951	12.31912
411.25	41.125	179.7049	12.57993
413.75	41.375	179.1239	12.94519
416.25	41.625	178.4082	12.96136
418.75	41.875	178.4507	12.37034
421.25	42.125	178.3577	12.06169
423.75	42.375	178.0747	11.9296
426.25	42.625	177.6784	11.56569
428.75	42.875	177.5423	11.24625
431.25	43.125	177.4432	11.2321
433.75	43.375	176.7619	10.99825
436.25	43.625	176.3858	10.49282
438.75	43.875	175.4774	10.39712
441.25	44.125	175.2786	10.29941
443.75	44.375	175.1768	9.596515
446.25	44.625	174.9059	9.277081
448.75	44.875	174.6546	9.574276
451.25	45.125	174.106	9.110624
453.75	45.375	173.7401	8.992689
456.25	45.625	173.0513	8.917211
458.75	45.875	172.6685	8.884863
461.25	46.125	172.3194	8.437385
463.75	46.375	172.1995	8.317429
466.25	46.625	171.5768	7.464256
468.75	46.875	171.2722	5.923692
471.25	47.125	170.7216	5.092757
473.75	47.375	169.8314	4.98291
476.25	47.625	169.6737	3.726737
478.75	47.875	169.2828	3.401911
481.25	48.125	168.3926	2.596585
483.75	48.375	168.3009	2.236716
486.25	48.625	167.7604	1.395673
488.75	48.875	167.7793	1.247412
491.25	49.125	166.9942	0.649652
493.75	49.375	165.8708	0.30663
496.25	49.625	164.6328	0.214304
498.75	49.875	163.6516	0.266869
501.25	50.125	163.3672	0.249348
503.75	50.375	162.4345	0.134783
506.25	50.625	162.1292	0.442761
508.75	50.875	161.237	0.135456

511.25	51.125	160.8279	0.141522
513.75	51.375	161.0233	0.532391
516.25	51.625	161.0725	0.515543
518.75	51.875	160.5637	0.625391
521.25	52.125	160.6965	1.123412
523.75	52.375	159.6007	0.475108
526.25	52.625	159.259	0.165782
528.75	52.875	158.7105	0.033696
531.25	53.125	158.7509	0.190043
533.75	53.375	158.9423	0.19813
536.25	53.625	159.1411	0.049196
538.75	53.875	159.007	0.199478
541.25	54.125	158.9726	0.132761
543.75	54.375	158.4362	0.291804
546.25	54.625	158.3243	0.732543
548.75	54.875	158.168	1.104543
551.25	55.125	158.4685	1.405108
553.75	55.375	158.4766	1.665238
556.25	55.625	157.92	1.98602
558.75	55.875	157.6699	1.638955
561.25	56.125	156.7204	2.169325
563.75	56.375	156.8026	2.421368
566.25	56.625	156.2965	3.744258
568.75	56.875	155.7068	4.333932
571.25	57.125	154.981	4.291475
573.75	57.375	154.5315	4.926975
576.25	57.625	154.2067	5.366366
578.75	57.875	153.9183	5.47554
581.25	58.125	153.3636	5.481605
583.75	58.375	153.2457	5.36367
586.25	58.625	152.9687	5.408822
588.75	58.875	153.1015	5.707366
591.25	59.125	152.904	5.753866
593.75	59.375	152.5226	5.408822
596.25	59.625	152.402	5.23967
598.75	59.875	151.8635	4.76591
601.25	60.125	151.2462	4.668866
603.75	60.375	151.4733	3.925541
606.25	60.625	150.8574	4.293497
608.75	60.875	150.325	5.126453
611.25	61.125	149.8249	6.024105
613.75	61.375	149.0425	6.306474
616.25	61.625	147.9818	6.721604

618.75	61.875	147.3699	7.045082
621.25	62.125	147.0289	7.138082
623.75	62.375	146.6622	6.869865
626.25	62.625	146.7889	7.162343
628.75	62.875	146.5302	7.001952
631.25	63.125	146.5814	6.589517
633.75	63.375	146.4736	6.514039
636.25	63.625	147.1144	6.455409
638.75	63.875	147.1306	6.487756
641.25	64.125	146.7964	6.487756
643.75	64.375	146.7478	6.187191
646.25	64.625	146.4715	6.098235
648.75	64.875	145.9957	5.471496
651.25	65.125	146.0652	5.240344
653.75	65.375	146.0166	5.341431
656.25	65.625	145.557	5.716126
658.75	65.875	145.5752	5.347496
661.25	66.125	145.9068	4.947192
663.75	66.375	146.6811	4.59204
666.25	66.625	146.7782	4.441084
668.75	66.875	146.923	4.447149
671.25	67.125	147.1946	3.760432
673.75	67.375	147.1643	4.209932
676.25	67.625	146.4372	3.852084
678.75	67.875	147.1872	2.902541
681.25	68.125	147.7863	2.136303
683.75	68.375	148.1442	1.89302
686.25	68.625	147.9939	2.095868
688.75	68.875	148.4515	1.305369
691.25	69.125	148.2028	1.403086
693.75	69.375	148.4265	1.163173
696.25	69.625	149.209	0.681326
698.75	69.875	150.2663	0.490608
701.25	70.125	150.3149	0.144217
703.75	70.375	149.5082	0.214978
706.25	70.625	149.7232	0.117261
708.75	70.875	149.8761	0.167804
711.25	71.125	150.1828	0.458261
713.75	71.375	150.6296	0.256761
716.25	71.625	150.7475	0.673913
718.75	71.875	150.8493	1.340412
721.25	72.125	150.8964	0.940108
723.75	72.375	151.0299	1.956368

726.25	72.625	151.7476	2.519085
728.75	72.875	151.3473	2.453042
731.25	73.125	151.6135	2.455064
733.75	73.375	151.2907	2.529868
736.25	73.625	151.1802	2.086433
738.75	73.875	151.3635	1.354564
741.25	74.125	151.8554	0.882825
743.75	74.375	151.5218	1.448238
746.25	74.625	151.4875	1.580999
748.75	74.875	151.2826	1.33839
751.25	75.125	149.959	0.649652
753.75	75.375	150.5386	0.04987
756.25	75.625	150.7886	0.549239
758.75	75.875	150.3802	0.140848
761.25	76.125	150.325	0.049196
763.75	76.375	149.9085	0.383456
766.25	76.625	150.0244	0.450848
768.75	76.875	150.1915	1.015586
771.25	77.125	150.5487	1.072195
773.75	77.375	151.0629	1.306043
776.25	77.625	151.0137	1.171934
778.75	77.875	151.2112	1.373434
781.25	78.125	151.0305	2.338477
783.75	78.375	151.3635	2.322303
786.25	78.625	151.5629	2.769781
788.75	78.875	150.9571	2.579063
791.25	79.125	151.2988	3.517824
793.75	79.375	150.9975	3.456498
796.25	79.625	151.7537	3.627671
798.75	79.875	152.2699	3.412019
801.25	80.125	152.063	3.118867
803.75	80.375	151.6721	3.879041
806.25	80.625	151.9875	4.291475
808.75	80.875	151.7564	4.641236
811.25	81.125	151.937	4.692453
813.75	81.375	151.4551	4.043475
816.25	81.625	151.1808	4.200497
818.75	81.875	150.7738	4.208584
821.25	82.125	150.325	4.990323
823.75	82.375	150.9632	4.418171
826.25	82.625	151.197	4.70054
828.75	82.875	150.6323	4.801627
831.25	83.125	150.8816	3.804236

833.75	83.375	150.7414	4.509149
836.25	83.625	151.0811	4.600801
838.75	83.875	150.4732	5.04154
841.25	84.125	150.8169	4.718062
843.75	84.375	150.6498	4.417497
846.25	84.625	150.1666	4.401997
848.75	84.875	150.3391	4.20791
851.25	85.125	150.6161	4.484888
853.75	85.375	151.0056	4.44041
856.25	85.625	151.0811	4.665497
858.75	85.875	150.8068	4.826562
861.25	86.125	150.7637	5.031431
863.75	86.375	150.8068	4.875084
866.25	86.625	150.7724	4.689758
868.75	86.875	150.8715	4.558345
871.25	87.125	150.701	5.232931
873.75	87.375	151.1882	5.675692
876.25	87.625	151.3965	6.297713
878.75	87.875	150.3984	5.59617
881.25	88.125	150.449	5.932452
883.75	88.375	149.8579	6.055778
886.25	88.625	149.8741	5.49104
888.75	88.875	149.8923	5.090062
891.25	89.125	149.9429	5.00717
893.75	89.375	149.2379	4.899344
896.25	89.625	149.2359	4.352801
898.75	89.875	149.0991	4.850823
901.25	90.125	149.1335	5.401409
903.75	90.375	148.9751	5.259214
906.25	90.625	149.4428	5.291562
908.75	90.875	149.5082	5.608974
911.25	91.125	149.9759	5.441844
913.75	91.375	149.9408	5.573931
916.25	91.625	149.9408	5.061757
918.75	91.875	150.0466	5.034127
921.25	92.125	150.61	5.039518
923.75	92.375	150.7738	5.28954
926.25	92.625	151.5872	5.655474
928.75	92.875	151.8446	5.799692
931.25	93.125	151.6398	5.058388
933.75	93.375	151.2725	5.356931
936.25	93.625	150.608	5.757235
938.75	93.875	150.5831	6.163604

941.25	94.125	151.0541	6.586148
943.75	94.375	151.0609	6.746539
946.25	94.625	150.0911	6.655561
948.75	94.875	149.3559	6.870539
951.25	95.125	148.8518	6.862452
953.75	95.375	148.3457	7.072039
956.25	95.625	147.5471	7.32206
958.75	95.875	147.1124	7.472343
961.25	96.125	146.6569	7.944081
963.75	96.375	146.4958	8.686059
966.25	96.625	146.3051	9.157124
968.75	96.875	146.0631	9.550015
971.25	97.125	145.9479	9.933471
973.75	97.375	145.6406	9.724558
976.25	97.625	146.2727	9.840471
978.75	97.875	146.3212	9.392993
981.25	98.125	145.8455	10.11678
983.75	98.375	145.1851	10.83375
986.25	98.625	145.539	11.40314
988.75	98.875	144.8496	12.01438
991.25	99.125	145.3597	12.51644
993.75	99.375	145.2093	12.93103
996.25	99.625	145.0142	12.0937

Stress growth from planar extension for the material in Ch. 3

Time s	Hencky Strain -	Closure Stress Pa	Closure Stress Std Dev Pa
0.500165	0	169.2701	136.6242478
1.00017	0.059091	351.0621	290.405217
1.50017	0.083803	677.2119	562.5357741
2.00017	0.118572	1214.782	980.8377551
2.50017	0.134173	1845.321	1282.889959
3.00017	0.162486	2490.848	1414.25146
3.50017	0.187216	3060.017	1448.517458
4.00017	0.212226	3607.984	1326.601067
4.50017	0.232729	4234.579	1079.930616

5.00017	0.257466	4786.535	902.4695813
5.50017	0.2819	5232.864	782.1174645
6.00017	0.310767	5572.408	701.919349
6.50017	0.335379	5853.448	633.1818008
7.00017	0.366463	6111.275	598.7742431
7.50017	0.385258	6399.386	613.0595526
8.00016	0.410105	6652.888	606.8412414
8.50016	0.435152	6836.826	559.2019965
9.00016	0.456183	7031.023	540.8120845
9.50016	0.481063	7313.574	487.2389418
10.0002	0.515466	7574.627	352.0262248
10.5002	0.534198	7779.45	290.4442592
11.0002	0.565067	8089.448	212.0107996
11.5002	0.584006	8279.985	311.2646131
12.0002	0.604851	8387.131	366.9191447
12.5002	0.630083	8567.055	397.1509966
13.0002	0.654617	8794.812	395.3346292
13.5002	0.679215	9010.992	383.8675979
14.0002	0.70813	9168.745	284.1354528
14.5002	0.729723	9288.631	318.8015682
15.0002	0.753877	9492.905	381.5793628
15.5002	0.78261	9655.505	351.9680493
16.0002	0.813775	9792.69	278.2597305
16.5002	0.828123	9912.647	290.6963529
17.0002	0.85745	10097.84	179.8268375
17.5002	0.877828	10323.78	96.93325866
18.0002	0.90312	10421.82	159.1163707
18.5002	0.928358	10510.23	218.642803
19.0002	0.957899	10644.56	432.1920206
19.5002	0.981578	10710.92	458.2610945
20.0002	1.003532	10724.68	410.466715
20.5002	1.03108	10809.58	385.0957467
21.0002	1.054966	11027.22	355.5749283
21.5002	1.092737	11157.27	391.411017
22.0002	1.105369	11313.17	496.6439759
22.5002	1.129384	11450.43	466.0630712
23.0002	1.166974	11514.09	439.4057787
23.5002	1.178304	11788.44	425.0752216
24.0002	1.20416	12056.78	532.984252
24.5002	1.228782	12039.62	334.7675024
25.0002	1.265399	12140.11	219.8580239
25.5002	1.277405	12263.23	257.3876651
26.0002	1.314835	12464.54	166.0133957

26.5002	1.326396	12769.11	75.80263565
27.0002	1.350468	12893.52	27.56224426
27.5002	1.3768	12957.23	2.585576385
28.0002	1.400423	12984.83	37.16766053
28.5002	1.425201	13058.35	173.5955985
29.0002	1.451806	13028.53	407.8035713
29.5002	1.48904	13032.91	480.7297532
30.0002	1.513592	13137	456.1473858
30.5002	1.525776	13268.18	472.3460218
31.0002	1.549936	13406.04	617.9980035
31.5002	1.588338	13559.99	716.7864132
32.0002	1.600777	13770.97	734.2390538
32.5002	1.625418	13763.67	788.8593549
33.0002	1.64922	13860.89	798.813824
33.5002	1.675849	13956.68	829.7114618
34.0002	1.699361	14128.69	853.6926828
34.5002	1.722654	14310.91	830.4871347
35.0002	1.747308	14495.97	865.8448918
35.5002	1.785048	14687.04	881.2290713
36.0002	1.795977	14910.5	874.1833756
36.5002	1.820797	15117.02	885.1074358
37.0002	1.846248	15319.73	912.7731032
37.5002	1.881529	15530.98	896.2254143
38.0002	1.89171	15786.95	810.9013936
38.5002	1.919057	16002.07	801.334761
39.0002	1.942269	16172.26	790.5399796
39.5002	1.966835	16312.01	819.3691563
40.0002	2.003708	16443.36	860.4798208
40.5002	2.027077	16620.47	832.8141535
41.0002	2.038862	16808.51	749.2353968
41.5002	2.061754	16863	802.3043521
42.0002	2.100423	16976.83	814.5212005
42.5002	2.112183	17121.69	853.3694857
43.0002	2.137194	17240.88	876.6396732
43.5002	2.165535	17349.93	886.400224
44.0002	2.184677	17444.11	884.7842388
44.5002	2.221248	17592.71	881.2290713
45.0002	2.245068	17750.76	869.7878958
45.5002	2.254517	17935.3	903.7235858
46.0002	2.291979	18089.86	875.8640003
46.5002	2.304692	18231.03	878.8374131
47.0002	2.339743	18404.97	861.9665272
47.5002	2.349546	18511.56	778.2584917

48.0002	2.385778	18690.16	791.8974072
48.5002	2.397278	18726.1	761.3876058
49.0002	2.443196	18819.25	789.2471914
49.5002	2.44465	18860.42	799.5248575
50.0002	2.471362	18994.16	803.9849768
50.5002	2.492681	19055.57	815.7493493
51.0002	2.519505	19137.34	778.9695253
51.5002	2.552277	19289.37	735.4025632
52.0002	2.576151	19392.79	676.192864
52.5002	2.599475	19497.51	657.8352716
53.0002	2.611631	19532.41	684.3374296
53.5002	2.648218	19527.82	704.0524495
54.0002	2.707629	19615.48	779.4220011
54.5002	2.684138	19667.7	762.2279182
55.0002	2.709524	19693.69	818.7227622
55.5002	2.732333	19741.78	782.2661351
56.0002	2.755452	19817.54	834.4947781
56.5002	2.762538	19833.63	861.0615755
57.0002	2.803592	19844.3	948.9065331
57.5002	2.827729	19822.52	993.5723652
58.0002	2.851491	19896.72	1059.504563
58.5002	2.875832	19892.2	1075.405858
59.0002	2.90975	19985.67	1112.508879
59.5002	2.922446	20045.78	1056.272592
60.0002	2.946461	20113.2	1071.979969
60.5002	2.979589	20147.52	1022.142984
61.0002	3.002489	20136.79	984.393569
61.5002	3.013567	20264.07	928.7390373
62.0002	3.035514	20269.63	912.0620696
62.5002	3.060346	20291.99	901.8490429
63.0002	3.094134	20272.21	894.9972655
63.5002	3.103778	20264.91	896.4839719
64.0002	3.128462	20392.38	855.8904227
64.5002	3.153115	20298.13	816.331104
65.0002	3.174357	20247.78	848.3276118
65.5002	3.198806	20388.63	843.2210984
66.0002	3.222812	20308.09	822.1486509
66.5002	3.257564	20278.8	908.3129839
67.0002	3.267456	20364.13	772.8287813
67.5002	3.301154	20315.2	786.984812
68.0002	3.312644	20277.9	810.5781966
68.5002	3.337211	20271.05	617.9527559
69.0002	3.370528	20297.74	807.023029

69.5002	3.393233	20247.71	666.4969525
70.0002	3.40457	20248.55	771.0188779
70.5002	3.428935	20223.21	580.8497348
71.0002	3.462375	20273.31	758.414193
71.5002	3.485916	20153.08	644.2609956
72.0002	3.508618	20187.99	716.5278556
72.5002	3.521351	20110.42	565.0130794
73.0002	3.543424	20108.74	719.2427108
73.5002	3.576975	20111.13	667.207986
74.0002	3.587568	19967.82	691.4477646
74.5002	3.622134	20132.72	588.7357428
75.0002	3.647654	19897.11	570.4427898
75.5002	3.658482	20052.83	615.1086219
76.0002	3.679385	19922.19	621.5079234
76.5002	3.713881	19818.44	556.5453168
77.0002	3.735399	19957.29	519.5715745
77.5002	3.761607	19693.04	526.5526307
78.0002	3.772529	19710.95	505.4155438
78.5002	3.806031	19763.82	631.3331137
79.0002	3.818091	19525.04	631.5916713
79.5002	3.853183	19576.89	494.556123
80.0002	3.865159	19586.71	577.4238461

Orientation data from startup of shear for the material in Ch. 3. 1 is the gap-wise direction, 2 is the flow direction, and 3 is the neutral direction. This data was collected using the sliding plate rheometer. Top entry in each block is the average value, and the bottom entry is the standard deviation.

Sample	A11	A12	A13	A22	A23	A33
0	0.101067	0.0185	-0.07673	0.502167	-0.1039	0.396767
	0.036034	0.090685	0.031168	0.037859	0.098239	0.04516
20	0.047367	-0.04483	0.002433	0.5615	0.038433	0.391133
	0.051221	0.061537	0.011095	0.094622	0.072217	0.108534
40	0.0657	-0.012	0.006167	0.698467	0.0201	0.2358
	0.048152	0.097494	0.006638	0.078552	0.003736	0.044772
60	0.0966	0.024167	-0.0101	0.701367	0.0104	0.202067
	0.064416	0.084461	0.0004	0.052271	0.058816	0.041189
80	0.0397	-0.04553	0.002333	0.741867	-0.09747	0.218433
	0.037174	0.080408	0.00872	0.09517	0.047737	0.059428

Orientation data from planar extension for the material in Ch. 3. 1 refers to the stretching direction, 2 to the neutral direction, and 3 to the gap-wise direction. Top entry in each block is the average, bottom entry is the standard deviation.

Hencky Strain	A11	A12	A22	A33	A13	A23
0	0.522	0.026	0.389	0.089	0.000	0.039
	0.031	0.010	0.053	0.002	0.029	0.005
1	0.789	-0.002	0.185	0.026	0.069	-0.027
	0.071	0.043	0.067	0.004	0.032	0.010
2	0.912	0.000	0.079	0.009	0.041	-0.012
	0.005	0.009	0.004	0.001	0.015	0.006
3.5	0.917	-0.005	0.078	0.005	0.051	-0.010
	0.046	0.028	0.042	0.005	0.079	0.007

Appendix B

FLD Data for the material in Chapter 4. This data corresponds to the material I actually made, not the material from Mark's previous work.

Bin Center mm	Normalized Adjusted Frequency -
0.0625	0.096362
0.1875	0.456263
0.3125	0.215096
0.4375	0.097089
0.5625	0.048982
0.6875	0.032329
0.8125	0.019141
0.9375	0.012012
1.0625	0.006432
1.1875	0.004243
1.3125	0.002812
1.4375	0.002487
1.5625	0.001769
1.6875	0.00125
1.8125	0.001055
1.9375	0.000507
2.0625	0.000358
2.1875	0.000229
2.3125	0.000218
2.4375	0.000527
2.5625	0.000101
2.6875	9.79E-05
2.8125	0.000377
2.9375	9.06E-05
3.0625	8.79E-05
3.1875	8.50E-05
3.3125	0
3.4375	0

FLD Data for the material in Chapter 4. This data corresponds to the material from Mark's previous work, not the material I made.

Bin Center mm	Normalized Adjusted Frequency -
0.0625	0.10922
0.1875	0.366441
0.3125	0.189699
0.4375	0.113043
0.5625	0.084271
0.6875	0.061963
0.8125	0.033802
0.9375	0.019273
1.0625	0.009712
1.1875	0.005705
1.3125	0.002401
1.4375	0.001352
1.5625	0.00101
1.6875	0.000407
1.8125	0.000774
1.9375	0.00023
2.0625	0.00022
2.1875	4.26E-05
2.3125	0.00016
2.4375	7.68E-05
2.5625	7.49E-05
2.6875	0
2.8125	3.40E-05
2.9375	0
3.0625	3.22E-05
3.1875	0
3.3125	0
3.4375	0
3.5625	2.88E-05
3.6875	2.74E-05
3.8125	0
3.9375	0
4.0625	0
4.1875	0

Orientation data for the initial state of the NLSF samples in Ch 4. 1 is the flow direction, 2 is the neutral direction, and 3 is the gap-wise direction. The top value of each block is the average value, the middle value is the standard deviation, and the bottom value is the 95% CI.

z/h	A11	A12	A22	A33	A13	A23
	0.429667	0.037167	0.476733	0.093567	-0.00313	0.007659
0.072	0.167461	0.128215	0.161379	0.007316	0.032776	0.009514
	0.189497	0.145086	0.182614	0.008279	0.037088	0.010766
	0.454567	-0.0277	0.438767	0.1067	-0.0158	0.0153
0.214	0.264122	0.14597	0.221369	0.045815	0.052603	0.020688
	0.298877	0.165178	0.250498	0.051844	0.059524	0.02341
	0.541367	0.050933	0.362433	0.0962	-0.00397	0.029967
0.357	0.312521	0.138291	0.294331	0.026057	0.081111	0.063464
	0.353644	0.156488	0.333061	0.029486	0.091784	0.071815
	0.4438	-0.0428	0.4433	0.112933	0.018469	0.011633
0.500	0.157084	0.233524	0.105687	0.051968	0.028051	0.061526
	0.177754	0.264252	0.119594	0.058806	0.031742	0.069622
	0.393567	-0.01827	0.514667	0.091767	0.015733	0.0412
0.642	0.066329	0.083365	0.076516	0.060048	0.047345	0.010914
	0.075057	0.094334	0.086585	0.067949	0.053575	0.01235
	0.439367	0.012833	0.468543	0.092133	0.026567	-0.02657
0.786	0.195659	0.150439	0.178027	0.020709	0.02502	0.038621
	0.221405	0.170234	0.201453	0.023434	0.028312	0.043703
	0.4655	-0.02923	0.414133	0.120367	0.004667	-0.0339
0.928	0.11285	0.161123	0.071244	0.045454	0.040796	0.062482
	0.127699	0.182324	0.080619	0.051435	0.046165	0.070703

Orientation data after 1 Hencky strain from the NLSF samples in Ch 4. 1 is the flow direction, 2 is the neutral direction, and 3 is the gap-wise direction. The top value of each block is the average value, the middle value is the standard deviation, and the bottom value is the 95% CI.

z/h	A11	A12	A22	A33	A13	A23
0.072	0.5818	0.0705	0.3589	0.0593	0.0166	0.0171
	0.1506	0.0805	0.1524	0.0094	0.0315	0.0280
	0.1704	0.0911	0.1725	0.0107	0.0356	0.0317
0.214	0.6346	0.0722	0.2276	0.1378	-0.0395	-0.0005
	0.0688	0.1172	0.0600	0.0653	0.0366	0.0067
	0.0779	0.1326	0.0679	0.0739	0.0414	0.0076
0.357	0.6937	0.0888	0.2559	0.0504	-0.0194	-0.0008
	0.0756	0.0422	0.0779	0.0054	0.0205	0.0165
	0.0856	0.0477	0.0881	0.0061	0.0232	0.0186
0.500	0.7621	0.0943	0.1884	0.0495	-0.0307	0.0053
	0.0561	0.0830	0.0525	0.0074	0.0188	0.0217
	0.0635	0.0939	0.0594	0.0084	0.0212	0.0245
0.642	0.7158	-0.0446	0.2082	0.0760	-0.0413	0.0164
	0.0630	0.1118	0.0227	0.0437	0.0147	0.0136
	0.0713	0.1265	0.0257	0.0494	0.0166	0.0154
0.786	0.6033	-0.0466	0.3135	0.0832	-0.0157	0.0013
	0.1059	0.1622	0.0569	0.0683	0.0364	0.0110
	0.1198	0.1836	0.0644	0.0773	0.0412	0.0125
0.928	0.5828	-0.0272	0.3720	0.0452	-0.0064	0.0230
	0.0371	0.1178	0.0421	0.0149	0.0368	0.0233
	0.0419	0.1333	0.0476	0.0168	0.0416	0.0264

Stress growth data for the NLSF samples in Ch. 4

Hencky Strain	Closure Stress Average	Closure Stress Std Dev	Closure Stress 95% CI
-	Pa	Pa	Pa
0.0000	-2.46E+02	4.93E+02	5.57E+02
0.0127	3.59E+03	5.17E+02	5.85E+02
0.0256	3.71E+03	5.10E+02	5.77E+02
0.0385	4.38E+03	1.37E+03	1.55E+03
0.0520	6.73E+03	1.59E+03	1.80E+03
0.0654	9.70E+03	3.32E+03	3.76E+03
0.0792	1.23E+04	1.89E+03	2.14E+03
0.0933	1.43E+04	2.35E+03	2.66E+03

0.1073	1.63E+04	2.31E+03	2.62E+03
0.1218	1.84E+04	1.45E+03	1.64E+03
0.1363	1.98E+04	1.22E+03	1.37E+03
0.1508	2.10E+04	1.31E+03	1.48E+03
0.1658	2.20E+04	1.47E+03	1.66E+03
0.1808	2.30E+04	1.64E+03	1.85E+03
0.1962	2.38E+04	1.82E+03	2.06E+03
0.2117	2.45E+04	2.06E+03	2.33E+03
0.2277	2.53E+04	2.30E+03	2.61E+03
0.2437	2.59E+04	2.53E+03	2.87E+03
0.2602	2.65E+04	2.78E+03	3.15E+03
0.2767	2.71E+04	3.00E+03	3.39E+03
0.2936	2.77E+04	3.26E+03	3.69E+03
0.3106	2.81E+04	3.49E+03	3.95E+03
0.3281	2.85E+04	3.68E+03	4.17E+03
0.3461	2.88E+04	3.85E+03	4.36E+03
0.3640	2.90E+04	4.07E+03	4.61E+03
0.3825	2.94E+04	4.07E+03	4.61E+03
0.4010	2.98E+04	4.01E+03	4.54E+03
0.4200	3.02E+04	4.14E+03	4.68E+03
0.4395	3.05E+04	4.46E+03	5.05E+03
0.4594	3.08E+04	4.72E+03	5.35E+03
0.4799	3.10E+04	4.98E+03	5.63E+03
0.5004	3.12E+04	5.21E+03	5.90E+03
0.5213	3.15E+04	5.36E+03	6.06E+03
0.5428	3.18E+04	5.44E+03	6.16E+03
0.5648	3.20E+04	5.57E+03	6.30E+03
0.5872	3.23E+04	5.74E+03	6.50E+03
0.6102	3.24E+04	5.98E+03	6.77E+03
0.6336	3.27E+04	6.28E+03	7.10E+03
0.6576	3.32E+04	6.54E+03	7.40E+03
0.6820	3.37E+04	6.71E+03	7.59E+03
0.7075	3.44E+04	6.85E+03	7.75E+03
0.7335	3.48E+04	7.07E+03	8.00E+03
0.7599	3.55E+04	7.22E+03	8.17E+03
0.7874	3.62E+04	7.40E+03	8.37E+03
0.8153	3.71E+04	7.74E+03	8.76E+03
0.8443	3.80E+04	8.12E+03	9.19E+03
0.8742	3.90E+04	8.56E+03	9.69E+03
0.9046	4.00E+04	8.96E+03	1.01E+04
0.9360	4.10E+04	9.46E+03	1.07E+04
0.9685	4.24E+04	9.93E+03	1.12E+04
0.9740	4.26E+04	1.00E+04	1.13E+04

Appendix C

Measured orientation data corresponding to the 30 wt% material in Ch. 5 during startup of shear. In each block, the top entry is the average data, the middle is the standard deviation, and the bottom is the 95% CI. 1 refers to the flow direction, 2 refers to the neutral direction, and 3 to the gap-wise direction

Strain	A11	A12	A22	A33	A13	A23
IC	0.1551	0.0263	0.8221	0.0228	0.0017	0.0088
	0.0067	0.0366	0.0117	0.0054	0.0039	0.0074
	0.007582	0.041416	0.01324	0.006111	0.004413	0.008374
25	0.285	-0.0315	0.6989	0.0161	-0.00081	0.0288
	0.0858	0.1459	0.0833	0.0041	0.0275	0.0251
	0.09709	0.165098	0.094261	0.00464	0.031119	0.028403
50	0.3701	-0.0171	0.6136	0.0163	-0.0061	0.0292
	0.0585	0.1089	0.0592	0.0065	0.0086	0.0198
	0.066198	0.12323	0.06699	0.007355	0.009732	0.022405
75	0.4859	0.0247	0.4989	0.0152	-0.0275	-0.0113
	0.0749	0.0083	0.0765	0.0016	0.0198	0.0074
	0.084756	0.009392	0.086566	0.001811	0.022405	0.008374
100	0.5425	0.0062	0.448	0.0094	-0.0105	0.0112
	0.0582	0.0102	0.0578	0.0013	0.0063	0.0021
	0.065858	0.011542	0.065406	0.001471	0.007129	0.002376

Measured orientation data corresponding to the 40 wt% material in Ch. 5 during startup of shear. In each block, the top entry is the average data, the middle is the standard deviation, and the bottom is the 95% CI. 1 refers to the flow direction, 2 refers to the neutral direction, and 3 to the gap-wise direction

Strain	A11	A12	A22	A33	A13	A23
IC	0.1551	0.0263	0.8221	0.0228	0.0017	0.0088
	0.0067	0.0366	0.0117	0.0054	0.0039	0.0074
	0.007582	0.041416	0.01324	0.006111	0.004413	0.008374
25	0.2363	-0.051	0.7436	0.0201	-0.0144	0.0091
	0.0228	0.0952	0.0212	0.0017	0.0127	0.0356
	0.0258	0.107727	0.02399	0.001924	0.014371	0.040284
50	0.2257	-0.0234	0.7577	0.0166	-0.0087	-0.0031
	0.000688	0.0549	0.0014	0.000715	0.0028	0.00198
	0.000954	0.076086	0.00194	0.000991	0.003881	0.002744
	0.246267	0.038767	0.741033	0.012667	0.001933	0.012833
	0.133325	0.107738	0.139187	0.0059	0.011418	0.014666
	0.184776	0.149314	0.192899	0.008177	0.015824	0.020326
100	0.3137	0.0671	0.6699	0.0164	-0.0063	0.0029
	0.0445	0.0731	0.0424	0.0035	0.0109	0.0184
	0.061673	0.10131	0.058762	0.004851	0.015106	0.025501

Measured orientation data corresponding to the 50 wt% material in Ch. 5 during startup of shear. In each block, the top entry is the average data, the middle is the standard deviation, and the bottom is the 95% CI. 1 refers to the flow direction, 2 refers to the neutral direction, and 3 to the gap-wise direction

Strain	A11	A12	A22	A33	A13	A23
IC	0.1551	0.0263	0.8221	0.0228	0.0017	0.0088
	0.0067	0.0366	0.0117	0.0054	0.0039	0.0074
	0.007582	0.041416	0.01324	0.006111	0.004413	0.008374
25	0.2128	0.0059	0.7704	0.0168	-0.0044	0.0182
	0.0632	0.0917	0.0638	0.0023	0.0058	0.0059
	0.071516	0.103766	0.072195	0.002603	0.006563	0.006676
50	0.24387	-0.0304	0.7357	0.0206	-0.0065	0.0093
	0.0536	0.7357	0.0582	0.0046	0.008	0.0135
	0.060653	0.832508	0.065858	0.005205	0.009053	0.015276
75	0.2665	0.0223	0.7147	0.0188	-0.009	-0.0076
	0.0901	0.05	0.0836	0.007	0.0127	0.0203
	0.101956	0.056579	0.094601	0.007921	0.014371	0.022971
100	0.3283	-0.0064	0.6443	0.0274	-0.0187	0.001
	0.0229	0.0972	0.0223	0.000568	0.0081	0.0092
	0.025913	0.10999	0.025234	0.000643	0.009166	0.010411

Measured orientation data for the gap-wise NLSF profile of the 30 wt% material at the initial state in Ch. 5. In each block, the top entry is the average data, the middle is the standard deviation, and the bottom is the 95% CI. 1 refers to the flow direction, 2 refers to the neutral direction, and 3 to the gap-wise direction

z/H	A11	A12	A22	A33	A13	A23
0.071	0.293	-0.015	0.688	0.020	-0.008	0.007
	0.097	0.076	0.082	0.016	0.023	0.003
	0.135	0.105	0.113	0.022	0.032	0.004
0.214	0.302	-0.035	0.681	0.017	0.005	-0.008
	0.173	0.029	0.160	0.011	0.022	0.012
	0.240	0.039	0.222	0.016	0.031	0.017
0.357	0.206	-0.009	0.775	0.019	0.004	-0.002
	0.008	0.012	0.012	0.004	0.014	0.018
	0.011	0.016	0.016	0.005	0.020	0.025
0.500	0.298	-0.015	0.685	0.017	-0.005	-0.008
	0.075	0.074	0.086	0.011	0.010	0.015
	0.104	0.102	0.119	0.016	0.014	0.021
0.643	0.397	0.054	0.590	0.013	-0.023	-0.008
	0.031	0.031	0.311	0.005	0.031	0.000
	0.042	0.044	0.430	0.007	0.042	0.001
0.786	0.238	0.039	0.740	0.022	-0.002	0.002
	0.032	0.048	0.040	0.008	0.023	0.008
	0.044	0.067	0.055	0.011	0.032	0.011
0.929	0.224	0.066	0.762	0.014	0.010	-0.004
	0.060	0.111	0.050	0.010	0.001	0.013
	0.083	0.153	0.069	0.014	0.001	0.017

Measured orientation data for the gap-wise NLSF profile of the 40 wt% material at the initial state in Ch. 5. In each block, the top entry is the average data, the middle is the standard deviation, and the bottom is the 95% CI. 1 refers to the flow direction, 2 refers to the neutral direction, and 3 to the gap-wise direction

z/H	A11	A12	A22	A33	A13	A23
0.071	0.241	0.121	0.727	0.032	0.001	0.016
	0.071	0.113	0.071	0.011	0.034	0.026
	0.081	0.128	0.080	0.013	0.038	0.029
0.214	0.356	0.120	0.618	0.026	-0.010	0.010
	0.146	0.050	0.146	0.007	0.039	0.018
	0.165	0.057	0.165	0.008	0.044	0.020
0.357	0.283	0.069	0.696	0.021	-0.011	-0.002
	0.153	0.057	0.151	0.010	0.029	0.019
	0.173	0.065	0.171	0.011	0.033	0.022
0.500	0.204	0.095	0.767	0.029	-0.006	0.012
	0.028	0.029	0.027	0.014	0.019	0.017
	0.032	0.033	0.030	0.015	0.021	0.020
0.643	0.321	0.164	0.659	0.020	-0.008	0.004
	0.166	0.080	0.153	0.013	0.004	0.011
	0.188	0.091	0.174	0.015	0.004	0.012
0.786	0.248	0.043	0.725	0.027	-0.012	-0.004
	0.027	0.066	0.034	0.008	0.004	0.003
	0.030	0.074	0.038	0.010	0.004	0.004
0.929	0.355	0.065	0.626	0.019	0.002	-0.004
	0.158	0.064	0.152	0.007	0.012	0.013
	0.179	0.073	0.172	0.008	0.013	0.014

Measured orientation data for the gap-wise NLSF profile of the 50 wt% material at the initial state in Ch. 5. In each block, the top entry is the average data, the middle is the standard deviation, and the bottom is the 95% CI. 1 refers to the flow direction, 2 refers to the neutral direction, and 3 to the gap-wise direction

z/H	A11	A12	A22	A33	A13	A23
0.071	0.306	0.045	0.654	0.040	0.014	-0.007
	0.028	0.092	0.033	0.007	0.011	0.033
	0.032	0.104	0.037	0.008	0.012	0.038
0.214	0.350	-0.016	0.617	0.034	-0.019	-0.010
	0.215	0.058	0.211	0.007	0.024	0.017
	0.243	0.065	0.239	0.007	0.027	0.019
0.357	0.382	0.147	0.586	0.032	0.008	-0.002
	0.165	0.155	0.154	0.015	0.021	0.008
	0.187	0.175	0.174	0.017	0.024	0.010
0.500	0.295	-0.018	0.668	0.037	0.007	-0.003
	0.074	0.089	0.059	0.015	0.019	0.010
	0.084	0.101	0.067	0.017	0.021	0.011
0.643	0.337	0.162	0.616	0.047	0.021	0.017
	0.079	0.132	0.070	0.037	0.016	0.006
	0.089	0.149	0.079	0.041	0.018	0.007
0.786	0.308	0.239	0.658	0.035	0.002	-0.004
	0.120	0.013	0.102	0.019	0.020	0.017
	0.135	0.015	0.115	0.022	0.023	0.019
0.929	0.240	0.068	0.720	0.040	-0.001	-0.003
	0.232	0.160	0.033	0.016	0.002	0.008
	0.263	0.181	0.037	0.019	0.002	0.009

Measured orientation data for the gap-wise NLSF profile of the 30 wt% material after 1 Hencky strain in Ch. 5. In each block, the top entry is the average data, the middle is the standard deviation, and the bottom is the 95% CI. 1 refers to the flow direction, 2 refers to the neutral direction, and 3 to the gap-wise direction

z/H	A11	A12	A22	A33	A13	A23
0.071	0.363	-0.019	0.607	0.302	0.002	-0.001
	0.016	0.080	0.171	0.008	0.006	0.000
	0.023	0.110	0.237	0.011	0.008	0.000
0.214	0.476	-0.061	0.500	0.024	-0.022	-0.004
	0.071	0.014	0.086	0.015	0.003	0.012
	0.099	0.020	0.119	0.020	0.004	0.016
0.357	0.571	-0.098	0.418	0.011	0.001	0.009
	0.077	0.092	0.085	0.008	0.004	0.006
	0.107	0.128	0.118	0.011	0.006	0.009
0.500	0.737	0.057	0.252	0.012	-0.021	-0.009
	0.020	0.117	0.024	0.004	0.009	0.018
	0.028	0.162	0.033	0.006	0.012	0.025
0.643	0.593	0.002	0.392	0.015	-0.028	-0.021
	0.016	0.011	0.010	0.006	0.015	0.015
	0.022	0.015	0.014	0.009	0.020	0.021
0.786	0.459	0.052	0.505	0.036	-0.002	0.000
	0.051	0.141	0.017	0.034	0.007	0.021
	0.070	0.195	0.024	0.046	0.009	0.028
0.929	0.522	-0.056	0.468	0.010	-0.012	-0.008
	0.043	0.038	0.420	0.010	0.022	0.006
	0.059	0.053	0.581	0.014	0.030	0.008

Measured orientation data for the gap-wise NLSF profile of the 40 wt% material after 1 Hencky strain in Ch. 5. In each block, the top entry is the average data, the middle is the standard deviation, and the bottom is the 95% CI. 1 refers to the flow direction, 2 refers to the neutral direction, and 3 to the gap-wise direction

z/H	A11	A12	A22	A33	A13	A23
0.071	0.520	0.010	0.018	0.462	0.013	-0.001
	0.032	0.001	0.007	0.025	0.012	0.014
	0.036	0.001	0.008	0.028	0.014	0.016
0.214	0.284	0.001	0.017	0.700	0.067	0.000
	0.074	0.007	0.009	0.065	0.022	0.005
	0.084	0.008	0.010	0.073	0.025	0.005
0.357	0.598	0.008	0.034	0.368	0.010	0.004
	0.055	0.002	0.008	0.047	0.040	0.008
	0.063	0.003	0.009	0.054	0.045	0.009
0.500	0.813	0.021	0.012	0.176	-0.007	-0.001
	0.091	0.001	0.004	0.096	0.041	0.006
	0.103	0.001	0.005	0.108	0.047	0.007
0.643	0.514	0.020	0.022	0.464	-0.060	0.001
	0.193	0.015	0.008	0.185	0.090	0.002
	0.219	0.017	0.009	0.209	0.102	0.003
0.786	0.466	0.016	0.042	0.492	-0.034	0.007
	0.014	0.025	0.003	0.018	0.108	0.005
	0.016	0.029	0.004	0.020	0.122	0.006
0.929	0.346	0.013	0.027	0.627	0.019	0.003
	0.057	0.004	0.008	0.049	0.016	0.011
	0.065	0.004	0.009	0.056	0.018	0.012

Measured orientation data for the gap-wise NLSF profile of the 50 wt% material after 1 Hencky strain in Ch. 5. In each block, the top entry is the average data, the middle is the standard deviation, and the bottom is the 95% CI. 1 refers to the flow direction, 2 refers to the neutral direction, and 3 to the gap-wise direction

z/H	A11	A12	A22	A33	A13	A23
0.071	0.407	0.065	0.562	0.031	0.008	0.005
	0.106	0.087	0.115	0.011	0.017	0.005
	0.120	0.098	0.131	0.013	0.019	0.006
0.214	0.503	0.051	0.481	0.016	0.016	0.009
	0.293	0.065	0.290	0.006	0.031	0.003
	0.332	0.073	0.328	0.006	0.036	0.003
0.357	0.625	0.095	0.352	0.023	0.035	0.000
	0.202	0.630	0.197	0.009	0.048	0.010
	0.229	0.713	0.222	0.010	0.054	0.012
0.500	0.746	0.088	0.234	0.020	0.041	0.008
	0.045	0.058	0.050	0.005	0.058	0.015
	0.051	0.065	0.057	0.006	0.065	0.017
0.643	0.603	-0.028	0.377	0.020	0.005	0.011
	0.109	0.057	0.110	0.004	0.035	0.007
	0.123	0.065	0.125	0.005	0.039	0.008
0.786	0.454	0.005	0.521	0.025	0.009	0.013
	0.105	0.101	0.106	0.007	0.029	0.005
	0.118	0.114	0.120	0.008	0.032	0.006
0.929	0.443	-0.063	0.527	0.030	0.002	0.022
	0.184	0.162	0.183	0.001	0.049	0.025
	0.208	0.183	0.207	0.001	0.055	0.028

Startup of Shear Stress Growth for the 30 wt% material in Ch. 5. This was not reported in the chapter but is included here for posterity

Shear Strain -	Shear Stress Avg Pa	Shear Stres Std Dev Pa
0	1	0
1	88.49889	26.9798609
2	132.5438	22.3629003
3	162.4877	11.0647641
4	188.3053	10.7962918
5	202.0674	4.07050086
6	215.8295	11.7864163
7	229.9342	21.3959457
8	244.15	30.874346
9	259.3877	37.4585405
10	277.6112	36.2810321
11	295.8347	36.2791579
12	320.4522	39.8022393
13	347.1446	44.9932901
14	370.9062	52.1646471
15	386.105	63.7037429
16	401.3038	75.4719721
17	408.0533	79.0753172
18	412.061	80.0456623
19	416.8206	82.1614241
20	423.7773	87.7890207
21	430.734	93.8271608
22	440.0884	111.532817
23	450.221	132.997449
24	461.7225	149.249401
25	477.2238	150.600685
26	492.7251	152.591993
27	502.917	148.401508
28	511.386	142.14841
29	521.5711	138.026348
30	536.7699	141.753814
31	551.9687	148.233734
32	547.5856	148.209817
33	536.8482	145.807504
34	534.4984	141.046387
35	556.6539	129.436682

36	578.8094	119.308316
37	608.5579	101.095508
38	640.7703	80.3136126
39	663.4188	61.0157602
40	658.1257	47.3208233
41	652.8325	42.8879922
42	635.3221	31.014325
43	613.8472	30.8945779
44	599.7573	44.2143513
45	607.2433	49.5116621
46	614.7293	56.6680939
47	638.4288	56.836224
48	667.3897	56.8567328
49	689.6019	55.3892521
50	692.0973	44.6619927
51	694.5926	39.1518305
52	694.1763	45.3689753
53	692.8152	69.2767085
54	689.8537	97.8957868
55	682.2165	125.740018
56	674.5793	155.458613
57	691.5479	173.205742
58	716.5012	188.248083
59	741.5509	196.057842
60	766.8823	179.421449
61	792.2136	162.787265
62	811.8931	152.149255
63	829.7384	143.694533
64	845.9063	135.173988
65	857.1731	126.042721
66	868.4398	117.620625
67	860.924	91.8356935
68	847.3131	67.9534638
69	835.8811	66.7559626
70	830.8148	86.9431245
71	825.7486	107.355883
72	814.4595	91.5527026
73	801.151	64.4276778
74	788.2861	47.7657494
75	776.7169	58.3592337
76	765.1476	68.9797594
77	759.687	84.0134481
78	756.2087	100.475612

79	757.9944	105.603667
80	775.1592	78.4299031
81	792.324	54.0237485
82	840.1462	53.7166522
83	897.9168	97.2694712
84	955.1283	137.006458
85	1010.706	137.50548
86	1066.284	138.356119
87	1089.263	149.450874
88	1101.664	165.114799
89	1106.989	185.37696
90	1091.639	216.234446
91	1076.289	247.251606
92	1060.653	249.909572
93	1044.925	246.747618
94	1028.773	235.832283
95	1011.381	192.851794
96	993.9892	151.955141
97	946.5682	87.1792363
98	889.4025	141.34348
99	770.1082	214.109301
100	469.3012	174.118181

Startup of Shear Stress Growth for the 40 wt% material n Ch. 5. This was not reported in the chapter but is included here for posterity

Shear Strain -	Shear Stress Avg Pa	Shear Stress Std Dev Pa
0	1	0
1	190.603	107.5192121
2	301.1108	171.0102117
3	385.9519	222.4484862
4	464.9313	274.836452
5	526.7852	328.759943
6	588.6391	384.9262253
7	633.5372	435.3041773
8	672.9332	483.7667062
9	704.1921	522.5335207
10	711.678	532.3662495
11	719.164	542.2032691

12	728.3627	558.432517
13	738.1172	576.9424687
14	743.0704	590.2392241
15	733.9965	587.8655877
16	724.9226	585.6771555
17	708.7695	542.2199577
18	690.3192	485.4723951
19	673.7007	428.911517
20	662.4339	372.9816093
21	651.1671	318.4286977
22	646.2944	283.9832525
23	643.4966	258.5861582
24	640.0239	234.3186489
25	634.5796	207.0811542
26	629.1352	189.0664118
27	628.7148	184.2362095
28	629.9247	181.5687056
29	630.4018	173.033804
30	628.7383	150.5589764
31	627.0747	136.2484419
32	629.5216	131.2037572
33	633.3024	129.3562971
34	635.6178	132.3667535
35	633.6518	143.7866671
36	631.6858	156.6212078
37	655.867	175.1403151
38	688.5331	196.753689
39	715.9931	209.8743997
40	728.2429	194.9827768
41	740.4927	180.1353321
42	718.9451	159.9812849
43	686.4302	138.447851
44	657.0198	125.3957069
45	636.6791	136.8821854
46	616.3384	149.9880325
47	623.458	165.0381075
48	639.4886	180.5694766
49	663.3284	194.7876672
50	709.9835	205.0672041
51	756.6386	215.5845972
52	817.7945	204.1303357
53	883.656	185.6004075
54	934.7089	167.7587989

55	942.4974	151.5728336
56	950.2858	135.3922976
57	946.485	154.2877774
58	938.9234	192.359251
59	938.3612	234.2689849
60	958.2482	276.552036
61	978.1352	321.3332481
62	1002.019	347.0769241
63	1027.199	366.3472285
64	1050.354	377.3458098
65	1067.595	364.3587914
66	1084.835	351.9380158
67	1088.203	325.1567699
68	1087.068	301.29669
69	1086.185	278.4546744
70	1086.034	236.4123317
71	1085.882	205.4988155
72	1087.387	174.0632358
73	1089.428	184.4086064
74	1084.509	219.4579952
75	1059.253	224.804118
76	1033.998	250.5470074
77	997.3239	246.137461
78	956.945	243.9230097
79	930.7962	242.0367943
80	946.2219	210.9254794
81	961.6475	211.2479382
82	1010.357	257.2347505
83	1069.866	344.9946219
84	1131.459	445.6380161
85	1199.135	540.7463287
86	1266.811	640.7713638
87	1304.401	657.6053547
88	1332.228	648.3564646
89	1353.094	621.9889842
90	1353.623	540.9719094
91	1354.152	460.1802776
92	1355.652	393.3888426
93	1357.467	331.169902
94	1349.159	265.2567442
95	1311.275	188.4532878
96	1273.391	112.9570321
97	1233.738	56.29258587

98	1193.51	92.56840722
99	1135.463	192.801948
100	1025.352	362.8186313

Startup of Shear Stress Growth for the 50 wt% material in Ch. 5. This was not reported in the chapter but is included here for posterity

Shear Strain -	Shear Stress Avg Pa	Shear Stress Std Dev Pa
0	1	0
1	228.8221345	56.49261577
2	384.8316478	50.71955593
3	517.5377278	29.46652641
4	634.3939381	30.09779441
5	704.9436661	47.93719474
6	775.4933941	66.39231327
7	827.8884766	91.03620481
8	874.3923166	122.0825955
9	918.3894862	154.8833149
10	955.0632462	193.325158
11	991.7370062	238.3410659
12	1006.088545	248.5677257
13	1013.196449	246.7428502
14	1016.987835	251.7812086
15	1011.089787	278.2898193
16	1005.191739	306.7780863
17	1014.936373	377.2170426
18	1029.757109	460.951363
19	1049.301955	542.0714137
20	1082.648611	617.4069317
21	1115.995267	694.9726422
22	1127.190972	703.814682
23	1131.19862	690.2298876
24	1133.37447	674.093968
25	1130.198598	649.8493331
26	1127.022726	625.6078647
27	1110.659046	579.5921902
28	1090.015878	527.9148225
29	1079.823597	498.6712753
30	1100.164301	531.0416947

31	1120.505005	565.1129735
32	1163.795921	563.2323563
33	1214.534257	549.4223073
34	1254.281808	540.6029403
35	1261.919024	546.3847958
36	1269.55624	552.3683575
37	1273.53969	565.8570031
38	1276.337482	581.7505686
39	1289.991085	603.8909098
40	1335.360685	646.5461296
41	1380.730285	692.3352857
42	1426.499516	760.5318745
43	1472.398428	839.9180655
44	1525.952326	904.8850776
45	1601.87079	920.2100926
46	1677.789254	939.5041958
47	1690.508999	878.4306878
48	1682.720551	790.5914805
49	1679.309135	679.6285917
50	1688.685519	501.6670234
51	1698.061903	326.7703615
52	1750.769658	248.4478956
53	1817.538586	260.7889166
54	1884.384642	307.4025067
55	1951.456034	298.4497904
56	2018.527426	295.8314192
57	2085.541728	294.403945
58	2152.537504	294.4068929
59	2200.135508	308.8178967
60	2191.061588	360.9240042
61	2181.987668	415.8267776
62	2177.138414	467.6544026
63	2173.660078	518.7887911
64	2177.238983	559.6777121
65	2201.436103	569.049501
66	2225.633223	578.4260552
67	2291.563192	578.0942408
68	2371.035608	586.0785093
69	2442.988012	611.2855092
70	2492.970188	657.3682883
71	2542.952364	707.2018899
72	2539.954946	645.8583971
73	2519.765474	555.0139006

74	2495.526765	459.5255632
75	2459.457933	348.3469189
76	2423.389101	317.6115335
77	2350.611348	286.2611612
78	2265.921428	273.2847999
79	2199.453073	293.0678608
80	2186.220273	302.5073934
81	2172.987473	344.7272793
82	2199.603549	397.406552
83	2239.150717	448.3715109
84	2274.263007	480.5035719
85	2296.418495	462.1238458
86	2318.573983	451.6290754
87	2365.335295	450.4887632
88	2420.081279	479.5769873
89	2483.157122	530.0107912
90	2570.569218	574.6071652
91	2657.981314	624.5558485
92	2610.603731	478.1097755
93	2519.486451	276.4126797
94	2427.405067	129.4539052
95	2332.506987	33.96004351
96	2237.608907	102.0902269
97	2213.159986	193.6574589
98	2211.57205	286.2480986
99	2043.610569	213.8684826
100	1389.577357	348.1093064

NLSF stress growth data for the 30 wt% material in Ch. 5. This was not reported in the chapter but is included here for posterity.

Time	Strain	Load	Load Std Dev	Load 95% CI
s	-	N	N	N
0	0	0.21625	0.347402	0.481465
0.076	0.038	36.1291	18.85444	26.13044
0.102	0.051	59.99465	3.565869	4.941951
0.128	0.064	86.7726	31.5767	43.76227
0.154	0.077	129.1122	25.99119	36.0213
0.18	0.09	170.644	8.650815	11.9892

0.207	0.1035	204.9228	3.725675	5.163427
0.234	0.117	234.1429	11.33902	15.7148
0.262	0.131	262.7531	19.52463	27.05926
0.291	0.1455	292.3029	28.09646	38.939
0.32	0.16	321.6843	36.63584	50.77375
0.349	0.1745	350.0784	45.09503	62.49737
0.379	0.1895	378.0387	53.4449	74.06949
0.409	0.2045	404.5977	61.94482	85.84956
0.44	0.22	431.2586	70.02288	97.04497
0.471	0.2355	456.8213	77.88343	107.9389
0.503	0.2515	482.1495	85.20319	118.0834
0.535	0.2675	505.9714	91.94149	127.4221
0.568	0.284	530.2317	98.20709	136.1056
0.601	0.3005	554.5674	104.1237	144.3055
0.635	0.3175	580.1673	109.9604	152.3945
0.669	0.3345	605.7267	115.507	160.0816
0.704	0.352	633.0401	121.9497	169.0105
0.74	0.37	661.6504	127.7582	177.0606
0.776	0.388	691.7626	134.6508	186.6131
0.813	0.4065	722.4149	141.2658	195.7808
0.85	0.425	754.3641	147.6783	204.6679
0.888	0.444	787.0485	153.2902	212.4455
0.927	0.4635	821.6863	158.5026	219.6693
0.967	0.4835	858.7097	164.8159	228.419
1.007	0.5035	897.2701	170.3937	236.1493
1.048	0.524	939.6333	179.19	248.3401
1.09	0.545	983.3571	188.049	260.6178
1.133	0.5665	1029.782	196.7452	272.67
1.177	0.5885	1079.716	205.8017	285.2213
1.222	0.611	1130.824	216.0955	299.4876
1.268	0.634	1186.736	226.6382	314.0987
1.315	0.6575	1245.875	236.9422	328.3791
1.363	0.6815	1310.957	249.6457	345.9849
1.412	0.706	1377.729	261.0389	361.7748
1.463	0.7315	1452.718	277.9567	385.2213
1.515	0.7575	1531.124	293.4238	406.6571
1.568	0.784	1615.434	310.4936	430.3143
1.623	0.8115	1708.997	333.8117	462.6309
1.679	0.8395	1808.403	357.5293	495.5012
1.735	0.8675	1915.728	383.735	531.8198
1.789	0.8945	2025.847	407.8783	565.2801
1.885	0.9425	2140.094	425.3198	589.4524
1.931	0.9655	2257.531	438.4099	607.5939

1.973	0.9865	2383.48	438.1381	607.2172
2	1	2457.914	513.6559	711.8777

NLSF stress growth data for the 40 wt% material in Ch. 5. This was not reported in the chapter but is included here for posterity.

Time	Strain	Load	Load Std Dev	Load 95% CI
s	-	N	N	N
0	0	0.1815	0.245038	0.277281
0.076	0.038	42.56103	6.790888	7.684471
0.102	0.051	50.60163	4.950997	5.602478
0.128	0.064	67.21607	19.69339	22.28476
0.154667	0.077333	123.6221	70.10116	79.32547
0.180667	0.090333	173.0663	109.6083	124.0312
0.207667	0.103833	206.7802	134.1688	151.8235
0.235333	0.117667	240.1515	141.3298	159.9268
0.263333	0.131667	272.4695	150.0097	169.7488
0.292333	0.146167	303.3537	163.8087	185.3636
0.321333	0.160667	333.0993	178.436	201.9157
0.350333	0.175167	360.929	192.2664	217.566
0.380333	0.190167	388.5776	205.9291	233.0264
0.410333	0.205167	414.3349	218.4664	247.2135
0.441333	0.220667	439.7882	230.6924	261.0482
0.472333	0.236167	464.1482	242.0709	273.924
0.504333	0.252167	488.1266	252.8461	286.117
0.536333	0.268167	510.6507	262.8719	297.4621
0.569333	0.284667	534.3048	273.5245	309.5164
0.602333	0.301167	556.9758	283.6115	320.9307
0.636333	0.318167	580.1049	293.3024	331.8969
0.670333	0.335167	602.6569	302.3892	342.1793
0.705333	0.352667	626.0459	312.1844	353.2634
0.741	0.3705	649.9297	321.6797	364.0081
0.777	0.3885	674.3936	331.3773	374.9819
0.814	0.407	700.4781	341.9799	386.9796
0.851667	0.425833	726.954	351.3882	397.6259
0.889667	0.444833	753.8909	361.3064	408.8492
0.928667	0.464333	781.2618	371.8995	420.8361
0.968667	0.484333	811.1766	383.4152	433.8672
1.009333	0.504667	842.0577	395.3659	447.3904
1.050333	0.525167	875.0269	409.7289	463.6434
1.092333	0.546167	909.733	426.5411	482.6679
1.135333	0.567667	944.9483	446.2502	504.9703

1.179333	0.589667	986.7659	466.9914	528.4409
1.224333	0.612167	1029.412	487.3706	551.5016
1.270333	0.635167	1074.069	507.6041	574.3976
1.317333	0.658667	1119.44	529.287	598.9337
1.365333	0.682667	1166.791	552.1912	624.8517
1.414333	0.707167	1219.669	573.7676	649.2672
1.465333	0.732667	1277.903	598.7935	677.5862
1.517333	0.758667	1341.253	628.626	711.3442
1.570333	0.785167	1406.858	659.3322	746.0909
1.625333	0.812667	1479.307	693.7092	784.9914
1.681333	0.840667	1556.907	729.8198	825.8537
1.739333	0.869667	1641.841	770.1366	871.4756
1.798667	0.899333	1735.228	811.6367	918.4365
1.859	0.9295	1831.44	854.2222	966.6256
1.918667	0.959333	1933.077	895.5396	1013.38
1.978	0.989	2036.806	933.596	1056.444
2	1	2088.965	981.2115	1110.325

NLSF stress growth data for the 50 wt% material in Ch. 5. This was not reported in the chapter but is included here for posterity.

Time s	Strain	Load Avg N	Load SD N	Load 95% CI N
0.000	0.000	-0.15417	0.065929	0.074604
0.076	0.038	17.32807	5.399043	6.10948
0.102	0.051	31.2676	9.26288	10.48174
0.128	0.064	51.11333	4.596187	5.200979
0.154	0.077	56.46797	1.839809	2.081902
0.180	0.090	70.70243	22.67011	25.65317
0.207	0.104	118.5848	42.22213	47.77796
0.235	0.117	173.5089	35.93947	40.66859
0.263	0.131	211.614	25.72285	29.10761
0.292	0.146	239.1367	22.02639	24.92475
0.321	0.160	262.3085	21.87162	24.74961
0.350	0.175	283.2715	22.55055	25.51788
0.380	0.190	303.758	23.61449	26.72182
0.410	0.205	323.1858	24.76667	28.02561
0.441	0.220	341.9211	26.3493	29.81649
0.472	0.236	359.9174	27.84697	31.51123
0.504	0.252	377.9259	29.42491	33.29681
0.536	0.268	395.3579	30.95023	35.02283
0.569	0.284	413.2524	32.9326	37.26606

0.602	0.301	430.7517	34.94566	39.54401
0.636	0.318	447.8862	36.62725	41.44688
0.670	0.335	464.5764	37.91913	42.90875
0.705	0.352	481.6844	38.76051	43.86084
0.740	0.370	498.5783	39.28138	44.45025
0.776	0.388	515.9257	39.83709	45.07909
0.813	0.407	533.8468	40.60841	45.95189
0.850	0.425	551.7951	41.34247	46.78255
0.888	0.444	570.1674	41.84976	47.3566
0.927	0.464	588.4764	42.65533	48.26817
0.967	0.484	608.0161	43.33883	49.0416
1.007	0.504	627.5949	43.71449	49.46669
1.048	0.524	647.8038	44.43895	50.28648
1.090	0.545	668.2829	45.06303	50.99268
1.133	0.567	688.9027	45.83314	51.86412
1.177	0.589	711.8491	46.36406	52.4649
1.222	0.611	734.2524	45.87668	51.91339
1.268	0.634	758.1549	44.91716	50.82762
1.315	0.658	783.2375	43.67296	49.4197
1.363	0.682	809.6026	41.74912	47.2427
1.412	0.706	838.2399	39.39709	44.58119
1.463	0.732	866.7875	38.99598	44.1273
1.515	0.758	896.5457	40.23991	45.53491
1.568	0.784	927.3113	41.09649	46.5042
1.623	0.812	961.4939	42.63228	48.24208
1.679	0.840	995.3427	44.26844	50.09353
1.737	0.869	1030.266	45.95058	51.99702
1.797	0.898	1068.572	49.58993	56.11525
1.858	0.929	1107.344	50.86346	57.55636
1.921	0.960	1146.913	52.82513	59.77616
1.986	0.993	1189.105	53.5322	60.57628
2.000	1.000	1198.395	55.05497	62.29942